SISSA
Scuola
Internazionale
Superiore di
Studi Avanzati

Physics Area - PhD course in
Astrophysics and Cosmology

High-redshift Dusty Star-Forming Galaxies: a panchromatic approach to constrain massive galaxy evolution

Candidate:
Lara Pantoni

Advisors:
Prof. Andrea Lapi
Dr. Marcella Massardi

Academic Year 2020-21

Declaration of Authorship

I, Lara Pantoni, declare that this thesis titled, "High-redshift Dusty Star-Forming Galaxies: a panchromatic approach to constrain massive galaxy evolution" and the work presented in it are my own. I confirm that:

- This work was done wholly or mainly while in candidature for a research degree at SISSA.
- Where any part of this thesis has previously been submitted for a degree or any other qualification at SISSA or any other institution, this has been clearly stated.
- Where I have consulted the published work of others, this is always clearly attributed.
- Where I have quoted from the work of others, the source is always given. With the exception of such quotations, this thesis is entirely my own work.
- I have acknowledged all main sources of help.
- Where the thesis is based on work done by myself jointly with others, I have made clear exactly what was done by others and what I have contributed myself.

To Trieste
that, over time,
I learnt to know and love.

Trieste
si colora di una bellezza silenziosa,
nel buio della notte.
Il vento le sussurra un racconto
di tempi passati, che rivive tra i bianchi palazzi,
nel gioco di luci dipinto
dal timido chiarore lunare.
E il mare, specchio della sua bellezza austera
e un po' altezzosa,
la avvolge e la abbraccia, quasi a volerla consolare,
orgogliosa e nostalgica.
Di notte, Trieste
si dipinge d'una bellezza silenziosa e, quieta,
sussurra per le strade deserte
il suo sospiro d'amore.

"We are stars wrapped in skin. The light you are seeking has always been within."

Gialal al-Din Rumi

Abstract

High-redshift Dusty Star-Forming Galaxies: a panchromatic approach to constrain massive galaxy evolution

by Lara Pantoni

The goal of this thesis is to investigate the early stages of massive galaxy evolution by defining an overall view of their physical properties combining the information extracted by all the details of their spectral behaviour. To this aim I focused on the population of Dusty Star-Forming Galaxies at the Cosmic Noon ($z \sim 2$). In my thesis project I first deal with the modelling of the spatially-averaged time evolution of galaxy baryonic components, namely gas, stars, metals and dust, on the basis of a simple but effective approach that allows to solve analytically the equations that describe their evolution. Contrariwise to most of the analytic models on the market, the one developed during this Ph.D. thesis self-consistently compute the metal and dust enrichment histories of the cold gas and stellar mass using as input the solutions for the evolution of the mass components. The solutions are coupled to specific prescriptions for parameter setting (inspired by *in-situ* galaxy-black hole co-evolution) and merger rates (based on numerical simulations) and, as such, reproduce the main statistical relationships followed by high-z massive star-forming galaxies and local ellipticals, that are thought to be their quiescent counterparts at $z \sim 0$. The analytic solutions are then exploited to interpret the spatially-averaged astrophysical properties of a pilot sample of (sub-)millimeter selected Dusty Star-Forming Galaxies in the multi-wavelength GOODS-S field and spectroscopically confirmed to be at the peak of Cosmic Star Formation History. Ultimately, they are used to disentangle the main physical processes regulating the evolution of these galaxies.

The study highlights the importance of multi-wavelength broad-band and spectroscopic data to constrain dusty galaxy evolution at high-z and their role in the formation of spheroids, along with the need of a complete theoretical scenario that allows to self-consistently interpret the outcomes obtained from observational analyses. One possible framework is the one provided by the *in-situ* scenario for galaxy-black hole co-evolution, that has been used in this work to interpret the reconstructed panchromatic view combining spatially integrated (i.e. galaxy age, Star Formation Rate, stellar mass, dust mass, dust attenuation), spatially resolved (multi-wavelength sizes) and spectral (i.e. molecular gas content, kinematics and AGN/stellar driven outflows) properties of the aforementioned pilot sample of DSFG.

The analysis is performed under specific requirements (e.g. spectroscopic measurement of galaxy redshift, complete sampling of galaxy multi-band emission) in order to unbiasedly constrain galaxy integral properties by performing an energy-balanced fit of the SED from the UV/optical to the radio band, including also galaxy X-ray emission, with the Code Investigating GALaxy Emission.

Galaxy optical, far-infrared and radio sizes are measured from continuum maps at the highest spatial resolution currently available ($\Delta\theta \lesssim 1$ arcsec). CO spectral emission lines are extracted from publicly available data cubes in the Atacama Large Millimeter/sub-millimeter Array Archive and allow to measure the molecular gas content and to disentangle between a disk dominated configuration of the gaseous component and molecular outflows possibly driven by the central active nucleus. The multiple pieces of information coming from such a panchromatic study offer a clear description of the properties of individual galaxies and, once each of them is inscribed in the evolutionary context, offer a general view of the evolutionary mechanisms.

This Ph.D. thesis is based on the following publications:

1. An ALMA view of 11 Dusty Star-Forming Galaxies at the peak of Cosmic Star Formation History, by **Pantoni, L.** ; Massardi, M. ; Lapi, A. ; Donevski, D. ; D'Amato, Q. ; Giulietti, M. ; Pozzi, F. ; Talia, M. ; Vignali, C. ; Cimatti, A. ; Silva, L. ; Bressan, A. ; Ronconi, T. ; *Monthly Notices of the RAS, Volume 507, Issue 3, pp.3998-4015, November 2021*.

2. Unveiling the nature of 11 Dusty Star-Forming Galaxies at the peak of Cosmic Star Formation History, by **Pantoni, L.** ; Lapi, A. ; Massardi, M. ; Donevski, D. ; Bressan, A. ; Silva, L. ; Pozzi, F. ; Vignali, C. ; Talia, M. ; Cimatti, A. ; Ronconi, T. ; Danese, L.; *Monthly Notices of the RAS, Volume 504, Issue 1, pp.928-950, June 2021*.

3. New Analytic Solutions for Galaxy Evolution. II. Wind Recycling, Galactic Fountains, and Late-type Galaxies, by **Lapi, A.** ; Pantoni, L. ; Boco, L. ; Danese, L. ; *The Astrophysical Journal, Volume 897, Issue 1, id.81, July 2020*.

4. New Analytic Solutions for Galaxy Evolution: Gas, Stars, Metals, and Dust in Local ETGs and Their High-z Star-forming Progenitors, by **Pantoni, L.** ; Lapi, A. ; Massardi, M. ; Goswami, S. ; Danese, L. ; *The Astrophysical Journal, Volume 880, Issue 2, article id. 129, 21 pp., August 2019*.

5. The Dramatic Size and Kinematic Evolution of Massive Early-type Galaxies, by **Lapi, A.** ; Pantoni, L. ; Zanisi, L. ; Shi, J. ; Mancuso, C. ; Massardi, M. ; Shankar, F. ; Bressan, A. ; Danese, L. ; *The Astrophysical Journal, Volume 857, Issue 1, article id. 22, 22 pp., April 2018*.

Other publications:

1. The effects of the initial mass function on Galactic chemical enrichment, by **Goswami, S.** ; Slemer, A. ; Marigo, P. ; Bressan, A. ; Silva, L. ; Spera, M. ; Boco, L. ; Grisoni, V. ; Pantoni, L. ; Lapi, A. ; *Astronomy & Astrophysics, Volume 650, id.A203, 26 pp., June 2021*.

2. Einstein, Planck and Vera Rubin: relevant encounters between the Cosmological and the Quantum Worlds, by **Salucci, P.** ; Esposito, G. ; Lambiase, G. ; Battista, E. ; Benetti, M. ; Bini, D. ; Boco, L. ; Sharma, G. ; Bozza, V. ; Buoninfante, L. ; Capolupo, A. ; Capozziello, S. ; Covone, G. ; D'Agostino, R. ; De Laurentis, M. ; De Martino, I. ; De Somma, G. ; Di Grezia, E. ; Di Paolo, C. ; Fatibene, L. ; Gammaldi, V. ; Geralico, A. ; Ingoglia, L. ; Lapi, A. ; Luciano, G. ; Mastrototaro, L. ; Naddeo, A. ; Pantoni, L. ; Petruzziello, L. ; Piedipalumbo, E. ; Pietroni, S. ; Quaranta, A. ; Rota, P. ; Sarracino, G. ; Sorge, F. ; Stabile, A. ; Stornaiolo, C. ; Tedesco, A. ; Valdarnini, R. ; Viaggiu, S. ; Yunge, A. ; *Frontiers in Physics, Volume 8, id.579, February 2021*.

3. In pursuit of giants. I. The evolution of the dust-to-stellar mass ratio in distant dusty galaxies, by **Donevski, D.** ; Lapi, A. ; Małek, K. ; Liu, D. ; Gómez-Guijarro, C. ; Davé, R. ; Kraljic, K. ; Pantoni, L. ; Man, A. ; Fujimoto, S. ; Feltre, A. ; Pearson, W. ; Li, Q. ; Narayanan, D. ; *Astronomy & Astrophysics, Volume 644, id.A144, 25 pp., December 2020*.

Contents

List of Figures

List of Tables

List of Abbreviations

ACS	**A**dvanced **C**amera for **S**urveys
AGN	**A**ctive **G**alactic **N**ucleus
ALMA	**A**tacama **L**arge **M**illimeter/submillimeter **A**rray
APEX	**A**tacama **P**athfinder **EX**periment
ASTE	**A**tacama **S**ubmillimeter **T**elescope **E**xperiment
BB	**B**lack **B**ody
BC	**B**irth **C**loud
CANDELS	**C**osmic **A**ssembly **N**ear-infrared **D**eep **E**xtragalactic **L**egacy **S**urvey
CIGALE	**C**ode **I**nvestigating **GA**laxy **E**mission
CDF-S	**C**handra **D**eep **F**ield **S**outh
DM	**D**ark **M**atter
DSFG	**D**usty **S**tar **F**orming **G**alaxy
DTD	**D**elay **T**ime **D**istribution
ETG	**E**arly **T**ype **G**alaxy
FIR	**F**ar **I**nfra**R**ed
GMRT	**G**iant **M**etre-Wave **R**adio **T**elescope
GOODS-S	**G**reat **O**bservatories **O**rigins **S**urvey **S**outh
H-ATLAS	**H**erschel **A**strophysical **T**erahertz **L**arge **A**rea **S**urvey
HerMES	**Her**schel **M**ulti-tired **E**xtra-galactic **S**urvey
HST	**H**ubble **S**pace **T**elescope
HUDF	**H**ubble **U**ltra **D**eep **F**ield
IGM	**I**nter **G**alactic **M**edium
IMF	**I**nitial **M**ass **F**unction
IRAC	**I**nfra**R**ed **A**rray **C**amera
ISAAC	**I**nfrared **S**pectrometer and **A**rray **C**amera
JWST	**J**ames **W**ebb **S**pace **T**elescope
LABOCA	**L**arge **A**PEX **BO**lometer **CA**mera
LMT	**L**arge **M**illimeter **T**elescope
LTG	**L**ate **T**ype **G**alaxy
MUSIC	**MU**ltiwavelength **S**outhern **I**nfrared **C**atalog
NFW	**N**avarro **F**renk **W**hite
NIR	**N**ear **I**nfra**R**ed
PACS	**P**hotodetector **A**rray **C**amera and **S**pectrometer
PEP	**P**ACS **E**volutionary **P**robe
PAH	**P**olycyclic **A**romatic **H**ydrocarbon
QSO	**Q**uasi **S**tellar **O**bject
SAM	**S**emi **A**nalytic **M**odel
SED	**S**pectral **E**nergy **D**istribution
SFH	**S**tar **F**ormation **H**istory
SFR	**S**tar **F**ormation **R**ate
SFRD	**S**tar **F**ormation **R**ate **D**ensity
SKA	**S**quare **K**ilometer **A**rray
SMBH	**S**uper **M**assive **B**lack **H**ole

SMG	**S**ub-**M**illimeter **G**alaxies
SPIRE	**S**pectral and **P**hotometric **I**maging **R**eceiver
SN	**S**uper**N**ova
SSP	**S**ingle **S**tellar **P**opulation
UV	**U**ltra-**V**iolet
VLA	**V**ery **L**arge **A**rray
VLT	**V**ery **L**arge **T**elescope
WFC3	**W**ide **F**ield **C**amera **3**

Physical Constants

Speed of Light	$c = 2.99792458 \times 10^{10}$ cm s^{-1}
Gravitational Constant	$G = 6.67 \times 10^{-8}$ g^{-1} cm^3 s^{-2}
Proton Mass	$m_p = 1.66 \times 10^{-24}$
Solar Mass	$M_\odot = 1.99 \times 10^{33}$ g
Solar Luminosity	$L_\odot = 3.90 \times 10^{33}$ erg s^{-1}
Matter Density	$\Omega_{\rm M} = 0.32$
Dark Energy Density	$\Omega_\Lambda = 0.63$
Baryon Density	$\Omega_{\rm b} = 0.05$
Hubble Constant	$H_0 = 100\ h$ km s^{-1} Mpc^{-1} ($h = 0.67$)
Mass Variance	$\sigma_8 = 0.81$ (on a scale of 8 h^{-1} Mpc)
Critical Density	$\rho_c = 2.8 \times 10^{11}\ h^2\ M_\odot$ Mpc^{-3}
Parsec	1 pc $= 3.09 \times 10^{18}$ cm
Year (solar)	1 yr $= 3.16 \times 10^7$ s

Chapter 1

Introduction

Dusty Star-Forming Galaxies (DSFGs) were discovered almost 20 years ago as an abundant population of distant galaxies characterized by a 850 μm flux density greater than a few mJy (e.g., Blain et al., 2002; Hodge et al., 2013; Casey, Narayanan, and Cooray, 2014; Simpson et al., 2015; da Cunha et al., 2015; Miettinen et al., 2015; Oteo et al., 2016). The subsequent multi-wavelength campaigns (e.g., HUDF; Beckwith et al., 2006), along with deep and large-area blind surveys in the IR domain, e.g. PEP (Lutz et al., 2011), HerMES (Oliver et al., 2012), and H-ATLAS (Eales et al., 2010), revealed their nature as massive and very IR luminous galaxies (with typical stellar masses $M_\star \sim$ a few $10^{10} - 10^{11}\ M_\odot$ and IR luminosity $L_{\rm IR} \sim 10^{11} - 10^{12}\, L_\odot$), characterized by extreme Star Formation Rates (SFRs), i.e. of the order of hundreds of $M_\odot\, yr^{-1}$ (e.g. Gruppioni et al., 2013; Béthermin et al., 2017). Due to the intense star formation and the rapid dust enrichment of the Inter Stellar Medium (ISM), these objects are usually very faint or invisible in the UV and optical domains (even where maps to very low flux density level are available), because dust extinction is very efficient in these spectral regimes (e.g. Smail et al., 1999; Walter et al., 2012; Franco et al., 2018; Williams et al., 2019).

Even if the interstellar dust constitute just a few per cent of the ISM mass of a typical star-forming galaxy (see e.g., Li and Mann, 2012), it greatly affects the integrated luminosity of galaxy through the absorption and the scattering of UV/optical stellar light (i.e. the aforementioned *dust extinction*) and then thermally re-radiating it in the FIR domain. In such a way, it was estimated that thermal dust emission contributes to more than 30% of the Universe IR luminosity (see Bernstein, Freedman, and Madore, 2002).

Interstellar dust shapes considerably the Spectral Energy Distribution (SED) of star-forming galaxy, that is well describe by a Modified Black Body (MBB) function in the FIR rest-frame (e.g., Casey, 2012; Bianchi, 2013; Gilli et al., 2014). Thanks to the particular shape of the SED in this wavelength range, the cosmological dimming of the flux density coming from DSFGs at high-z (i.e. proportional to the square of the luminosity distance D_L) is offset, when observed in the millimeter regime, by the shifting of the thermal dust peak into the observing band (the so-called *negative k-correction*). As a result, the flux density remains almost constant over a large redshift range, i.e. $z \sim 1 - 10$ (see the review by Casey, Narayanan, and Cooray, 2014, in particular their Sect. 2.2 and Fig. 3). The first spectroscopic follow-up campaigns revealed the number density of DSFGs to peak at redshift $\sim$ 2.5 (Chapman et al., 2003; Chapman et al., 2005), that is almost coincident with the peak of Cosmic Star Formation History (SFH; see the review by Madau and Dickinson, 2014) and Black Hole Accretion History (BHAH; e.g. Shankar, Weinberg, and Miralda-Escudé, 2009; Aird et al., 2010; Delvecchio et al., 2014). Hence, these galaxies are expected to contribute significantly to both the Star Formation Rate Density (SFRD) and the stellar mass density of the Universe, supplying respectively with the $\sim$ 20% and the

$\sim 30-50\%$ at $z = 2-4$ (see e.g., Michałowski, Hjorth, and Watson, 2010), and to assume a central role in the evolution of Active Galactic Nuclei (AGN) and ultimately in the building up of galactic spheroids and massive Early Type Galaxies (ETGs; see e.g., Swinbank et al., 2006; Cimatti et al., 2008; van Dokkum et al., 2008; Barro et al., 2013; Simpson et al., 2014; Scoville et al., 2017; Toft et al., 2014; Oteo et al., 2017; Rujopakarn et al., 2019). In addition, DSFGs were found to lie both on and above the *main sequence* of star-forming galaxies (e.g., Dunlop et al., 2017; Elbaz et al., 2018), an empirical relation between galaxy stellar mass and SFR (i.e., $\mathrm{SFR} \propto M_\star^\alpha$) followed by the majority of galaxies that are forming stars (e.g., Daddi et al., 2007; Elbaz et al., 2007; Noeske et al., 2007; Speagle et al., 2014) that slightly varies with cosmic time ($0.6 \lesssim \alpha \lesssim 1$ and $\alpha \propto (1+z)^{\sim 3.5}$, becoming flatter at $z > 3$; see Rodighiero et al., 2011).

High-z DSFGs represent, then, a crucial tool to solve the complex puzzles of stellar mass assembly and massive galaxies evolution out to $z > 3$ (e.g., Gruppioni et al., 2020; Talia et al., 2020). To this aim, many progresses have been made in the recent past years, in particular with the advent of ALMA (see the review by Hodge and da Cunha, 2020). For example, ALMA helped in constraining the Rayleigh-Jeans tail of thermal dust emission of $z \sim 2-3$ DSFGs, sampling the light coming from the coldest grains that constitute the bulk of interstellar dust in terms of mass content (e.g., Dunlop et al., 2017). A well sampled FIR SED is indeed essential to fairly estimate the SFR of these objects and then asses their final contribution in the Cosmic stellar mass assembly. However, the study of spatially integrated properties of galaxies alone is not sufficient for characterizing the underling mechanisms driving galaxy evolution across cosmic time. Indeed, many of the most fundamental processes in galaxy evolution that are still not understood (such as stellar and AGN feedback, the triggering and quenching mechanisms of star formation, the build up of spheroids, galaxy-BH co-evolution) lie down to sub-galactic scales.

ALMA observations at sub-arcsecond spatial resolution, investigating scales that are smaller than a tenth of kpc, were very helpful in this respect. They revealed the high-z DSFG dust continuum to be compact ($r \lesssim 1-5$ kpc) and settled in the inner regions of galaxy, both in *starbursts* and main-sequence objects (e.g., Simpson et al., 2015; Barro et al., 2016a; Barro et al., 2017; Hodge et al., 2016; Oteo et al., 2016; Rujopakarn et al., 2016; Fujimoto et al., 2017; Tadaki et al., 2017a; Tadaki et al., 2017b; Massardi et al., 2018; Talia et al., 2018; Nelson et al., 2019). Mostly, the size of dust FIR emission is almost consistent with typical radii measured in the radio band but a way smaller than the optical sizes from HST maps ($r \approx 2-10$ kpc; see e.g., Barro et al., 2016a; Rujopakarn et al., 2016; Chen et al., 2017; Lang et al., 2019; Nelson et al., 2019; Rujopakarn et al., 2019), even if a fraction (~20%; see e.g. Chen et al., 2015) of (sub-)millimeter selected DSFGs are not detected at all in deep HST imaging (e.g., Smail et al., 1999; Walter et al., 2012), including those in *blind* ALMA surveys (e.g., Franco et al., 2018).

The multi-wavelength morphology of these galaxies is still unclear. Many recent work that make use of both ALMA and HST imaging at great spatial resolution (~ a few hundreds of parsec) identify the presence of multiple clumps in the optical rest-frame, while the emission in the FIR rest-frame appears smoother and presents often a gaussian very compact core on sub-kpc scales and a more extended disk with typical radii of a few kpc (see e.g. Rujopakarn et al., 2019). However, clumpy structures on scales of hundreds of parsec were also observed with ALMA in the FIR rest-frame continuum (e.g., Hodge et al., 2019). Moreover, on larger scales, of the order of a few kpc, both isolated and disturbed morphology are observed (see e.g., Hodge et al., 2016; Elbaz et al., 2018), and often multiple components fitting are necessary to model the galaxy multi-wavelength emission (e.g., Targett et al., 2013;

Rujopakarn et al., 2016). These evidences possibly play a role in characterizing the gas supply in galaxies and the diverse routes to mildly obscured and dust-enshrouded star formation, observed in the optical and in the (sub-)millimeter, respectively. Spatially-resolved radio emission, instead, can help in discerning the stellar emission from the AGN contribution. Until now, only a limited number of studies with very good quality spatially-resolved data have been published, and just on small samples of DSFGs, mostly as a consequence of the long integration times (i.e., orders of several hours or more) that this analysis requires at high-z.

Therefore, even if many step forward have been taken towards a more comprehensive characterization of high-z DSFGs since their discover, we are far away from fully physically characterizing this class of galaxies and from thoroughly understanding their role in the framework of galaxy formation and evolution. In particular, we lack of a comprehensive observational characterization of mechanisms and astrophysical processes in the various stages of the evolutionary landscape. In order to reach this goal, on the one hand it is essential to better constrain the spatially integrated properties of galaxies (i.e., stellar mass, dust and gas content, gas metallicity, the activity of the central SMBH) throughout a complete sampling of their SEDs (see e.g., Béthermin et al., 2014; Magdis et al., 2012; Małek et al., 2018; Bianchini et al., 2019; Donevski et al., 2020; Dudzevičiūtė et al., 2020). On the other hand, it is important to proceed with an in-depth investigation of the main baryonic processes occurring inside galaxies using the information supplied by e.g. molecular spectral lines and spatially-resolved multi-band imaging, that can be useful also to determine their respective importance in driving the galaxy subsequent evolution. Spatially-resolved studies on sub-galactic scales and the analysis of spectral lines are essential to asses galaxy and ISM physical conditions, to model the kinematics of gas and measure its content (e.g., Tadaki et al., 2015; Talia et al., 2018; Chen et al., 2017; Hodge et al., 2019; Rizzo et al., 2020; Fraternali et al., 2021; Lelli et al., 2021; Rizzo et al., 2021). Moreover, they allow to guess the presence of an AGN and its impact on the host galaxy (i.e., AGN *feeding & feedback* cycle; e.g., Bischetti et al., 2021) and, on a statistical basis, on DSFG evolution.

In this Chapter I will go through an insight into the most popular theoretical frameworks describing the formation and evolution of high-z DSFGs (Sect. 1.1); then, I will describe the basic concepts of a possible theoretical scenario (i.e. the *in-situ* galaxy-BH co-evolution scenario; e.g. Lapi et al., 2014; Aversa et al., 2015; Mancuso et al., 2016b; Mancuso et al., 2016a; Mancuso et al., 2017; Shi et al., 2017; Lapi et al., 2018), to which I will refer in this thesis to self-consistently interpret data that we have at our disposal for the $z \sim 2$ population of DSFGs (Sect. 1.2). Finally, I will sketch the main scope of this thesis (see Sect. 1.3).

1.1 Theoretical evolutionary frameworks

Understanding the formation and evolution of galaxies in a cosmological context is one of the main challenge of modern astrophysics (e.g., Mo, van den Bosch, and White, 2010; Maiolino and Mannucci, 2019). The issue is intrinsically very complex, since it involves many physical processes occurring on vastly different spatial, time, and energy scales. While, in the last decades, we were able to successfully model the formation of dark matter (DM) *halos*, i.e. the bound virialized structures hosting galaxies and galaxy clusters that evolved under the action of gravity, and the matter large scale distribution in the Universe through *N-body* simulations (see Diemand, Kuhlen, and Madau, 2007; Springel et al., 2008; Tinker et al., 2008; Stadel et al., 2009),

we still have to succeed in providing a consistent theoretical picture that encompasses all the relevant processes associated to baryonic physics, which are relevant on (sub-)galactic scales and possibly play a major role in determining galaxy evolution.

The ultimate approach to address the problem in fine details would require the exploitation of intensive hydro-dynamical simulations (e.g., Bekki, 2013; Dubois et al., 2014; Genel et al., 2014; Hopkins et al., 2014; Vogelsberger et al., 2014; Bekki, 2015; Schaye et al., 2015; Dubois et al., 2016; McAlpine et al., 2016; Zhukovska et al., 2016; Aoyama et al., 2017; McKinnon et al., 2017; Pallottini et al., 2017; Aoyama et al., 2018; Hopkins et al., 2018; McKinnon et al., 2018; Springel et al., 2018; McAlpine et al., 2019; Ricarte et al., 2019; Torrey et al., 2019; Naab and Ostriker, 2017, for a review and further references). However, despite the considerable increase in resolution achieved recently, many of the physical processes relevant to the description of galaxy evolution constitute sub-grid physics and must be modeled via parametric recipes. In addition, a detailed exploration of the related parameter space or of different modeling prescriptions is often limited by exceedingly long computational times.

An alternative route to investigate the issue relies on Semi-Analytic Models (SAMs; e.g., Lacey and Cole, 1993; Kauffmann, White, and Guiderdoni, 1993; Cole et al., 2000; Croton et al., 2006; Arrigoni et al., 2010; Benson, 2012; De Lucia et al., 2014; Porter et al., 2014; Cousin et al., 2016; Hirschmann, De Lucia, and Fontanot, 2016; De Lucia, Fontanot, and Hirschmann, 2017; Fontanot et al., 2017; Popping, Somerville, and Galametz, 2017; Collacchioni et al., 2018; Lagos et al., 2018; Forbes, Krumholz, and Speagle, 2019; Somerville and Davé, 2015, for a review and further references). These are based on DM merger trees extracted from, or gauged on, *N-body* simulations, while the physics relevant for galaxy evolution inside dark halos is modeled via several parametric expressions partly set on a number of (mainly local) observables. Such models are less computationally expensive than hydrodynamic simulations and allow to disentangle more clearly the relative role of the various physical processes at work. However, the considerable number of fudge parameters can lead to degenerate solutions and limit somewhat the predictive power, especially toward high redshift.

Some specific issues related to the global evolution of the baryonic content in galaxies can be tackled with analytic models, i.e., models with analytic solutions, that are, however, necessarily based on approximate and spatially/time-averaged descriptions of the most relevant astrophysical processes (e.g., Schmidt, 1963; Talbot and Arnett, 1971; Tinsley, 1974; Pagel and Patchett, 1975; Hartwick, 1976; Chiosi, 1980; Matteucci and Greggio, 1986; Edmunds, 1990; Dwek, 1998; Hirashita, 2000; Chiappini, Matteucci, and Romano, 2001; Draine, 2003; Inoue, 2003; Greggio, 2005; Naab and Ostriker, 2006; Erb, 2008; Zhukovska, Gail, and Trieloff, 2008; Valiante et al., 2009; Bouché et al., 2010; Draine, 2011; Dwek and Cherchneff, 2011; Davé, Finlator, and Oppenheimer, 2012; Asano et al., 2013; Lilly et al., 2013; de Bennassuti et al., 2014; Dekel and Mandelker, 2014; Forbes et al., 2014; Pipino, Lilly, and Carollo, 2014; Feldmann, 2015; Hirashita et al., 2015; Mancini et al., 2015; Mollá et al., 2015; Recchi and Kroupa, 2015; Rodríguez-Puebla et al., 2016; Andrews et al., 2017; Gioannini et al., 2017; Spitoni, Vincenzo, and Matteucci, 2017; Weinberg, Andrews, and Freudenburg, 2017; Vincenzo, Matteucci, and Spitoni, 2017; Grisoni, Spitoni, and Matteucci, 2018; Imara et al., 2018; Tacchella et al., 2018; Dekel et al., 2019; Matteucci, 2012, for a review and further references).

The poor predictive capability of these approaches leaves some issues that are still open. Among them, the most debated ones are:

- the triggering mechanisms of star-forming bursts,
- the evolution of gas metallicity and dust fraction through cosmic time,
- the quenching of galaxy star formation,
- the role of galaxy-BH co-evolution in linking the high-z population of DSFGs and local ($z < 1$) massive ellipticals.

The different interpretations of the above open issues generated many diverse theoretical scenarios, that try to outline a consistent framework explaining the formation and evolution of galaxies across cosmic time. Currently, the most accounted scenarios are three.

The first one, known as *merger-driven* scenario, asserts that the intense and dusty bursts of star formation observed in DSFGs must be traced back to merging events between gas-rich spirals at high-z, supporting also their prominent role in driving the accretion of matter onto the central BH and the galaxy subsequent evolution (e.g., Hopkins et al., 2006).

An alternative scenario is the one suggesting that the star formation in galaxies is a smooth process fuelled by steady cold gas streams along filaments of the cosmic web (e.g., Dekel et al., 2009; Bournaud et al., 2011). Under this view, the intense burst experienced by DSFGs is mainly triggered by huge gas reservoirs coming from cosmological distances and just occasionally by wet merging and/or galaxy interactions, in particular in very densely populated environments.

Finally, another framework envisages star formation and BH accretion in galaxies to be essentially *in situ* and time-coordinated processes (e.g., Granato et al., 2004; Lapi et al., 2006; Lapi et al., 2011; Aversa et al., 2015; Mancuso et al., 2016a), triggered by the early collapse of baryons in the host DM halos and subsequently controlled by self-regulated baryonic physics, in particular by energy feedback from SNe and the central nucleus.

Along this Ph.D. thesis I will provide some indications that may be useful to further address the aforementioned issues, concerning galaxy evolution. In order to interpret the main phenomenological outcomes of this study, I will exploit the predictions by the *in-situ* scenario, that I will briefly describe in the next Section.

1.2 A possible scenario: the *in-situ* galaxy-black hole co-evolution

The *in-situ* scenario attempts to provide a self-consistent and physically-motivated description of the evolution of massive ETGs, that encompasses their high-z star-forming progenitors, their high-z quiescent counterparts and their configurations in the local Universe. The scenario comprises the main astrophysical processes that are thought to play a relevant role in massive galaxy evolution and, in such a way, it offers a holistic view on their typical sizes and kinematics, along with a characterization of their star formation, BH accretion and feedback, that includes the typical timescales and physical conditions. Furthermore, it allows to give a consistent interpretation of the *main-sequence* of star-forming galaxies and, in particular, of the *locus* where galaxies are located with respect to it (see Mancuso et al., 2016b; Mancuso et al., 2016a).

In a nutshell, the *in-situ* scenario envisages the star formation in the high-z counterparts of ETGs to be triggered by the early collapse (*biased collapse*; see Eke, Efstathiou, and Wright, 2000; Fall, 2002; Granato et al., 2004; Romanowsky and Fall,

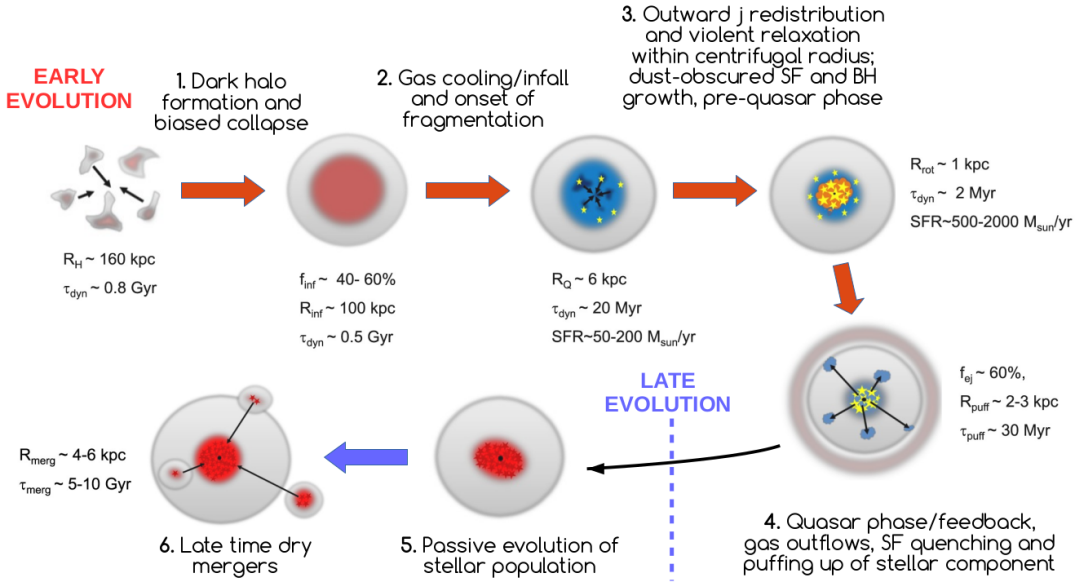

FIGURE 1.1: Cartoon that illustrates the main processes determining the size evolution of massive ($M_\star \sim 10^{11}\,M_\odot$) ETG progenitors. Typical sizes and timescales of the system along the evolution are also reported. The dashed vertical line in light blue separates the early fast evolution over some 10^8 yr (indicated by red arrows) from the late slow evolution over cosmological timescales of several Gyrs (light blue arrow).

2012; Shi et al., 2017) of low angular momentum gaseous baryons in the host DM halo. Then, the early evolution of the high-z star-forming galaxy is led by cooling, fragmentation and infall of the gas down to the radius set by the centrifugal barrier and by its subsequent rapid compaction via (clumps) migration toward the galaxy center, where strong heavily dust-enshrouded star-formation takes place and most of the stellar mass is accumulated. The star-formation quenching, that causes the ejection of a substantial amount of gas from the inner regions by AGN/stellar feedback processes, is associated to a dramatic puffing up of the stellar component. The later slow evolution of the quenched galaxy is characterized by the passive aging of stellar populations and mass additions by dry merger events. In Fig. 1.1 I show a cartoon that sketches the evolutionary phases summarized above, along with the typical sizes and timescales predicted by the *in-situ* scenario.

For this thesis purposes, I first describe the size evolution predicted by the *in-situ* scenario (Sect. 1.2.1; see also Lapi et al., 2018) and then the suggested interpretation of galaxy *main-sequence*, that includes a self-consistent theoretical description of galaxy-SMBH co-evolution (Sect. 1.2.2; see also Mancuso et al., 2016a; Mancuso et al., 2017).

1.2.1 Size-mass evolution

In the following, after setting the basic framework for DM halo and baryons joint evolution, I turn into the description of the main processes determining the size evolution of ETGs star-forming progenitors, i.e. gas cooling and fragmentation, gas compaction towards the inner region of galaxy, puffing-up by stellar and AGN feedbacks, late growth by dry merging events. The main prescriptions are inspired by basic physical arguments and numerical simulations. In order to facilitate the

reading, the analytical estimates of the relevant sizes, timescales, and kinematic properties are normalized with respect the typical values for a reference galaxy of stellar mass $M_\star \approx 10^{11}\, M_\odot$ at $z \approx 2$ (i.e. star-formation efficiency $f_\star \approx 0.2$ and a infall fraction $f_{\rm inf} \approx 0.6$). I note that these values are indeed the ones commonly accepted for dusty star-forming galaxies at the peak of Cosmic SFH, that are thought to evolve in massive quiescents and are investigated in this thesis. For a detailed description of the theory behind the *in-situ* scenario I refer the reader to Lapi et al. (2018). However, some of the most relevant equations are reported in the text for reader convenience.

Biased collapse

The *biased-collapse* scenario (see e.g., Eke, Efstathiou, and Wright, 2000; Fall, 2002; Granato et al., 2004; Romanowsky and Fall, 2012; Shi et al., 2017), that is supposed to trigger star formation in high-z ETG progenitors, prescribes that only a fraction $f_{\rm inf} = M_{\rm inf}/f_b\, M_{\rm H}$ of the available baryons within the halo (i.e. $f_b\, M_{\rm H}$) of mass $M_{\rm H}$ is able to cool and infall toward the central region of the galaxy where star formation takes place; under such circumstances, the specific angular momentum $j_{\rm inf}$ associated to the infalling baryons is expected to be somewhat lower than the one associated to the DM halo$j_{\rm H}$. I note, instead, that the classic assumptions envisages that the mass distribution of the baryons and of the DM mirror each other initially, implying $j_b(< r) = j_{\rm H}(< r)$. However, the above biased collapse prescription for central galaxy formed in massive halos has been confirmed by independent determination of $f_{\rm inf}$.

Shi et al. (2017) have been the first to infer the infall fraction $f_{\rm inf}$ in ETGs by exploiting diverse observations on the star-formation efficiency and the chemical abundance. Based on simple mass and metal conservation arguments, these authors found that the infall fraction can be closely estimated as

$$f_{\rm inf} \simeq \frac{y_Z\, f_\star}{Z_\star}\,, \tag{1.1}$$

in terms of the effective true metal yield of a single stellar population y_Z, of the star-formation efficiency $f_\star$, and of the stellar metallicity $Z_\star$. The above approximated estimate provides for ETGs outcomes to within 10% accuracy relative to the exact expression derived by Shi et al. (2017).

The star formation efficiency $f_\star$ is assumed to follow the outcomes by Lapi et al. (2017) via abundance matching of the halo and stellar mass function at $z \approx 2$ and checked against estimates at $z \sim 1-2$ from mass profile modelling (see Burkert et al., 2016). As to the average metal yield, it is adopted the fiducial value $y_Z \approx 0.069$ appropriate for a Chabrier IMF, solar metallicity and the Romano et al. (2010) stellar yield models (see Krumholz, Dekel, and McKee, 2012; Feldmann, 2015; Vincenzo et al., 2016). A systematic dispersion is allowed within the range $y_Z \sim 0.05-0.08$ that embraces values for different chemical compositions and stellar yield models (e.g. Romano et al., 2010; Nomoto, Kobayashi, and Tominaga, 2013; Vincenzo et al., 2016). It is worth noticing that for a massive galaxy formed at $z \approx 2$ with a star-formation duration of $\lesssim 1$ Gyr, the metal yield y_Z changes by less than 30% from the epoch of quenching to the present time. The stellar metallicity of ETGs is assumed to be the average determination $Z_\star(M_\star)$ as a function of stellar mass at $z \approx 0$ by Gallazzi et al. (2014, with its scatter ~ 0.15 dex). Indeed, many evidences suggest that the average metallicity of present-day massive ETGs was already in place at redshift $z \sim 2$ (see e.g. Gallazzi et al., 2006; Gallazzi et al., 2014; Citro et al., 2016; Kriek et al., 2016; Rodriguez-Gomez et al., 2016; Martín-Navarro et al., 2018). The resulting dependence of the infall fraction $f_{\rm inf}$ on the stellar mass at $z \approx 2$ is illustrated in

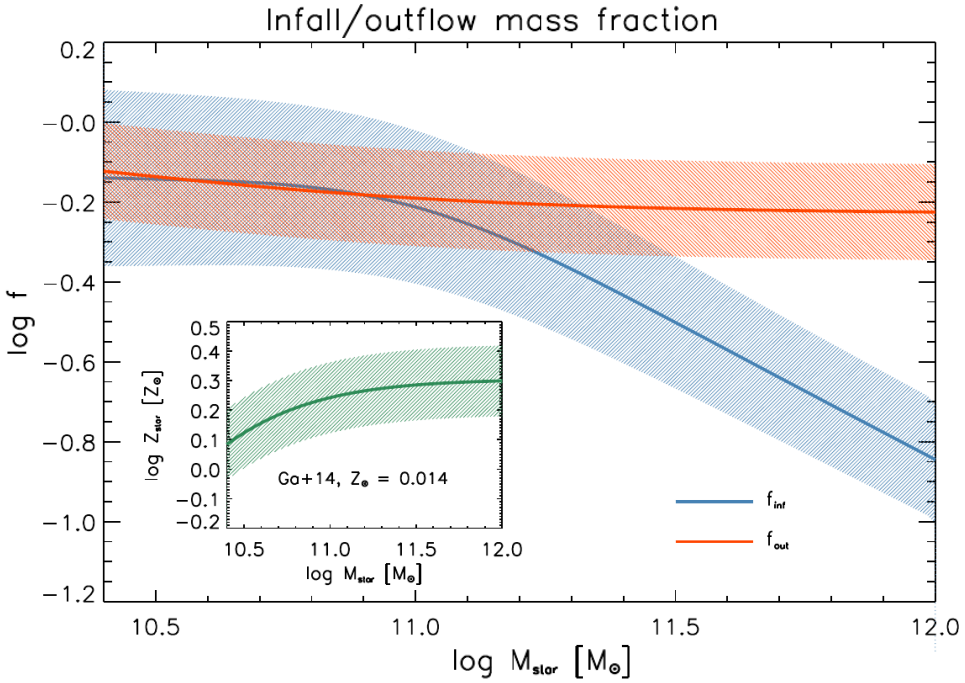

FIGURE 1.2: Fractions of infalling $f_{\rm inf}$ and out-flowing $f_{\rm out}$ mass vs. stellar mass $M_\star$ by Lapi et al. (2018). Solid lines illustrate the average infall mass fraction $f_{\rm inf} \simeq y_Z\, f_{\rm star}/Z_\star$ (blue) and outflow mass fraction $f_{\rm out} \simeq 1 - Z_\star/y_Z$ (orange), with the shaded areas showing the corresponding scatter. In the inset the solid green line illustrates the adopted average stellar metallicity $Z_\star$ vs. stellar mass $M_\star$ relationship from Gallazzi et al. (2014) for local ETGs, re-normalized for a solar metallicity $Z_\odot \approx 0.014$, and the shaded area shows the associated scatter.

Fig. 1.2 (stellar metallicity by Gallazzi et al., 2014, in the inset); it features typical values ranging from $f_{\rm inf} \approx 0.7$ to 0.6 to 0.2 for $M_\star$ increasing from a few 10^{10} to 10^{11} to $10^{12}\,M_\odot$, and logarithmic scatter around $\sigma_{\log f_{\rm inf}} \approx 0.25$ dex (Lapi et al., 2018). Such behavior is indeed consistent with a scenario of biased collapse where only a fraction of the gas initially present in the halo is processed within the central regions.

Cooling and fragmentation

Given a halo of mass $M_{\rm H}$, its virial radius is defined as $R_{\rm H} \equiv [3\,M_{\rm H}/4\pi\,\rho_c\,\Delta_{\rm H}\,E_z]^{1/3}$, where $\rho_c \approx 2.8\times10^{11}\,h^2\,M_\odot\,{\rm Mpc}^{-3}$ is the critical density, $\Delta_{\rm H} \simeq 18\,\pi^2 + 82\,[\Omega_M\,(1+z)^3/E_z - 1] - 39\,[\Omega_M\,(1+z)^3/E_z - 1]^2$ is the nonlinear density contrast at collapse, and $E_z = \Omega_\Lambda + \Omega_M\,(1+z)^3$ is a redshift dependent factor. The virial radius $R_{\rm H}$ and circular velocity $v^2_{c,{\rm H}} \equiv G\,M_{\rm H}/R_{\rm H}$ of the halo can be expressed in terms of the stellar mass $M_\star$ enclosed in the host galaxy and of its star-formation efficiency $f_\star \equiv M_\star/f_b\,M_{\rm H}$, where $f_b \equiv \Omega_b/\Omega_{\rm M} \approx 0.16$ is the universal baryon to DM mass ratio. For a reference galaxy of $M_\star \approx 10^{11}\,M_\odot$ at $z \approx 2$ (see above) the outcome reads

$$\begin{aligned} R_{\rm H} &\approx 160\,f_{\star,0.2}^{-1/3}\,M_{\star,11}^{1/3}\,[E_z/E_{z=2}]^{-1/3}\ {\rm kpc}\,, \\ v_{c,{\rm H}} &\approx 300\,f_{\star,0.2}^{-1/3}\,M_{\star,11}^{1/3}\,[E_z/E_{z=2}]^{1/6}\ {\rm km\ s^{-1}}\,, \end{aligned} \tag{1.2}$$

where $M_{\star,11} = M_\star/10^{11}\,M_\odot$ and $f_{\star,0.2} \equiv f_\star/0.2$ are the normalized quantities to the reference galaxy at $z \approx 2$ (see above). The related dynamical time is

$$t_{\rm dyn}(R_{\rm H}) \simeq \frac{\pi}{2}\sqrt{\frac{R_{\rm H}^3}{G\,M_{\rm H}}} \approx 8.5\times10^8\,[E_z/E_{z=2}]^{-1/2}\ {\rm yr}\,. \tag{1.3}$$

The initial radius $R_{\rm inf}$ that encloses the infalling mass $M_{\rm inf} = f_{\rm inf}\,f_b\,M_{\rm H}$ subject to the biased collapse can be computed as follows.

Adopting a standard Navarro-Frenk-White (NFW) profile (Navarro, Frenk, and White, 1997), the logarithmic slope of the mass distribution $M(<r) \propto r^\mu$ reads $\mu \equiv {\rm d}\log M/{\rm d}\log r = [cx/(1+cx)]^2\,[\ln(1+cx) - cx/(1+cx)]^{-1}$, in terms of the normalized radius $x \equiv r/R_{\rm H}$ and of the concentration c. For values $c \approx 4$ typical of massive galaxy halos virialized at $z \gtrsim 2$ (e.g. Bullock et al., 2001; Zhao et al., 2003), the slope μ ranges from 0.8 to 1.2 in moving from $R_{\rm H}$ to $0.3\,R_{\rm H}$, and can be effectively approximated with unity down to $\sim 0.4 - 0.6\,R_{\rm H}$. For smaller radii the slope progressively approach the central value $\mu \sim 2$, which can be approximately used for $r \lesssim 0.1\,R_{\rm H}$. For the radial range of interest it is sensible to assume that the baryon and DM mass approximately scale with radius as $M(<r) \propto r$, so that

$$R_{\rm inf} \simeq f_{\rm inf}\,R_{\rm H} \approx 96\,f_{\rm inf,0.6}\,f_{\star,0.2}^{-1/3}\,M_{\star,11}^{1/3}\,[E_z/E_{z=2}]^{-1/3}\ {\rm kpc}\,. \tag{1.4}$$

Note that the size $R_{\rm inf}$ is consistent with the scale over which both observations (see e.g. Hodge et al., 2013; Karim et al., 2013; Simpson et al., 2015) and high-resolution simulations (see Narayanan et al., 2015) indicate that gas, possibly segregated in

multiple components, inflows toward the central regions of galaxy halos. The corresponding dynamical time reads

$$t_{\rm dyn}(R_{\rm inf}) \simeq \frac{\pi}{2}\sqrt{\frac{R_{\rm inf}^3}{G}\,M_{\rm H}(<R_{\rm inf})} = f_{\rm inf}\,t_{\rm dyn}(R_H) \approx$$
$$\approx 5\times10^8\,f_{\rm inf,0.6}\,[E_z/E_{z=2}]^{-1/2}\ {\rm yr}\ . \tag{1.5}$$

Thus, a high formation redshift $z \gtrsim 1.5$ and a low infall fraction $f_{\rm inf} \lesssim 0.6$ enforced by the biased collapse concur to set a rather short dynamical timescale driving the subsequent evolution of ETG progenitors.

On the other hand, the cooling time at $R_{\rm inf}$ reads:

$$t_{\rm cool}(R_{\rm inf}) \simeq \frac{3\,k_{\rm B}T}{2\,\mu\,C\,n(R_{\rm inf})\,\Lambda(T,Z)} \tag{1.6}$$

where T is the temperature, $\mu \approx 0.6$ is the mean molecular weight, $n(R_{\rm inf})$ is the gas density, C is the clumping factor and $\Lambda(T,\,Z)$ is the cooling function in cgs units dependent on temperature and metallicity (see Sutherland and Dopita, 1993). The infalling gas is expected to have temperatures close to the virial, i.e.

$$T \simeq 0.5\,\mu\,m_p\,v_{c,\rm H}^2 \approx 1.5\times10^6\,M_{\rm H,12}^{2/3}\,[E_{z_{\rm form}}/E_{z_{\rm form}=2}]^{1/3}\,{\rm K}$$

correspondingly, $\Lambda(T,Z) \gtrsim 2\times10^{-23}$ erg cm^3 s^{-1} for $Z \gtrsim Z_\odot/10$ (recall from Sect. 2.1.2 that this value is attained quite rapidly within $\lesssim 10^{-1}\,\tau_{\rm cond} \sim$ a few 10^7 yr). The gas density is expected to be on the order of the average baryon density within $R_{\rm inf}$, which reads $n(R_{\rm inf}) \approx 4\times10^{-4}\,f_{\rm inf}^{-2}\,[E_{z_{\rm form}}/E_{z_{\rm form}=2}]$ cm^{-3} having assumed $n(r)$ to follow an isothermal distribution; the clumping factor is expected to be close to that in the IGM, which cosmological simulations (see Iliev et al., 2007; Pawlik, Schaye, and van Scherpenzeel, 2009; Finlator et al., 2012; Shull et al., 2012) indicate around $C \sim 6-20$ at $z \simeq 2$, so that I take $C \approx 10$. I would note that the cooling time $t_{\rm cool}(r) \sim 4\times10^8\,(r/R_{\rm inf})^{-2}$ yr within $r \lesssim R_{\rm inf}$ is comparable or shorter than the dynamical time, so that the gas can effectively cool and infall over the timescale $t_{\rm dyn}(R_{\rm inf})$. Furthermore, such gas is rotating, being endowed with the specific angular momentum $j_{\rm inf}$.

The fraction of gas that becomes available for star formation during the infall can be addressed by looking at the fragmentation of the rotating material. Rotating discs are stable to gravitational fragmentation as far as the Toomre (1964) parameter $Q \equiv \sqrt{2}\,\Omega\,\sigma/\pi\,G\Sigma$ exceeds the critical values $0.7-1-2$ (for thick, thin, and composite discs, respectively), where $\Omega \equiv v/R \simeq j/R^2$ is the angular rotation velocity, σ is the intrinsic velocity dispersion of the gas and $\Sigma \simeq M_{\rm gas}(<R)/\pi\,R^2$ is the gas surface density. The Toomre parameter can be arranged in terms of the gas mass contrast $\delta_{\rm gas}(R) \equiv M_{\rm gas}(<R)/M_{\rm tot}(<R)$, i.e. the ratio between the gas mass and the total mass (including DM; see Dekel and Mandelker, 2014):

$$Q \approx \frac{\sqrt{2}}{\delta_{\rm gas}}\,\frac{\sigma}{v}\ . \tag{1.7}$$

The condition $Q \sim 1$ defines the stability radius $R_{\rm Q}$.

In absence of substantial fragmentation the specific angular momentum $j_{\rm inf}$ is approximately conserved (e.g. Mo, Mao, and White, 1998; Mo, van den Bosch, and

White, 2010) during contraction from the initial radius $R_{\rm inf}$ to $R_{\rm Q}$; then one finds that

$$R_{\rm Q} \approx j_{\rm inf} \frac{Q}{\sqrt{2}} \sigma \, \delta_{\rm gas}(R_{\rm Q}) \approx 6.3 \, Q \, \sigma_{60}^{-1} \, \lambda_{0.035} \, f_{\rm inf,0.6}^{s} \, f_{\star,0.2}^{-2/3} \, M_{\star,11}^{2/3} \, [E_z/E_{z=2}]^{-1/6} \ {\rm kpc} \ , \quad (1.8)$$

where $Q \equiv 1$. The gas mass contrast $\delta_{\rm gas}(R_{\rm Q}) \approx 0.38$ is computed by Lapi et al. (2018), taking into account the effects of adiabatic contraction. In the above expression the gas intrinsic velocity dispersion $\sigma_{60} \equiv \sigma/60$ km s^{-1} is normalized to a fiducial value of 60 km s^{-1} as measured in high redshift $z \approx 2$ star-forming galaxies endowed with SFR $\gtrsim 30 \, M_\odot$ yr^{-1} (see Law et al., 2009; Genzel et al., 2011; Wisnioski et al., 2015; Turner et al., 2017).

The corresponding dynamical time at $R_{\rm Q}$ ($Q \equiv 1$) amounts to

$$\begin{aligned} t_{\rm dyn}(R_{\rm Q}) \ &\simeq \ \frac{\pi}{2} \sqrt{\frac{R_{\rm Q}^3}{G} M_{\rm inf}} \approx 2.2 \times 10^7 \, Q^{3/2} \, \sigma_{60}^{-3/2} \, \lambda_{0.035}^{3/2} \times \\ &\times \ f_{\rm inf,0.6}^{(3s-1)/2} \, f_{\star,0.2}^{-1/2} \, M_{\star,11}^{1/2} \, [E_z/E_{z=2}]^{-1/4} \ {\rm yr} \ . \end{aligned} \quad (1.9)$$

When reaching the size $R_{\rm Q}$, the gas tends to fragment in clumps with radial velocity dispersion relative to each other of order σ. The mass of the clumps can be estimated as $M_{\rm clump} \lesssim \pi^2 \, \delta_{\rm gas}^2 \, M_{\rm inf}/16 \lesssim 10^{-1} \, M_{\rm inf}$ and amounts to several percent of the disk gas mass (e.g. Dekel and Mandelker, 2014; Bournaud et al., 2011), consistently with observations in high-redshift galaxies (see Elmegreen et al., 2007; Guo et al., 2018) and with the outcomes of numerical simulations (see Ceverino, Dekel, and Bournaud, 2010; Mandelker et al., 2014; Mandelker et al., 2017; Oklopčić et al., 2017).

At this point, rotation is not sufficient to sustain gravity (Lapi et al., 2018) and gas and clumps can continue to infall within $R_{\rm Q}$ over a dynamical time $t_{\rm dyn}(R_{\rm Q})$, while closely maintaining their initial specific angular momentum $j_{\rm inf}$ (see also Danovich et al., 2015). The infall will then be halted close to the radius where the centrifugal and gravitational forces balance.

During the infall, star formation proceeds in the gas (and clumps) over a timescale $t_{\rm SFR}$. Observations of the correlation between star formation to gas surface density in high-redshift disks suggest values $\sim 50 - 100$ times longer than the dynamical time (see Elmegreen, Elmegreen, and Ferguson, 2005; Krumholz, Dekel, and McKee, 2012, and references therein), i.e.

$$t_{\rm SFR} \simeq (50 - 100) \times t_{\rm dyn}(R_{\rm Q}) \approx 1 - 2 \times 10^9 \ {\rm yr} \ . \quad (1.10)$$

Energy/momentum feedback via outflows from supernovae and stellar winds is expected to regulate star formation. On spatially-averaged grounds, the effects of such feedback processes are often described in terms of a mass loading factor $\epsilon_{\rm out}$, defined as the ratio between the outflow mass loss rate and the SFR (e.g. Feldmann, 2015); semi-analytic estimates (e.g. Lapi et al., 2014) and self-consistent hydrodynamical simulations (e.g. Hopkins, Quataert, and Murray, 2012) suggest that $\epsilon_{\rm out} \approx 1 - 2$ for massive galaxies with $M_\star \gtrsim 3{\times}10^{10} \, M_\odot$ of interest here. Basing on mass conservation arguments, a simple estimate of the ensuing average SFRs around $R_{\rm Q}$ reads

$${\rm SFR}(R_{\rm Q}) \simeq \frac{1}{1 - \mathcal{R} + \epsilon_{\rm out}} \frac{M_{\rm inf}}{t_{\rm SFR}} \lesssim 50 - 200 \, M_\odot \ {\rm yr}^{-1} \ ; \quad (1.11)$$

here $\mathcal{R}$ is the return fraction of gaseous material from the formed stars, taking on values $\mathcal{R} \approx 0.45$ for a Chabrier IMF (e.g. Vincenzo et al., 2016).

The above approximate analytical estimates of the SFRs and sizes $R_{\rm Q}$ are consistent with the values measured via near-IR/optical observations of $z \sim 1-2$ star-forming, massive galaxies (e.g. van Dokkum et al., 2015; Barro et al., 2016b).

Compaction

Since gas is not rotationally supported (as described in the previous section), gas and clumps can infall within $R_{\rm Q}$ over a dynamical timescale $t_{\rm dyn}(R_{\rm Q}) \sim$ a few 10^7 yr, approximately maintaining their initial specific angular momentum $j_{\rm inf}$. The process can continue down to the radius $R_{\rm rot}$ where the gravitational and centrifugal force balance

$$\frac{G\,M_{\rm tot}(<R_{\rm rot})}{R_{\rm rot}^2} = \Omega^2\,R_{\rm rot} \simeq \frac{j_{\rm inf}^2}{R_{\rm rot}^3}\,. \tag{1.12}$$

The resulting $R_{\rm rot}$ can be expressed as

$$R_{\rm rot} \approx \frac{j_{\rm inf}^2}{G\,M_{\rm inf}}\,\delta(R_{\rm rot}) \approx 1.3\,\lambda_{0.035}^2\,f_{\rm inf,0.6}^{2s-1}\,f_{\star,0.2}^{-1/3}\,M_{\star,11}^{1/3}\,[E_z/E_{z=2}]^{-1/3}\ \ {\rm kpc}\,, \tag{1.13}$$

where the baryonic mass contrast is $\delta(R_{\rm rot}) \approx 0.88$, as computed by Lapi et al. (2018), taking into account the effects of adiabatic contraction. Eq. (1.13) implies an extremely high mass concentration of gas (and eventually of stars) inside ~ 1 kpc (see van Dokkum et al., 2014).

Since the gas and clumps are rotationally supported at $R_{\rm rot}$, further infall can only occur by spreading out specific angular momentum via dynamical friction and gravitational torques over the migration time:

$$t_{\rm migr}(R_{\rm rot}) \simeq \frac{2.1\,Q^2(R_{\rm rot})}{\delta_{\rm gas}^2(R_{\rm rot})}\,t_{\rm dyn}(R_{\rm rot}) \approx 9.4\times10^5\ \ {\rm yr}\,. \tag{1.14}$$

As $t_{\rm migr}(R_{\rm rot})$ is extremely short, the net result is a very rapid migration of the star-forming gas and clumps toward the inner regions.

Meanwhile, the star formation within $R_{\rm rot}$ occurs over a timescale

$$t_{\rm SFR}(R_{\rm rot}) \approx (50-100)\times t_{\rm dyn}(R_{\rm rot}) \approx (1-2)\times10^8\ \ {\rm yr}\,. \tag{1.15}$$

An estimate of the ensuing average SFR is given by

$${\rm SFR}(R_{\rm rot}) \simeq \frac{1}{1-\mathcal{R}+\epsilon_{\rm out}}\,\frac{M_{\rm inf}}{t_{\rm SFR}(R_{\rm rot})} \lesssim 500-2000\ \ M_\odot\,{\rm yr}^{-1}\,. \tag{1.16}$$

Thus, the gas and clumps around or within $R_{\rm rot}$ are expected to feature large SFRs, rapid metal enrichment, and dust production. Note that during the early stages of this strong star-formation phase the galaxy is expected to lie above the main sequence relationship, because the stellar mass is still growing (see Mancuso et al., 2016a). All in all, mildly obscured SFRs are expected in the region between $R_{\rm Q}$ and $R_{\rm rot}$, and a much stronger, obscured SFR in the innermost regions within $R_{\rm rot}$, where most of the stellar mass is accumulated; therefore the SFRs probed by UV and FIR data are expected to be spatially disconnected (e.g. Gómez-Guijarro et al., 2018), with the UV morphology particularly knotty and irregular (e.g. Huertas-Company et al., 2015). Notice that, as $t_{\rm migr}(R_{\rm rot}) \lesssim t_{\rm dyn}(R_{\rm rot})$, violent relaxation will operate inside $R_{\rm rot}$

toward setting up a new configuration in virial equilibrium, eventually originating a bulge-like structure with Sersic index $n \gtrsim 2$.

In Fig. 1.3 I show the size-mass evolution for the high-z star-forming progenitors of ETGs, as predicted by the *in-situ* scenario, with the corresponding dispersion. From the above description, in between the size $R_{\rm Q}$ and $R_{\rm rot}$, it is expected just a moderate star formation and a mild or negligible dust obscuration, so that these regions can be probed by NIR/optical observations. Around or within $R_{\rm rot}$ star formation is expected to be strong and associated by a heavy dust obscuration, so that these regions are hidden to NIR/optical observations and can be only probed via MIR and FIR data. As an end-product of significantly larger SFRs in the central regions $\lesssim 1$ kpc with respect to the outskirts, a very high stellar mass concentration will be originated, as indicated by observations of $z \sim 2$ massive quiescent galaxies van Dokkum et al. (see 2014).

The predictions are consistent with the measured sizes of $z \approx 2$ star-forming galaxies (see van Dokkum et al., 2015; Barro et al., 2016b; Barro et al., 2017; Hodge et al., 2016; Genzel et al., 2017; Tadaki et al., 2017b; Massardi et al., 2018; Talia et al., 2018). Specifically, sizes inferred from NIR/optical data (light blue symbols in Fig. 1.3) are seen to be located in between $R_{\rm Q}$ and $R_{\rm rot}$, while sizes inferred from MIR/FIR data (dark blue symbols in Fig. 1.3) lie around and within $R_{\rm rot}$. For the samples by Barro et al. (2016b) and Tadaki et al. (2017b) both the NIR/optical size measured from HST data and the FIR sizes from ALMA data are reported, for the very same bunch of objects, to show that the FIR sizes are typically a factor $2-4$ smaller than the NIR/optical ones. High-resolution, multi-band observations (e.g., Negrello et al., 2014; Massardi et al., 2018) of strongly lensed dusty star-forming galaxies have also highlighted a clear spatial segregation between the UV and FIR emissions, with the latter being substantially more concentrated. I note that the extremely large dispersion in the data points for star-forming galaxies is in part spuriously due to this difference between NIR and FIR sizes; however, even when considering data with homogeneous selection, the dispersion remains substantial, in agreement with the scatter on $R_{\rm Q}$ and $R_{\rm rot}$.

In the end, I further note that the compaction process, described above, can also create physical conditions extremely favorable to increase the gas inflow toward the innermost regions of the galaxy (from parsec to tens of parsec scale) at disposal for formation of, and rapid accretion onto a SMBH (e.g. Bournaud et al., 2011; Gabor and Bournaud, 2013; DeGraf et al., 2017; Rujopakarn et al., 2018). This will have important consequence for the subsequent evolution of these systems, and specifically both for the quenching of star formation and for the puffing up of the stellar distribution.

Puffing-up by stellar and AGN feedbacks

An additional process contributing to alter somewhat the sizes of ETG progenitors is related to the outflow/ejection of a substantial fraction of gaseous material from the central region by feedback events (e.g., due to supernovae, stellar winds, and to the emission from the central SMBH during its quasar phase), that are thought to regulate or even quench star formation. As a consequence, the stellar component feels the change in the gravitational potential and relaxes to a more extended equilibrium configuration.

For massive star-forming galaxies, like the reference object at $z \approx 2$ with $M_\star \approx 10^{11}\,M_\odot$, the star-formation process is expected to be quenched by energy feedback from stellar winds/supernovae or, most likely, from the central SMBH during its

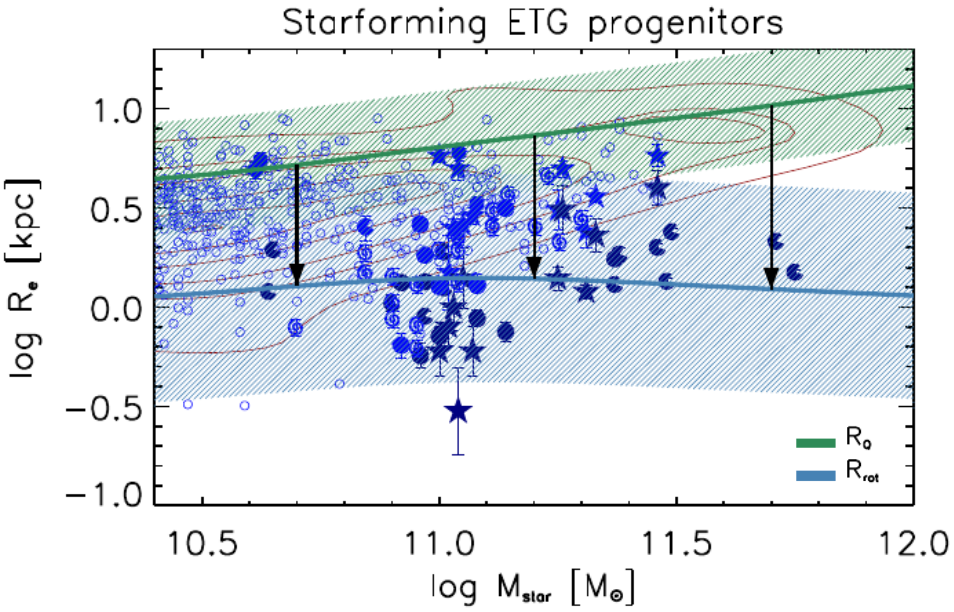

FIGURE 1.3: Size R_e vs. stellar mass $M_\star$ relationship by Lapi et al. (2018). The colored lines with shaded areas illustrate the size-mass relationship and the associated scatter expected along the evolution of ETG progenitors: green line refers to the fragmentation size R_Q of Eq. (1.8) and blue line refers to the centrifugal size R_{rot} of Eq. (1.13). Black arrows illustrate the evolution from one radius to the other. Blue points refer to star-forming galaxies: light blue for sizes inferred from optical/near-IR observations, deep blue for sizes inferred from mid-/far-IR observations. Data are from Barro et al. (2016b, circles) at $z \sim 2.5$, Hodge et al. (2016, pacmans) at $z \sim 1.6$, Tadaki et al. (2017b, stars) at $z \sim 2$, van Dokkum et al. (2014, spirals) at $z \sim 2$, van der Wel et al. (2014, dots) at $z \sim 2$. The dark red contours report the size distributions of local ETGs from the ATLAS^{3D} survey by Cappellari et al. (2013).

powerful quasar phase. In such a way the star-formation in the host galaxy is abruptly stopped and a high-z, massive quiescent galaxy is originated.

The star-forming burst in ETG progenitors is expected to last for $\lesssim$ Gyr. The sudden ejection of a substantial amount of matter ($f_{\rm out} \approx 0.5 - 0.7$; see Fig. 1.2) from the central region, due to AGN feedback, puffs up the stellar component to a new, more extended equilibrium configuration, i.e. $R_{\rm puff} \sim 3 - 5$ kpc, a factor a few to several larger than $R_{\rm rot}$. The resulting size $R_{\rm puff}$ illustrated in Fig. 1.4 as an orange solid line (the orange dashed line includes puffing up by adiabatic mass loss during passive evolution) is in agreement with the measured size of high-z massive quiescent galaxies (van der Wel et al., 2008; van de Sande et al., 2013; Belli, Newman, and Ellis, 2017; Glazebrook et al., 2017; Toft et al., 2017; Hill et al., 2018). Interestingly, even the sizes of local compact quiescent galaxies measured by Yıldırım et al. (2017) agree well with the predicted $R_{\rm puff}$. These are galaxies stayed compact till the present, because of a lack in size evolution due to late-time dry merger events. Moreover, they are known to host extremely massive BHs at their centers, that may have originated a strong puffing up at the peak time of their activity. A detailed and self-consistent analysis of galaxy-SMBH co-evolution in the light of *in-situ* scenario is provided by Mancuso et al. (2016a) and Mancuso et al. (2017). I will briefly summarize their outcomes in Sect. 1.2.2, where I present a possible interpretation of galaxy *main-sequence* and of the *locus* on the SFR $- M_\star$ plane occupied by galaxies during their evolution.

Notice that, due to the presence of DM, the puffing up process is more pronounced in galaxies that initially were more compact; as a consequence, the dispersion in the size $R_{\rm puff}$ is considerably smaller than that in the initial size $R_{\rm rot}$ (cf. Fig. 1.4). Finally, as a consequence of the size expansion, the mass concentration in the central region $\lesssim 1$ kpc of quiescent galaxies is somewhat decreased with respect to that of their star-forming progenitors.

Growth by dry merging

During the late-time passive evolution of ETG progenitors toward the present time, the size is expected to increase because of mass additions from external dry merger events. This is true especially for massive systems, such as the reference galaxy of $M_\star \approx 10^{11}\,M_\odot$. In Fig. 1.5 I show the final size $R_{\rm merg}$ (solid magenta line) that, for the most massive galaxies, increases by factor around $2 - 3$ from $z \sim 2$ to 0, while its dispersion (shaded area) is somewhat enhanced if compared with $R_{\rm puff}$, because of the variance in merging histories.

The average size $R_{\rm merg}$ and its dispersion agree pretty well with the size vs. mass relationship of local ETGs as measured by the ATLAS$^{\rm 3D}$ survey (dark red contours in Fig. 1.5; Cappellari et al., 2013).

Finally, by comparing Fig. 1.4 with Fig. 1.3, it is possible to notice that, by chance, the final size of ETGs is not so different from the initial fragmentation size $R_{\rm Q}$ of their star-forming progenitors, which is, basically, the size inferred via NIR/optical observations. Without the recent size measurements from FIR/sub-millimeter data it would have been very difficult to envisage a self-consistent evolutionary path for ETG progenitors in the size-mass diagram.

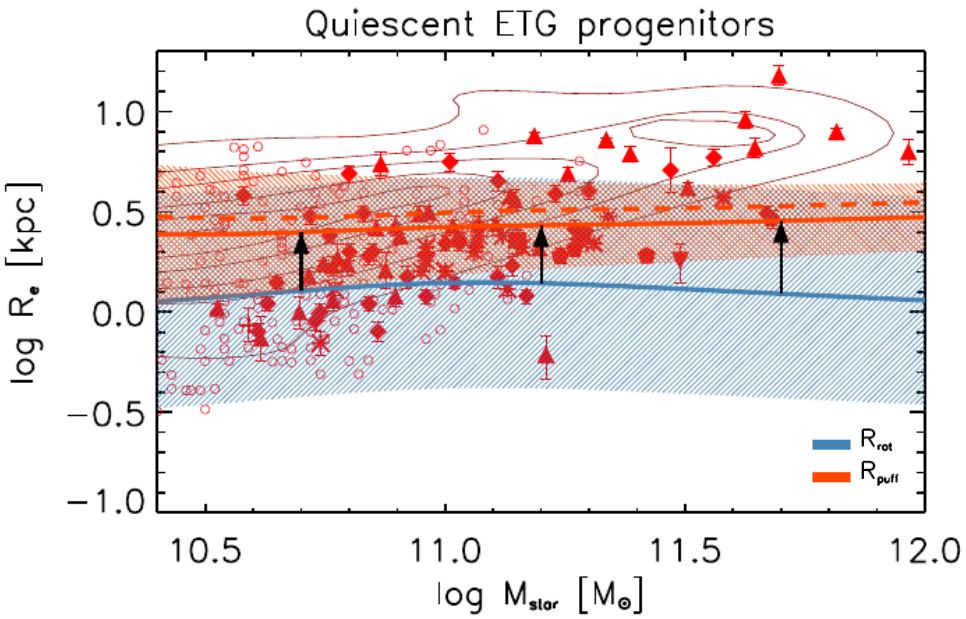

FIGURE 1.4: Size R_e vs. stellar mass $M_\star$ relationship by Lapi et al. (2018). The colored lines with shaded areas illustrate the size-mass relationship and the associated scatter expected along the evolution of ETG progenitors: blue line refers to the centrifugal size $R_{\rm rot}$ of Eq. (1.13) and orange line to the size $R_{\rm puff}$ after puffing up (solid for impulsive puffing due to feedbacks and dashed for adiabatic puffing due to stellar evolution). Black arrows illustrate the evolution from one radius to the other. Red points refer to quiescent galaxies. Data are from Belli, Newman, and Ellis (2017, diamonds) at $z \sim 2$, Genzel et al. (2017, hexagons) at $z \sim 2$, Glazebrook et al. (2017, triangles) at $z \sim 2$, Hill et al. (2018, plus sign) at $z \sim 2.8$, Newman, Belli, and Ellis (2015, reverse triangles) at $z \sim 2.6$, Toft et al. (2017, squares) at $z \sim 2$, van de Sande et al. (2013, pentagons) at $z \sim 2$, van der Wel et al. (2008, crosses) at $z \sim 1$, van der Wel et al. (2014, dots) at $z \sim 2$, Yıldırım et al. (2017, asterisks) at $z \sim 0$ for compact ETGs. The dark red contours report the size distributions of local ETGs from the ATLAS^{3D} survey by Cappellari et al. (2013)

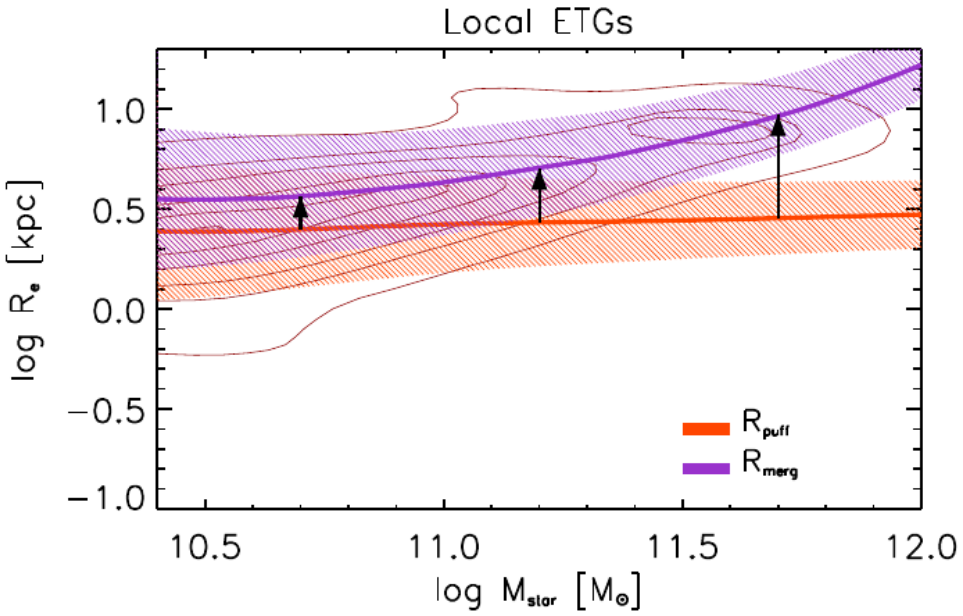

FIGURE 1.5: Size R_e vs. stellar mass $M_\star$ relationship by Lapi et al. (2018). The colored lines with shaded areas illustrate the size-mass relationship and the associated scatter expected along the evolution of ETG progenitors: orange line to the size $R_{\rm puff}$ after puffing up and magenta line to the final size $R_{\rm merg}$ after dry merging. Black arrows illustrate the evolution from one radius to the other. The dark red contours report the size distributions of local ETGs from the ATLAS^{3D} survey by Cappellari et al. (2013).

1.2.2 Interpreting the *main-sequence* of star-forming galaxies

The basic framework of *in-situ* co-evolution provides also the possibility to give a consistent interpretation of the observed *main-sequence* of star-forming galaxies, first discovered by Daddi et al. (2007) and Elbaz et al. (2007) and, more recently, empirically constrained by Speagle et al. (2014) up to $z \sim 6$. Indeed, it was outlined very well by Mancuso et al. (2016b), Mancuso et al. (2016a), and Mancuso et al. (2017). In the following I focus on the main ingredients that they exploited to populate the SFR $- M_\star$ plane from theoretical arguments and predictions checked against significant observations.

At first, the authors derived the global SFR function, namely the number density of galaxies per logarithmic bin of SFR (i.e. $[\log \dot{M}_\star + d \log \dot{M}_\star]$) at a given redshift z, on the basis of the most recent FIR and UV data from $z \sim 0$ to $z \sim 6$ by assuming a standard Schechter shape (Mancuso et al., 2016b). In Fig. 1.6 I show for reference their outcome, that was validated against independent data sets, including galaxy number counts in the FIR/(sub-)millimeter regime, redshift distribution of gravitationally lensed galaxies, and cosmic IR background.

Afterwards they modelled the galaxy SFH, namely the behaviour of the galaxy star formation as a function of galaxy *proper time* τ (i.e., the *galactic age*, meaning the time since the beginning of star formation), given galaxy stellar mass $M_\star$ and redshift z. To this aim, they based on indications emerging from good studies of SED-modelling of $z \gtrsim 2$ star-forming galaxies (e.g. Papovich et al., 2011; Smit et al., 2012; Moustakas et al., 2013; Steinhardt et al., 2014; Cassarà et al., 2016; Citro et al., 2016), that suggest a slow power-law increase of the SFR over a timescale τ_b, followed by an exponential decline with timescale $\tau_{\rm SFR}$, often referred as *delayed exponential* SFH. Its overall behaviour can be described as follows:

$$\begin{aligned} \mathrm{SFR}\,(\tau \mid M_\star,\, t) &= \dot{M}_{\star,b}(\tau/\tau_b)^k \quad \text{for } 0 \lesssim \tau \lesssim \tau_b \\ &= \dot{M}_{\star,b} \exp\left[-(\tau - \tau_b)/\tau_{\rm SFR}\right] \quad \text{for } \tau \gtrsim \tau_b, \end{aligned} \tag{1.17}$$

with $k \approx 0.5$ and $\mathrm{SFR}\,(\tau_b) = \dot{M}_\star[\tau_b/(k+1) + \tau_{\rm SFR}]^{-1}$. As to the value of the free parameters entering the above expression, i.e. τ_b and $\tau_{\rm SFR}$, recent observations by ALMA have shown that in massive high-redshift galaxies the star formation occurred over timescales $\tau_b \lesssim 0.5 - 1$ Gyr at violent rates SFR a few $10^2\, M_\odot\, yr^{-1}$ in heavily dust-enshrouded environments (e.g. Scoville et al., 2014; Scoville et al., 2016; Scoville et al., 2017). This is also confirmed by the observed α-enhancement (i.e. iron under-abundance compared to α elements) in stellar population of local ellipticals and also consistent with the predictions by the size-mass evolution for the high-z star-forming progenitors of ETGs by Lapi et al. (2018), that have been summarized in Sect. 1.2.1. The duration of the main star-forming burst is then parametrized as:

$$\tau_b = 1\,\mathrm{Gyr}\left(\frac{1+z}{3.5}\right)^{-3/2}\left[1 + 2\,\mathrm{erfc}\left(\frac{4}{3}\log\frac{\mathrm{SFR}}{5\,M_\odot yr^{-1}}\right)\right], \tag{1.18}$$

following Aversa et al. (2015). As to the quenching timescale $\tau_{\rm SFR}$, the observed fraction of FIR-detected host galaxies in X-ray (e.g. Mullaney et al., 2012; Page et al., 2012; Rosario et al., 2012) and optically selected AGNs (e.g. Mor et al., 2012; Wang et al., 2013; Willott, Bergeron, and Omont, 2015) points toward a SFR abruptly stopping, at least in massive galaxies, after τ_b over a short timescale $\tau_{\rm SFR} \lesssim 10^8$ yr due to the action of AGN feedback. I note that no merging/interaction with ambient and/or

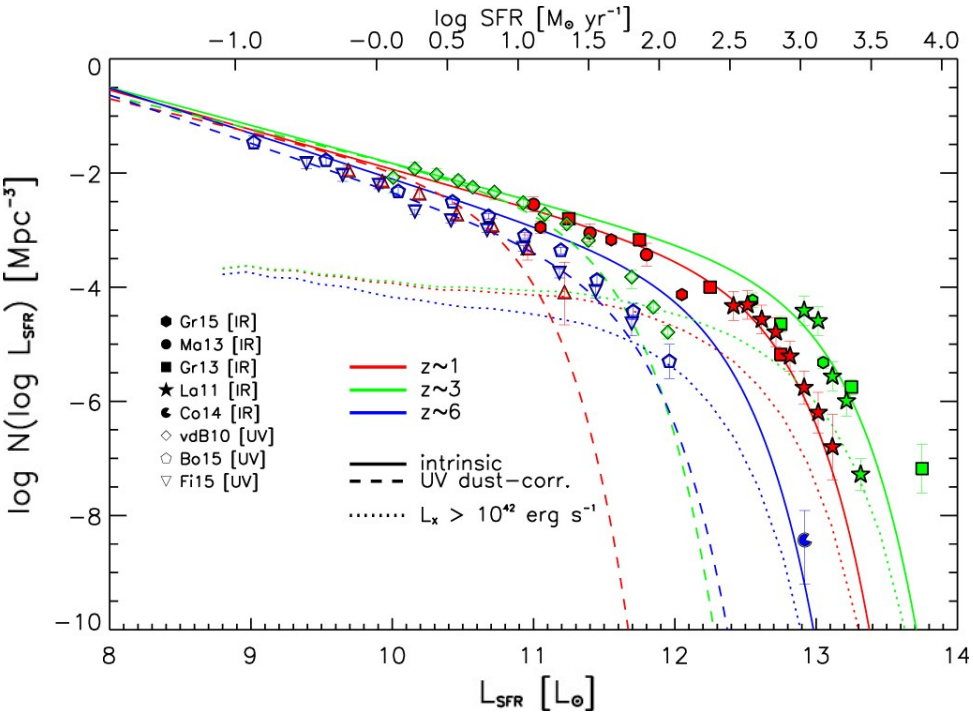

FIGURE 1.6: SFR functions by Mancuso et al. (2016b) at redshifts z = 1 (red lines), 3 (green lines) and 6 (blue lines). Solid lines refer to the global SFR function based on UV+far-IR measurements, while dashed lines to that based solely on UV measurements (dust-corrected via the UV slope). Dotted lines are the SFR functions of galaxies hosting an AGN with X-ray luminosity larger than 10^{42} erg/s. UV data (open symbols) are from van der Burg, Hildebrandt, and Erben (2010, diamonds), Bouwens et al. (2015, pentagons) and Finkelstein et al. (2015, inverse triangles); FIR data from Gruppioni et al. (2015, hexagons), Magnelli et al. (2013, circles), Gruppioni et al. (2013, squares), Lapi et al. (2011, stars) and Cooray et al. (2014, pacmans).

companions is considered while modelling galaxy SFH. The reference theoretical framework envisages star formation and accretion of the central BH to be mainly local, *in-situ* processes, and eventual interactions are not thought to significantly alter the picture, at least for the high-z progenitors of massive ETGs. For reference, in Fig. 1.7 I show the resulting star formation and BH accretion histories as a function of galaxy proper time τ. Following the prescriptions by the *in-situ* galaxy-BH co-evolution scenario, star formation in galaxies must be regulated mainly by energy feedback from SNe and central SMBH. In the early stages SFR is regulated by SN feedback and slightly increases with time, while AGN luminosity rises exponentially. After a fraction of Gyr in massive galaxies ($M_\star \gtrsim 3 \times 10^{10}\, M_\odot$) the nuclear power becomes dominant. The central BH shines as X-ray source and its luminosity becomes comparable and eventually overwhelms that associated with star formation in the host. Finally the thermal and mechanical feedback of the active nucleus removes gas and dust from the galaxy ISM and abruptly quenches the star formation in the host: the quasar shines as an optical source. Thereafter the nucleus luminosity exponentially fades out; stellar populations evolve passively and the galaxy becomes a *red and dead* elliptical.

Given the above SFR functions and galaxy SFH, Mancuso et al. (2016a) computed the number density of galaxies per unit co-moving volume (in Mpc^{-3}) that populates the SFR $- M_\star$ plane:

$$\frac{d^2N}{d\log \mathrm{SFR}\, d\log M_\star} \simeq \frac{dN}{d\log \mathrm{SFR}} \frac{d\delta}{d\log M_\star}. \tag{1.19}$$

The factors on the r.h.s. are the SFR functions and the relative time δ spent by the star-forming galaxy in a given logarithmic bin of $M_\star$. According to the star formation history described by Eq. (1.17), the latter just reads:

$$\frac{d\delta}{d\log M_\star} = \frac{M_\star}{\mathrm{SFR}} \frac{1}{\tau_b + \xi\tau_{SFR}} \ln 10 \tag{1.20}$$

Here the total duration of the star formation period is taken as $\tau_b + \xi\tau_{\mathrm{SFR}}$ with $\xi \approx 3$ since after that time the stellar luminosity is already decreased by a factor $\exp(-\xi) \lesssim 0.05$ and the stellar mass has already attained its final value to a very good approximation.

In Fig. 1.8 (upper panel) I show for reference the logarithmic number density of galaxies (color-coded) per unit co-moving volume after the above Eq. (1.19) for the interest redshift $z \approx 2$. The lilac line with error bars illustrates the number density-weighted mean relationship at given stellar mass with its 2σ variance and, as such, stands for the *main-sequence* of star-forming galaxies. Then, the main-sequence is found as a statistical *locus* in the SFR $- M_\star$ plane. However, this does not imply that an individual galaxy evolves by climbing along the main sequence. Typical evolutionary tracks followed by individual objects, as inspired by the *in-situ* co-evolution scenario, are illustrated by dotted black lines. Their characteristic shape is dictated by the slowly increasing of the SFR $\propto \tau^{1/2}$ and the rising of stellar mass $M_\star \propto \tau^{3/2}$, which imply SFR $\propto M_\star^{1/3}$. Then the main-sequence with its associated variance correspond to the portions of such tracks where galaxies spend most of their lifetime, in logarithmic bins of stellar mass, see Eq. (1.20). I note that the the main-sequence by Mancuso et al. (2016a) compares very well with the observational determinations based on large multi-wavelength (UV+IR), mass-selected samples (white shaded areas in Fig. 1.8) by Rodighiero et al. (2011) and Rodighiero et al.

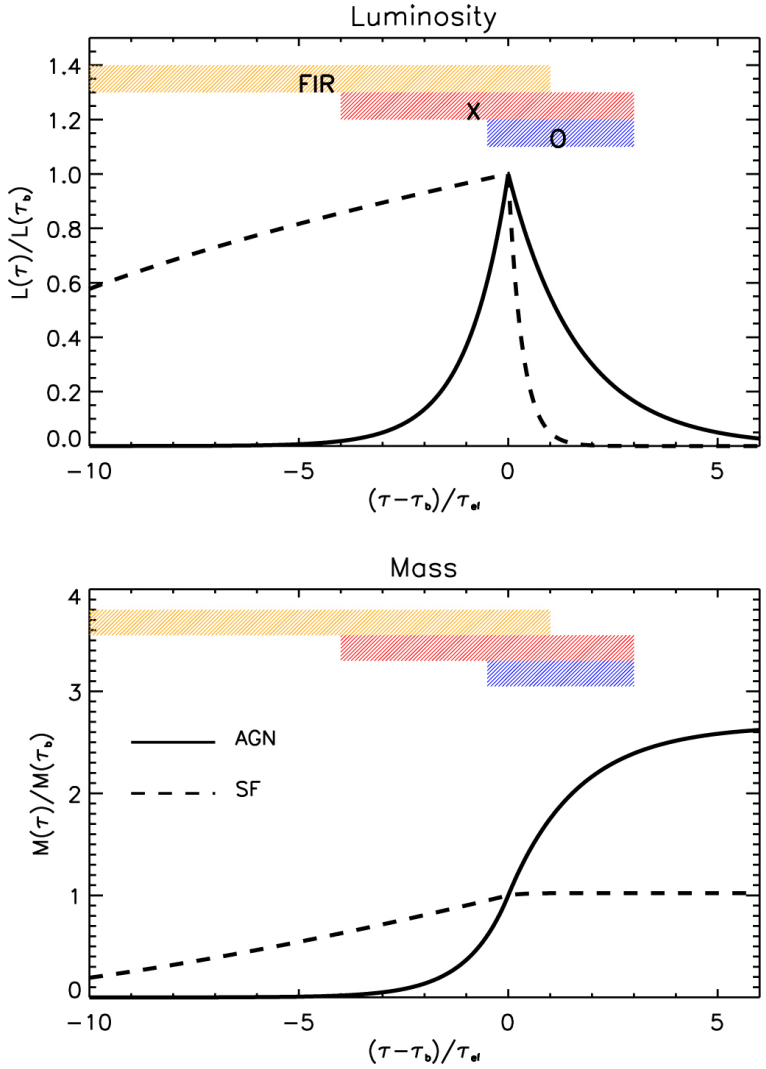

FIGURE 1.7: Galaxy star formation history and central BH accretion history by Mancuso et al. (2016a). Evolution with galactic age (in units of BH e-folding time $\tau_{\rm ef}$) of the luminosity (top panel) and mass (bottom panel), normalized at the time τ_b when the AGN luminosity peaks and the star formation is quenched by the AGN feedback. Solid lines refer to AGN-related quantities and dashed lines to star formation-related quantities. The orange area sketches the stage when the star-forming galaxy is dust-enshrouded and appears as a FIR bright source; the red area sketches the stage when the AGN X-ray (intrinsic) luminosity becomes comparable and eventually overwhelms that associated with star formation in the host; the blue area sketches the optical phase, setting in right after the quasar feedback removes gas and dust from the medium and quenches star formation.

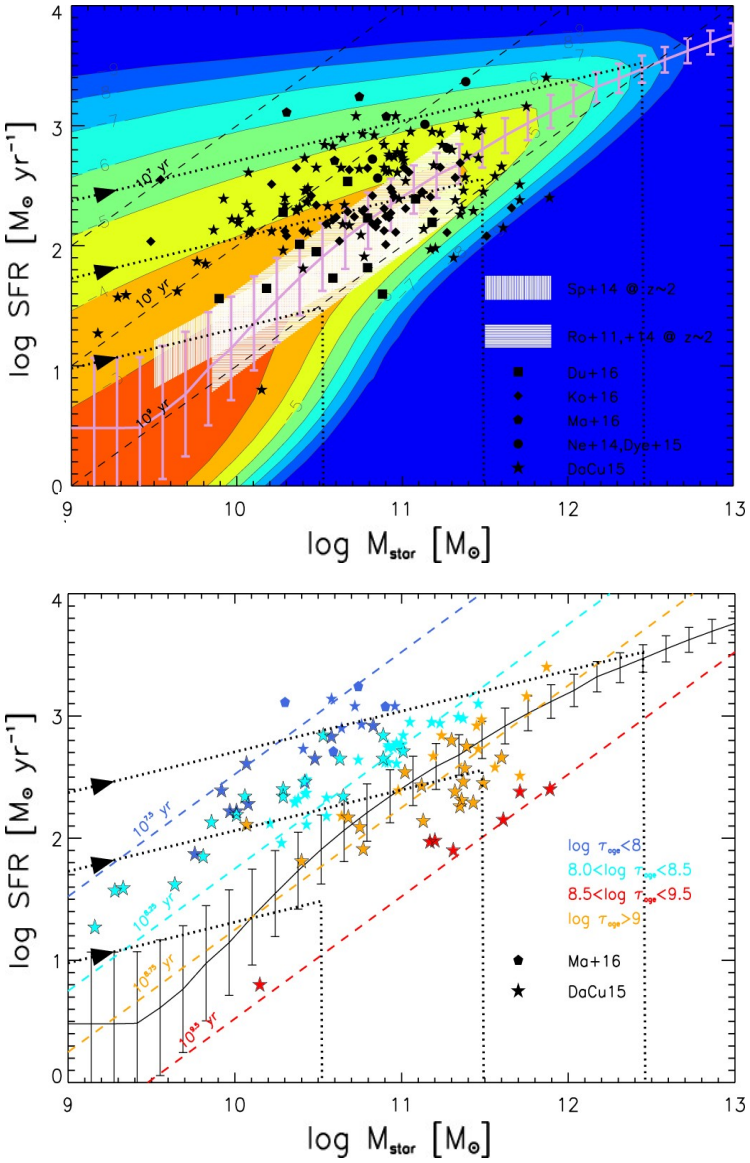

FIGURE 1.8: Galaxy main-sequence by Mancuso et al. (2016a, solid lines with error bars), based on the global (UV+FIR) SFR functions by Mancuso et al. (2016b). Upper panel: colored contours illustrate the number density of galaxies (labels are in log units of Mpc^{-3}) in the SFR$-M_\star$ plane. The lilac line illustrates the mean relationship with its 2σ scatter. The dotted lines show three evolutionary tracks (forward time direction indicated by arrows) for galaxies with final stellar mass $\sim 10^{10.5}$, $10^{11.5}$, $10^{12.5}\,M_\odot$. White shaded areas are the observational determinations of main-sequence at $z \sim 2$ by Rodighiero et al. (2011) and Rodighiero et al. (2014, horizontal line pattern) and Speagle et al. (2014, vertical line pattern). Filled black symbols (error bars omitted for clarity) refer to FIR data for individual objects by Dunlop et al. (2017, squares), Koprowski et al. (2016, diamonds), Ma et al. (2015, pentagons), Negrello et al. (2014, plus), Dye et al. (2015, circles) and da Cunha et al. (2015, stars). Lower panel: the same but data points are color-coded by galaxy age.

(2014) and Speagle et al. (2014). In addition, an appreciable fraction of individual, FIR selected galaxies (filled black symbols in Fig. 1.8) lie above the main-sequence, i.e., at SFR values higher than expected on the basis of the average relationship at given stellar mass. The off main-sequence objects are commonly interpreted as they are experiencing an episode of starburst triggered by a stochastic merger event. Although these instances may well occur, especially at low redshift $z \lesssim 1$, basing on the evolutionary tracks of individual galaxies predicted by the *in-situ* scenario, actually these objects should be caught in an early evolutionary stage, and still accumulating their stellar mass. Since the SFR changes slowly during the evolution, FIR selection is unbiased with respect to the stellar mass and young star-forming galaxies should be found to be preferentially located above the main sequence (i.e., to the left of it). As time goes by and stellar mass increases, the galaxy moves toward the average main sequence relationship, around which it will spend most of its lifetime. Afterwards, the SFR either slowly decreases because of gas exhaustion for galaxies with small final stellar mass ($M_\star < 10^{11}\,M_\star$), or is abruptly quenched by AGN feedback for galaxies with high final stellar mass ($M_\star \gtrsim 10^{11}\,M_\star$). After quenching, massive galaxies will evolve passively and will populate a region of the SFR$-M_\star$ diagram that is substantially below the main sequence. This *locus* of *red and dead* galaxies is indeed observed locally (e.g. Renzini and Peng, 2015), and start to be pinpointed even at high redshift (e.g. Man et al., 2016). This evolutionary picture is supported, e.g., by the estimates of the galaxy ages inferred from galaxy SED-fitting by da Cunha et al. (2015) and Ma et al. (2015). In Fig. 1.8 (lower panel) are shown the data points from the latter authors, with galaxy age highlighted in different colors. Galaxies at $z \sim 2$ (data points with black contours) located above the main-sequence are preferentially younger and less massive, with ages $\lesssim$ a few 10^8 yr: the ones more distant from the main-sequence feature smaller and smaller ages.

Many recent studies of high-z DSFGs (e.g. Stacey et al., 2020; Fraternali et al., 2021; Lelli et al., 2021; Rizzo et al., 2021), support the theoretical framework depicted by the *in-situ* scenario. As an example, the new finding by Rizzo et al. (2020) of a massive ($M_\star \simeq 1.2 \times 10^{10}\,M_\odot$) rotationally-supported ($v/\sigma = 9.7 \pm 0.4$) IR-luminous ($L_{\rm IR} = (2.4 \pm 0.4) \times 10^{12}\,L_\odot$) galaxy at $z \sim 4.2$, experiencing an intense episode of star-formation (SFR$= 352 \pm 65\,M_\odot\,yr^{-1}$ and $\tau_{\rm depl} = 38 \pm 9$ Myr), is in perfect alignment with the *in-situ* scenario and with its prediction on galaxy kinematics (see Lapi et al., 2018), witnessing that the main channels of such a strong and dusty star formation activity must be *in-situ*. Indeed, if the star-forming burst had been triggered by high-z wet merging events, we would have expected the galaxy to be dynamically hot, chaotic and strongly unstable: e.g., the most recent cosmological magneto-hydrodynamical simulation TNG50 gives $v/\sigma < 3$ for those values of stellar mass and redshift (Pillepich et al., 2019). Recently, an increasing number of studies on $z \sim 2$ massive star-forming galaxy kinematics have recognized the interaction/merging triggered bursts not to dominate DSFG population (e.g. Förster Schreiber et al., 2006; Förster Schreiber et al., 2011). A similar result is found by cosmological simulations, showing that the merger rate at the peak of Cosmic SFH (i.e., $z \sim 2$, corresponding to a cosmic time of ~ 3 Gyr) is too small to explain alone the abundant population of DSFGs observed at that epoch (e.g. Dekel et al., 2009; Stewart et al., 2009; Hopkins and Hernquist, 2010; Rodriguez-Gomez et al., 2016).

Although these evidences concurrently suggest that the main mechanisms leading high-z DSFG evolution can be mostly ascribed to local, *in-situ* condensation processes, certainly mergings and galaxy interactions play a role in determining the evolution of galaxies, especially in galaxy (proto-)clusters and densely populated environments (e.g., Tadaki et al., 2019), but mostly at $z \lesssim 1$, that is a range far away from

the one of interest for this work. However, in the following analysis y evidence of interaction/merging, as well as any signature of AGN feedback, will be then included in the final interpretative picture.

1.3 Thesis objective

The goal of this thesis is to characterize the early stages of DSFG evolution by investigating the spectral multi-band traces of the ongoing astrophysical processes (such as gas condensations, star formation, BH accretion and feedback).

To this aim, I will develop a *new* analytic model, describing the evolution with galaxy proper time of the main baryonic components (i.e., stars, dust and gas), that I will apply to the case of high-z DSFGs in Chapter 2.

Then, I will focus on a pilot sample of DSFGs that are spectroscopically confirmed to be at the peak of Cosmic SFH and I will exploit the wealth of information coming from multi-wavelength photometry, spectroscopy and imaging at high-resolution to investigate the nature of these galaxies (Chapters 3 and 4).

Finally, I will provide a possible and physically-motivated interpretation of the observational outcomes in the framework of the *in-situ* galaxy formation and evolution scenario. As such, I will exploit the model developed in Chapter 2 and I will refer mainly to the *in-situ* galaxy-BH co-evolution scenario.

In Chapter 5 I will deal with my conclusions and future perspectives.

Chapter 2

A new model to study the evolution of galaxy baryonic components

In this Chapter I will present the set of analytic solutions that, on the basis of the *in-situ* model receipts, can self-consistently describe the spatially-averaged time evolution of the gas, dust, stellar and metals content in star-forming galaxies, focusing on the high-z counterparts of local ETGs.

Specifically, in Sect. 2.1 I will solve analytically the differential equation describing the evolution of the baryonic components mentioned above with galaxy proper time and I will give the corresponding solutions for an individual galaxy. For the sake of completeness, I will compare the outcomes with classic analytic models describing the time evolution of the gaseous component, i.e., no inflow models (leaky/closed-box solution) and constant inflow models (gas-regulator/bath-tube solution).

In Sect. 2.2 I will specialize the analytic solutions to the high-z population of DSFGs, including halo and stellar mass growth by merging events on the basis of the merger rates from state-of-the-art numerical simulations; then, I will derive the statistical relationships followed by this class of galaxies by averaging over the possible formation redshifts, after setting the main free parameters to follow the framework defined by the *in-situ* galaxy-BH co-evolution scenario. Finally, I will compare the theoretical predictions with observational data concerning local ETGs and their high-z star-forming progenitors, finding a pleasing overall agreement.

2.1 Analytic solution for individual galaxies

Here, I present the analytic solutions for the time evolution of the gas, stellar, metal and dust content in high-z star-forming galaxies, and in particular in massive progenitors of ETGs. These are derived from a quite general framework, meant to capture the main physical processes regulating galaxy formation on a spatially-averaged ground.

2.1.1 Gas and stars

In the following, I consider a one-zone description of a galaxy with three interlinked mass components: the infalling gas mass $M_{\rm inf}$, the cold gas mass $M_{\rm cold}$[1], and the stellar mass $M_\star$. The evolution of these components is described by the following

[1]I note that, in this approach, even the infalling gas is cold in the sense it can cool fast, and then it is infalling toward the central region over the dynamical timescale.

system of ordinary differential equations:

$$\begin{cases} \dot{M}_{\rm inf} = -\frac{M_{\rm inf}}{\tau_{\rm cond}} \\ \dot{M}_{\rm cold} = +\frac{M_{\rm inf}}{\tau_{\rm cond}} - \gamma\,\frac{M_{\rm cold}}{\tau_\star} \\ \dot{M}_\star = \frac{M_{\rm cold}}{\tau_\star} \end{cases} \tag{2.1}$$

where $\gamma \equiv 1 - \mathcal{R} + \epsilon_{\rm out}$. These equations prescribe that the infalling gas mass $M_{\rm inf}$ cools and condenses into the cold gas phase $M_{\rm cold}$ on a timescale $\tau_{\rm cond}$; then, the stellar mass $M_{\rm star}$ is formed from the cold mass $M_{\rm cold}$ at a rate $\dot{M}_{\rm star}$ on a timescale $\tau_\star$; the cold gas mass is further replenished at a rate $\mathcal{R}\,\dot{M}_{\rm star}$ by stellar recycling, where $\mathcal{R}$ is the return fraction of gaseous material from stellar evolution, and it is removed at a rate $\epsilon_{\rm out}\,\dot{M}_{\rm star}$ by outflows driven from SNe II and stellar winds (mainly from AGB stars), where $\epsilon_{\rm out}$ is the mass loading factor. In Eqs. (2.1) the quantity $M_\star(\tau) = \int_0^\tau d\tau' \dot{M}_\star(\tau')$ represents the integral of the SFR over the galactic age, while the true relic stellar mass after the loss due to stellar evolution is $M_\star^{\rm relic} \simeq (1-\mathcal{R})M_\star$. I have adopted a IMF $\phi(m_\star)$ uniform in space and constant in time, and assumed the instantaneous mixing (gas is well mixed at anytime) and instantaneous recycling (stars with mass $m_\star \gtrsim 1 M_\odot$ die as soon as they form, while those with $m_\star \lesssim 1 M_\odot$ live forever) approximations, so that the recycled fraction (fraction of a stellar population not locked into long-living dark remnants) can be computed as:

$$\mathcal{R} = \int_{1\,M_\odot}^{100\,M_\odot} dm_\star (m_\star - m_{\rm rem})\phi(m_\star) \tag{2.2}$$

where $m_{\rm rem}(m_\star)$ is the mass of the remnants. Under the assumption of the fiducial Chabrier (2003) and Chabrier (2005) IMF, the recycling fraction amounts to $\mathcal{R} \approx 0.45$.

Standard initial conditions read $M_{\rm inf}(0) = f_{\rm inf}\,M_{\rm b}$ and $M_{\rm cold}(0) = M_\star(0) = 0$. Here $M_b = f_b\,M_{\rm H}$ is the baryonic mass originally present in the host halo with mass $M_{\rm H}$, while $f_{\rm inf} = M_{\rm inf}/f_b\,M_{\rm H}$ is the fraction of such a mass that can effectively cool and inflow toward the inner regions of the halo.

Being the main focus to derive analytic solutions for high-z star-forming galaxies, and in particular for the progenitors of local spheroids/ETGs, I have not included in the equations above a number of processes that can be otherwise relevant for the evolution of local LTGs, such as galactic fountains and radial gas flows (e.g., Bregman, 1980; Lacey and Fall, 1985; Pitts and Tayler, 1989; Spitoni, Recchi, and Matteucci, 2008; Fu et al., 2013; Spitoni, Matteucci, and Marcon-Uchida, 2013; Pezzulli and Fraternali, 2016; Stevens, Croton, and Mutch, 2016; Stevens and Brown, 2017; Stevens et al., 2018), differential galactic winds (e.g., Pilyugin, 1993; Marconi, Matteucci, and Tosi, 1994; Recchi et al., 2008), multi-zonal structures and stellar mixing (see Kubryk, Prantzos, and Athanassoula, 2015; Spitoni et al., 2015; Grisoni, Spitoni, and Matteucci, 2018). For the sake of completeness, an application to LTGs is presented in Appendix B.

I note that he star formation timescale and the duration of the main star formation episode in high-z (i.e. $z > 1$) star-forming galaxies, and in particular in ETG progenitors, range typically from a few 10^8 to 10^9 yr (e.g. Thomas et al., 2005; Gallazzi et al., 2006; Gallazzi et al., 2014); moreover, most of the star formation process occurs in a central compact region of size around a few kpcs (e.g., Scoville et al., 2014; Scoville et al., 2016; Ikarashi et al., 2015; Simpson et al., 2015; Spilker et al., 2015; Tadaki et al., 2017a; Tadaki et al., 2017b; Lang et al., 2019). Given that, it is possible

to safely neglect in Eqs. (2.1) additional terms describing the growth of the host DM halo and of the stellar content due to accretion and/or mergers, that typically occur over cosmological timescales of several Gyrs and large spatial scales that range from several tens of kpc (stellar mass addition by galaxy mergers) to several hundreds of kpc (growth of DM halo and gaseous baryon reservoir). Nonetheless, these mass additions will become relevant in the long-term evolution of ETG progenitors toward the present and, as such, they will be included in the computations in Sect. 2.2.4.

A classic way to link the SFR and the cold gas mass, adopted by many analytic models focused on disk galaxies, is the classic Schmidt-Kennicutt law (Schmidt, 1959; Kennicutt, 1998). This prescribes:

$$\dot{\Sigma}_{\star} \propto \Sigma_{\rm cold}^{1.4} \tag{2.3}$$

in terms of the stellar and gas disk surface densities $\dot{\Sigma}_{\star}$ and $\Sigma_{\rm cold}$. However, in Eqs. 2.1 I have adopted instead a spatially-averaged star formation law, i.e. $\dot{M}_{\star} \propto M_{\rm cold}$, linking linearly the SFR and the total cold gas mass, as it is indicated by recent observations of local starbursts and high-z star-forming galaxies (Scoville et al., 2016; Scoville et al., 2017), and also suggested for local disk galaxies by spatially resolved observations of dense gas in molecular clouds (e.g., Bigiel et al., 2008; Lada, Lombardi, and Alves, 2010). I further note that the star formation law $\dot{M}_{\star} = M_{\rm cold}/\tau_{\star}$ has been written in terms of the total cold gas mass, but it can be equivalently expressed as $\dot{M}_{\star} = f_{H_2} M_{\rm cold}/\tau_{\star,H_2}$ in terms of the molecular gas fraction f_{H_2} by simply redefining the star formation timescale $\tau_{\star} = \tau_{\star,H_2}/f_{H_2}$ (see Feldmann, 2015).

The above system of linear equations (Eqs. 2.1) can be easily solved analytically in the form:

$$\begin{cases} M_{\rm inf}(x) = f_{\rm inf}\, M_{\rm b}\, e^{-x} \\ M_{\rm cold}(x) = \frac{f_{\rm inf}\, M_{\rm b}}{s\,\gamma - 1}\, [e^{-x} - e^{-s\,\gamma\,x}] \\ M_{\star}(x) = \frac{f_{\rm inf}\, M_{\rm b}\, s}{s\,\gamma - 1}\, \left[1 - e^{-x} - \frac{1}{s\,\gamma}\, (1 - e^{-s\,\gamma\,x})\right] \end{cases} \tag{2.4}$$

where $x = \tau/\tau_{\rm cond}$ is a dimensionless time variable normalized to the condensation timescale, and $\tau_{\rm cond}/\tau_{\star}$ is the ratio between the condensation and the star formation timescales. The above solution is physically meaningful (specifically, the cold and stellar masses are non-negative for any x) whenever $s\gamma > 1$. Since $1/\gamma = 1/(1 - \mathcal{R} + \epsilon_{\rm out}) \lesssim 1/(1 - \mathcal{R}) \lesssim 2$ it is sufficient that $s > 2$. For ETG progenitors typical values $s \simeq 3$ apply at any mass and redshift, so that the above condition is regularly met. In Fig. 2.2 is shown the behaviour of the main parameters entering the analytic solutions relevant for ETG progenitors as a function of host halo mass M_H and formation redshift $z_{\rm form}$.

According to Eqs. (2.1), the infalling gas mass declines exponentially with time, while the cold gas mass (hence the SFR) features an initial growth, then attains a maximum and eventually declines exponentially, as it is shown in Figs. 2.4 and 2.5.

It is instructive to examine the initial behavior of the solutions for $\tau \ll \tau_{\rm cond}$, that reads:

$$\begin{cases} M_{\rm inf} \simeq f_{\rm inf} M_b \left(1 - \frac{\tau}{\tau_{\rm cond}}\right) \\ M_{\rm cold} \simeq f_{\rm inf} M_b \left(\frac{\tau}{\tau_{\rm cond}}\right) \\ M_\star \simeq \frac{s f_{\rm inf} M_b}{2} \left(1 - \frac{\tau}{\tau_{\rm cond}}\right)^2 \end{cases} \tag{2.5}$$

where the dimensionless independent variable x has been re-expressed as $\tau/\tau_{\rm cond}$. In addition, the maximum of cold gas mass (and SFR) occurs for

$$\tau_{\rm max} = \tau_{\rm cond} \ln (s\gamma)^{1/(s\gamma-1)} \tag{2.6}$$

when the mass of the various gas components writes:

$$\begin{cases} M_{\rm inf}(\tau_{\rm max}) \simeq f_{\rm inf} M_b (s\gamma)^{-1/(s\gamma-1)} \\ M_{\rm cold}(\tau_{\rm max}) \simeq f_{\rm inf} M_b (s\gamma)^{-s\gamma/(s\gamma-1)} \\ M_\star(\tau_{\rm max}) \simeq \frac{f_{\rm inf} M_b}{\gamma} \left[1 - (1+s\gamma)(s\gamma)^{-s\gamma/(s\gamma-1)}\right]. \end{cases} \tag{2.7}$$

Finally, for $\tau \gg \tau_{\rm cond}$ the solutions behave as:

$$\begin{cases} M_{\rm inf} \simeq f_{\rm inf}\, M_b\, e^{-\tau/\tau_{\rm cond}} \\ M_{\rm cold} \simeq \frac{f_{\rm inf}\, M_b}{s\gamma - 1}\, e^{-\tau/\tau_{\rm cond}} \\ M_\star \simeq \frac{f_{\rm inf}\, M_b}{\gamma} \ . \end{cases} \tag{2.8}$$

These expressions highlight a few interesting facts.

First, the overall time behavior of the cold gas mass and of the SFR, i.e. $\dot{M}_\star(\tau) \propto M_{\rm cold}(\tau)$, is very similar to the empirical delayed exponential shape $M_\star \propto \tau^k e^{-\tau/\tau_{\rm cond}}$ with $k \lesssim 1$, which is routinely used to describe the star formation histories and to interpret the SED of high-z star-forming galaxies and progenitors of local spheroids (see Papovich et al., 2011; Moustakas et al., 2013; Steinhardt et al., 2014; da Cunha et al., 2015; Citro et al., 2016; Cassarà et al., 2016; Boquien et al., 2019); thus the solutions may provide a physical basis to that empirical shape.

Second, after the peak of the SFR for $\tau \gtrsim \tau_{\rm max}$ the infall rate and the SFR are proportional, such that $\dot{M}_{\rm inf} \propto -(s\gamma - 1)\dot{M}_\star$. This explains why models where a similar proportionality is assumed *a priori* (e.g., Matteucci and Chiosi, 1983; Matteucci, 2012) produce results not substantially different from those with a generic exponential infall (see Recchi et al., 2008).

Third, the specific star formation rate, i.e. sSFR $\equiv \dot{M}_\star/M_\star$, is a monotonic function of the galaxy age, since at early times it behaves like sSFR $\simeq 2/\tau$ and at late times as sSFR $\simeq s\gamma\, e^{-\tau/\tau_{\rm cond}}/(s\gamma - 1)$; thus a selection in sSFR is equivalent to a selection in galaxy age.

Lastly, the true relic stellar mass after the loss due to stellar evolution is:

$$M_\star^{\rm relic} \simeq (1 - \mathcal{R}) M_\star = \frac{1 - \mathcal{R}}{1 - \mathcal{R} + \epsilon_{\rm out}} f_{\rm inf} M_b \ ; \tag{2.9}$$

thus, in absence of any outflows $\epsilon_{\rm out} \approx 0$, all the available (infalling) baryons would be converted into stars.

2.1.2 Metals in the cold gas phase

In this Section I discuss the time evolution of the cold gas metallicity. First, I will focus on the instantaneous production of α-elements by SNe II and stellar winds. Then, I will turn to the delayed production of iron-group elements by SNe I*a*.

Instantaneously produced elements

The time evolution of the cold gas metallicity $Z_{\rm cold}$ contributed by instantaneously produced chemical elements can be described as:

$$\frac{d}{d\tau}(M_{\rm cold}\, Z_{\rm cold}) = -\gamma \dot{M}_\star Z_{\rm cold} + y_Z(1-\mathcal{R})\dot{M}_\star. \tag{2.10}$$

This equation prescribes that the mass of metals in cold gas, i.e. $M_{\rm cold}Z_{\rm cold}$, evolves because of instantaneous metal production at a rate $y_Z(1-\mathcal{R})\dot{M}_\star$, outflow depletion at a rate $\epsilon_{\rm out}\dot{M}_\star Z_{\rm cold}$ and astration (i.e. metal mass locking into stellar remnants) at a rate $(1-\mathcal{R})\dot{M}_\star Z_{\rm cold}$. The infalling gas metallicity is neglected, since the infalling gas is assumed to be primordial (but its metallicity can be otherwise included very easily in the analytic solutions). Under the instantaneous mixing and recycling approximation, the metal production yield y_Z is given by:

$$y_Z \equiv \frac{1}{1-\mathcal{R}} \int_{1\,M_\odot}^{100\,M_\odot} dm_\star m_\star p_{Z,\star} \phi(m_\star), \tag{2.11}$$

where $p_{Z,\star}$ is the mass fraction of newly synthesized metals a star of initial mass $m_\star$. With this definition, that is relative to $(1-\mathcal{R})$, the yield y_Z is actually the ratio between the mass of heavy elements ejected by a stellar generation and the mass locked up in remnants.

In many previous analytic models, to solve the chemical evolution equation, an empirical shape of the SFR is adopted. Remarkably, here it is used the self-consistent solutions for the time evolution of infalling and cold gas masses. Then Eq. (2.10) can be recast into the form:

$$\dot{Z}_{\rm cold} = -\frac{Z_{\rm cold}}{\tau_{\rm cold}} \frac{s\gamma - 1}{1 - e^{-(s\gamma-1)\tau/\tau_{\rm cond}}} + \frac{y_Z(1-\mathcal{R})s}{\tau_{\rm cond}} \tag{2.12}$$

with initial condition $Z_{\rm cold}(0) = 0$. The corresponding analytic solution for the cold gas metallicity reads:

$$Z_{\rm cold}(\tau) = \bar{Z}_{\rm cold}\left[1 - \frac{(s\gamma-1)x}{e^{(s\gamma-1)x} - 1}\right], \tag{2.13}$$

where

$$\bar{Z}_{\rm cold} = \frac{s y_Z (1-\mathcal{R})}{s\gamma - 1} \tag{2.14}$$

represents the asymptotic value for $\tau \gg \tau_{\rm cond}$. It turns out that the evolution of the gas metallicity is very rapid, so it attains values $\gtrsim Z_\odot/10$ in quite a short time scale, i.e. $\tau \lesssim \tau_{\rm cond}/10 \approx$ a few 10^7 yr. This is relevant for the metal and dust enrichment of primordial galaxies and quasars at high redshift (see e.g. Saracco et al., 2020).

It is instructive to look at the initial behavior of the gas metallicity for $\tau \ll \tau_{\rm cond}$, which reads:

$$Z_{\rm cold}(\tau) \simeq \frac{s\, y_Z\, (1-\mathcal{R})}{2} \frac{\tau}{\tau_{\rm cond}} \ ; \tag{2.15}$$

the resulting evolution is almost linear with galactic age until a saturation to the final, stationary value $\bar{Z}_{\rm cold}$ takes place.

Interestingly, the cold gas metallicity evolution at early times can be expressed in terms of the sSFR $\equiv \dot{M}_\star / M_\star$ such that it behaves like:

$$Z_{\rm cold}(\tau) \simeq \frac{s\, y_Z\, (1-\mathcal{R})}{\rm sSFR\, \tau_{\rm cond}} \propto \frac{M_\star}{\dot{M}_\star} \ ; \tag{2.16}$$

thus a selection based on small $M_\star$ or large sSFR will tend to pick up objects for which the gas metallicity scales inversely with the SFR.

On the other hand, at late times, the gas metallicity saturates to a constant value $\bar{Z}_{\rm cold}$; thus a selection based on large $M_\star$ or small sSFR will tend to pick up galaxies for which the cold gas metallicity is uncorrelated with the SFR. This is the essence of the fundamental metallicity relation, established observationally by Mannucci et al. (2010); see also Lara-López, López-Sánchez, and Hopkins (2013).

Delayed produced elements

Here, I deal with the delayed production of metals due to SNe I*a*, related to the iron-group elements.

To a good approximation, one can decompose $Z_{\rm cold} \simeq Z^{\Delta=0}_{\rm cold} + Z^{\Delta}_{\rm cold}$ into an instantaneous production component $Z^{\Delta=0}_{\rm cold}$, as described in the previous section, and a delayed production component $Z^{\Delta}_{\rm cold}$, governed by the equation:

$$\frac{d}{d\tau}(M_{\rm cold}\, Z_{\rm cold}) = -\gamma\, \dot{M}_\star\, Z^{\Delta}_{\rm cold} + y^{\Delta}_Z\, (1-\mathcal{R})\, \dot{M}_\star(\tau) \times \frac{\dot{M}_\star(\tau-\Delta)}{\dot{M}_\star(\tau)} \tag{2.17}$$

with y^{Δ}_Z being the stellar yield for delayed metals, and Δ the delay time for the enrichment by SNe I*a*, that for the moment I consider fixed to some particular values.

I note that this equation is very similar to that for instantaneously produced metals, apart from the factor $\dot{M}_\star(\tau-\Delta)/\dot{M}_\star(\tau)$ in the last term on the r.h.s., which accounts for the delayed contribution of SNe I*a* in polluting the cold medium.

Using the self-consistent solutions for the SFR, the evolution equation for the delayed metallicity $Z^{\Delta}_{\rm cold}$ becomes:

$$\begin{aligned} \dot{Z}^{\Delta}_{\rm cold} = &- \frac{Z^{\Delta}_{\rm cold}}{\tau_{\rm cond}} \frac{s\,\gamma - 1}{1 - e^{-(s\,\gamma-1)\,\tau/\tau_{\rm cond}}} + \frac{y^{\Delta}_Z\,(1-\mathcal{R})\,s}{\tau_{\rm cond}} \times \\ &\times \frac{e^{\Delta/\tau_{\rm cond}} - e^{s\,\gamma\,\Delta/\tau_{\rm cond}}\, e^{-(s\,\gamma-1)\,\tau/\tau_{\rm cond}}}{1 - e^{-(s\,\gamma-1)\,\tau/\tau_{\rm cond}}} \end{aligned} \tag{2.18}$$

with initial condition $Z^{\Delta}_{\rm cold}(\tau) = 0$ for $\tau < \Delta$. The corresponding analytic solution reads:

$$Z^{\Delta}_{\rm cold}(\tau) = \begin{cases} \bar{Z}^{\Delta}_{\rm cold} \left[1 - \dfrac{e^{(s\,\gamma-1)\,x_\Delta}\,[1 + (s\,\gamma-1)\,(x - x_\Delta)] - 1}{e^{(s\,\gamma-1)\,x} - 1} \right] & \text{for} \quad x \geq x_\Delta \ , \\ \\ 0 & \text{for} \quad x < x_\Delta \ , \end{cases}$$

where $x_\Delta \equiv \Delta/\tau_{\rm cond}$ and $\bar{Z}^\Delta_{\rm cold}$ is the delayed metallicity asymptotic behavior for $\tau \gg \tau_{\rm cond}$:

$$\bar{Z}^\Delta_{\rm cold} = \frac{s\, y^\Delta_Z\,(1-\mathcal{R})\; e^{\Delta/\tau_{\rm cond}}}{s\,\gamma - 1}\,. \tag{2.19}$$

I note that, as it should be, for $\Delta = 0$ the time dependence in Eq. (2.19) converges to that of cold gas metallicity for instantaneously produced elements in Eq. (2.10). The behavior of $Z^\Delta_{\rm cold}$ for $\tau \simeq \Delta$ reads:

$$Z^\Delta_{\rm cold}(\tau) \simeq \frac{s\, y^\Delta_Z\,(1-\mathcal{R})}{2}\,\frac{(s\gamma-1)\,e^{s\gamma\,\Delta/\tau_{\rm cond}}}{e^{(s\gamma-1)\,\Delta/\tau_{\rm cond}}-1}\left(\frac{\tau-\Delta}{\tau_{\rm cond}}\right)^2\,. \tag{2.20}$$

The above solution holds when a single delay time Δ is assumed. However, it is well known that SNe I*a* feature a non-trivial delay time probability distributions $\mathrm{d}p/\mathrm{d}\Delta$, or DTDs. Typically, universal DTDs with shapes $\mathrm{d}p/\mathrm{d}\Delta \propto \Delta^{-1}$, $\propto e^{-\Delta/\Delta_c}$, $\propto e^{-(\Delta-\bar{\Delta})^2/\sigma^2_\Delta}$ or combination of these, are consistent with observations and widely adopted in chemical evolution models (e.g. Greggio, 2005; Mannucci, Della Valle, and Panagia, 2006; Totani et al., 2008; Walcher et al., 2016; Schönrich and Binney, 2009; Maoz and Graur, 2017; Maoz, Mannucci, and Nelemans, 2014, for a review and further references). In such a case, one can easily recognize that, since the differential equation involved is linear, the above solution actually constitutes the *Green function* of the problem, i.e. the solution for a Dirac-δ_D delay time distribution centered at a delay time Δ. Thus, the overall solution for a generic $\mathrm{d}p/\mathrm{d}\Delta$ is just the superposition of the previous solution for given Δ weighted by the DTD, so that:

$$Z^{\rm DTD}_{\rm cold}(\tau) = \int \mathrm{d}\Delta\,\frac{\mathrm{d}p}{\mathrm{d}\Delta}\,Z^\Delta_{\rm cold}(\tau)\,. \tag{2.21}$$

As a working example, I take the (analytically convenient) exponential DTD with normalized shape $\mathrm{d}p/\mathrm{d}\Delta = (\omega/\tau_{\rm cond})\,e^{-\omega\,\Delta/\tau_{\rm cond}}$, where $\tau_{\rm cond}/\omega$ is the average typical DTD timescale. Then, one can compute explicitly:

$$Z^{\rm DTD}_{\rm cold}(\tau) = \bar{Z}^{\rm DTD}_{\rm cold}\left[1-\left(\frac{s\gamma-1}{s\gamma-\omega}\right)^2\,\frac{e^{(s\,\gamma-\omega)\,x}-1-x\,(\omega-1)\,(s\gamma-\omega)/(s\gamma-1)}{e^{(s\,\gamma-1)\,x}-1}\right]\,,$$

where

$$\bar{Z}^{\rm DTD}_{\rm cold} = \frac{s\,\omega\,y^\Delta_Z\,(1-\mathcal{R})}{(\omega-1)\,(s\,\gamma-1)}\,. \tag{2.22}$$

As in Eqs. (2.1), one can easily check that for $\omega > 0$ the above solution Eq. (2.22) is physically meaningful (non-negative for any x) when $s\gamma > 1$. The solution is also defined for $\omega \simeq 1$ and explicitly writes down as:

$$Z^{\rm DTD}_{\rm cold}(\tau) \simeq s\;y^\Delta_Z\,(1-\mathcal{R})\left[\frac{x}{s\gamma-1}\,\frac{e^{(s\gamma-1)\,x}+1}{e^{(s\gamma-1)\,x}-1}-\frac{2}{(s\gamma-1)^2}\right]\,. \tag{2.23}$$

The early-time behavior of Eq. (2.22) for $\tau \ll \tau_{\rm cond}$ reads:

$$Z^{\rm DTD}_{\rm cold}(\tau) \simeq \frac{s\,\omega\,y^\Delta_Z\,(1-\mathcal{R})}{6}\left(\frac{\tau}{\tau_{\rm cond}}\right)^2\,, \tag{2.24}$$

so that initially the increase in metallicity of delayed metals $Z^{\rm DTD}_{\rm cold} \propto \tau^2$ is clearly

retarded with respect to that of instantaneously produced metals $Z_{\rm cold} \propto \tau$, even when averaged over the DTD. On the other hand, the late-time behavior for $\tau \gg \tau_{\rm cond}$ depends on ω as:

$$Z_{\rm cold}^{\rm DTD}(\tau) \simeq \begin{cases} \dfrac{s\,\omega\,y_Z^\Delta\,(1-\mathcal{R})}{(\omega-1)\,(s\,\gamma-1)} & \text{for} \quad \omega > 1\,, \\ \dfrac{s\;y_Z^\Delta\,(1-\mathcal{R})}{s\,\gamma-1}\,\dfrac{\tau}{\tau_{\rm cond}} & \text{for} \quad \omega = 1\,, \\ \dfrac{s\,\omega\,y_Z^\Delta\,(1-\mathcal{R})\,(s\,\gamma-1)}{(1-\omega)\,(s\,\gamma-\omega)^2}\,e^{(1-\omega)\,\tau/\tau_{\rm cond}} & \text{for} \quad \omega < 1\,. \end{cases}$$

The solution converges for $\omega > 1$ to $\bar{Z}_{\rm cold}^{\rm DTD}$, while it diverges linearly for $\omega = 1$ and exponentially for $\omega < 1$. However, these divergences occur only at very late-times, so that the solution behaves very similarly out to $\tau/\tau_{\rm cond} \lesssim 10^2$ for any value of ω.

2.1.3 Comparison with classic analytic models describing the gas component

In this Section I compare the analytic solutions for the evolution of gas metallicity (cf. Sect. 2.1.2) with classic analytic models, extensively adopted to describe the spatially-averaged behavior of star-forming galaxies. Specifically, I will focus on the two classes of models that have, as limiting cases, the classical *closed-box* and gas regulator (or *bath-tube*) solutions respectively.

No inflow models and the leaky/closed-box solution

A class of simple analytic models can be obtained by imposing no inflow of gas. The relevant equations describing the evolution of gas mass and metallicity can be written as:

$$\begin{cases} \dot{M}_{\rm cold} = -\gamma\,\dot{M}_\star \\ \dot{Z}_{\rm cold} = \frac{y_Z\,(1-\mathcal{R})}{\gamma}\,\frac{\dot{M}_{\rm cold}}{M_{\rm cold}}\,, \end{cases} \tag{2.25}$$

with initial conditions $M_{\rm cold}(0) = M_{\rm cold,0}$ and $Z_{\rm cold}(0) = 0$. The interesting feature of this class of models is that, irrespective of the shape of the SFR (i.e. $\dot{M}_\star$) and of its relation with the gas mass $M_{\rm cold}$, an implicit solution can be provided in terms of the gas mass fraction $\mu \equiv M_{\rm cold}/M_{\rm cold} + M_\star$. Solving the above equations in terms of μ one easily obtains:

$$\begin{cases} M_{\rm cold} = M_{\rm cold,\,0}\,\frac{\mu}{\gamma-(\gamma-1)\,\mu} \\ Z_{\rm cold} = \frac{y_Z\,(1-\mathcal{R})}{\gamma}\,\ln\left(\frac{1}{\mu}-\frac{\gamma-1}{\gamma}\right)\,. \end{cases} \tag{2.26}$$

Since at late times one expect $\mu \ll 1$, the metallicity asymptotically behaves as $Z_{\rm cold} \simeq y_Z(1-\mathcal{R})\gamma^{-1}\ln\mu^{-1}$: this is often referred to as the *leaky-box* solution. For $\gamma \simeq 1$ (i.e., $\epsilon_{\rm out} = \mathcal{R} = 0$), which corresponds to neglecting outflow and recycling, one finds the classical *closed-box* solution: in such a case the total mass is constant in time and hence $\mu \simeq M_{\rm cold}/M_{\rm cold,\,0}$ and $Z_{\rm cold} \simeq y_Z \ln\mu^{-1}$.

Coming back to the solution in Eqs. (2.26), one can find an explicit time dependence by specifying the relation between the SFR and the gas mass. In the way of comparing the outcome with the result of Eqs. (2.4) and (2.13), I prescribe as in Eqs. (2.1) that $\dot{M}_\star = M_{\rm cold}/\tau_\star = s M_{\rm cold}/tau_{\rm cond}$, and that $M_{cold,0} = f_{\rm inf} M_b$. In such a case it is found that:

$$\begin{cases} M_{\rm cold}(x) = f_{\rm inf}\, M_b\, e^{-s\gamma\, x} \\ \\ Z_{\rm cold}(x) = \frac{y_Z\,(1-\mathcal{R})}{\gamma}\,(s\gamma\, x - \ln\gamma) \end{cases} \tag{2.27}$$

with $x \equiv \tau/\tau_{\rm cond}$. Clearly, the absence of dilution due to inflow makes the metallicity to increase almost linearly with galactic age, while the cold gas reservoir diminishes and gets progressively exhausted. In particular, for the closed-box model ($\gamma \simeq 1$), one has $M_{\rm cold} \propto \exp -s\tau/\tau_{\rm cond}$ and $Z_{\rm cold} \propto y_Z \tau/\tau_{\rm cond}$. The evolution of the gas mass and metallicity is illustrated in Fig. 2.1.

Constant inflow models and the gas-regulator (or bath-tube) solution

Another class of more realistic analytic models can be obtained when the inflow of gas is assumed to occur at a constant rate $\dot{M}_{\rm inf}$. The relevant evolution equations reads:

$$\begin{cases} \dot{M}_{\rm cold} = \dot{M}_{\rm inf} - \gamma\, \dot{M}_\star \\ \\ \dot{Z}_{\rm cold} = -\frac{\dot{M}_{\rm inf}}{M}_{\rm cold} Z_{\rm cold} + y_Z\,(1-\mathcal{R})\,\frac{\dot{M}_\star}{M_{\rm cold}}\ , \end{cases} \tag{2.28}$$

with initial conditions $M_{\rm cold}(0) = Z_{\rm cold}(0) = 0$. To solve the system a prescription linking the SFR to the gas mass is needed. In the way of comparing with the result I adopt $\dot{M}_\star = M_{\rm cold}/\tau_\star = s M_{\rm cold}/\tau_{\rm cond}$ as in Eqs. (2.1).

The remarkable aspect of the constant inflow model is that it admits self consistent steady state solutions for both the cold gas mass and the cold gas metallicity. In steady state, the SFR adjusts such that the mass loss due to feedback and the mass addition due to inflow exactly compensate and, at the same time, the metal dilution due to inflow and the metal production due to star formation also balance. Posing $\dot{M}_{\rm cold} = \dot{Z}_{\rm cold} = 0$ in the equations above one finds:

$$\begin{cases} \bar{M}_{\rm cold} \simeq \frac{\dot{M}_{\rm inf}\,\tau_{\rm cond}}{s\gamma} \\ \\ \bar{Z}_{\rm cold} \simeq \frac{y_Z\,(1-\mathcal{R})}{\gamma}. \end{cases} \tag{2.29}$$

This steady-state solution is known as gas-regulator or bath-tube model. In the context of galaxy formation, the inflow rate $\dot{M}_{\rm inf}$ is assumed to originate via continuous accretion of gas from the environment outside the host DM halo. This is reasonable for galaxies which have long star formation timescales, like local spirals, while clearly it cannot be retained for high-z star-forming galaxies and specifically for ETG progenitors.

The steady state solution is an attractor, i.e., in the long run the system converges to it. The overall evolution, derived by solving the Eqs. (2.28), is given by:

$$\begin{cases} M_{\rm cold}(x) = \frac{f_{\rm inf}\, M_b}{s\gamma}\,(1 - e^{-s\gamma\, x}) \\ \\ Z_{\rm cold}(x) = \frac{y_Z\,(1-\mathcal{R})}{\gamma}\left(1 - \frac{s\gamma\, x}{e^{s\gamma\, x}-1}\right)\ , \end{cases} \tag{2.30}$$

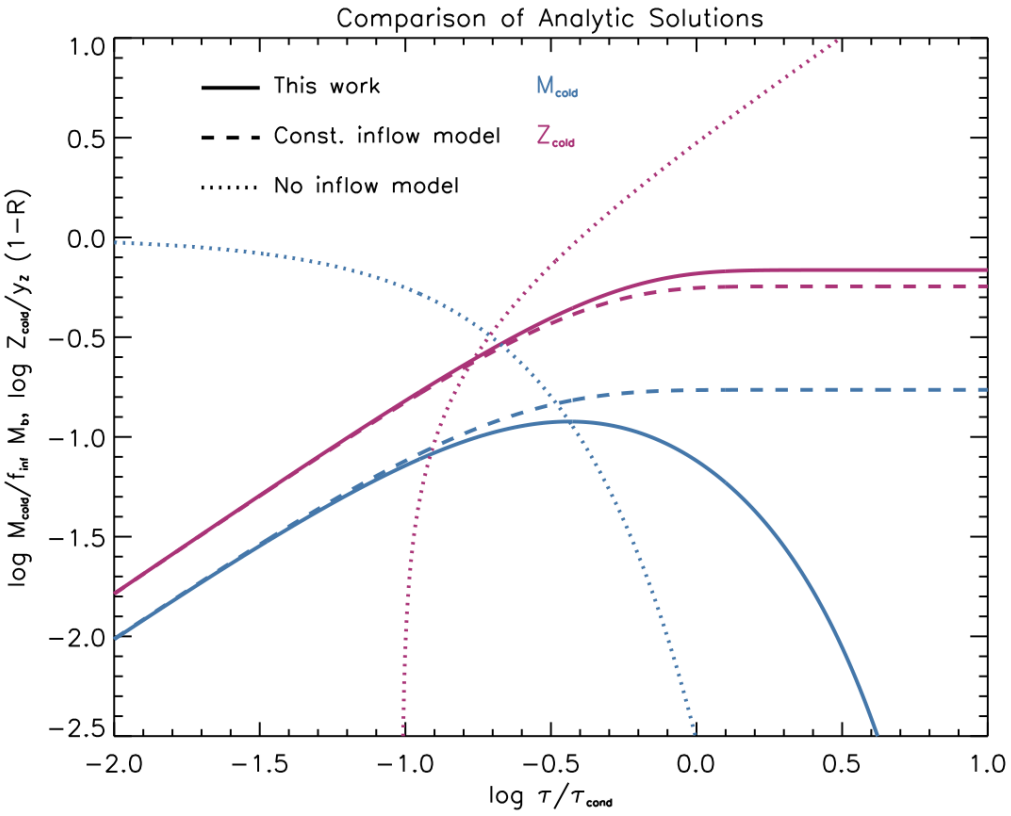

FIGURE 2.1: Comparison of the analytic solutions (solid lines) with the classical no inflow/closed/leaky-box models (dotted lines) and constant inflow/gas regulator models (dashed lines). Blue lines illustrate the time evolution of the cold gas mass $M_{\rm cold}/f_{\rm inf}M_b$, and red lines that of the cold gas metallicity $Z_{\rm cold}/y_Z(1-\mathcal{R})$. For a sensible comparison, I have adopted values of the relevant parameters $s \sim 3$ and $\gamma \sim 2$ apt for a galaxy hosted in a halo with mass $M_{\rm H} \sim 10^{12}\,M_\odot$ formed at $z_{\rm form} \sim 3$.

where $x \equiv \tau/\tau_{\rm cond}$, and for easing the comparison with the solutions in Eqs. (2.4) and (2.13) I have prescribed $\dot{M}_{\rm inf} = f_{\rm inf}\, M_b/\tau_{\rm cond}$. The evolution of the gas mass and metallicity is illustrated in Fig. 2.1.

2.1.4 Metals locked in stars

The metallicity $Z_\star$ in the stellar component is computed by averaging the cold gas metallicity over the star formation history:

$$Z_\star(\tau) = \frac{1}{M_\star(\tau)} \int_0^\tau {\rm d}\tau'\, Z_{\rm cold}(\tau')\, \dot{M}_\star(\tau')\,, \tag{2.31}$$

so that $Z_\star$ represents the amount of metal stocked into the stellar component. Using the self-consistent expression of the cold gas metallicity for instantaneously produced elements, one obtains:

$$Z_\star(\tau) = \bar{Z}_\star \left[1 - \frac{s\,\gamma}{s\,\gamma - 1}\, \frac{e^{-x} - e^{-s\,\gamma\,x}\,[1 + (s\,\gamma - 1)\,x]}{s\gamma - 1 + e^{-s\,\gamma\,x} - s\gamma\, e^{-x}}\right]\,, \tag{2.32}$$

where the asymptotic behavior for $\tau \gg \tau_{\rm cond}$ writes:

$$\bar{Z}_\star = \frac{y_Z\,(1-\mathcal{R})}{\gamma} = \frac{s\gamma - 1}{s\gamma}\,\bar{Z}_{\rm cold}\,; \tag{2.33}$$

it is seen that the analytic solutions, differently from other models in the literature, predict that the stellar metallicity is not equal, but rather somewhat lower, than the cold gas one. The early-time behavior of $Z_\star$ for $\tau \ll \tau_{\rm cond}$ reads:

$$Z_\star(\tau) \simeq \frac{s\,y_Z\,(1-\mathcal{R})}{3}\,\frac{\tau}{\tau_{\rm cond}}\,, \tag{2.34}$$

so that initially $Z_\star(\tau) \simeq 2\,Z_{\rm cold}(\tau)/3$, i.e., the stellar and cold gas metallicity evolve in parallel.

An analogous computation can be performed for the delayed cold gas metallicity (see Section 2.1.2) by inserting $Z^\Delta_{\rm cold}$ from Eq. (2.19) in Eq. (2.31), to yield:

$$Z^\Delta_\star(\tau) = \begin{cases} \bar{Z}^\Delta_\star \left[1 - \dfrac{s\,\gamma}{s\,\gamma - 1} \times \right. & \\ \quad \times \dfrac{e^{-(x-x_\Delta)} - e^{-s\,\gamma\,(x-x_\Delta)}\,[1 + (s\,\gamma - 1)\,(x - x_\Delta)]}{s\gamma - 1 + e^{-s\,\gamma\,x} - s\gamma\, e^{-x}} + & \\ \quad \left. - \dfrac{e^{-s\gamma\,x} - e^{-s\,\gamma\,(x-x_\Delta)} - s\gamma\,[e^{-x} - e^{-(x-x_\Delta)}]}{s\gamma - 1 + e^{-s\,\gamma\,x} - s\gamma\, e^{-x}}\right] & \quad \text{for} \quad x \geq x_\Delta, \\ 0 & \quad \text{for} \quad x < x_\Delta, \end{cases}$$

where the value for $\tau \gg \tau_{\rm cond}$ reads:

$$\bar{Z}_\star^\Delta = \frac{y_Z^\Delta\,(1-\mathcal{R})}{\gamma}\,. \tag{2.35}$$

It is interesting to note that, if star formation proceeded for long times, the ratio of the stellar metallicity for instantaneously and delayed elements would amount to $\bar{Z}_\star^{\Delta=0}/\bar{Z}_\star^\Delta \approx y_Z/y_Z^\Delta$, i.e., the ratio of the respective yields. On the contrary, if star formation is quenched after some time (as it is the case for massive galaxies because of BH feedback, see Sect. 2.2.2) then the different evolution of $Z_\star^{\Delta=0}$ in Eq. (2.32) and of $Z_\star^\Delta$ in Eq. (2.35) would imply an under-abundance of delayed with respect to instantaneously produced elements; this will be at the origin of the α-enhancement (see Sect. 2.1.4).

I note that, as it should be, for $\Delta = 0$ the time dependence in Eq. (2.35) converges to that of the stellar metallicity for instantaneously produced elements in Eq. (2.32). The behavior of $Z_\star^\Delta$ for $\tau \simeq \Delta$ reads:

$$Z_\star^\Delta(\tau) \simeq \frac{s\,y_Z^\Delta\,(1-\mathcal{R})}{6}\,\frac{s\gamma\,(s\gamma-1)}{s\gamma-1+e^{-s\gamma\,x_\Delta}-s\gamma\,e^{-x_\Delta}}\left(\frac{\tau-\Delta}{\tau_{\rm cond}}\right)^3\,. \tag{2.36}$$

In case of a non-trivial SNe I*a* DTD $\mathrm{d}p/\mathrm{d}\Delta$, the overall solution for the stellar metallicity may be derived from:

$$Z_\star^{\rm DTD}(\tau) = \int \mathrm{d}\Delta\,\frac{\mathrm{d}p}{\mathrm{d}\Delta}\,Z_\star^\Delta(\tau) = \frac{1}{M_\star(\tau)}\int_0^\tau \mathrm{d}\tau'\,Z_{\rm cold}^{\rm DTD}(\tau')\,\dot{M}_\star(\tau')\,. \tag{2.37}$$

The expression for an exponential DTD is still analytic but rather cumbersome, so I do not report it here.

2.1.5 Interstellar dust

In this Section I describe in simple analytic terms the global evolution of the dust mass and dust-to-gas mass ratio. As in many previous analytic approaches, the dust is assumed to consist of two interlinked components, namely, a refractory *core* and a volatile *mantle*, subject to the evolution equations:

$$\begin{cases} \dfrac{\mathrm{d}}{\mathrm{d}\tau}(M_{\rm cold}\,D_{\rm core}) = -\,\gamma\,\dot{M}_\star\,D_{\rm core} - \kappa_{\rm SN}\,\dot{M}_\star\,D_{\rm core} + y_D\,(1-\mathcal{R})\,\dot{M}_\star\,, \\ \dfrac{\mathrm{d}}{\mathrm{d}\tau}(M_{\rm cold}\,D_{\rm mantle}) = -\,\gamma\,\dot{M}_\star\,D_{\rm mantle} - \kappa_{\rm SN}\,\dot{M}_\star\,D_{\rm mantle} + \\ \qquad\qquad + \epsilon_{\rm acc}\,\dot{M}_\star\,D_{\rm core}\,(Z - D_{\rm mantle})\,. \end{cases} \tag{2.38}$$

The first equation prescribes that the evolution of the mass in grain cores $M_{\rm cold}\,D_{\rm core}$ results from the competition of various processes:

- the production due to stellar evolution at a rate $y_D\,(1-\mathcal{R})\,\dot{M}_\star$ with an average yield y_D;
- astration by star-formation and ejection from galactic outflows, that combine in the rate term $-\gamma\,\dot{M}_\star\,D_{\rm core}$;
- dust sputtering, spallation and destruction via SN shock-waves at a rate $\kappa_{\rm SN}\,\dot{M}_\star\,D_{\rm core}$ with a strength parameter $\kappa_{\rm SN}$.

The second equation in 2.38 describes the evolution of the mass in dust mantles, which differs from the previous one for the production term: mantle growth is assumed to be driven by accretion of metals onto pre-existing grain cores at a rate $\epsilon_{\rm acc}\,\dot{M}_\star\,D_{\rm core}\,(Z - D_{\rm mantle})$ with an efficiency $\epsilon_{\rm acc}$.

Using the self-consistent expression for the cold gas mass, Eqs. (2.38) can be recast in terms of the dust mass fractions:

$$\begin{cases} \dot{D}_{\rm core} = -\,\dfrac{D_{\rm core}}{\tau_{\rm cond}}\left[s\,\kappa_{\rm SN} + \dfrac{s\,\gamma - 1}{1 - e^{-(s\,\gamma-1)\,x}}\right] + \dfrac{y_D\,(1-\mathcal{R})\,s}{\tau_{\rm cond}}\;; \\ \\ \dot{D}_{\rm mantle} = -\,\dfrac{D_{\rm mantle}}{\tau_{\rm cond}}\left[s\,\kappa_{\rm SN} + s\,\epsilon_{\rm acc}\,D_{\rm core} + \dfrac{s\,\gamma - 1}{1 - e^{-(s\,\gamma-1)\,x}}\right] + \\ \qquad\qquad + \dfrac{s\,\epsilon_{\rm acc}\,D_{\rm core}}{\tau_{\rm cond}}\,Z_{\rm cold}\;. \end{cases} \tag{2.39}$$

with initial conditions $D_{\rm core}(0) = D_{\rm mantle}(0) = 0$. The corresponding analytic solution for grain cores is

$$D_{\rm core}(\tau) = \bar{D}_{\rm core}\left[1 - \frac{s\,\gamma - 1}{e^{(s\,\gamma-1)\,x} - 1}\,\frac{1 - e^{-s\,\kappa_{\rm SN}\,x}}{s\,\kappa_{\rm SN}}\right]\,, \tag{2.40}$$

where the asymptotic value for $\tau \gg \tau_{\rm cond}$ reads

$$\bar{D}_{\rm core} = \frac{s\,y_D\,(1-\mathcal{R})}{s\,(\gamma + \kappa_{\rm SN}) - 1}\;. \tag{2.41}$$

In solving the equation for the mantle, I assume the core fraction $D_{\rm core}(\tau)$ to be fixed at its asymptotic value $\bar{D}_{\rm core} \ll \bar{Z}_{\rm cold}$, since from Eq. (2.40) this is seen to be attained very rapidly after a time $\tau \gtrsim \tau_{\rm cond}/s\,\kappa_{\rm SN}$; for typical values of the parameters (see also Sect. 2.2.3 this amounts to a few $10^{-2}\,\tau_{\rm cond}$. I then obtain:

$$D_{\rm mantle}(\tau) = \bar{D}_{\rm mantle}\left\{1 - \frac{(s\,\gamma-1)\,x}{e^{(s\,\gamma-1)\,x} - 1}\left[1 + \frac{s\,\gamma - 1}{s\,\tilde{\epsilon}}\left(1 - \frac{1 - e^{-s\,\tilde{\epsilon}\,x}}{s\,\tilde{\epsilon}\,x}\right)\right]\right\}\,, \tag{2.42}$$

where $\tilde{\epsilon} \equiv \kappa_{\rm SN} + \epsilon_{\rm acc}\,\bar{D}_{\rm core}$ and the asymptotic value for $\tau \gg \tau_{\rm cond}$ reads

$$\bar{D}_{\rm mantle} = \frac{s\,\epsilon_{\rm acc}\,\bar{D}_{\rm core}\,\bar{Z}_{\rm cold}}{s\,(\gamma + \kappa_{\rm SN} + \epsilon_{\rm acc}\,\bar{D}_{\rm core}) - 1}\;; \tag{2.43}$$

thus if the accretion process is very efficient, Eq. (2.43) implies that the final dust fraction tends to the gas metallicity.

The early-time behavior for $\tau \ll \tau_{\rm cond}$ writes:

$$\begin{cases} D_{\rm core}(\tau) \simeq \dfrac{s\,y_D\,(1-\mathcal{R})}{2}\,\dfrac{\tau}{\tau_{\rm cond}}\,, \\ \\ D_{\rm mantle}(\tau) \simeq \dfrac{s^3}{6}\,\dfrac{\epsilon_{\rm acc}\,y_D\,y_Z\,(1-\mathcal{R})^2}{s\,(\gamma + \kappa_{\rm SN}) - 1}\left(\dfrac{\tau}{\tau_{\rm cond}}\right)^2\,, \end{cases} \tag{2.44}$$

so that the mantle component overwhelms the core one soon after dust production has started. I note that the second equation above is strictly valid for times

$\tau_{\rm cond}/s\kappa_{\rm SN} \lesssim \tau \lesssim \tau_{\rm cond}$ when $D_{\rm core}$ has already saturated to its asymptotic value $\bar{D}_{\rm core}$.

It is worth stressing that total dust production and enrichment (core plus mantle) are in general very rapid with respect to the condensation timescale, of order a few $10^{-1}\,\tau_{\rm cond}$. This is extremely relevant for very high redshift star-forming galaxies and quasar hosts (see Sect. 2.3.4).

2.1.6 outflowing mass and metals

The effect of galactic outflows driven by SN explosions and stellar winds is to heat and remove the cold gas at a rate $\epsilon_{\rm out}\,\dot{M}_\star$ proportional to the star formation rate. A sort of impulsive energy/momentum feedback can be also included, which may be driven by the emission from the central SMBH, that is thought to quench star formation in the star-forming progenitors of elliptical galaxies.

To a crude approximation, the action of such impulsive feedback can be described as heating/ejection of all the residual mass in cold gas $M_{\rm cold}(\tau_{\rm burst})$ at a galactic age $\tau_{\rm burst}$. Then, the overall outflowing gas mass at $\tau_{\rm burst}$ reads:

$$M_{\rm out} = \epsilon_{\rm out}\,M_\star(\tau_{\rm burst}) + M_{\rm cold}(\tau_{\rm burst})\,. \tag{2.45}$$

In addition, the metallicity of the mass outflow by SNe and stellar winds is $\epsilon_{\rm out}\,Z_\star$, while the one associated to impulsive feedback is $Z_{\rm cold}(\tau_{\rm burst})$. Thus, the average metallicity of the outflowing gas at $\tau_{\rm burst}$ writes:

$$Z_{\rm out} = \frac{\epsilon_{\rm out}\,Z_\star(\tau_{\rm burst})\,M_\star(\tau_{\rm burst}) + Z_{\rm cold}(\tau_{\rm burst})\,M_{\rm cold}(\tau_{\rm burst})}{\epsilon_{\rm out}\,M_\star(\tau_{\rm burst}) + M_{\rm cold}(\tau_{\rm burst})}\,. \tag{2.46}$$

It is found to strike an intermediate course between the cold gas and the stellar metallicity. This is relevant in particular for the enrichment of the warm and hot medium pervading/surrounding massive ETGs, as it will be stressed in Sect. 2.3.7.

2.2 Application to ETGs and their star-forming progenitors

In this Section I apply the analytic solutions to the case of local ETGs and their high-z star-forming progenitors.

To this purpose, in Sects. 2.2.1-2.2.3 I will set the parameters entering the analytic solutions via physical arguments inspired by *in-situ* galaxy-BH co-evolution scenarios for ETG formation (e.g., Granato et al., 2004; Lapi et al., 2006; Lapi et al., 2014; Lapi et al., 2018), with particular focus on the role of gas cooling and condensation, and feedback processes.

Then, in Sect. 2.2.4 I will discuss the mass additions by mergers in the DM and stellar components, and in Sect. 2.2.5 I will describe how to deal with different formation redshifts in order to obtain the spatially-averaged quantities that can be compared with observations.

Finally, in Sects. 2.2.6 and 2.3.1-2.3.7 I will present and discuss the time evolution of baryons in an individual star-forming high-z progenitor and the resulting statistical relations, once the analytic solutions are applied to ETGs and their star-forming progenitors, and I will compare them with recent data.

2.2.1 Infall fraction and star formation timescales

To start with, I set the infall fraction $f_{\rm inf}$, the condensation timescale $\tau_{\rm cond}$ and the ratio $s = \tau_{\rm cond}/\tau_\star$ between the star formation and the condensation timescale, entering the analytic solutions presented in Sect. 2.1. To this aim, I refer to the *in-situ* galaxy-BH co-evolution scenario by Lapi et al. (2018). In the following I recall the basic notions that are relevant for the present context.

The *in-situ* scenario envisages that only a fraction $f_{\rm inf} = M_{\rm inf}/f_b\,M_{\rm H}$ of the available baryons $f_b\,M_{\rm H}$ in a DM halo of mass $M_{\rm H}$, initially located within a radius $R_{\rm inf}$, is able to cool and fall in toward the central region of the galaxy, where strong star formation takes place. The radius $R_{\rm inf}$ and the infall fraction can be estimated along the following lines.

Given a DM halo of mass $M_{\rm H}$ formed at redshift $z_{\rm form}$, its virial radius and virial circular velocity are approximately given by $R_{\rm H} \approx 110\,M_{\rm H,12}^{1/3}\,[E_{z_{\rm form}}/E_{z_{\rm form}=2}]^{-1/3}$ kpc and $v_{c,{\rm H}} \approx 200\,M_{\rm H,12}\,[E_{z_{\rm form}}/E_{z_{\rm form}=2}]^{1/6}$ km s^{-1} in terms of the redshift dependent factor $E_{z_{\rm form}} = \Omega_\Lambda + \Omega_M\,(1+z_{\rm form})^3$ and the normalized DM halo mass $M_{\rm H,12} = M_{\rm H}/10^{12}\,M_\odot$. Adopting a standard NFW (Navarro, Frenk, and White, 1997) profile for the DM component yields an approximate scaling $M_{\rm H}(<r) \propto r$ (see Lapi et al., 2018, their Sect. 3.1), so that $R_{\rm inf} \simeq f_{\rm inf}\,R_{\rm H}$ and $M_{\rm H}(<R_{\rm inf}) \simeq f_{\rm inf}\,M_{\rm H}(<R_{\rm H})$. Therefore, the dynamical time at $R_{\rm inf}$ is given by:

$$t_{\rm dyn}(R_{\rm inf}) \simeq \frac{\pi}{2}\sqrt{\frac{R_{\rm inf}^3}{G\,M_{\rm H}(<R_{\rm inf})}} \approx 6\times10^8\,f_{\rm inf}\,[E_{z_{\rm form}}/E_{z_{\rm form}=2}]^{-1/2}\,{\rm yr}\,. \tag{2.47}$$

On the other hand, the cooling time at $R_{\rm inf}$ reads:

$$t_{\rm cool}(R_{\rm inf}) \simeq \frac{3\,k_{\rm B}T}{2\,\mu\,C\,n(R_{\rm inf})\,\Lambda(T,Z)}\,, \tag{2.48}$$

where T is the temperature, $\mu \approx 0.6$ is the mean molecular weight, $n(R_{\rm inf})$ is the gas density, C is the clumping factor and $\Lambda(T,Z)$ is the cooling function in cgs units dependent on temperature and metallicity (see Sutherland and Dopita, 1993). The infalling gas is expected to have temperatures close to the virial $T \simeq 0.5\,\mu\,m_p\,v_{c,{\rm H}}^2 \approx 1.5\times10^6\,M_{\rm H,12}^{2/3}\,[E_{z_{\rm form}}/E_{z_{\rm form}=2}]^{1/3}$ K; correspondingly, $\Lambda(T,Z) \gtrsim 2\times10^{-23}$ erg cm^3 s^{-1} for $Z \gtrsim Z_\odot/10$ (recall from Sect. 2.1.2 that this value is attained quite rapidly within $\lesssim 10^{-1}\,\tau_{\rm cond} \sim$ a few 10^7 yr). The gas density is expected to be on the order of the average baryon density within $R_{\rm inf}$, which reads $n(R_{\rm inf}) \approx 4\times10^{-4}\,f_{\rm inf}^{-2}\,[E_{z_{\rm form}}/E_{z_{\rm form}=2}]$ cm^{-3} having assumed $n(r)$ to follow an isothermal distribution; the clumping factor is expected to be close to that in the IGM, which cosmological simulations (see Iliev et al., 2007; Pawlik, Schaye, and van Scherpenzeel, 2009; Finlator et al., 2012; Shull et al., 2012) indicate around $C \sim 6-20$ at $z \simeq 2$, so that I take $C \approx 10$.

When $t_{\rm dyn} \lesssim t_{\rm cool}$ the gas cools efficiently while infalling toward the central regions on the dynamical timescale. Therefore, $f_{\rm inf}$ can be set by requiring that the above timescales $t_{\rm dyn}(R_{\rm inf}) \propto f_{\rm inf}$ and $t_{\rm cool} \propto f_{\rm inf}^2$ match. Then, I prescribe that the fraction $f_{\rm inf}$ of the baryons located within $R_{\rm inf}$ can cool and condense toward the central regions over a timescale $\tau_{\rm cond} \approx t_{\rm dyn}(R_{\rm inf})$.

In Fig. 2.2 I plot $f_{\rm inf}$ and $\tau_{\rm cond}$ as a function of the halo mass and formation redshift. The parameter $f_{\rm inf}$ is essentially unity for halo masses $M_{\rm H} \lesssim$ a few $10^{12}\,M_\odot$, while for larger masses it drops to low values because cooling becomes progressively inefficient and prevents condensation toward the central regions; the dependence on formation redshift is negligible. As to $\tau_{\rm cond}$, it scales with halo mass similarly to $f_{\rm inf}$, while the

constant value for $M_{\rm H} \lesssim$ a few $10^{12}\,M_\odot$ depends on formation redshift approximately as $(1+z_{\rm form})^{-3/2}$, reflecting the increased density of the ambient medium at earlier cosmic epochs.

To proceed further, I note that such infalling gas rotates, being endowed with the specific angular momentum:

$$j_{\rm inf} \equiv f_{\rm inf}\, j_{\rm H} \approx 1100\, f_{\rm inf}\, \lambda_{0.035}\, M_{\rm H,12}^{2/3}\, [E_{z_{\rm form}}/E_{z_{\rm form}=2}]^{-1/6}\ {\rm km\ s^{-1}\ kpc}\ ; \tag{2.49}$$

here $j_{\rm H} \equiv \sqrt{2}\,\lambda\, R_{\rm H}\, v_{c,{\rm H}}$ is the halo specific angular momentum and $\lambda_{0.035} \equiv \lambda/0.035$ is the halo spin parameter. Numerical simulations (see Barnes and Efstathiou, 1987; Bullock et al., 2001; Macciò et al., 2007; Zjupa and Springel, 2017) have shown that λ exhibits a log-normal distribution with average value $\langle\lambda\rangle \approx 0.035$ and dispersion $\sigma_{\log\lambda} \approx 0.25$ dex, nearly independent of mass and redshift. In deriving the above equation the specific angular momentum of the baryonic gas has been assumed to initially follow the radial profile of the DM's $j_{\rm H}(<r) \propto M_{\rm H}^{\alpha}(<r)$ with $\alpha \approx 1$, which in turn is found from simulations to closely follow the mass profile (e.g., Bullock et al., 2001; Shi et al., 2017)

Given that $j_{\rm inf}$ is approximately conserved, the inflow of the gas from $R_{\rm inf}$ toward the central region can proceed until the radius $R_{\rm rot}$ where the rotational support balance the gravitational pull, i.e., $G\,M_{\rm tot}(<R_{\rm rot})/R_{\rm rot}^2 = j_{\rm inf}^2/R_{\rm rot}^3$. Such a condition yields:

$$R_{\rm rot} \simeq \frac{j_{\rm inf}^2}{G\,M_{\rm inf}} \approx 1.5\,\lambda_{0.035}^2\, f_{\rm inf}\, [E_{z_{\rm form}}/E_{z_{\rm form}=2}]^{-1/3}\ {\rm kpc}\ , \tag{2.50}$$

and the corresponding dynamical time amounts to:

$$t_{\rm dyn}(R_{\rm rot}) \simeq \frac{\pi}{2}\sqrt{\frac{R_{\rm rot}^3}{G\,M_{\rm inf}}} \approx 4\times10^6\,\lambda_{0.035}^3\, f_{\rm inf}\, [E_{z_{\rm form}}/E_{z_{\rm form}=2}]^{-1/2}\ {\rm yr}\ . \tag{2.51}$$

Recent observations of high-z star-forming galaxies have revealed that most of the star formation occurs within a compact region a few kiloparsecs under heavy dust-enshrouded conditions (e.g., Scoville et al., 2014; Ikarashi et al., 2015; Simpson et al., 2015; Straatman et al., 2015; Spilker et al., 2015; Tadaki et al., 2017a; Tadaki et al., 2017b). In particular, the size $R_{\rm rot}$ derived above has been shown by Lapi et al. (2018) to be consistent with those measured via FIR/sub-millimeter and CO line observations of $z \sim 1-2$ star-forming galaxies (e.g., Barro et al., 2016b; Barro et al., 2017; Hodge et al., 2016; Tadaki et al., 2017a; Talia et al., 2018; Lang et al., 2019).

Further infall of the gas within $R_{\rm rot}$ can only occur by spreading out specific angular momentum via dynamical friction and gravitational torques, as indicated by specific simulations and suggested by dynamical measurements in high-z star-forming galaxies (see e.g., Dekel et al., 2009; Genzel et al., 2011; Zolotov et al., 2015).

The cold baryonic gas mass $M_{\rm cold}(R_{\rm rot}) \lesssim f_{\rm inf}\, f_b\, M_{\rm H} \sim 10^{10}-10^{11}\,M_\odot$, namely a fraction $f_{\rm inf}$ of the baryons already present in the halo at formation, will be driven by such processes within $R_{\rm rot} \sim$ kpc and will form star on a timescale $t_{\rm SFR}(R_{\rm rot}) \approx 50\times t_{\rm dyn}(R_{\rm rot}) \approx (1-2)\times10^8$ yr (see Elmegreen, Elmegreen, and Ferguson, 2005; Krumholz, Dekel, and McKee, 2012, and references therein), implying SFRs $\dot{M}_\star \lesssim M_{\rm cold}(R_{\rm rot})/t_{\rm SFR} \lesssim 10^2-10^3\,M_\odot\ {\rm yr}^{-1}$ and hence rapid metals enrichment and dust formation. These conditions have been indeed observed in ETG progenitors, in particular via high-resolution interferometric observations with ALMA (see Scoville et al., 2016; Barro et al., 2017; Tadaki et al., 2017a; Tadaki et al., 2017b; Talia et al., 2018;

Lang et al., 2019). I note that in such systems cooling and the ensuing star formation from baryons accreted during later halo growth over cosmological timescales will be hampered by the effects of stellar and AGN feedbacks. This is at variance with respect to present-day disc-dominated galaxies, where the cold gas accretion is not inhibited by strong AGN feedbacks and the star formation process is prolonged over several Gyrs (further details can be found in Appendix B).

On the basis of the above discussion, I set the parameter $s \equiv \tau_{\rm cond}/\tau_\star$ entering the analytic solutions as $s = t_{\rm dyn}(R_{\rm inf})/t_{\rm SFR}(R_{\rm rot})$. In Fig. 2.2 it is shown to take on values around 3 – 3.5, weakly dependent on halo mass and formation redshift.

2.2.2 Feedback parameters

Another important parameter entering the analytic solutions is the mass loading factor $\epsilon_{\rm out}$ of slow outflows related to SNe II and stellar winds. The standard expression used in many literature studies since the pioneering work of White and Frenk (1991)(but see also Mo, van den Bosch, and White, 2010; Somerville and Davé, 2015) is:

$$\epsilon_{\rm out} = \frac{\epsilon_{\rm SN}\,\eta_{\rm SN}\,E_{\rm SN}}{E_{\rm bind}} \approx \epsilon_{SN,0.05}\,\eta_{\rm SN,-2}\,E_{\rm SN,51}\,M_{\rm H,12}^{-2/3}\,[E_{z_{\rm form}}/E_{z_{\rm form}=2}]^{-1/3}\,. \tag{2.52}$$

The mass loading factor $\epsilon_{\rm out}$ is expressed in terms of the occurrence of SNe per unit solar mass formed into stars $\eta_{\rm SN,-2} = \eta_{\rm SN}/0.01\,M_\odot$ (apt for the fiducial Chabrier IMF), of the average energy per single SN II explosion $E_{\rm SN,51} = E_{\rm SN}/10^{51}$ erg, of the energy fraction effectively coupled to the interstellar medium and available to drive the outflow $\epsilon_{\rm SN,0.05} = \epsilon_{\rm SN}/0.05$ (that is comparable to the overall coupled energy when cooperative SN blast-wave propagation takes place, like in violent starbursts; e.g., Mac Low and Ferrara, 1999; Mo, van den Bosch, and White, 2010), and of the gas specific binding energy $E_{\rm bind} \approx 2.5\times10^{14}\,M_{\rm H,12}^{2/3}\,[E_{z_{\rm form}}/E_{z_{\rm form}=2}]^{1/3}$ cm^2 s^{-2} in the halo potential well (see Zhao et al., 2003; Mo and Mao, 2004).

The outcome is illustrated in Fig. 2.2 as a function of halo mass and formation redshift. It takes on values in the range $\epsilon_{\rm out} \sim 0.1 - 10$ for halo masses $M_{\rm H} \sim 10^{13.5} - 10^{11}\,M_\odot$, with a weak dependence on formation redshift. Such a behavior is indeed in agreement with self-consistent hydrodynamical simulations of stellar feedback (e.g., Hopkins, Quataert, and Murray, 2012).

The above Eq. (2.52) is meant to describe an energy-driven, slow outflow that can offset gas infall from large scales out to $R_{\rm inf} \gg R_{\rm rot}$, where the binding energy is dominated by the DM halo. An alternative prescription for stellar feedback invokes momentum-driven outflows (e.g., Murray, Quataert, and Thompson, 2005; Oppenheimer and Davé, 2006), that in the context of this work can indeed operate to blow some of the cold gas out of $R_{\rm rot}$, where the binding energy is largely dominated by baryons. In such a case the relevant mass loading factor reads:

$$\epsilon_{\rm out} = \eta_{\rm SN}\,E_{\rm SN}/v_{\rm SN}\,v_{\rm rot} \approx v_{\rm SN,3}\,\eta_{\rm SN,-2}\,E_{\rm SN,51}\,\lambda_{0.035}\,M_{\rm H,12}^{-2/3}\,[E_{z_{\rm form}}/E_{z_{\rm form}=2}]^{-1/6}\,, \tag{2.53}$$

that is in terms of the typical velocity of SN ejecta $v_{\rm SN,3} \equiv v_{\rm SN}/10^3$ km s^{-1} and of the escape velocity $v_{\rm rot} \approx j_{\rm inf}/R_{\rm rot}$ at $R_{\rm rot}$.

The resulting $\epsilon_{\rm out}$ for the energy-driven and momentum-driven outflows are comparable within the uncertainties of the parameters entering the respective expressions (cf. Fig. 2.2), and produce similar evolution in the gas/stellar mass and metallicity when used in the analytic solutions presented here.

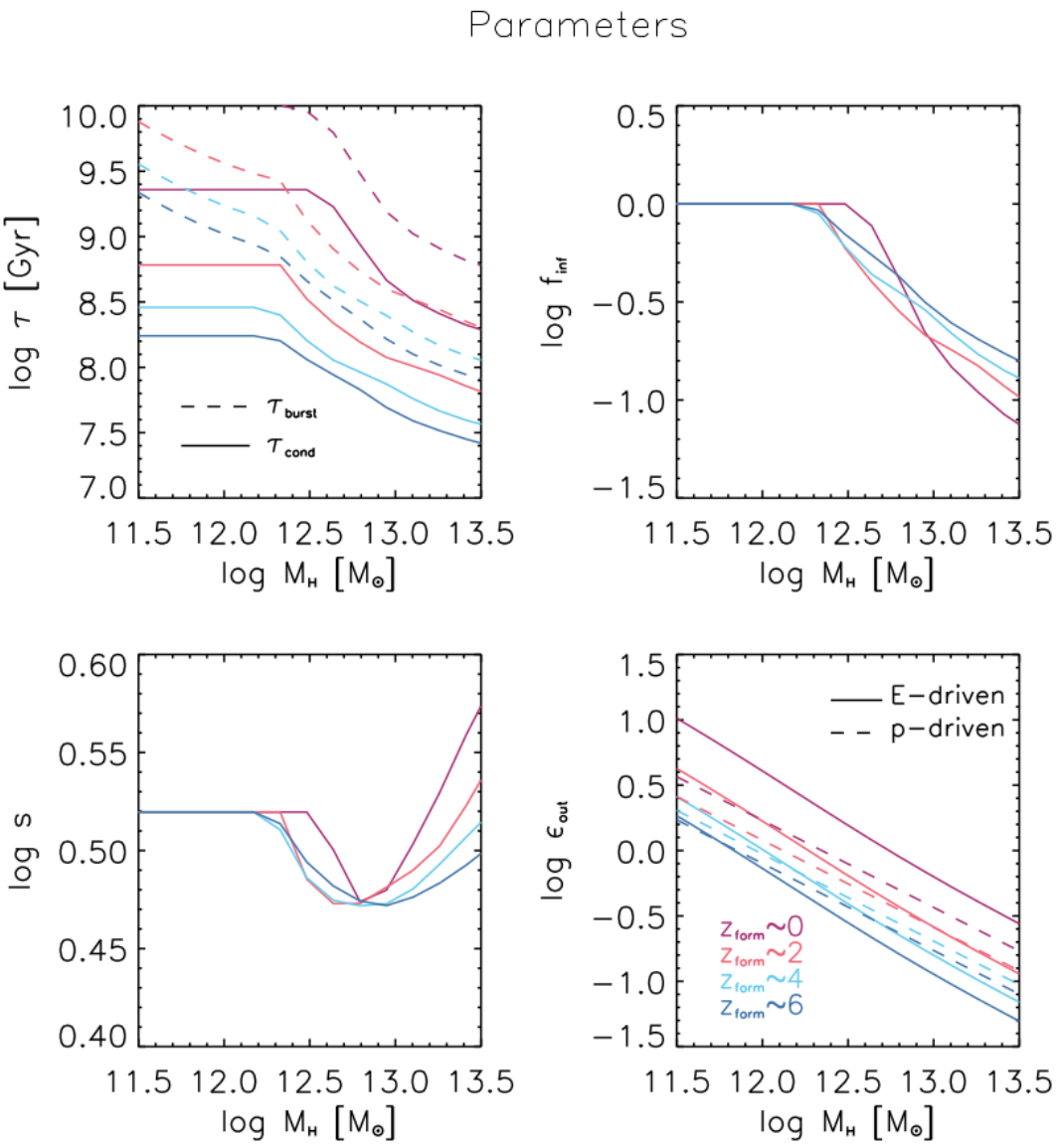

FIGURE 2.2: Main parameters entering the analytic solutions relevant for ETG progenitors, as a function of host halo mass M_H and formation redshift $z_{\rm form}$. Top left panel: condensation timescale $\tau_{\rm cond}$ (solid lines) and duration of the star-forming burst $\tau_{\rm burst} \equiv \tau_\star$ (dashed lines). Top right panel: infall fraction $f_{\rm inf}$. Bottom left panel: ratio $s = \tau_{\rm cond}/\tau_\star$ of the condensation to star-formation timescale. Bottom right panel: mass loading factor of the outflows from stellar feedback $\epsilon_{\rm out}$, for energy-driven (solid lines) and momentum-driven (dashed lines) outflows. In all panels the color-code refer to different formation redshifts $z_{\rm form} = 0$ (purple), 2 (orange), 4 (cyan), and 6 (blue).

Another form of feedback, that is thought to be extremely relevant in the formation of ETGs, is related to the hosted accreting SMBH (see e.g., Silk and Rees, 1998; Fabian, 1999; King, 2003; Granato et al., 2004; Murray, Quataert, and Thompson, 2005; Lapi et al., 2006; Lapi et al., 2014; King, 2014). In this respect, the basic scope of this work is to describe phenomenologically the impact of BH feedback on the host galaxy by abruptly quenching the star formation and ejecting the residual gas mass after a time $\tau_{\rm burst}$.

Constraints on $\tau_{\rm burst}$ comes from SED modelling of dusty ETG star-forming progenitors (see Papovich et al., 2011; Moustakas et al., 2013; Steinhardt et al., 2014; da Cunha et al., 2015; Citro et al., 2016; Cassarà et al., 2016; Boquien et al., 2019), that suggest a duration $\lesssim 0.5-1$ Gyr for massive galaxies with $M_\star \gtrsim$ a few $10^{10}\,M_\odot$. Similar values in massive ETGs are also concurrently indicated by local observations the stellar mass-metallicity relationship and of the α-enhancement, i.e., iron underabundance compared to α-elements (occurring because star formation is stopped before SN I*a* explosions can pollute the interstellar medium with substantial amounts of iron; e.g., Thomas et al., 2005; Gallazzi et al., 2006; Gallazzi et al., 2014; Renzini, 2006, for a review).

On the contrary, in low-mass spheroidal galaxies with $M_\star \lesssim 10^{10}\,M_\odot$ data on the age of the stellar population and chemical abundances indicate that star formation proceeded for longer times, mainly regulated by SN feedback and stellar winds (see the review by Conroy, 2013). A possible example to treat this case analytically is given in Appendix B.

Here, the timescale that gives the duration of the main SFR episode s phenomenologically parameterized via the smooth expression:

$$\tau_{\rm burst} \simeq 3\,\tau_{\rm cond}\,(1+M_{\rm H,12}^{-1})\,, \tag{2.54}$$

holding in the range $M_{\rm H}\sim 10^{11}-10^{13.5}\,M_\odot$. This formula is meant to interpolate between the aforementioned behaviors for less and more massive galaxies; e.g., at $z_{\rm form}\approx 2$ it prescribes short timescales $\tau_{\rm burst}$ ~a few 10^8 yr for galaxies in massive halos with $M_{\rm H}\sim 10^{13}\,M_\odot$, and appreciably longer $\tau_{\rm burst}\sim$ several 10^9 for galaxies in small halos with $M_{\rm H}\sim 10^{11.5}\,M_\odot$. With a similar formula Mancuso et al. (2016b) and Mancuso et al. (2016a) reproduced the main sequence of star-forming galaxies at $z\approx 2$, and Lapi et al. (2017) linked the statistics of star-forming galaxies, AGNs and massive quiescent galaxies via a continuity equation approach. Actually the results are rather insensitive to the specific shape of such a phenomenological parameterization.

Summarizing, infall, condensation and feedback processes set the main parameters entering the analytic solutions. Their behaviour vs. DM halo mass M_H and galaxy formation redshift $z_{\rm form}$ is shown in Fig. 2.2.

2.2.3 Yields and other IMF-related parameters

Other relevant parameters are mainly determined by the adopted Chabrier (2003) and Chabrier (2005) IMF and the Romano et al. (2010) stellar yield models: the resulting instantaneous recycling fraction is $\mathcal{R}\approx 0.45$, the average yield of instantaneously produced metals is $y_Z\approx 0.06$ and the oxygen yield is $y_O\approx 0.04$ (see also Krumholz, Dekel, and McKee, 2012; Feldmann, 2015; Vincenzo et al., 2016). These values are weakly dependent on the chemical composition and somewhat dependent on the stellar yield models (e.g., Romano et al., 2010; Nomoto, Kobayashi, and Tominaga,

2013; Vincenzo et al., 2016); e.g., the metal yield can vary within the range $y_Z \sim 0.05 - 0.07$.

The yield for delayed metals is adopted to be $y_Z^\Delta \approx 2.7 \times 10^{-3}$; this was computed taking into account that the occurrence of SNe I*a* is around $2 \times 10^{-3}/M_\odot$ per stellar mass formed, and that $0.63\,M_\odot$ of iron-group elements are produced on average per explosion (see Bell et al., 2003; Maoz, Mannucci, and Nelemans, 2014). The outcome is also consistent with the normalization of the observed SN I*a* delay time distribution (e.g., Vincenzo, Matteucci, and Spitoni, 2017).

Finally, in the treatment of dust production, the adopted dust yield is $y_D \approx 7{\times}10^{-4}$ (see Bianchi and Schneider, 2007; Zhukovska, Gail, and Trieloff, 2008; Feldmann, 2015), the strength parameter for dust spallation by SN winds is $\kappa_{\rm SN} \approx 10$ (see de Bennassuti et al., 2014), and dust accretion efficiency is $\epsilon_{\rm acc} \approx 10^5$ (see Hirashita, 2000; Asano et al., 2013; Feldmann, 2015). I note that these parameters are rather uncertain, and mainly set basing on previous literature and on obtaining a good match to the dust vs. stellar mass relationship observed in $z \gtrsim 2$ star-forming galaxies.

2.2.4 Halo and stellar mass growth by mergers

After virialization, both the DM halo and the stellar content are expected to grow because of merging events. To describe these processes, I rely on the outcomes of *N-body* and hydro simulations, and in particular on the `Illustris` project (see `http://www.illustris-project.org/`). As to the halo growth, the merger rates per bin of redshift z and of halo mass ratio $\mu_{\rm H}$ can be described with the fitting formula originally proposed by Fakhouri and Ma (2008) and Fakhouri, Ma, and Boylan-Kolchin (2010):

$$\frac{{\rm d}N_{\rm H,merg}}{{\rm d}t\,{\rm d}\mu_{\rm H}} = N_{\rm H}\,M_{\rm H,12}^{a}\,\mu_{\rm H}^{-b-2}\,e^{(\mu_{\rm H}/\tilde{\mu}_{\rm H})^c}\,\frac{{\rm d}\delta_c}{{\rm d}t} \tag{2.55}$$

that is in terms of the descendant halo mass $M_{\rm H,12} = M_{\rm H}/10^{12}\,M_\odot$ and of the linear threshold for collapse $\delta_c(z)$ (Lapi, Salucci, and Danese, 2013, see also).

Genel et al. (2010) determined the parameters entering the above expression from the `Illustris`-Dark simulations, finding $N_{\rm H} = 0.065$, $a = 0.15$, $b = -0.3$, $c = 0.5$ and $\tilde{\mu}_{\rm H} = 0.4$. The average halo mass growth $\langle \dot{M}_{\rm H,merg} \rangle$ is obtained by multiplying the above expression by $\mu_{\rm H}/(1+\mu_{\rm H})$ and integrating over $\mu_{\rm H}$ from a minimum value $\mu_{\rm H,min}$; I use $\mu_{\rm H,min} \approx 10^{-5}$ that corresponds to include all mergers, since the contribution from smaller mass ratios to the halo mass growth is essentially negligible.

As to the stellar mass growth, Rodriguez-Gomez et al. (2016) and Rodriguez-Gomez et al. (2016) inferred from the analysis of the full hydrodynamic `Illustris` simulation the fitting formula:

$$\frac{{\rm d}N_{\star,\rm merg}}{{\rm d}t\,{\rm d}\mu_\star} = N_\star(z_{\rm form})\,M_{\star,10}^{a(z_{\rm form})}\,[1 + (M_\star/\tilde{M}_\star)^{d(z_{\rm form})}]\,\mu_\star^{b(z_{\rm form})+c\,\log M_{\star,10}}\ , \tag{2.56}$$

that is in terms of the descendant stellar mass $M_{\star,10} = M_\star/10^{10}\,M_\odot$, where $\tilde{M}_\star = 2 \times 10^{11}\,M_\odot$, $N_\star(z_{\rm form}) = N_0\,(1+z_{\rm form})^{N_1}$ with $\log N_0[{\rm Gyr}^{-1}] = -2.2287$ and $N_1 = 2.4644$, $a(z_{\rm form}) = a_0\,(1+z_{\rm form})^{a_1}$ with $a_0 = 0.2241$ and $a_1 = -1.1759$, $b(z_{\rm form}) = b_0\,(1+z_{\rm form})^{b_1}$ with $b_0 = -1.2595$ and $b_1 = 0.0611$, $c = -0.0477$, $d(z_{\rm form}) = d_0\,(1+z_{\rm form})^{d_1}$ with $d_0 = 0.7668$ and $d_1 = -0.4695$.

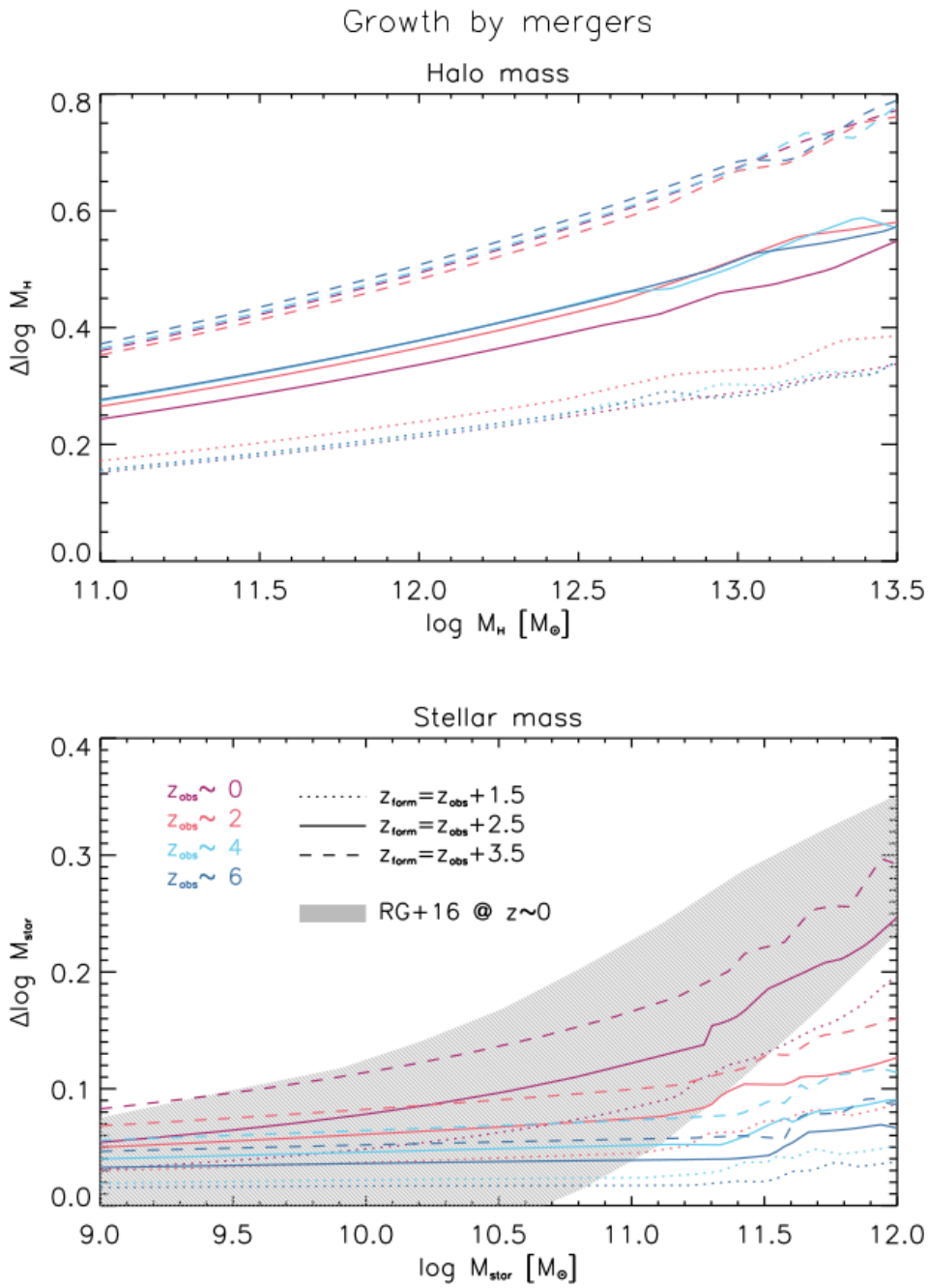

FIGURE 2.3: Growth of the halo mass (top panel) and of the stellar mass (bottom panel) by mergers, as a function of the final halo and stellar masses, respectively. I illustrate the outcomes at observation redshifts $z_{\rm obs} = 0$ (red), 2 (orange), 4 (cyan), and 6 (blue) for different formation redshifts $z_{\rm form} = z_{\rm obs} + 1.5$ (dotted), $z_{\rm form} = z_{\rm obs} + 2.5$ (solid) and $z_{\rm form} = z_{\rm obs} + 3.5$ (dashed). For $z_{\rm obs} = 0$ I also show the typical stellar mass growth via mergers from the *Illustris* simulation by Rodriguez-Gomez et al. (2016, grey shaded area).

To obtain the average stellar mass growth $\langle \dot{M}_{\star,\mathrm{merg}} \rangle$ via mergers I followed Rodriguez-Gomez et al. (2016) in multiplying the above expression by $\mu_\star/(1+3\,\mu_\star)$ and integrating over $\mu_\star$ from a minimum value $\mu_{\star\mathrm{min}} \approx 10^{-2}$. The latter value includes all relevant mergers, since the cumulative effect from those with smaller stellar mass ratios is negligible with respect to the stellar mass growth (see Rodriguez-Gomez et al., 2016).

I note that I have exploited the above merging rates from *Illustris* but not the related prescriptions for *in-situ* star formation, that are instead based on the framework presented in this work. This approach is aimed to reproduce the halo to stellar mass ratio at different redshifts (see Sect. 2.3.1 and Fig. 2.6).

During each time-step $\mathrm{d}t$ after halo formation at z_form until the observation redshift z_obs, the halo and the stellar mass are increased by the amounts $\langle \dot{M}_{\mathrm{merg,H}} \rangle\,\mathrm{d}t$ and $\langle \dot{M}_{\mathrm{merg},\star} \rangle\,\mathrm{d}t$, respectively. To have a grasp on such mass additions, in Fig. 2.3 it is illustrated the growth of halo and stellar mass via mergers as a function of the descendant final masses. Specifically, it shows the outcomes at observation redshifts $z_\mathrm{obs} = 0, 2, 4$, and 6 (color coded), and at different formation redshifts $z_\mathrm{form} = z_\mathrm{obs}$+1.5, z_obs + 2.5, and z_obs + 3.5 (line-style coded). Plainly, at given observation and formation redshift the amount of relative mass addition by mergers increases with the descendant mass, while at given descendant mass and observation redshift the mass additions increase for increasing formation redshift. The halo mass addition depends weakly on the observation redshift, while the stellar mass addition appreciably increases for decreasing z_obs. Typically, the halo mass increase at $z_\mathrm{obs} \approx 0$ amounts to a factor ~ 3, for a descendant halo mass $M_\mathrm{H} \approx 10^{13}\,M_\odot$ formed at $z_\mathrm{form} \approx 2.5$; correspondingly, the stellar mass increase at $z_\mathrm{obs} \approx 0$ amounts to $\sim 50\%$, for a galaxy with descendant stellar mass $M_\star \approx 3 \times 10^{11}\,M_\odot$ formed at $z_\mathrm{form} \approx 2.5$.

2.2.5 Average over formation redshift

In order to derive the statistical properties of the galaxy population concerning a quantity Q (e.g., halo mass, star formation rate, stellar mass), I proceeded as follows.

I have exploited the analytic solutions of Sect. 2.1 for the evolution of individual galaxies with different formation redshift z_form and halo masses M_H at formation (the halo mass at z_obs is larger because of mass addition by mergers, see previous Sect.), to obtain $Q(\tau : M_\mathrm{H}, z_\mathrm{form})$. Given an observation redshift $z_\mathrm{obs} \lesssim z_\mathrm{form}$, I have picked up the value of Q at $\tau = t_{z_\mathrm{obs}} - t_{z_\mathrm{form}}$, where t_z is the cosmic time at redshift z. Finally, I have performed the average over different formation redshift to get:

$$\langle Q \rangle (M_\mathrm{H}, z_\mathrm{obs}) \propto \int_{z_\mathrm{obs}}^{\infty} \mathrm{d}z_\mathrm{form}\, \frac{\mathrm{d}^2 N_\mathrm{H}}{\mathrm{d}\log M_\mathrm{H}\,\mathrm{d}z_\mathrm{form}}\, Q(t_{z_\mathrm{obs}} - t_{z_\mathrm{form}} : M_\mathrm{H}, z_\mathrm{form})\ , \qquad (2.57)$$

where $\mathrm{d}^2 N_\mathrm{H}/\mathrm{d}\log M_\mathrm{H}\,\mathrm{d}z_\mathrm{form}$ is the halo formation rate computed via the excursion set framework, and checked against *N-body* simulations, by Lapi, Salucci, and Danese (2013); see also Lacey and Cole (1993), Kitayama and Suto (1996), Moreno, Giocoli, and Sheth (2009), and Giocoli, Tormen, and Sheth (2012). The normalization constant in the above Eq. (2.57) is clearly the same integral without Q, and the 1σ variance is computed as $\sigma_Q = \sqrt{\langle Q^2 \rangle - \langle Q \rangle^2}$.

To compute the formation rate one needs the halo mass function, i.e., the comoving number density of halo per halo mass bin, as provided by state-of-the-art *N-body* simulations. I have adopted the determination by Tinker et al. (2008); see also Watson et al. (2013), Bocquet et al. (2016), Comparat et al. (2017), and Comparat et al. (2019). Since this work is mainly concerned with the properties of ETGs residing

at the center of halos, I have exploited the galaxy halo mass function, i.e., the mass function of halos hosting one individual galaxy (though the difference with respect to the halo mass function emerge only for $z \lesssim 1$ and $M_{\rm H} \gtrsim$ several $10^{13}\,M_{\odot}$). This can be built up from the overall halo mass function by adding to it the contribution of sub-halos and by probabilistically removing from it the contribution of halos corresponding to galaxy systems via halo occupation distribution modeling. I refer the reader to Appendix A of Aversa et al. (2015) for details on such a procedure.

2.2.6 Time evolution of individual galaxies

Here I present the evolution with galactic age τ (i.e. galaxy proper time) of the relevant spatially-averaged quantities described by the analytic solutions: infalling gas mass, $M_{\rm inf}$; cold gas mass, $M_{\rm cold}$; stellar mass, $M_{\star}$; gas and stellar metallicity, $Z_{\rm cold}$ and $Z_{\star}$; dust mass, $M_{\rm dust}$. In Figs. 2.4 and 2.5 I illustrate representative galaxies with different halo masses $M_{\rm H} = 10^{12.5}\,M_{\odot}$ and $10^{11.5}\,M_{\odot}$ formed at different redshifts $z_{\rm form} = 3$ and 6.

I note that the infalling gas mass (solid cyan line in upper panels; Figs. 2.4 and 2.5) decreases exponentially with the galactic age as it condenses in the cold gas component (solid blue line in upper panels; Figs. 2.4 and 2.5), which in turn feeds star formation; on the other hand, both components are affected by SN feedback. The balance of these processes makes the cold gas mass (hence the SFR) to slowly grow at early times, to attain a maximum and then to decrease exponentially; correspondingly, the stellar component increases almost linearly and then saturates. In massive halos, with $M_{\rm H} \gtrsim 10^{12}\,M_{\odot}$, the star formation is abruptly quenched by BH feedback and soon after ($\tau_{\rm burst} \sim$ a few 10^8 yr) the residual gas mass is removed; conversely, in less massive halos, with $M_{\rm H} \lesssim 10^{12}\,M_{\odot}$, BH feedback is inactive, so that the star formation can proceed for longer times ($\tau_{\rm burst} \gtrsim$ a few 10^9 yr) until the gas reservoir gets exhausted. This differential behavior is induced by the dependence of $\tau_{\rm burst}$ on halo mass, as specified by Eq. (2.54), and phenomenologically renders the well-known *downsizing* behavior. In galaxy halos formed earlier, the typical SFRs are larger, and the accumulated stellar masses higher.

The metallicity in cold gas and in stars (blue and red lines in lower panels; Figs. 2.4 and 2.5) rises almost linearly, so that after a few 10^7 yr it attains values above $\gtrsim Z_{\odot}/10$. This rapid increase is particularly relevant for the metal enrichment of high redshift galaxies and quasar (QSO) hosts (see Maiolino et al., 2005; Wang et al., 2008; Omont et al., 2013; Michałowski, 2015; Willott, Bergeron, and Omont, 2015; Venemans et al., 2018). In massive halos the metallicity saturates after a time a few 10^8 yr to (super)solar values, and the contribution by delayed metals from SNe I*a* to the stellar metallicity is minor since the BH feedback stops the star formation before any significant pollution. On the other hand, in low mass halos only sub-solar values are attained, and the contribution from delayed metals becomes relatively more important, especially at old ages. This differential behavior in the relative fraction of instantaneous and delayed metals is at the origin of the observed α-enhancement in massive ETGs. The dust-to-gas ratio (dark magenta line in lower panels; Figs. 2.4 and 2.5) follows a behavior similar to the metal enrichment, with a quite rapid growth within $\sim 10^8$ yr driven mainly by accretion onto preformed core grains, up to a saturation value which can be close to unity in massive halos, while it stays $\lesssim 0.3$ in smaller ones. The evolution of metals and dust is quite rapid, and being mainly related to in-situ processes, is weakly dependent on redshift. This could be important for detecting primordial galaxies at $z \gtrsim 6$ in future wide-area IR surveys, that will be routinely achievable with ALMA and JWST (see De Rossi and Bromm, 2019).

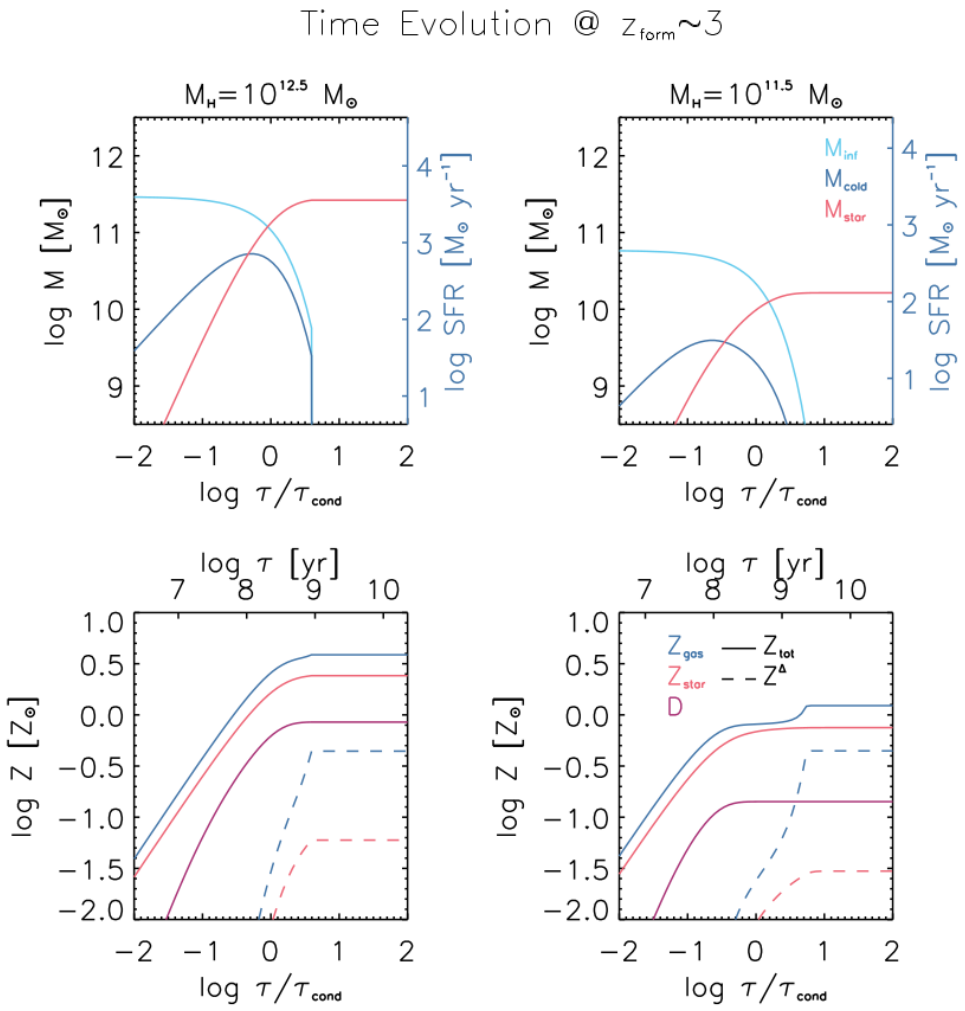

FIGURE 2.4: Evolution of the mass components (top panels), metallicity and dust-to-gas ratio (bottom panels) as a function of the galactic age (normalized to the condensation timescale $\tau_{\rm cond}$ or in absolute units of yr), for galaxies hosted in halos with mass $M_H = 10^{12.5}\ M_\odot$ (left panels) and $M_H = 10^{11.5}\ M_\odot$ (right panels) at formation redshift $z_{\rm form} = 3$; to highlight in-situ evolution, halo and stellar mass additions by mergers are switched off. In the top panels, cyan lines refer to the infalling mass $M_{\rm inf}$, orange lines to the stellar mass $M_\star$ (actually the integral of the SFR), blue lines to the cold gas mass $M_{\rm cold}$ (the corresponding SFR values $\dot{M}_\star = sM_{\rm cold}/\tau_{\rm cond}$ can be read off on the right y-axis). In the bottom panels, blue lines refer to the cold gas metallicity $Z_{\rm cold}$, orange lines to the stellar metallicity $Z_\star$, and red lines to the dust-to-gas mass ratio D; solid lines are for the total metallicity, while dashed lines represent the contribution from delayed metals.

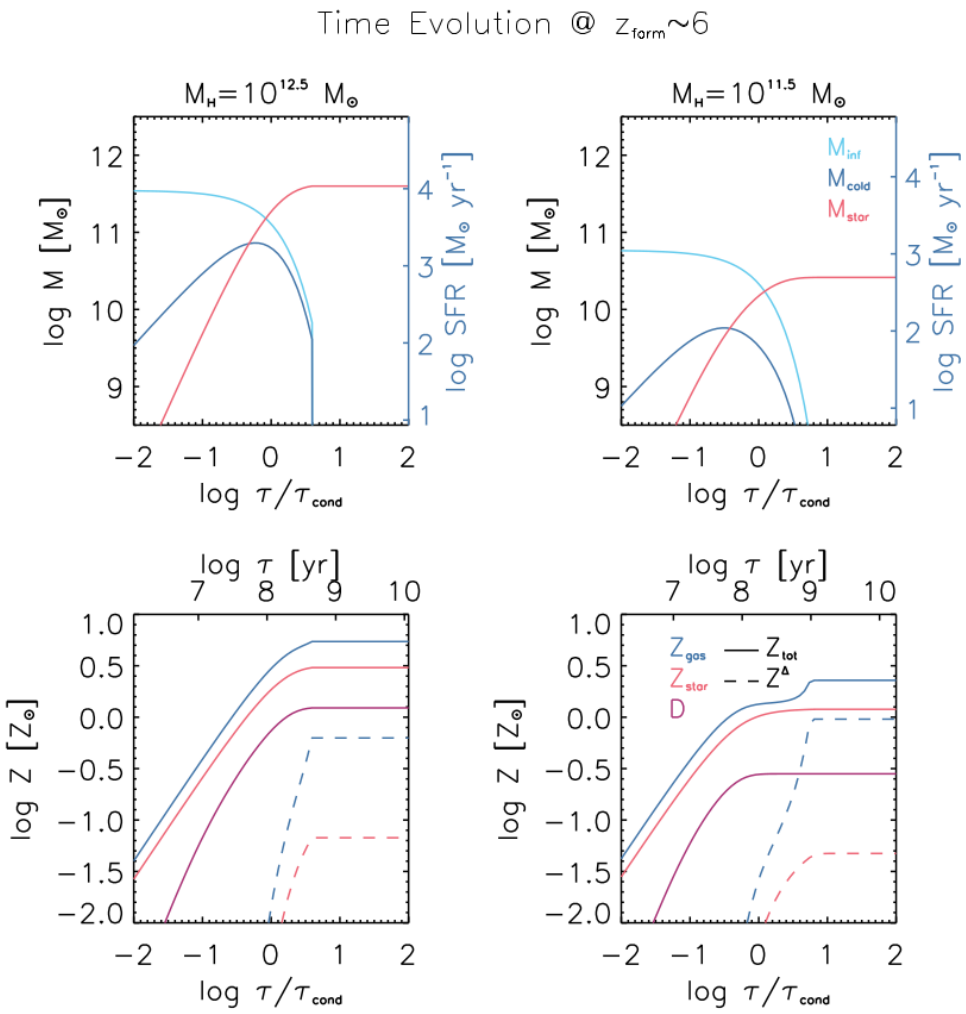

FIGURE 2.5: Same as Fig. 2.4 at formation redshift $z_{\rm form} = 6$.

2.3 Statistical relations for ETG star-forming progenitors

In this Section I present, compare with recent data and discuss the statistical relations that result once the analytic solutions derived and commented in Sect. 2.1 are applied to ETGs and their star-forming progenitors, with the prescriptions presented in Sect. 2.2.

2.3.1 Star formation efficiency

In Fig. 2.6 I show the star formation efficiency $f_\star \equiv M_\star / f_b\, M_{\rm H}$, namely the fraction of initial baryonic mass converted into stars, as a function of the stellar mass $M_\star$, for different observation redshifts $z_{\rm obs}$ = 0, 2, 4, and 6 (color-coded). Shaded areas illustrate the 1σ scatter associated to the average over formation redshifts. The star formation efficiency $f_\star$ is found to be a non-monotonic function of the $M_\star$, with a maximum value of $20-30\%$ slowly increasing with redshift around $M_\star \simeq 10^{11}\, M_\odot$, and a decrease to values less than 10% for $M_\star \sim$ a few $10^9\, M_\odot$ and for $M_\star \simeq 10^{12}\, M_\odot$; all in all, star formation in galaxies is a very inefficient process.

Such a behavior is easily understood in terms of infall/condensation and feedback processes. At small masses, infall and condensation are efficient ($f_{\rm inf} \approx 1$) but star formation is regulated by outflows from SNe and stellar winds; conversely, at high masses infall and condensation become less efficient ($f_{\rm inf} \lesssim 1$) and star formation is also hindered by BH feedback. All in all, the maximum value of the star formation efficiency occurs at a mass corresponding approximately to the transition between the stellar and BH feedback (see Shankar et al., 2006; Moster, Naab, and White, 2013; Aversa et al., 2015).

The outcome at $z_{\rm obs} \approx 0$ is compared with the local data for ETGs from various authors, determined via weak lensing (see Velander et al., 2014; Hudson et al., 2015; Rodríguez-Puebla et al., 2015; Mandelbaum et al., 2016) and satellite kinematics (see More et al., 2011; Wojtak and Mamon, 2013), while the outcome at $z \approx 2$ should be compared with the estimates by Burkert et al. (2016) via Hα data and mass profile modeling. The agreement in normalization and scatter is very good, within the still large observational uncertainties. The results as a function of redshift are also similar, within a factor of 2, to the determinations via abundance matching technique by Moster, Naab, and White (2013), Behroozi, Wechsler, and Conroy (2013), Aversa et al. (2015), and Lapi et al. (2017).

The similarity of the efficiency at $z \approx 2$ to the local values is indicative that star formation is mainly an in situ process (see Lilly et al., 2013; Moster, Naab, and White, 2013; Aversa et al., 2015; Mancuso et al., 2016b); actually, the difference in $f_\star$ between these redshifts is mainly driven by the increase in the stellar and halo mass due to late-time mergers.

2.3.2 Galaxy main-sequence

In Fig. 2.7 I present the results concerning the so-called *main-sequence* (MS) of star-forming galaxies (e.g., Daddi et al., 2007; Elbaz et al., 2007; Noeske et al., 2007; Rodighiero et al., 2011; Speagle et al., 2014; Whitaker et al., 2014; Rodighiero et al., 2015; Schreiber et al., 2017; Tacchella et al., 2018; Popesso et al., 2019), namely the relation between the SFR and stellar mass at different observation redshifts $z_{\rm obs}$ = 2, 4, 6 (color-coded). The outcomes at $z \sim 2$ are in pleasing agreement with the observational determination from the large statistics of mass-selected galaxy samples

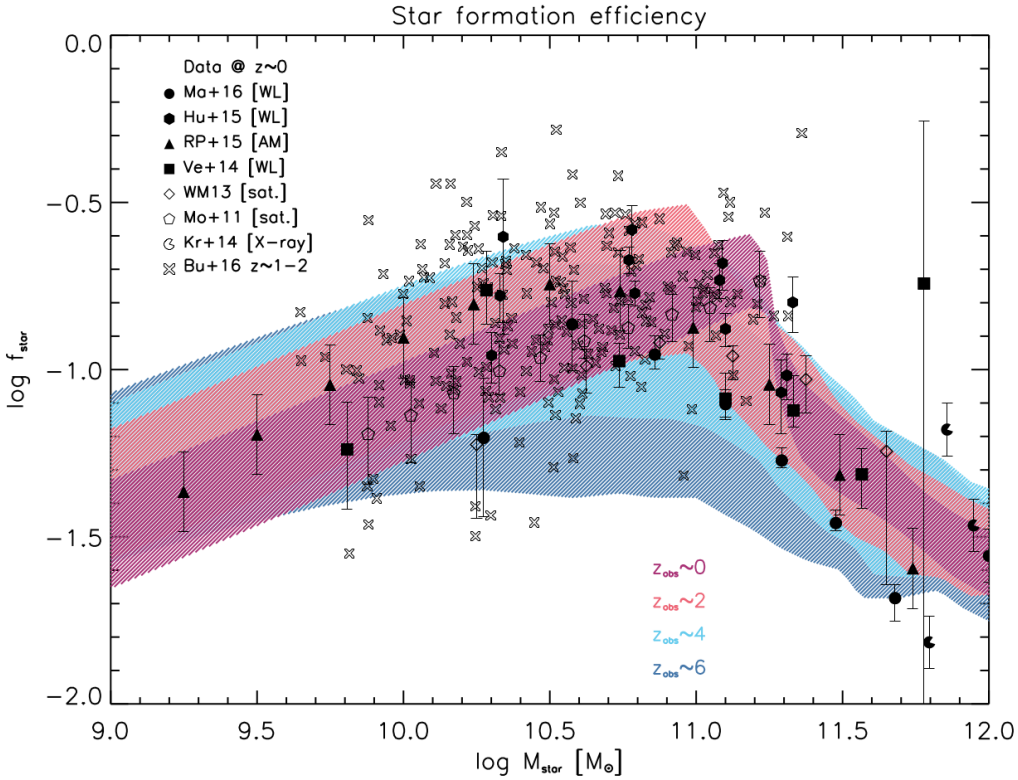

FIGURE 2.6: Star formation efficiency $f_\star = M_\star / f_b\, M_H$ vs. stellar mass $M_\star$, at different observation redshifts $z \approx 0$ (red), 2 (orange), 4 (cyan), and 6 (blue); the shaded areas illustrate the 1σ variance associated to the average over different formation redshifts. Data points are from Mandelbaum et al. (2016, circles), Hudson et al. (2015, hexagons) and Velander et al. (2014, squares) via weak lensing, Rodríguez-Puebla et al. (2015, triangles) via sub-halo abundance matching, Wojtak and Mamon (2013, diamonds) and More et al. (2011, pentagons) via satellite kinematics, Kravtsov, Vikhlinin, and Meshcheryakov (2018, pacmans) via X-ray observations of BCGs, and Burkert et al. (2016, crosses) via mass profile modeling of galaxies at $z \sim 1-2$. If not indicated explicitly, error bars are ≈ 0.25 dex.

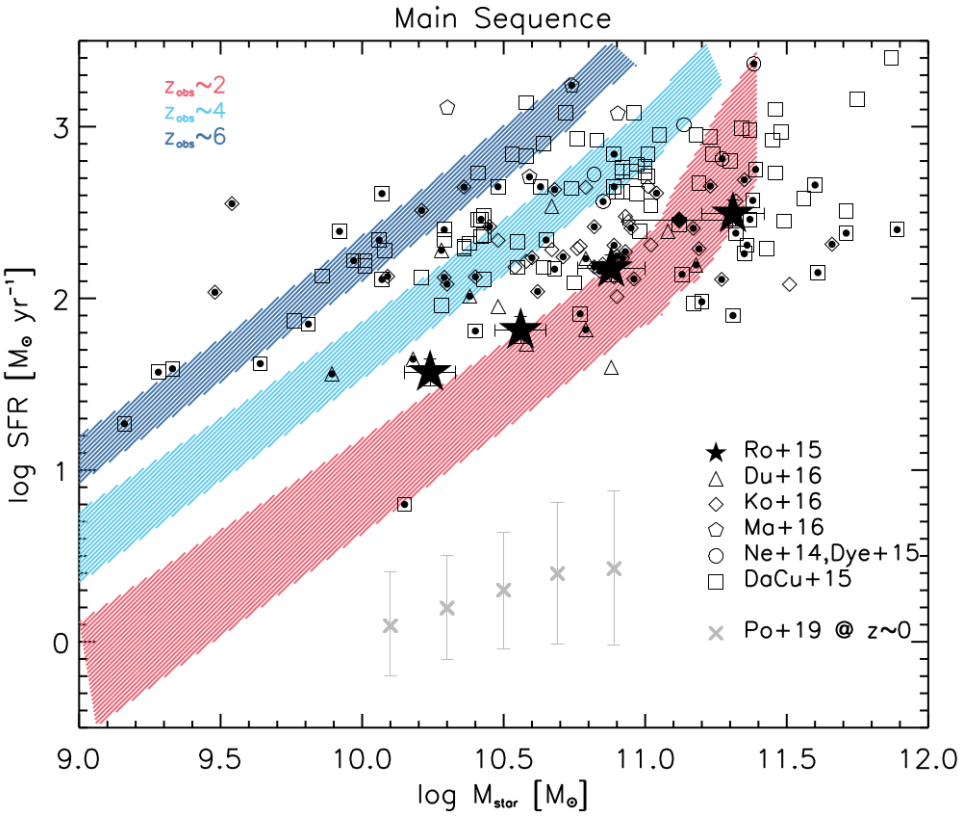

FIGURE 2.7: Star formation rate SFR vs. stellar mass $M_\star$, alias the main sequence of star-forming galaxies, at different observation redshifts $z \approx 2$ (orange), 4 (cyan), and 6 (blue); the shaded areas illustrate the 1σ variance associated to the average over different formation redshifts. The black filled stars are the observational determinations of the main sequence at $z \sim 2$ based on the statistics of large mass-selected samples by Rodighiero et al. (2015). The other symbols (error bars omitted for clarity) refer to far-IR data for individual objects at $z \sim 1-4$ (those in the range $z \sim 1.5-2.5$ are marked with a dot) by Dunlop et al. (2017, triangles), Koprowski et al. (2016, diamonds), Ma et al. (2016, pentagons), Negrello et al. (2014), Dye et al. (2015, circles), and da Cunha et al. (2015, squares); for reference the determination at $z \approx 0$ by Popesso et al. (2019, crosses) is also reported.

by Rodighiero et al. (2015): this further substantiates the solutions for the time evolution of the star formation and stellar mass in individual galaxies.

To highlight the relevance of observational selections different from that based on stellar mass, in Fig. 2.7 I also report data points for individual, FIR-selected galaxies by Ma et al. (2016), Koprowski et al. (2016), and Negrello et al. (2014), along with Dye et al. (2015), da Cunha et al. (2015), and Dunlop et al. (2017), mainly at redshifts $z \sim 1-4$. An appreciable fraction of the individual, far-IR selected galaxies around $z \sim 2$ (highlighted by dots within hollow symbols) lie above the main sequence, i.e., at SFR values higher than expected on the basis of the average relationship at a given $M_\star$. These off-main-sequence objects can be simply interpreted (see Mancuso et al., 2017; Lapi et al., 2017) as galaxies caught in an early evolutionary stage and still accumulating their stellar mass. Thus, young star-forming galaxies are found to be preferentially located above the main sequence or, better, to the left of it. As time goes by and the stellar mass increases, the galaxy moves toward the average main-sequence relationship, around which it will spend most of its lifetime. Afterwards, the SFR is quenched by feedback and the galaxy will then evolve passively to become a local early type; it will then populate a region of the SFR versus stellar mass diagram that is substantially below the main sequence. These loci of "red and dead" galaxies are indeed observed locally (see Renzini and Peng, 2015) and start to be pinpointed even at increasing redshift (see Man et al., 2016). For reference in Fig. 2.7 I also report the determination at $z \approx 0$ by Popesso et al. (2019), which is mainly representative of the local disk-dominated galaxies (not included in this work); typically, these have star formation histories prolonged over several Gyrs and continue to form stars, though at rather low rates of a few $M_\odot$ yr^{-1}, even toward $z \approx 0$.

The overall redshift evolution of the main sequence for ETG and their progenitors is consistent with a scenario which traces the bulk of the star formation in galaxies back to local, in situ condensation processes. Specifically, at higher z and in massive galaxies, the interstellar medium is on average denser and the condensation/star formation timescales are shorter. Thus, the star formation in a galaxy of given stellar mass is higher, causing the main sequence locus to shift upwards. Moving toward higher redshift, the fraction of off-main-sequence objects decreases appreciably: this is because, given the evolution of the SFR function and the shorter age of the universe, it is more and more difficult to spot galaxies of appreciably different ages and featuring very high SFRs.

2.3.3 Gas mass

In Fig. 2.8 I illustrate the relationship between the gas mass, $M_{\rm gas}$, and the stellar mass, $M_\star$, for different observation redshifts $z_{\rm obs} \sim 2$, 4 and 6 (color-coded). Over most of the stellar mass range, the gas mass increases monotonically. The relationship holds up to $M_\star \sim 10^{11}\,M_\odot$, where a decrease in the gas mass is enforced since the infall/condensation processes becomes inefficient. As to the redshift evolution, the gas mass is slightly higher for star-forming galaxies observed at earlier epochs: this can be traced back to the fact that objects observed at higher redshift are on average younger and are expected to have converted less gas into stars. At $z_{\rm obs} = 0$ the descendants of these star-forming galaxies, i.e., local ETGs, have very small gas reservoirs, since most of the gas was consumed via star formation and/or ejected by feedback events. In fact, the $z \approx 0$ determination from Saintonge et al. (2017), reported as a reference, refers mainly to disk-dominated galaxies which are gas rich and still star-forming in the local Universe.

The results for star-forming ETG progenitors are compared with the gas mass estimates from Tacconi et al. (2018) from ALMA data for a large sample of star-forming galaxies at redshifts $z \sim 1-4$; the agreement with the data is good in normalization, scatter and redshift evolution, although still large observational uncertainties hinder a more detailed comparison.

2.3.4 Dust mass

In Fig. 2.9 I show the dust mass, $M_{\rm dust}$, as a function of the stellar mass, $M_\star$, for different observation redshifts $z_{\rm obs} \sim 2$, 4, and 6 (color-coded). A direct relationship is expected since both dust and stellar mass are strictly related to the SFR. In fact, the dust mass is produced in SN ejecta/stellar winds, that are more efficient when the SFR is higher. High SFRs also favor metal rich environments, in turn triggering efficient growth of dust grains by accretion. At given stellar mass, higher redshift galaxies are expected to produce slightly larger amount of dust: the trend can be traced back to their denser environment, in turn yielding shorter star formation timescales.

The results for star-forming ETG progenitors are in good agreement with the observational estimates by Santini et al. (2014) at $z \sim 2$ from stacked FIR photometry, by da Cunha et al. (2015) at $z \sim 4$ from sub-mm SED modelling, and by Mancini et al. (2015) from upper limits to thermal dust emission in at $z \sim 6$ star-forming galaxies. For reference I also report the $z \approx 0$ dust mass estimates by Rémy-Ruyer et al. (2014), mainly referring to disk-dominated galaxies, which are still star-forming and moderately gas rich even in the local Universe.

2.3.5 Gas metallicity

In Fig. 2.10 I present the mass-metallicity relationship (see Tremonti et al., 2004; Erb et al., 2006; Maiolino et al., 2008; Steidel et al., 2014; Zahid et al., 2014; de los Reyes et al., 2015; Sanders et al., 2015; Faisst et al., 2016; Onodera et al., 2016; Suzuki et al., 2017), i.e., the relation between the gas metallicity $Z_{\rm gas}$ of the cold gas and the stellar mass $M_\star$ at different observation redshifts $z_{\rm obs} \sim 2$, 4 and 6 (color-coded). The gas metallicity shows an increasing behavior as a function of the final stellar mass, related to the more efficient production of metals in galaxies with higher SFRs, that will also yield larger stellar masses; the corresponding redshift evolution is negligible, being the gas metallicity essentially related to in-situ processes.

The results are in agreement with gas metallicity estimates (traced mainly by Oxygen abundance, and converted to PP04O3N2 calibration, see Kewley and Ellison, 2008) from strong rest-frame optical emission lines in UV/optically selected star-forming galaxies by de los Reyes et al. (2015), Onodera et al. (2016), and Suzuki et al. (2017), spanning the redshift interval $z \sim 1-4$.

2.3.6 Stellar metallicity and alpha-enhancement

In Fig. 2.11 I illustrate the stellar mass-metallicity relationship (see Thomas et al., 2005; Gallazzi et al., 2006; Thomas et al., 2010; Johansson, Thomas, and Maraston, 2012; Gallazzi et al., 2014), i.e., the relationship between the stellar metallicity, $Z_\star$, and the stellar mass, $M_\star$, at different observation redshifts $z_{\rm obs} = 0$, 2, and 4 (color-coded). The stellar metallicity increases monotonically with stellar mass, mirroring the gas metallicity behavior (see Fig. 2.10). This is because massive galaxies are characterized on average by higher SFRs, that imply larger stellar masses and metal

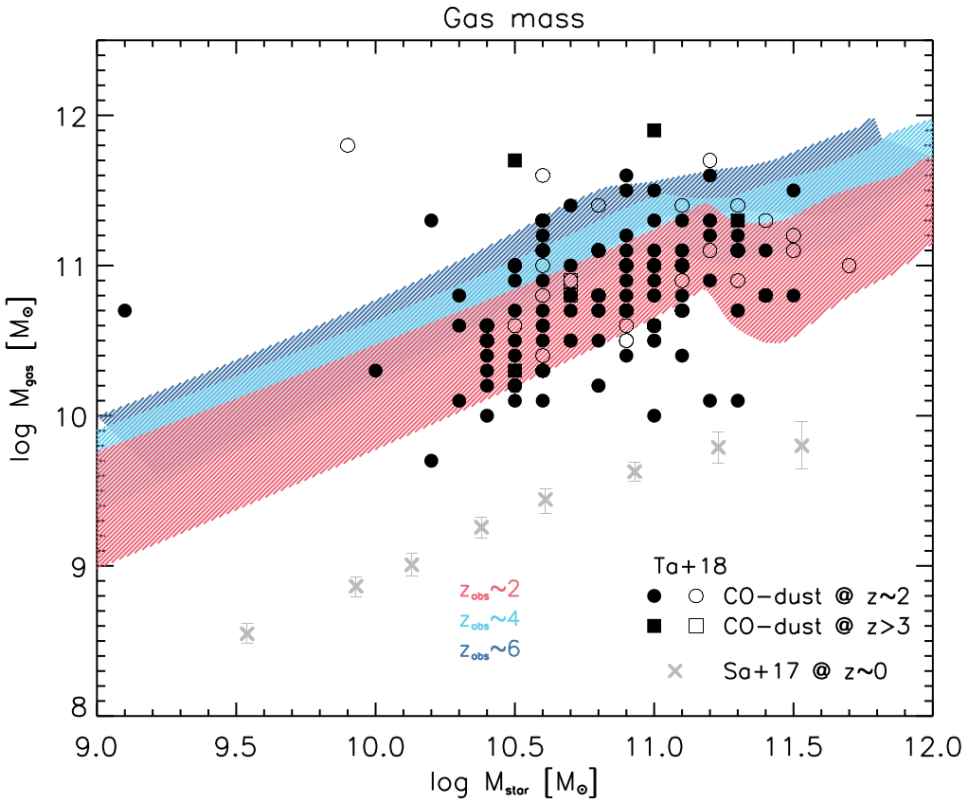

FIGURE 2.8: Gas mass $M_{\rm gas}$ vs. stellar mass $M_\star$ at different observation redshifts, $z \approx 2$ (orange), 4 (cyan), and 6 (blue); the shaded areas illustrate the 1σ variance associated to the average over different formation redshifts. Data points are from Tacconi et al. (2018); circles represent objects at $z \sim 2$ while squares stand for galaxies at redshifts $z \gtrsim 3$. Filled symbols refer to gas mass estimates from CO lines, and empty symbols from dust FIR/sub-mm continuum. Error bars on data points (omitted for clarity) are of order ≈ 0.25 dex; for reference data at $z \approx 0$ from Saintonge et al. (2017, crosses) are also reported.

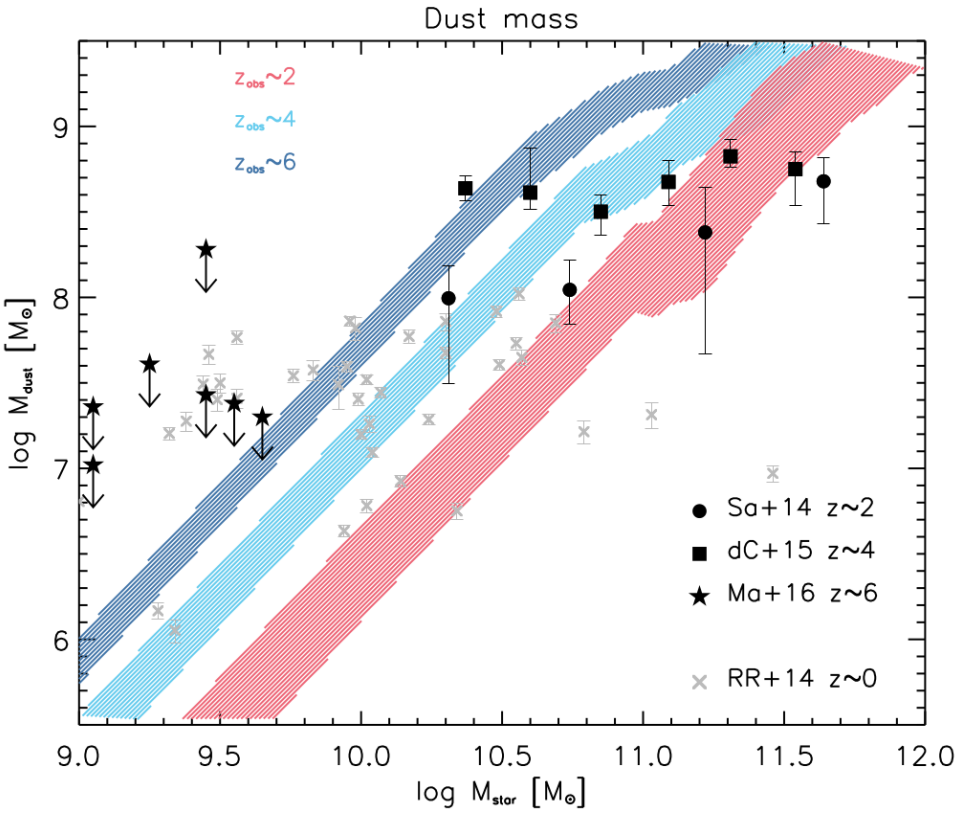

FIGURE 2.9: Dust mass $M_{\rm dust}$ vs. stellar mass $M_\star$, at different observation redshifts $z \approx 2$ (orange), 4 (cyan), and 6 (blue); the shaded areas illustrate the 1σ variance associated to the average over different formation redshifts. Data points are from Santini et al. (2014, circles) at $z \sim 2$, da Cunha et al. (2015, squares) at $z \sim 4$, and from Mancini et al. (2015, stars) at $z \sim 6$ (upper limits only); for reference measurements at $z \approx 0$ by Rémy-Ruyer et al. (2014, crosses) are also reported.

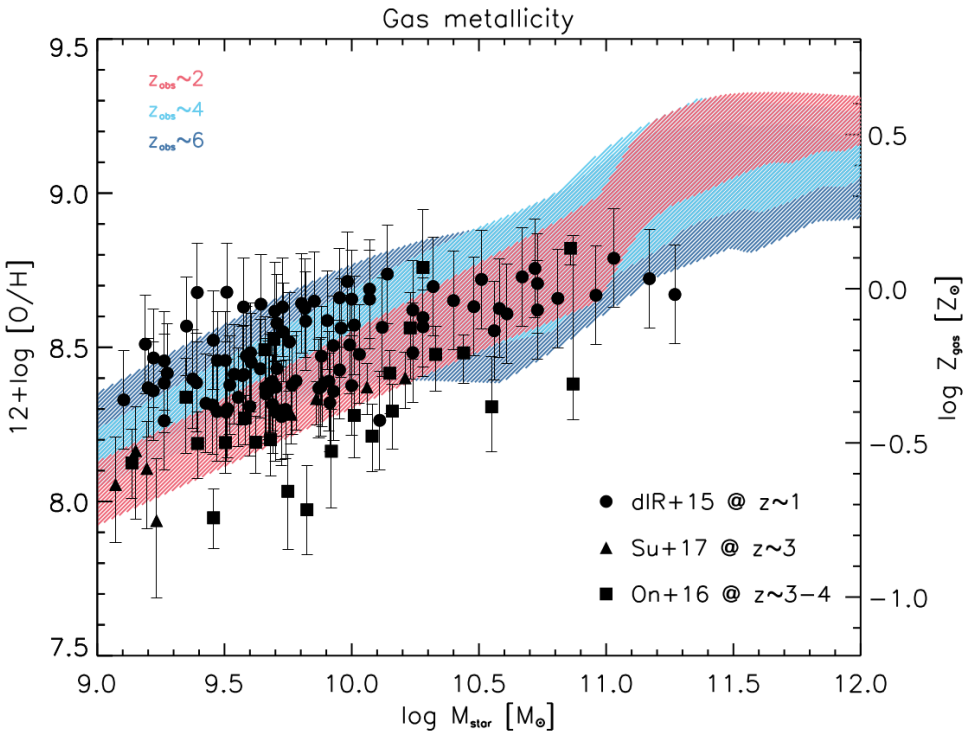

FIGURE 2.10: Gas metallicity $Z_{\rm gas}$ vs. stellar mass $M_\star$ at different observation redshifts $z \approx 2$ (orange), 4 (cyan), and 6 (blue); the shaded areas illustrate the 1σ variance associated to the average over different formation redshifts. Data points are from de los Reyes et al. (2015, circles) at $z \sim 1$, Suzuki et al. (2017, triangles) at $z \sim 3$ and Onodera et al. (2016, squares) at $z \sim 3-4$; for reference the determination at $z \approx 0$ by Saintonge et al. (2017, crosses) is also reported. All gas metallicity have been converted to PP04O3N2 calibration.

production. Moreover, in low mass galaxies the depletion of metals by stellar feedback is enhanced due to the shallower potential wells associated to the host halos. Contrariwise, high-mass galaxies can retain greater amounts of chemical-enriched gas, that could be converted and locked into new metal-rich stars, resulting in a higher stellar metallicity. The evolution in redshift is minor, as the stellar metallicity is mainly determined by in-situ star formation processes in the central regions; if any, at higher z and given stellar mass, the stellar metallicity increases slightly since the average SFR is larger.

The results are in agreement with measurements of stellar metallicity in local ETGs by Thomas et al. (2010) from the SDSS, and with the estimates by Gallazzi et al. (2014) at $z \sim 0.7$, that are broadly consistent with the local relationship within their large uncertainties and intrinsic variance. Note that other few works attempted to derive stellar metallicity out to $z \sim 3$ in star-forming galaxies, but these analysis are based on rest-frame UV absorption features, which are good tracers only of the youngest stellar populations (e.g., Halliday et al., 2008; Sommariva et al., 2012).

In the inset of Fig. 2.11 I show the $\alpha-$enhancement (see Thomas et al., 2005; Thomas et al., 2010; Johansson, Thomas, and Maraston, 2012), i.e., the local α-elements to iron abundance ratio [α/Fe] as a function of galaxy stellar mass $M_\star$. At small stellar masses $M_\star \lesssim 10^{10}\,M_\odot$ an almost constant [α/Fe] ≈ 0.05 is found, while in moving toward higher masses [α/Fe] increases up to a value ~ 0.25. This trend can be strictly related to the diverse star formation histories characterizing small and high mass galaxies. In particular, in massive galaxies BH feedback is able to quench the star formation and deplete the residual gas mass within a fraction of Gyr, well before SNe I*a* can pollute the ISM with substantial iron content; this results in an under-abundance of iron with respect to α elements in the stellar component, that in turn cause an excess in [α/Fe]. Contrariwise, in low mass galaxies star formation proceeds longer, and SNe I*a* have time to enrich the ISM and the stars with relatively larger amount of iron. I find a good agreement of this result with the observed α-enhancement of local ETGs, as estimated by Thomas et al. (2010).

2.3.7 Outflow metallicity

In Fig. 2.12 I illustrate the metallicity of the outflowing material $Z_{\rm out}$ as a function of the stellar mass $M_\star$, for different observation redshifts $z \sim 0, 2, 4$, and 6 (color-coded). Relevant measurements of the metallicity concern the warm (temperatures 10^4 K; e.g., Caon, Macchetto, and Pastoriza, 2000; Ferrari et al., 2002; Athey and Bregman, 2009) and hot gas (temperatures $10^6 - 10^7$ K; see Loewenstein and Mathews, 1991; Mathews and Brighenti, 2003; Humphrey and Buote, 2006) in local massive ETGs, as the outflowing chemical enriched gas has been possibly retained in the host halo potential well. As to the hot gas I report estimates by Humphrey and Buote (2006), who exploited X-ray observations to derive the iron amount and its abundance ratios with other elements in the hot ISM. As to the warm gas I report the estimates by Athey and Bregman (2009), who determined lower limit to the ISM metallicity of their ETGs sample via oxygen emission lines.

The data points are clustered in the high-mass end of the plot, and are consistent with the results at $z_{\rm obs} \approx 0$, albeit their large uncertainties (omitted for clarity but amounting to about 0.5 dex) does not allow to draw strong conclusion. Finally, it is worth noticing that the solar or even super-solar metallicities found in the hot and warm medium of local ETGs indicate the ISM metals to have mostly an in-situ, internal origin. As also stressed by Humphrey and Buote (2006) and Athey and Bregman (2009) a significant external contribution from cosmic scale primordial

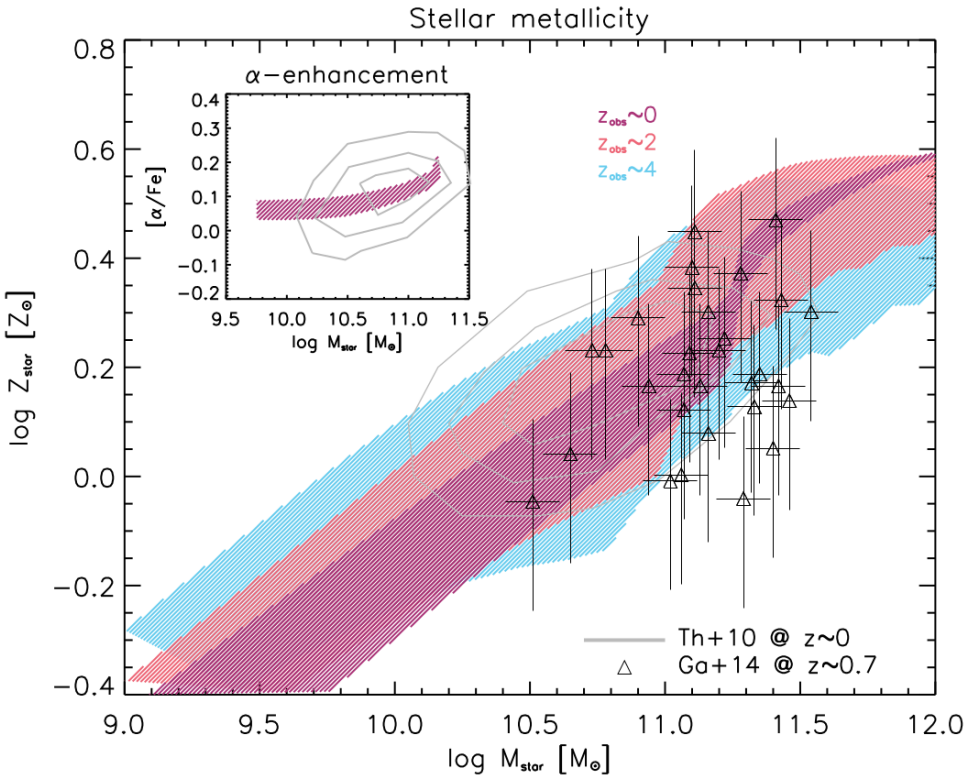

FIGURE 2.11: Stellar metallicity $Z_\star$ vs. stellar mass $M_\star$ at different observation redshifts $z \approx 0$ (red), 2 (orange), and 4 (cyan); the shaded areas illustrate the 1σ variance associated to the average over different formation redshifts. Data for SDSS samples of local ETGs are from Thomas et al. (2010, solid contours), and for individual galaxies at $z \sim 0.7$ are from Gallazzi et al. (2014, triangles). Inset: as above for α-elements to iron abundance ratio $[\alpha/\mathrm{Fe}]$ vs. stellar mass $M_\star$ at observation redshift $z \approx 0$ (red).

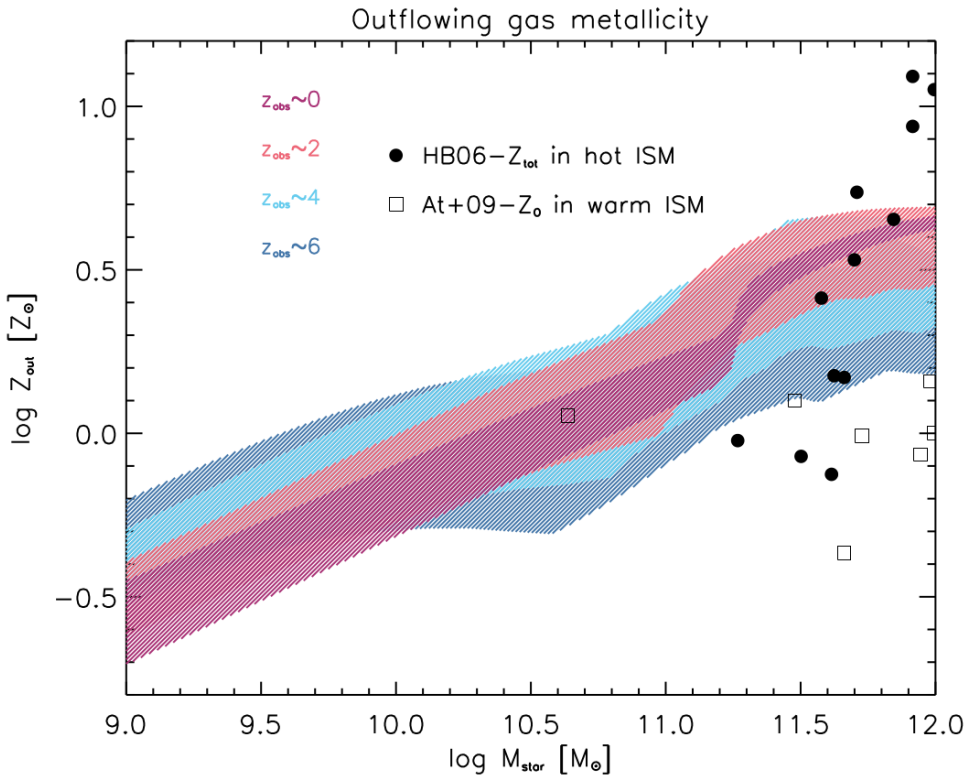

FIGURE 2.12: Outflowing gas metallicity $Z_{\rm out}$ vs. stellar mass $M_\star$ at different observation redshifts $z \approx 0$ (red), 2 (orange), and 4 (cyan), and 6 (blue); the shaded areas illustrate the 1σ variance associated to the average over different formation redshifts. Data points referring to total α-elements abundances in the hot ISM of local ETGs are from from Humphrey and Buote (2006, filled circles), and referring to Oxygen abundance in the warm ISM of local ETGs are from Athey and Bregman (2009, squares); the latter may be considered lower limits to the total outflowing gas metallicity. Error bars on data points of order $\lesssim 1$ dex have been omitted for clarity.

gas or minor mergers should imply a significant dilution of the ISM in ETGs, with a ensuing reduction in metallicity. I caveat, however, that the issue is still debated, given the still large observational uncertainties in the ISM metallicity determinations.

2.4 Summary

In Sect. 2.1 I presented a set of new analytic solutions aimed at describing the spatially-averaged evolution of the gas/stellar/dust mass and metal content in a star-forming galaxy hosted within a dark halo of given mass and formation redshift. The basic framework pictures the galaxy as an open, one-zone system comprising three interlinked mass components: a reservoir of warm gas subject to cooling and condensation toward the central regions; cold gas fed by infall and depleted by star formation and stellar feedback (SNe II and stellar winds); stellar mass, partially restituted to the cold phase by stars during their evolution. The corresponding metal enrichment history of the cold gas and stellar mass is self-consistently computed using as input the solutions for the evolution of the mass components; the metal equations includes effects of feedback, astration, instantaneous production during star formation, and delayed production by SNe Ia, possibly following a specified delay time distribution. Finally, the dust mass evolution takes into account the formation of grain cores associated to star formation, and of the grain mantles due to accretion onto preexisting cores; astration of dust by star formation and stellar feedback, and spallation by SN shock-waves are also included.

In Sect. 2.2 I applied the analytic solution to describe the formation of ETGs and the evolution of their star-forming progenitors. To this purpose, I have supplemented the solutions with a couple of additional ingredients, that are: specific prescriptions for parameter setting, inspired by *in-situ* galaxy-BH co-evolution scenarios for ETG formation; estimates of the average halo and stellar mass growth by mergers, computed on the basis of the merger rates from state-of-the-art numerical simulations.

In Sect. 2.3 I derived a bunch of fundamental relationships involving spatially-averaged quantities as a function of the observed stellar mass: star formation efficiency, SFR, gas mass, dust mass, gas metallicity, stellar metallicity and $[\alpha/\mathrm{Fe}]$ ratio, and outflowing gas metallicity. Finally, I compared these relationships with the data on local ETGs and their high-z star-forming progenitors, finding a pleasing overall agreement.

Chapter 3

Constraining dusty galaxy evolution from broad-band emission

In this Chapter I will focus on the pieces of information that can be recovered by galaxy broad-band emission, mainly through the fit of their SED when physically-motivated prescriptions to describe the underling processes are adopted. The study will be applied on a pilot sample of 11 DSFGs, that are spectroscopically confirmed to be at the peak of Cosmic SFH.

Specifically, in Sect. 3.1 I will describe the main approaches to study DSFGs at high-z from observations and motivate my choice; then, I will list the selection criteria that I required to build the sample of 11 DSFGs and I will present the multi-wavelength data available for each source, their sky position and redshift distribution.

In Sect. 3.2 I will illustrate the method we followed to model galaxy SEDs and the corresponding outcomes, also including other evidences coming from galaxy multi-band emission.

Finally, in Sect. 3.3 I will discuss the results by referring to the *in-situ* (see Mancuso et al., 2016a; Mancuso et al., 2017; Lapi et al., 2018; Pantoni et al., 2019) and compare the findings with other recent studies on small and statistical samples of high-z DSFGs.

3.1 Characterizing Dusty Star-Forming Galaxies from observations

Currently on the market there are two main different but complementary approaches that use the wealth of data recently collected by the numerous photometric and spectroscopic wide-area and deep surveys to characterize high-z DSFGs. In this Section, I describe the principal pros and cons of these approaches and provide a motivation of my choice, in order to fulfill the main scopes of this work. Finally, I illustrate the sample selection criteria and list the resulting selected-sources that will be the object of my next analysis.

3.1.1 Statistically-relevant studies

The first approach relies on the analysis of statistically significant samples of DSFGs with the purpose of constraining one or a few specific properties of the galaxy population (such as stellar mass, dust mass, attenuation, metallicity, environment; see e.g., Béthermin et al., 2014; da Cunha et al., 2015; Casey et al., 2018; Pearson et al., 2018; Franco et al., 2018; Donevski et al., 2018). The analysis is often built on a few

well-sampled spectral bands (e.g. Magdis et al., 2012; Małek et al., 2018), while just in some cases it is multi-messenger (e.g. Pearson et al., 2018; Buat et al., 2019; Donevski et al., 2020).

To preserve the statistical relevance of the outcomes, this approach extensively exploits, e.g., the building of synthesized SEDs, especially when the sampling is scarce and not uniform for every objects (e.g. Bianchini et al., 2019), and the analysis of stacked data (e.g. Santini et al., 2014; Scoville et al., 2016). Indeed, one of the main drawbacks is probably the data incompleteness: the available pieces of information (e.g., observed frequency, sensitivity, redshift) are typically not homogeneous over the whole sample. In addition, the outcomes may suffer from selection-biases (depending on the survey exploited to collect data) and could be affected by uncertainties due to the exploitation of photometric redshift and, eventually, to arbitrary assumptions on galaxy under-sampled properties.

3.1.2 Individual source analysis

The second approach focuses on the analysis of small samples or individual objects with a great number of photometric and spectroscopic quality data, with the aim of gaining a deep insight into the ongoing astrophysical processes. Typically, this objective is reached with the exploitation of high resolution imaging (usually in the optical and millimeter/radio regimes) and the analysis of spectral lines, that provides an almost secure determination of galaxy spectroscopic redshift, of its kinematics and multi-wavelength sizes (e.g., Tadaki et al., 2015; Decarli et al., 2016b; Barro et al., 2016b; Barro et al., 2016a; Talia et al., 2018; Fraternali et al., 2021; Lelli et al., 2021).

At high-z, this analysis requires very long integration times (i.e., orders of a few hours at least) that do not allow the method to be applied to statistical samples. Some studies partially overcome this problem by focusing on gravitationally lensed objects (e.g., Negrello et al., 2014; Massardi et al., 2018; Stacey et al., 2020; Rizzo et al., 2020; Rizzo et al., 2021), even if this strategy requires to model the foreground lens in order to obtain the *original* (i.e., unbent) image of the target galaxy.

Although the outcomes do not have any statistical relevance for the whole population of DSFGs, their accuracy can provide an exquisite characterization of the individual object, that encompasses all the galaxy properties when complemented with the wealth of multi-wavelength photometry currently available (see e.g., Rujopakarn et al., 2016; Elbaz et al., 2018).

3.1.3 A panchromatic study of 11 Dusty Star-Forming Galaxies at $z \sim 2$

In this work I follow the latter approach (cf. Sect. 3.1.2), focusing on a sample of 11 (sub-)millimeter selected DSFGs and spectroscopically confirmed to be at the peak of Cosmic SFH ($z \sim 2$; see e.g., Madau and Dickinson, 2014). This requirement is fundamental for the scopes of this thesis, since the main interest is to investigate the nature of massive dusty galaxies that account for the most of the SFRD of the Universe. The sample is selected in the Great Observatories Origins Survey South (GOODS-S; Dickinson and GOODS Legacy Team, 2001; Giavalisco et al., 2004) field, in order to ensure the widest multi-wavelength coverage of galaxy broad-band emission currently achievable (from X-rays to radio band). Such accurate sampling is important to fairly derive galaxy integral properties from their SED, since the latter is the outcome of all the complex processes occurring between galaxy baryonic components, i.e. stars and their remnants, cold and warm gas, interstellar dust and central SMBH. Furthermore, a complete sampling of galaxy emission may be crucial to shed

light on the role of AGN in quenching the star formation in the host and driving the morphological transition from star-forming disks to ellipticals/quiescents.

Selection criteria and multi-wavelength counterparts association

The sample was selected in the (sub-)millimeter regime, requiring the following criteria to be fulfilled for each galaxy:

- 3 or more detections in the optical domain ($\lambda_{\rm obs} = 0.3 - 1$ μm);
- 6 or more detections in the NIR & MIR bands ($\lambda_{\rm obs} = 1 - 25$ μm);
- 2 or more detections in the FIR band ($\lambda_{\rm obs} = 25 - 400$ μm);
- spectroscopically confirmed redshift in the range $1.5 < z < 3$;
- 1 or more detections and/or upper limits in the radio and/or X-ray regimes.

It is important to note that *Herschel* photometry is crucial to sample the thermal dust FIR peak of z $\sim$ 2 galaxies and, as a consequence, to constrain the intrinsic (i.e., unobscured) stellar light. For this reason, the sources were selected to have at least two detections in *Herschel* photometric bands (either PACS or SPIRE). I further note that the requirement of a spectroscopic measurement of galaxy redshift is essential to overcome some degeneracies that affect SED analysis (such as the age-metallicity degeneracy; see e.g. Worthey, 1999) and do not allow to properly constrain some fundamental properties of the galaxy, e.g. its stellar mass and age.

The sample was selected from the catalogs by Yun et al. (2012), Targett et al. (2013) and Dunlop et al. (2017). These catalogs are built on (sub-)millimeter surveys in the GOODS-S field, that used either ALMA ($\lambda_{\rm B6} = 1.1 - 1.4$ mm; covering ~ 1 arcsec^2 in the HUDF South), LABOCA ($\lambda = 0.870$ mm) on APEX, or AzTEC ($\lambda = 1.1$ mm) on ASTE (now on LMT). The wide and deep broad-band coverage of the GOODS-S field allows to ensure an almost complete association between the (sub-)millimeter sources and their optical, infrared, radio and X-rays counterparts, that can be currently found in the literature and public catalogs. In order to reconstruct the (sub-)millimeter sources multi-band emission, I used data from:

- GOODS-MUSIC[1] (Grazian et al., 2006), whose optical and NIR photometry was associated with *Spitzer* and *Herschel* MIR and FIR maps by Magnelli et al. (2013);
- the $\simeq$ 7 Ms *Chandra* Deep Field South Catalog (Luo et al., 2017), for the emission in the X-ray;
- the VLA radio catalogs by Miller et al. (2013), Thomson et al. (2014) and Rujopakarn et al. (2016).

The optical-IR photometric catalog resulting from the association of the NIR-selected sources in GOODS-MUSIC with the *Herschel*-detected source by Magnelli et al. (2013) is made of 263 sources. As a first step, I associated these objects with the (sub-)millimeter sources by Yun et al. (2012), Targett et al. (2013) and Dunlop et al. (2017). Specifically, to perform the sky-match with the millimeter sources observed

[1]GOODS-MUSIC is a multi-band catalog ($\lambda = 0.3 - 8.0$ μm) of NIR (i.e. Z and K_s) selected objects in the GOODS-S field. It includes: two images in the U filter by ESO; one image in the B band by the VIMOS/VLT; the ACS/HST images in B, V, i, z bands; the ISAAC-VLT photometry (J, H, K_s bands); the IRAC/*Spitzer* photometry at $\lambda = 3.5$, 4.5, 5.8, 8 μm.

in the ALMA survey by Dunlop et al. (2017) I used a searching radius of 1 arcsec, compatible with ALMA and HST beam size; then I matched the (sub-)millimeter sources in Yun et al. (2012) and Targett et al. (2013) catalogs using a 1.5 arcsec searching radius from the optical/CANDELS coordinates and a 3 arcsec radius from the NIR/IRAC ones (both consistent with the respective beam size). From these sky-matches I obtain 29 secure associations, 11 in Dunlop et al. (2017) and 18 in Yun et al. (2012) and Targett et al. (2013) catalogs.

Due to the selection criteria (requiring more than 3 detections in the optical and NIR domains), these 29 objects are faint, but not completely obscured, in the UV/optical rest-frame band and bright in the IR rest-frame domain[2]. In the FIR rest-frame they are detected with the following flux limits (including confusion noise): $S_{5\sigma} = 1.2$ mJy/beam at $\lambda = 0.87\,\mu$m (LABOCA); $S_{5\sigma} = 0.48 - 0.73$ mJy/beam at $\lambda = 1.1$ mm (AzTEC); $S_{\rm rms} = 35\,\mu$Jy at $\lambda = 1.3$ mm (ALMA).

To fulfill the selection criterion on source redshift, I exploited:

- the ESO compilation of GOODS/CDF-S spectroscopy[3];
- the millimeter spectroscopy by Tacconi et al. (2018);
- the (sub-)millimeter catalogs by Dunlop et al. (2017), Yun et al. (2012) and Targett et al. (2013), and references therein.

Between the aforementioned 29 sources, I selected only the ones with spectroscopic redshift in the range $1.5 < z_{\rm spec} < 3$. In particular, I chose all the sources having a measurement of their redshift from optical and/or millimeter spectral lines with a precision on the third decimal place (at least). As a result, I ended up with 11 objects, that are listed in Tab. 3.1: the first 7 have an ALMA (sub-)millimeter counterpart, the last 4 an AzTEC-LABOCA.

To complete the multi-band information, I searched for galaxy X-ray counterparts in the $\simeq 7$ Ms *Chandra* Deep Field South Catalog by Luo et al. (2017)[4]. I performed a sky match using a search radius of 1.5 arcsec: 9 sources out of 11 have a robust association (separation $\lesssim 0.7$ arcsec). No association wass found for the remaining 2 sources (UDF5 and AzTE.GS22), neither in the main or in the ancillary low significance catalogs.

In the radio regime, the 7 millimeter sources by Dunlop et al. (2017) have been followed up at 6 GHz (VLA) by Rujopakarn et al. (2016) and 6 of them are detected (UDF1, UDF3, UDF5, UDF8, UDF11, UDF13). Yun et al. (2012), Targett et al. (2013) and Thomson et al. (2014) identified their AzTEC-LABOCA sources in the 1.4 GHz VLA deep map of GOODS-S field by Miller et al. (2013). From this association all the 4 AzTEC-LABOCA sources in the sample (ALESS067.1, AzTEC.GS25, AzTEC.GS21, AzTEC.GS22) have a robust radio counterpart. Moreover, ALESS067.1 has an additional detection at 610 MHz by the GMRT (Thomson et al., 2014). As to UDF10, the (sub-)millimeter source without a secure radio detection (i.e., radio flux $< 3\sigma$), I took into consideration just the upper limit that is reported in the aforementioned

[2]The UV/optical rest-frame band is sampled by ACS/HST and WFC3/HST, with a magnitude limit $m_{AB,\,lim} = 25 - 26$ mag; see Windhorst and Cohen (2010); the IR rest-frame is sampled by SPIRE on *Herschel*, with a 5σ confusion limited fluxes of $\sim 24.0, 27.5, 30.5$ mJy at $\lambda = 250, 350, 500\,\mu$m respectively; see Nguyen et al. (2010) and Oliver et al. (2012).

[3]*Spectroscopy Master Catalog*, publicly available at the web page https://www.eso.org/sci/activities/garching/projects/goods.html (updated to 2012).

[4]Luo et al. (2017) mapped the CDF-S (~ 500 arcmin^2, centered in the GOODS-S field) in the 0.5-7 keV band with an on-axis exposure time of $\simeq 7$ Ms, reaching a sensitivity of $\simeq 1.9 \times 10^{-17}$ erg s^{-1} cm^{-2}. Images in the sub-bands at 0.5-2 keV and 2-7 keV have been then produced and they reach a sensitivity of $\simeq 6.4 \times 10^{-18}$ erg s^{-1} cm^{-2} and $\simeq 2.7 \times 10^{-17}$ erg s^{-1} cm^{-2}, respectively.

ID*	ID**	z_{spec}	RA_{ALMA} [h:m:s]	DEC_{ALMA} [°:':'']	RA_{HST} [h:m:s]	DEC_{HST} [°:':'']	RA_{mm} [h:m:s]	DEC_{mm} [°:':'']
J033244.01-274635.2$^{\star,\circ,\bullet,\heartsuit}$	UDF1	$2.698 \pm 0.002^{(e,a)}$	03:32:44.04	-27:46:36.01	03:32:44.04	-27:46:36.01	–	–
J033238.53-274634.6$^{\star,\circ,\bullet,\heartsuit}$	UDF3	$2.543 \pm 0.005^{(e)}$	03:32:38.55	-27:46:34.57	03:32:38.55	-27:46:34.57	–	–
J033236.94-274726.8*	UDF5	$1.759 \pm 0.008^{(b)}$	03:32:36.96	-27:47:27.13	03:32:36.97	-27:47:27.28	–	–
J033239.74-274611.4*	UDF8	$1.549 \pm 0.005^{(e)}$	03:32:39.74	-27:46:11.64	03:32:39.73	-27:46:11.24	–	–
J033240.73-274749.4*	UDF10	$2.086 \pm 0.006^{(b)}$	03:32:40.75	-27:47:49.09	03:32:40.73	-27:47:49.27	–	–
J033240.06-274755.5*	UDF11	$1.9962 \pm 0.0014^{(c,d)}$	03:32:40.07	-27:47:55.82	03:32:40.06	-27:47:55.28	–	–
J033235.07-274647.6*	UDF13	$2.497 \pm 0.008^{(b)}$	03:32:35.09	-27:46:47.78	03:32:35.08	-27:46:47.57	–	–
J033243.19-275514.3$^{\triangle,\heartsuit}$	ALESS067.1	$2.1212^{+0.0014}_{-0.0005}{}^{(e,j)}$	03:32:43.20	-27:55:14.16	03:32:43.3	-27:55:17	03:32:43.18	-27:55:14.49
J033246.83-275120.9$^{\spadesuit,\circ}$	AzTEC.GS25	$2.292 \pm 0.001^{(g)}$	03:32:46.83	-27:51:20.97	03:32:46.96	-27:51:22.4	03:32:46.84	-27:51:21.23
J033247.59-274452.3$^{\diamond,\circ,\heartsuit}$	AzTEC.GS21	$1.910 \pm 0.001^{(h)}$	03:32:47.59	-27:44:52.43	03:32:47.60	-27:44:49.3	03:32:47.59	-27:44:52.32
J033212.55-274306.1$^{\heartsuit}$	AzTEC.GS22	$1.794 \pm 0.005^{(i)}$	03:32:12.52	-27:43:06.00	03:32:12.60	-27:42:57.9	03:32:12.56	-27:43:05.37

TABLE 3.1: Identification codes (IDs), spectroscopic redshifts (z_{spec}) and multi-band coordinates of the 11 DSFGs. IDs in the first two columns refer to: *) GOODS (IAU); **) (sub-)millimeter surveys (Yun et al., 2012; Hodge et al., 2013; Targett et al., 2013; Dunlop et al., 2017). Spectroscopic redshifts and ALMA, HST and LABOCA-AzTEC (labelled as mm) sky positions are listed in the central columns. References for ALMA counterparts: △) Hodge et al. (2013); ♠) Fujimoto et al. (2017); ⋆) Dunlop et al. (2017); ◇) Hatsukade et al. (2018); ○) Cowie et al. (2018); ●) Franco et al. (2018); ♡) Pantoni et al. (2021a). References for spectroscopic redshifts (uncertainty at least on the third decimal digit): *a*) Szokoly et al. (2004) found $z_{H_\alpha} = 2.688 \pm 0.005$, consistent with Pantoni et al. (2021a) measurement within 2σ; *b*) Momcheva et al. (2016); *c*) Kurk et al. (2013); *d*) Dunlop et al. (2017); *e*) Pantoni et al. (2021b); *f*) Straughn et al. (2009); *g*) Popesso et al. (2009); *h*) Vanzella et al. (2008); *i*) Targett et al. (2013) and reference therein; *j*) Kriek et al. (2006) and Kriek et al. (2007) found $z_{H_\alpha} = 2.122 \pm 0.053$, consistent with Pantoni et al. (2021a) measurement within the uncertainties.

reference articles. Since all the 11 objects have at least one detection/upper limit in the radio band and/or in the X-rays, I considered the latter selection criterion to be fulfilled.

For completeness, I searched for other ALMA counterparts in the recent catalogs by Hodge et al. (2013) at $\lambda = 870\,\mu$m (ALMA B7); Fujimoto et al. (2017), the so-called DANCING ALMA catalog at $\lambda_{B7}/\lambda_{B6} = 0.8 - 1.1/1.1 - 1.4$ mm; Hatsukade et al. (2018) at $\lambda_{B6} = 1.1 - 1.4$ mm; Franco et al. (2018) in the ALMA B6 and centered at $\lambda = 1.13$ mm; and Cowie et al. (2018) in the ALMA B7, centered at $\lambda = 850\,\mu$m. Three objects selected from LABOCA and AzTEC surveys show robust associations within 1 arcsec (ALESS067.1, AzTEC.GS25, AzTEC.GS21), as well as two objects selected from the ALMA survey by Dunlop et al. (2017), i.e. UDF1 and UDF3. Due to blending, I discarded the AzTEC photometry of the source AzTEC.GS21, since it corresponds to two ALMA detections (similar separation, within the searching radius), and I considered only the ALMA counterpart associated to the IRAC source (i.e., ASAGAO.ID6; see Hatsukade et al., 2018, their Sect. 3.4).

Finally, I complemented the (sub-)millimeter continuum with public ALMA data from the ALMA Science Archive[5] that have the best spatial resolution ($\Delta\theta \lesssim 1 - 2$ arcsec) in the wavelength range $\lambda_{obs} \sim 500\,\mu$m $- 3$ mm (corresponding to the frequency range $\nu_{obs} \sim 100 - 600$ GHz). Indeed, the size and the spatial distribution of dust thermal emission are essential to locate and characterize galaxy dust-obscured star formation, as I will widely explain in Chapter 4. In addition, I searched for public CO line detections in the ALMA Archive, finding five $J > 1$ CO lines for 4 objects of the sample (UDF1, UDF3, UDF8, ALESS067.1) CO spectral line analysis is very important for the study of high-z DSFGs. Indeed, CO(1-0) traces the molecular gas phase inside galaxy and allow to derive its mass, to measure its density and spatial distribution, and to study its kinematics (e.g. Yang et al., 2017; Joblin et al., 2018; Boogaard et al., 2020). In addition, CO lines can be exploited to characterize both the activity of the nucleus and the host galaxy star formation. For a deeper analysis and further details and discussion on the topic I refer to Chapter 4.

In Tabs. 3.2 and 3.3 I provide a schematic summary of the multi-wavelength data for the 11 DSFGs that are currently publicly available.

The final sample

In Sect. 3.1.3 I built a multi-wavelength sample composed by 11 (sub-)millimeter selected DSFGs, with a robust spectroscopic measurement of their redshift (in the range where the Cosmic SFH reaches its maximum, i.e. $z \sim 2$) and an almost complete sampling of their SED, from the X-rays to the radio band. Here I sum up the main characteristics of the sample, such as galaxy sky positions, the multi-band data at disposal and the redshift distribution, and I briefly explain why they match the scopes of this thesis.

In Fig. 3.1 (upper panel) I show the galaxy positions on the sky (magenta filled circles), highlighting the multi-band coverage of the well studied GOODS-S field.

In Fig. 3.1 (lower panel), I show the redshift distribution of the sample, peaking at $z \sim 2$, with a median redshift $z = 2.1$ (first quartile 1.8, third quartile 2.5).

In order to render at a glance the amount of multi-wavelength data that is available for the 11 DSFGs, in Fig. 3.2 I show a histogram that displays how data are distributed in the diverse spectral bands. In particular the histogram shows the number of sources in the sample (y-axis) that are detected in each photometric filter (x-axis), listed also in Tabs. 3.2 and 3.3. Data from optical to millimeter will be

[5] https://almascience.eso.org/asax/

ID	B[a]	V[a]	i[a]	z[a]	J[b]	H[b]	Ks[b]	IR_{36}[c]	IR_{45}[c]	IR_{58}[c]	IR_{80}[c]	IRS_{16}[c]	F_{24}[c]	F_{70}[d]	F_{100}[d]	F_{160}[d]
UDF1	✓	✓	✓	✓	✓	✓	✓	✓	✓	✓	✓	nd	✓	nd	✓	✓
UDF3	✓	✓	✓	✓	✓	✓	✓	✓	✓	✓	✓	✓	✓	nd	✓	✓
UDF5	✓	✓	✓	✓	✓	✓	✓	✓	✓	✓	✓	✓	✓	nd	✓	✓
UDF8	nd	✓	✓	✓	✓	✓	✓	✓	✓	✓	✓	✓	✓	nd	✓	✓
UDF10	✓	✓	✓	✓	✓	✓	✓	✓	✓	✓	✓	nd	nd	nd	✓	✓
UDF11	✓	✓	✓	✓	✓	✓	✓	✓	✓	✓	✓	✓	✓	nd	✓	✓
UDF13	✓	✓	✓	✓	✓	✓	✓	✓	✓	✓	✓	nd	✓	nd	✓	nd
ALESS067.1	✓	✓	✓	✓	✓	✓	✓	✓	✓	✓	✓	nd	✓	nd	✓	✓
AzTEC.GS25	✓	✓	✓	✓	✓	nd	✓	✓	✓	✓	✓	nd	✓	nd	✓	✓
AzTEC.GS21	✓	✓	✓	✓	✓	nd	✓	✓	✓	✓	✓	✓	✓	✓	✓	✓
AzTEC.GS22	nd	✓	✓	✓	✓	✓	✓	✓	✓	✓	✓	nd	✓	nd	nd	✓

TABLE 3.2: Up-to-date publicly available optical, NIR and MIR photometry for the 11 DSFGs. Optical and NIR photometry from MUSIC catalog (Grazian et al., 2006): *a*) ACS-HST, λ_c = 0.433, 0.594, 0.771, 0.886 μm ; *b*) ISAAC-VLT, λ_c = 1.255, 1.656, 2.163 μm ; *c*) Spitzer, λ_c = 3.6, 4.5, 5.8, 8, 16, 24 μm. MIR photometry from Magnelli et al. (2011) and Magnelli et al. (2013), as result from the sky-match between GOODS-MUSIC catalog and MIPS-Herschel photometry: *d*) PACS-Herschel, λ_c = 70, 100, 160 μm. Checkmark stands for *detection*; nd stands for *non-detection / upper-limits*.

ID	F_{250} [a]	F_{350} [a]	B9 [c]	F_{500} [a]	F_{870} [b]	B7 [c]	F_{1100} [d]	B6 [c]	B4 [c]	B3 [c]	C [e]	L [e]	F_{610} [f]	X [g]	J(CO)
UDF1	✓	✓		✓		✓		✓			✓			✓	3
UDF3	nd	nd		nd		✓		✓			✓			✓	3
UDF5	✓	✓		nd				✓			✓			nd	
UDF8	✓	✓		nd				✓			✓			✓	2
UDF10	nd	nd		nd				✓			nd			✓	
UDF11	✓	✓		nd				✓			✓			✓	
UDF13	nd	✓		nd		✓		✓			✓			✓	
ALESS067.1	✓	✓		✓	✓	✓	nd		✓	✓		✓	✓	✓	3, 6
AzTEC.GS25	✓	✓		✓		✓	✓					✓		✓	
AzTEC.GS21	✓	✓	✓	nd		✓	(✓)	✓				✓		✓	
AzTEC.GS22	✓	✓	✓	nd			✓					✓		nd	

TABLE 3.3: Up-to-date available FIR, (sub-)millimeter, radio and X-ray photometry and CO lines detections for the 11 DSFGs. FIR photometry from Magnelli et al. (2011) and Magnelli et al. (2013), as result from the sky-match between GOODS-MUSIC catalog and MIPS-Herschel photometry: *a*) SPIRE-Herschel, $\lambda_c = 250,\ 350,\ 500\ \mu m$. (sub-)millimeter and radio photometry from Miller et al. (2013), Yun et al. (2012), Hodge et al. (2013), Targett et al. (2013), Thomson et al. (2014), Dunlop et al. (2017), Rujopakarn et al. (2016), Fujimoto et al. (2017), Hatsukade et al. (2018), Franco et al. (2018), Cowie et al. (2018), ALMA Archive, resulting from the cross-match with GOODS-MUSIC catalog: *b*) LABOCA/APEX, $\lambda_c = 870\ \mu m$; *c*) ALMA, $\lambda_c = 0.450,\ 0.870 - 1,\ 1.3,\ 2,\ 3$ mm; *d*) AzTEC/ASTE, $\lambda_c = 1100\ \mu m$; *e*) JVLA, $\nu_C = 6$ GHz, $\nu_L = 1.49$; *f*) GMRT, $\nu = 610$ MHz. X-ray data resulting from the catalog by Luo et al. (2017): *g*) Chandra ACIS, $0.5 - 7.0$ keV. CO spectral lines are from ALMA Archive. Checkmark stands for *detection*; nd stands for *non-detection/upper-limits*; void means the source has not been observed with the corresponding device. Brackets mean that the source is detected but the data has not be taken in consideration.

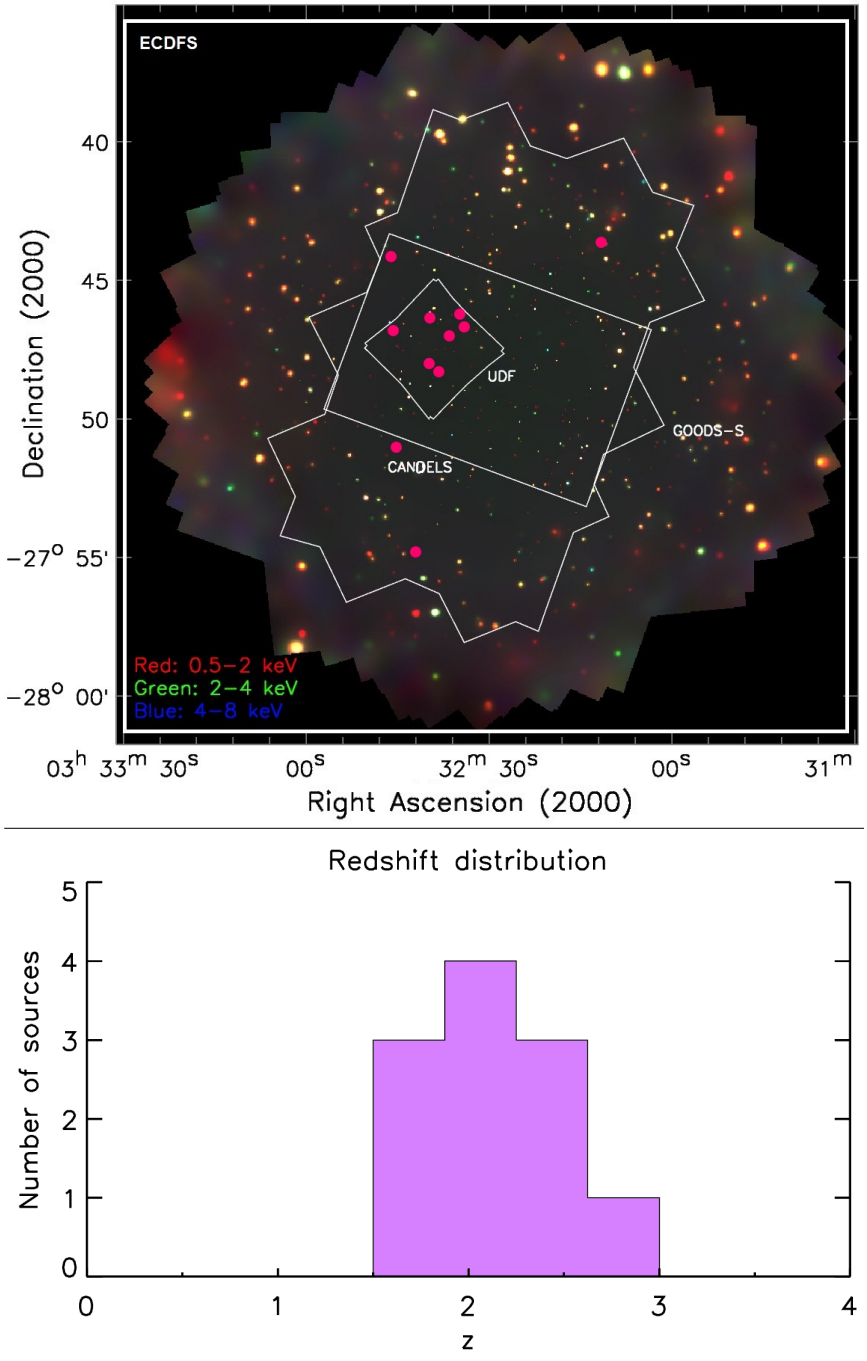

FIGURE 3.1: The upper panel shows the sky positions of the 11 (sub-)millimeter selected DSFGs at the peak of Cosmic SFH in the GOODS-S. The galaxy position is indicated by a magenta filled circle. White solid lines delimit the multi-band survey sky areas overlapping the GOODS-S field, i.e. ECDF-S, CANDELS and HUDF. The *Chandra* map in the background is taken from http://www2.astro.psu.edu/users/niel/cdfs. The lower panel shows the redshift distribution of the sample, peaked at $z \sim 2$.

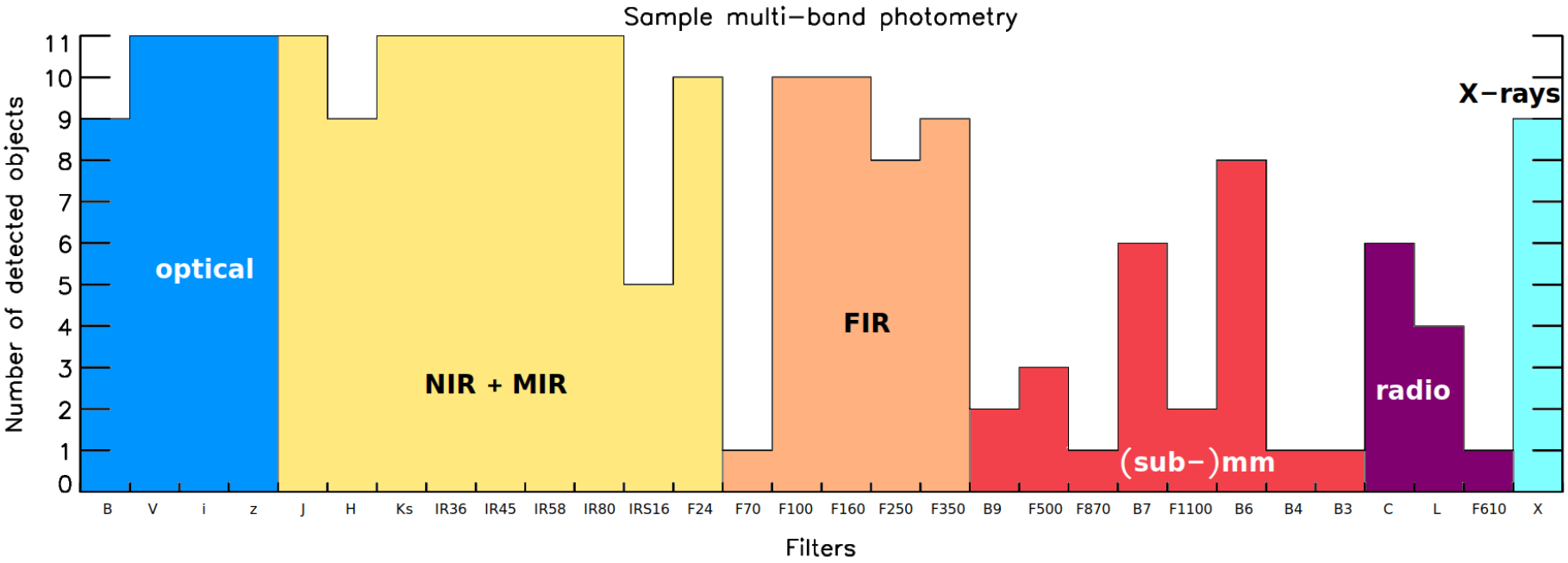

FIGURE 3.2: Histogram showing the multi-band sampling of the 11 DSFGs. On the x-axis I report the photometric filters used in this work, already listed in Tabs. 3.2 and 3.3. On the y-axis I report the number of objects in the sample that are detected by each photometric filter. The diverse spectral bands are highlighted with different colors: optical in light blue; NIR and MIR in yellow; FIR in orange; (sub-)millimeter in red; radio in violet; X rays in cyan.

exploited to fit galaxy SEDs, while radio photometry and X-rays data will be used to deepen the analysis on galaxy-BH co-evolution (see Sects. 3.2.2 and 3.2.1).

Summarizing, I selected solely the (sub-)millimeter sources that are spectroscopically confirmed to be at the peak of Cosmic SFH, requiring an almost complete sampling of galaxy SED, from the X-rays to the radio regime, with particular care on the FIR peak and the optical/NIR emission by stars, that are essential to constrain interstellar dust attenuation, galaxy age and SFR. The photometry was complemented with CO spectral lines, that are important to characterize galaxy ISM, in particular its molecular phase. When combined together, these requirements allow to get an insight into both the main processes triggering DSFG star formation and leading their subsequent evolution, and galaxy co-evolution with central SMBH.

The requested multi-band data and the condition on the availability of spectroscopic redshift did not allow to include in the final sample objects that are totally obscured in the UV/optical rest-frame, and seriously limit the sample size and completeness. Even if none statistical indications on the whole DSFG population at $z \sim 2$ can be traced, this panchromatic approach allow to extract essential information on the individual galaxy, as I will describe in the following analysis and in Chapter 4.

Finally, I would stress that the analysis presented in this thesis may be easily extended to other multi-band fields (e.g., COSMOS and H-ATLAS; see e.g. Neri et al., 2020) and exploited for studying future big samples of spectroscopically confirmed DSFGs with multi-band follow up (see e.g. the ongoing z-GAL NOEMA Large Program[6]; PIs: P. Cox; T. Bakx; H.Dannerbauer).

3.2 Spectral Energy Distribution fitting and multi-band analysis

Modelling the SED of galaxies is an extremely complex task to deal with, since different objects with very diverse properties can show much similar SEDs. This is a direct consequence of the degeneracies that may arise because redshift, stellar age, dust extinction and metallicity have similar effects on the observed galaxy SED, especially in the UV-NIR rest-frame wavelength range (see e.g., Worthey, 1999; Noll et al., 2009; Leja et al., 2017; Battisti et al., 2019). This is true, in particular, when just a restricted wavelength range of galaxy emission is considered (rather than the full SED) and/or the source redshift is unknown.

Another relevant issue consists in the building of physically motivated models that allow an accurate derivation of the integral properties of galaxies, whose efficacy is usually strictly related to galaxy type. In the case of high-z DSFGs probably the most intricate problem is the accurate modelling of the FIR thermal emission from interstellar dust grains, along with the attenuated UV/optical stellar light and the eventual MIR emission coming from AGN torus.

Since the discovery of the high-z dusty star-forming galaxy population, many techniques have been developed in order to model dust extinction and the way in which it affects galaxy multi-wavelength emission.

On the one hand, detailed radiative transfer models (e.g., Silva et al., 1998; Dopita et al., 2005; Siebenmorgen and Krügel, 2007) and empirical template libraries (e.g., Dale et al., 2001; Dale and Helou, 2002; Chary and Elbaz, 2001; Draine and Li, 2007; Rieke et al., 2009) have been used to model the complex emission from stars,

[6]http://www.iram.fr/ z-gal/Home.htm

molecular clouds and dust grains over a wide range of galaxy morphology and luminosity. However, testing the accuracy and/or applicability of these approaches with observations is very hard, since we do not dispose of sufficiently detailed data to disentangle the effects of, e.g., dust geometry, spatial distribution and optical depth.

On the other hand, very simple methods were developed in order to fit directly the FIR thermal emission of interstellar dust (e.g., Dunne and Eales, 2001; Casey, 2012; Gilli et al., 2014), using a Modified Black Body (MBB) fitting function or a composite power-law or a combination of the two, that can be easily tested with observations. Although these models succeed in reproducing with great accuracy the FIR spectrum of dusty galaxy (especially in the Rayleigh-Jeans regime), they have some difficulties in modelling the quite common MIR excess (i.e. above the Wien tail), that can be traced back to the radiation coming from the warmer dust surrounding galaxy nucleus or located in very compact and dense star-forming regions. In addition, these models are not useful to reproduce the whole galaxy SED and, as such, they can not be exploited to derive some fundamental galaxy properties, like e.g. the stellar mass.

An alternative approach is represented by techniques based on the *energy balance principle*, that constrain the UV-FIR galaxy SED by physically preserving an energy balance between the stellar light emitted in the UV/optical and re-radiated in the IR by dust. These methods rely on numerous modules that account for a wide range of SFHs, adjustable stellar synthesis template libraries, attenuation curves, AGN and interstellar dust emission models, and can reproduce the whole multi-band emission of galaxy, from the UV to the radio band (e.g., da Cunha, Charlot, and Elbaz, 2008; Boquien et al., 2019). These methods are however affected by degeneracies between the modules free parameters, especially when the galaxy SED is scarcely sampled. In addition they require to define *a priori* the range of values in which each free parameter should vary.

In this Section I describe the method that I used to fit the SED of the 11 DSFGs at $z \sim 2$ (whose selection was extensively described in Sect. 3.1.3) and I give the main motivations of my choices. Finally, I present the results and, basing on them, I give a first characterization of the sample.

3.2.1 SED fitting with CIGALE

In order to model the whole SED of the 11 DSFGs in the final sample (see Sect. 3.1.3), I used CIGALE (Boquien et al., 2019), a Python code that can reproduce galaxy broad-band emission by physically preserving an energy balance between stellar UV/optical light and dust thermal emission in the FIR. This basic goal is achieved by fitting a large grid of models to the data.

In a nutshell, CIGALE builds composite stellar populations by combining diverse Single Stellar Populations (SSP) with flexible SFHs, calculates the emission of the gas ionized by young stars and exploits flexible attenuation curves to attenuate both the stellar and the ionized gas emission. The galaxy FIR emission is estimated by balancing the energy absorbed in the optical/UV domain and the energy re-emitted at longer wavelengths by dust. The main physical properties, such as SFR, attenuation, dust luminosity, stellar mass, the presence of an AGN and the measure in which it affects galaxy MIR emission, are estimated by means of both χ^2 and Bayesian analyses.

In the following, I will briefly describe the modules exploited to model galaxy SED and I will explain which are the main motivations that have driven these choices.

In Tab. 3.4 I show the complete list of modules along with the priors that I have assumed for the corresponding free parameters.

Star Formation History

One of the more influential but yet scarcely constrained components of SED fitting is the functional form of galaxy SFH. Since a large variety of SFHs can yield similar SEDs, broad-band fitting alone can not provide certain information on the past star formation phases of galaxies. This problem has traditionally led to the exploitation of quite simple SFHs, such as constant, exponential (decaying or rising), delayed or periodic (e.g., Elbaz et al., 2018); in the case of high-z DSFGs, additional bursts of star formation are often included (e.g., Ciesla, Elbaz, and Fensch, 2017; Forrest et al., 2018; Donevski et al., 2020).

In this work, I have assumed a delayed exponential SFH, basing this choice on many studies that model the SED of high-z star-forming galaxies, suggesting a slow power-law increase of galaxy SFR over a timescale $\tau_\star$ (i.e., burst duration), followed by a rapid exponential decline (e.g., Papovich et al., 2011; Smit et al., 2012; Moustakas et al., 2013; Steinhardt et al., 2014; Cassarà et al., 2016; Citro et al., 2016). In particular, for $\tau \lesssim \tau_\star$, I have adopted the functional form used by Mancuso et al. (2016a):

$$\mathrm{SFR}(\tau) \propto \left(\frac{\tau}{\tau_\star}\right)^{0.5}, \qquad \text{for} \quad \tau \lesssim \tau_\star \tag{3.1}$$

(see their Eq. 3 and Fig. 3, top panel, dashed line) and simplified the evolution for $\tau > \tau_\star$ by assuming that star formation stops at $\tau \sim \tau_\star$, quenched by AGN feedback.

Even if still largely discussed (see Chapter 1, Sect. 1.1), the latter assumption is validated by the large observed fraction of FIR-detected host galaxies in the X-rays (e.g., Mullaney et al., 2012; Page et al., 2012; Rosario et al., 2012) and in optically-selected AGNs (e.g., Mor et al., 2012; Wang et al., 2013; Willott, Bergeron, and Omont, 2015), along with the numerous powerful AGN-driven outflows observed in high-z star-forming galaxies and local analogues (see e.g., Cicone et al., 2014; King and Pounds, 2015; Fiore et al., 2017; Bischetti et al., 2019; Herrera-Camus et al., 2019; Bischetti et al., 2021).

As such, the adopted SFH has just one free parameter, i.e. the main star-forming burst duration ($\tau_\star$), assumed to vary in the range $[0.15 - 2]$ Gyr (see Tab. 3.4). I note that this range of burst duration is suggested by recent observations with ALMA, characterising the dust-enshrouded star formation of massive high-redshift galaxies (e.g., Scoville et al., 2014; Scoville et al., 2016), and by the α-enhancement (i.e. iron under-abundance compared to α-elements) observed in the stellar populations of local ellipticals and massive quiescents (see e.g., Thomas et al., 2005; Thomas et al., 2010; Renzini, 2006, for a review). Basing on these evidences, even if one assumes an alternative quenching mechanisms to AGN feedback (such as starvation and gravitational heating; see e.g. Cattaneo et al., 2009), galaxy star formation must stop on similar timescales. This further validate the assumed range of possible values for $\tau_\star$, whatever it is the favoured quenching scenario.

Stellar emission

The stellar light has been modelled following the prescriptions in Bruzual and Charlot (2003). Galaxy stellar population has been divided into two SSPs: the first is constituted by young stars, which are supposed to be completely enshrouded into

CIGALE module	Shape	Free parameters	Symbol	Priors
Star Formation History	Constant[a]	Age [Gyr]	$\tau_\star$	2, 1.5, 1.0, 0.8, 0.7, 0.6, 0.5, 0.4, 0.3, 0.2, 0.15
Single Stellar Population	Two SSPs[b]	Initial mass function	IMF	Chabrier (fixed)
		Metallicity	Z	0.02 (fixed)
		Separation age [Myr]	$\Delta_\star$	10, 20, 30, 50, 100, 150, 200
Dust Attenuation	Double power-law[c]	V-band attenuation in BCs	A_V^{BC}	10000 (fixed)
		Power-law slope in BCs	δ_{BC}	-1.6, -1.8, -2.0, -2.2, -2.4, -2.6
		A_V^{ISM}/A_V^{BC}	f_{att}	0.0001, 0.0002, 0.0003
		Power-law slope in ISM	δ_{ISM}	-0.7, -0.5, -0.3, -0.1
Dust Emission	Power-law + Single-T Modified BB[d]	MIR power-law slope	α_{dust}	1.6, 1.8, 2.0, 2.2
		Dust emissivity index	β_{dust}	1.6, 1.8, 2.0, 2.2, 2.4, 2.6
		Dust temperature [K]	T_{dust}	20, 30, 40, 50, 60, 70

TABLE 3.4: Input parameters configuration used to fit the broad-band emission of the 11 DSFGs with CIGALE. Columns show (in order): the choosed CIGALE modules in input (**CIGALE module**); the assumed functional shape for the modelled quantity (when required; **Shape**); the list of module free parameters (units in square brackets; **Free parameters**); the free parameter symbol (**Symbol**); the priors for the corresponding parameter (**Priors**). References for the adopted shapes are: *a*) Mancuso et al. (2016a); *b*) Bruzual and Charlot (2003) ; *c*) Lo Faro et al. (2017) ; *d*) Casey (2012).

their molecular Birth Clouds (BCs); the second is composed by old stars, that live in the ISM and have already dissolved their BCs. The separation age between these two SSPs has been set to be a free parameter. I have fixed its priors to the typical values found to be valid for star-forming progenitors of massive ellipticals (e.g., Schurer et al., 2009) (listed in Tab. 3.4). Finally, I have assumed a Chabrier (2003) IMF ($M_\star = 0.1 - 100\,M_\odot$) and set the stellar metallicity to the solar one, i.e. $Z = 0.02$.

Stellar light attenuation by dust

I have modelled the interstellar dust attenuation in the UV/optical rest-frame with a double power-law, reproducing the different contributions from young star BCs and the ISM (Lo Faro et al., 2017):

$$\tau_\lambda^{\rm BC} = (1-\mu)\tau_V(\lambda/5500\text{Å})^{\delta_{\rm BC}} \simeq A_{\rm V}^{\rm BC}(\lambda/5500\text{Å})^{\delta_{\rm BC}}\,; \tag{3.2}$$

$$\tau_\lambda^{\rm ISM} = \mu\tau_V(\lambda/5500\text{Å})^{\delta_{\rm ISM}} \simeq A_{\rm V}^{\rm ISM}(\lambda/5500\text{Å})^{\delta_{\rm ISM}}\,. \tag{3.3}$$

Eqs. (3.2) and (3.3) describe how the opacity varies in terms of λ in the stellar BC and ISM respectively; the two laws are then expressed in terms of the attenuation in the V-band, i.e. $A_{\rm V}^{\rm BC}$ and $A_{\rm V}^{\rm ISM}$ respectively. In both Eqs. (3.2) and (3.3), τ_V is the total opacity in the V-band (i.e. determined by both the BCs and the diffuse ISM); μ is the fraction of the total effective optical depth contributed by the diffuse ISM, while $(1-\mu)$ is the fractional contribution due to BC only.

In the case of high-z DSFGs, the light coming from young stars is expected to be completely absorbed by the dust populating the surrounding dense molecular BC. For this reason I have fixed the BC attenuation in the V-band to the value $A_{\rm V}^{\rm BC} = 10^4$. The energy balance provided by CIGALE ensures that the radiation absorbed by dust is re-emitted in the FIR (i.e., dust thermal emission). To be self-consistent, I have fixed the slope $\delta_{\rm BC}$ to the dust FIR spectral index ($\beta_{\rm dust}$) best value, as it is obtained by the fitting procedure. After $t_0 \sim 10^7$ yr from their birth, old stars have already dissipated/escaped their BC, and the light they emit is expected to be attenuated just by the dust populating galaxy ISM. Following the prescriptions in Lo Faro et al. (2017), the ISM attenuation slope $\delta_{\rm ISM}$ can span the range: [-0.7, -0.5, -0.3, -0.1] (see Tab. 3.4).

Dust emission

The dust emission has been modelled by decomposing the IR light into two different components, as suggested by Casey (2012), that are:

- a power-law, describing the MIR emission coming from PAHs and central AGN;
- a single-temperature modified-BB, modelling the FIR thermal emission of cold interstellar dust grains.

This simple approach is very convenient for modelling the dust emission of the 11 DSFGs, since their MIR SED is scarcely sampled (each source has just one or two photometric data points in this spectral range). I have exploited the following fitting function by Casey (2012, Eq. 3), since it ensures a more accurate fit to those systems with fewer MIR photometric data:

$$F(\lambda) = N_{\rm BB}\,\frac{\left(1-e^{-(\lambda_0/\lambda)^{\beta_{\rm dust}}}\right)\left(\frac{c}{\lambda}\right)}{e^{hc/\lambda kT_{\rm dust}}-1} + N_{\rm pl}\,\lambda^{\alpha_{\rm dust}}\,e^{-(\lambda/\lambda_c)^2}\,; \tag{3.4}$$

where $F(\lambda)$ is in units of Jy; $T_{\rm dust}$ is the galaxy characteristic *cold* dust temperature, i.e. the dust temperature dominating most of the IR luminosity and dust mass; λ_0 is the wavelength at which the optical depth is equal to unity, that is fixed at $\lambda_0 = 200\,\mu$m (see also e.g. Conley et al., 2011); $\beta_{\rm dust}$ is the dust emissivity index; $\alpha_{\rm dust}$ is the MIR power-law slope; and λ_c is the wavelength where the MIR power-law turns over and no longer dominates the emission. The latter is parametrized as follows:

$$\lambda_c = \frac{3}{4}\left[(26.68 + 6.246\,\alpha_{\rm dust})^{-2} + (1.905\times10^{-4} + 7.243\times10^{-5}\alpha_{\rm dust})\,T\right]^{-1}. \quad (3.5)$$

In Eq. 3.4, the power-law coefficient ($N_{\rm pl}$) is tied to the normalization of the modified-BB ($N_{\rm BB}$), as it is explained in Casey (2012). This leaves with just three free parameters, that are: the MIR power-law slope, $\alpha_{\rm dust}$; the dust emissivity index, $\beta_{\rm dust}$; the dust temperature, $T_{\rm dust}$.

The spectral index $\alpha_{\rm dust}$ has been set to vary in the range [1.6, 1.8, 2.0, 2.2], following the results obtained by Mullaney et al. (2011). The value of $\beta_{\rm dust}$ is usually assumed to be 1.5 and historically ranges between $1-2$ (see e.g., Hildebrand, 1983). Some recent works suggest a wider range for $\beta_{\rm dust}$, between 1 and 2.5 (e.g. Casey et al., 2011; Chapin et al., 2011; Gilli et al., 2014; Bianchi, 2013; Bianchini et al., 2019; Pozzi et al., 2020), favouring the higher values in the range (i.e. $\beta_{\rm dust} > 1.5$). For this reason, the dust spectral index $\beta_{\rm dust}$ is set to freely vary in the range $[1.6-2.6]$. The dust temperature $T_{\rm dust}$ can vary between $[20-70]$ K, which almost corresponds to the normal range of dust temperatures expected for ISM heated solely by star formation (see Tab. 3.4). A more realistic approach consists in including more than one family of cold dust grains, with different temperatures, in order to model dust thermal emission in the FIR. However, fitting the dust thermal emission with a multi-temperature modified-BB requires at least five photometric data points in the FIR regime[7], which are currently not available for the whole sample.

Furthermore, considering the absence of any spectral information in the MIR band, I have fairly avoided the exploitation of more sophisticated models that include PAH and silicate lines, such as Draine and Li (2007).

CIGALE provides also the opportunity to model the AGN MIR emission alone. However, the most quoted AGN models (e.g., Fritz, Franceschini, and Hatziminaoglou, 2006; Nenkova et al., 2008; Feltre et al., 2012) are extremely complex and characterized by a number of free parameters that would be hardly constrained by the under-sampled MIR emission of the 11 DSFGs. For this reason I have not included any AGN modules in the fitting procedure.

I stress that the latter choices do not affect significantly the resulting IR total luminosity. Indeed, the net effect of the MIR emission coming from both AGN and PAHs on the integrated IR luminosity attains less than 10-20%, meaning that the cold dust modified-BB still dominates the bulk of the total IR emission, when integrated. This fact has been recently demonstrated by the analysis of a (local) sample of IR galaxies hosting a moderate powerful X-ray AGN (i.e., $L_{2-10\,\rm keV} \sim 10^{42} - 10^{44}$ erg s^{-1}) by Mullaney et al. (2011), and it is still valid for our 11 DSFGs (as I will discuss in Sect. 3.2.2).

Finally, I note that the adopted approach to model dust emission is *luminosity-weighted*. This is strictly related to the fact that the single-temperature SED fitting procedure estimates the dust temperature from the modified-BB FIR peak, which is more sensitive to the warmest population of dust grains. As such, it tends to return

[7]Five detections are enough for a double-temperature modified-BB fit to the FIR SED, since the free parameters, in this case, are four (i.e., $T_{\rm dust,1}$, $\beta_{\rm dust,1}$ and $T_{\rm dust,2}$, $\beta_{\rm dust,2}$)

values of $T_{\rm dust}$ higher than the mean one. This tendency and how it affects the SED-derived dust mass have been widely discussed and investigated in the last decade, both in local and high-z Universe (e.g., Dale et al., 2012; Magdis et al., 2012; Berta et al., 2016; Schreiber et al., 2018; Liang et al., 2019; Martis et al., 2019). Magdis et al. (2012) quantify this effect on a statistical sample of $z \gtrsim 2$ SMGs finding that the fit with single-temperature modified-BB gives dust masses that are (on average) lower by a factor of ~ 2 when compared with Draine and Li (2007) model. I will comment on this result in Sects. 3.2.2 and 3.2.2, where I will describe the derivation of dust and gas masses of the 11 DSFGs.

3.2.2 Properties of the sample extracted from galaxy SED

In this Section I present and comment on the information extracted from galaxy SED fitting and broad-band emission in the X-rays and radio band.

In Fig. 3.3 (left column) I show the best SEDs (thick solid black lines) of the 11 DSFGs of the sample, as they are obtained by the SED fitting performed with CIGALE (Sect. 3.2.1). The contribution of each component to the total SED is color-coded and comprises: the UV/optical/NIR emission coming from young stars (i.e., enshrouded in their BC; Sect. 3.2.1); the UV/optical/NIR emission of old stars (i.e., in the galaxy ISM, outside their BC; Sect. 3.2.1); the warm dust MID power-law and the cold dust FIR modified-BB (Sect. 3.2.1). The spectroscopic redshift of each source and the reduced χ^2 (i.e., $\chi^2_{\rm red} = \chi^2/{\rm dof}$) are written on the corresponding panel. For reference, the predicted radio emission coming solely from the host galaxy star formation is also shown (solid yellow line; its derivation will be described in Sect. 3.2.2). The observed fluxes in the radio band (at $\nu_{\rm obs}$ = 6 GHz, 1.4 GHz, 610 MHz; yellow filled circles) are consistent with the yellow solid line (within the uncertainties). Radio photometry is not included in SED fitting in order to avoid any strong assumption on the radio-to-(sub)mm spectral index. The latter is well constrained when at least two fluxes in the radio band are available, but this requirement is satisfied only for one source, i.e. ALESS067.1.

The main physical quantities (e.g., SFR, $\tau_\star$, $M_{\rm star}$, $T_{\rm dust}$) are obtained both with χ^2 analysis and Bayesian analysis. The latter approach estimates galaxy physical properties from likelihood-weighted parameters on a fixed grid of models (whose set up for this work has been described in Sect. 3.2.1), exploring the parameter space around some given priors (listed in Tab. 3.4). The latter analysis provides the most precise and accurate estimations of the main SED-inferred quantities: the corresponding outcomes are listed in Tabs. 3.5 and 3.6, along with their uncertainties. I note that these quantities are well constrained only if the probability distribution function (pdf) is well behaved (e.g., single peaked). This is the case for the majority of the marginalized pdfs. The most common exceptions are found for: the BC-to-ISM V-band attenuation, $f_{\rm att}$; the BC attenuation spectral index, $\delta^{\rm BC}$; the separation age between the old and young SSPs, $\Delta_\star$. Instead, the χ^2 analysis can be exploited to have a hint on fits goodness, i.e. $\chi^2_{\rm red} \sim 1$ (cf. Tab. 3.5, second column).

Given the outcomes listed in Tabs. 3.5 and 3.6, in the following I will discuss the resulting attenuation laws for the 11 objects, derive their dust and gas masses and provide the analysis on their X-ray and radio emission.

Attenuation law

The individual galaxy attenuation law (i.e., $A_\lambda/A_{\rm V}$; thick solid black line in Fig. 3.3, right column) is calculated starting from stellar luminosities given in output by

ID	$\mathbf{z_{spec}}$	$\chi^2_{\mathbf{red}}$	**SFR** $[M_\odot\ \mathrm{yr}^{-1}]$	$\tau_\star$ [Myr]	$\mathbf{M_\star}$ $[10^{10}\ M_\odot]$	$\mathbf{\Delta_\star}$ [Myr]	$\mathbf{M_R}$ $[10^{10}\ M_\odot]$	$\mathbf{f_{att}}$ $[10^{-4}]$	$\delta^{\mathbf{BC}}$	$\delta^{\mathbf{ISM}}$
UDF1	2.698	1.15	352 ± 18	334 ± 58	8 ± 1	10.0 ± 0.5	3.3 ± 0.6	3.0 ± 0.2	-2.1 ± 0.3	-0.1 ± 0.003
UDF3	2.543	3.28	519 ± 38	234 ± 47	9 ± 1	30 ± 4	3.2 ± 0.6	3.0 ± 0.2	-2.1 ± 0.3	-0.1 ± 0.002
UDF5	1.759	1.69	85 ± 6	404 ± 85	2.4 ± 0.3	20 ± 1	1.0 ± 0.2	1.0 ± 0.05	-2.1 ± 0.3	-0.7 ± 0.003
UDF8	1.549	2.27	100 ± 5	992 ± 50	6.5 ± 0.3	160 ± 23	3.4 ± 0.2	2.0 ± 0.1	-2.4 ± 0.3	-0.7 ± 0.003
UDF10	2.086	1.02	41 ± 5	917 ± 137	2.5 ± 0.3	50 ± 9	1.2 ± 0.2	1.0 ± 0.05	-2.1 ± 0.3	-0.54 ± 0.08
UDF11	1.9962	1.76	241 ± 19	380 ± 82	6.4 ± 0.9	51 ± 9	2.6 ± 0.5	1.0 ± 0.05	-2.1 ± 0.3	-0.49 ± 0.09
UDF13	2.497	0.99	111 ± 17	879 ± 149	6.5 ± 1.4	51 ± 58	3.3 ± 0.8	1.8 ± 0.4	-2.1 ± 0.3	-0.6 ± 0.1
ALESS067.1	2.1212	1.73	487 ± 24	903 ± 100	29 ± 3	10.0 ± 0.6	15 ± 2	3.0 ± 0.2	-1.8 ± 0.3	-0.3 ± 0.003
AzTEC.GS25	2.292	1.77	401 ± 20	290 ± 88	8 ± 2	29 ± 20	3 ± 1	2.5 ± 0.5	-2.1 ± 0.3	-0.1 ± 0.008
AzTEC.GS21	1.910	1.76	360 ± 18	746 ± 105	18 ± 2	50 ± 3	9 ± 1	3.0 ± 0.5	-2.0 ± 0.3	-0.5 ± 0.004
AzTEC.GS22	1.794	1.37	91 ± 5	940 ± 74	5.7 ± 0.5	11 ± 4	2.9 ± 0.3	3.0 ± 0.5	-2.4 ± 0.3	-0.7 ± 0.01

TABLE 3.5: CIGALE outputs from stellar (star formation + emission + attenuation) Bayesian analysis for the sources of the sample (ID and spectroscopic redshift in the first two columns). Third column shows the corresponding best-fit reduced χ^2. In the order, the table lists the outcomes from: SFH module (SFR and galaxy age $\tau_\star$, i.e. the burst duration), stellar emission (stellar mass, $M_\star$; age separation between old and young stars, $\Delta_\star$; restituted gas mass to ISM from stellar evolution, M_R) and stellar attenuation (ISM-to-BC V-band attenuation, f_att; BC attenuation spectral index, δ^BC; ISM attenuation spectral index, δ^ISM). Units are indicated between square brackets.

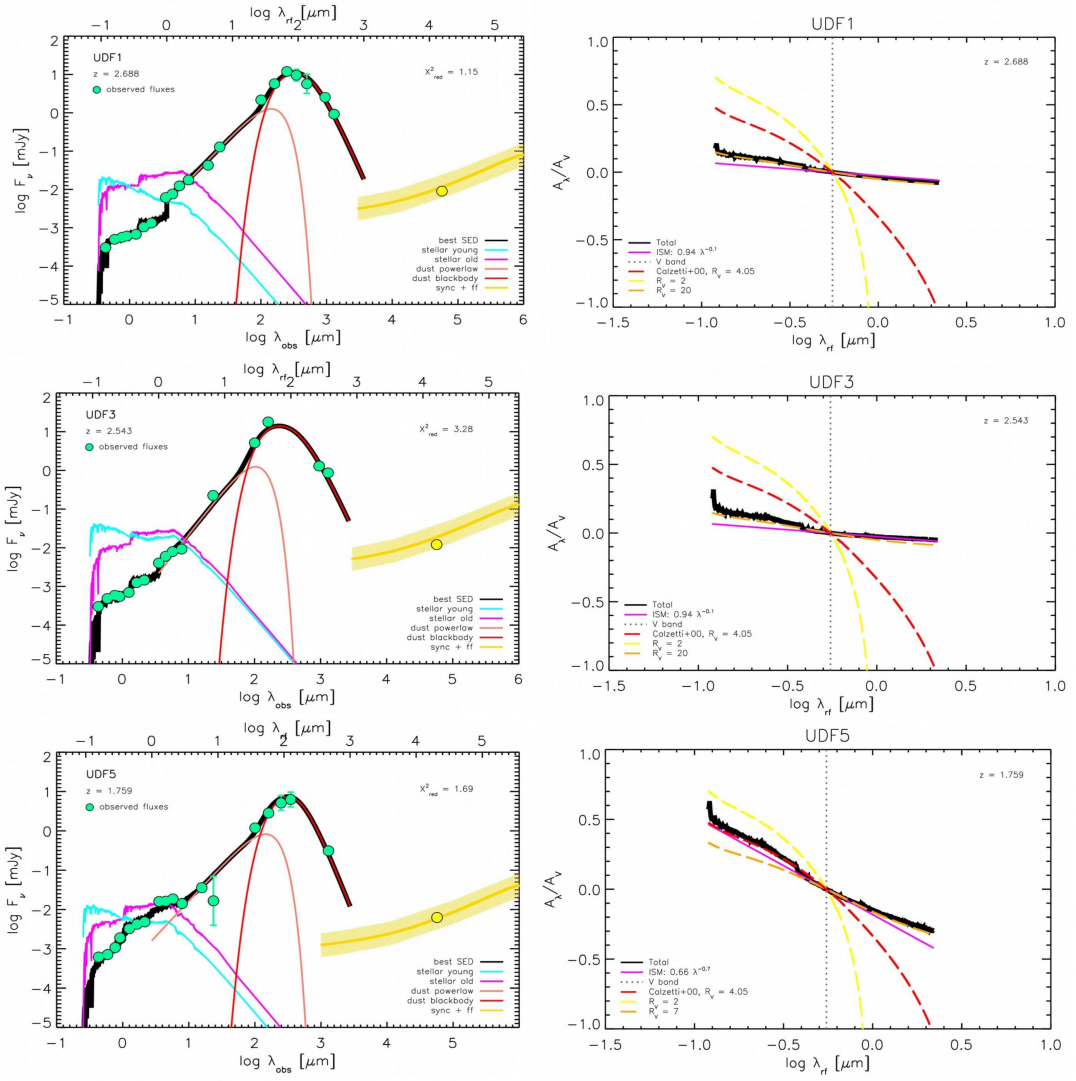

FIGURE 3.3: Galaxy best SEDs (left column) and best attenuation laws (right column). Left panels: thick solid black line stands for the total best galaxy SED; solid cyan line indicates the UV/optical/NIR emission coming from young stars; solid magenta line stands for the old stars UV/optical/NIR emission; solid orange line represents the warm dust MID power-law; solid red line shows the cold dust FIR modified BB emission; thick solid yellow line represents the radio emission coming solely from host galaxy star formation; green filled circles are the observed fluxes included in SED fitting and yellow filled circles are the observed fluxes in the radio bands (not included in the fit). Error bars are omitted for clarity when they are comparable to the symbol size. Right panels: thick solid black line stands for the total best attenuation law; solid magenta line is the ISM attenuation law; dashed red line represents the standard Calzetti attenuation law; dashed yellow and orange lines are the Calzetti attenuation laws obtained by decreasing (yellow) or increasing (orange) the standard value for R_V, as it is indicated in the legends. The Figure continues in the next two pages.

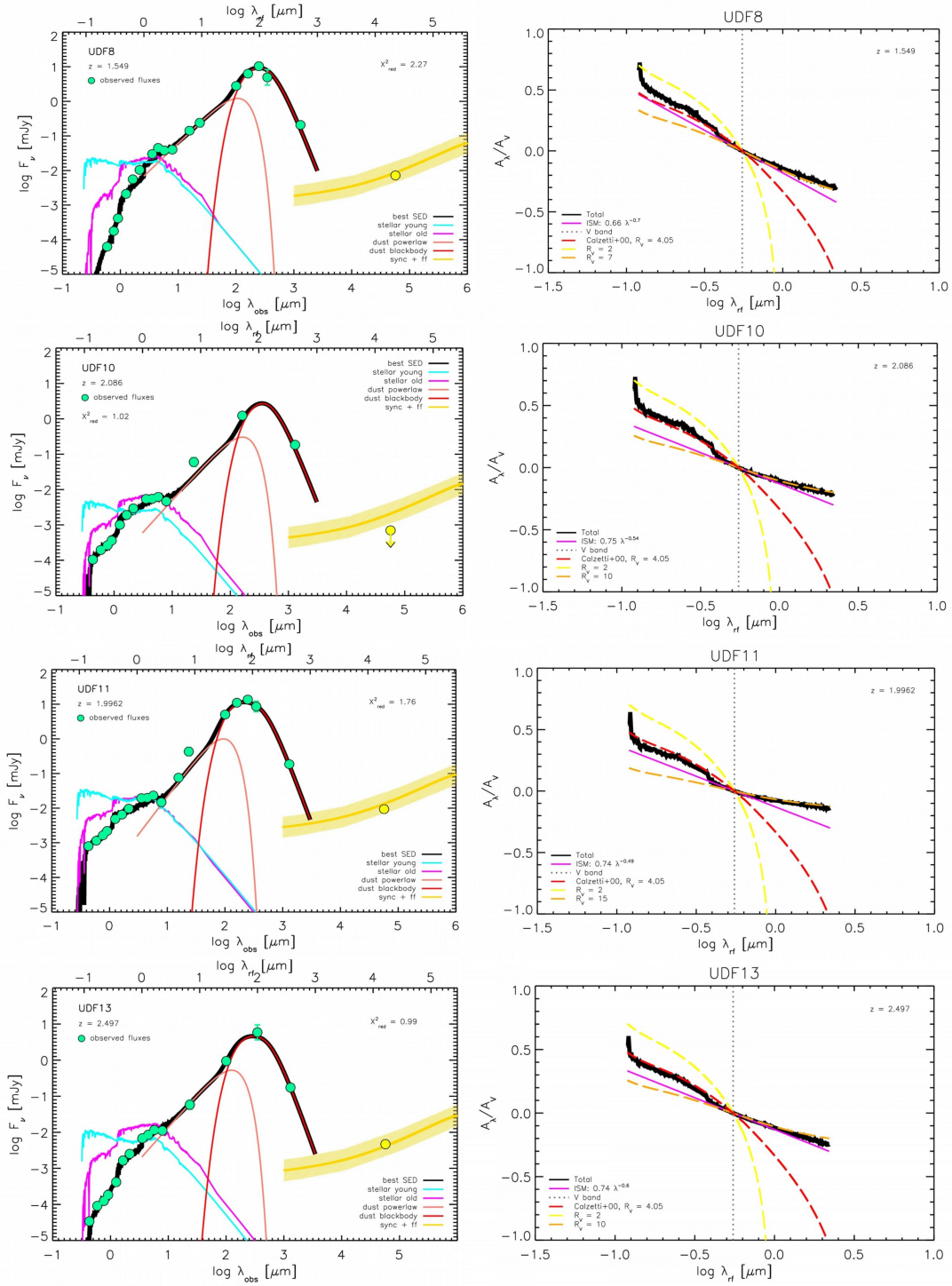
UDF8
z = 1.549
observed fluxes
χ^2_{red} = 2.27
best SED
stellar young
stellar old
dust powerlaw
dust blackbody
sync + ff
log F$_\nu$ [mJy]
log λ$_{obs}$ [μm]
log λ$_{rf}$ [μm]
A$_\lambda$/A$_V$
Total
ISM: 0.66 λ$^{-0.7}$
V band
Calzetti+00, R$_v$ = 4.05
R$_v$ = 2
R$_v$ = 7
UDF10
z = 2.086
observed fluxes
χ^2_{red} = 1.02
ISM: 0.75 λ$^{-0.54}$
R$_v$ = 10
UDF11
z = 1.9962
observed fluxes
χ^2_{red} = 1.76
ISM: 0.74 λ$^{-0.49}$
R$_v$ = 15
UDF13
z = 2.497
observed fluxes
χ^2_{red} = 0.99
ISM: 0.74 λ$^{-0.6}$
R$_v$ = 10

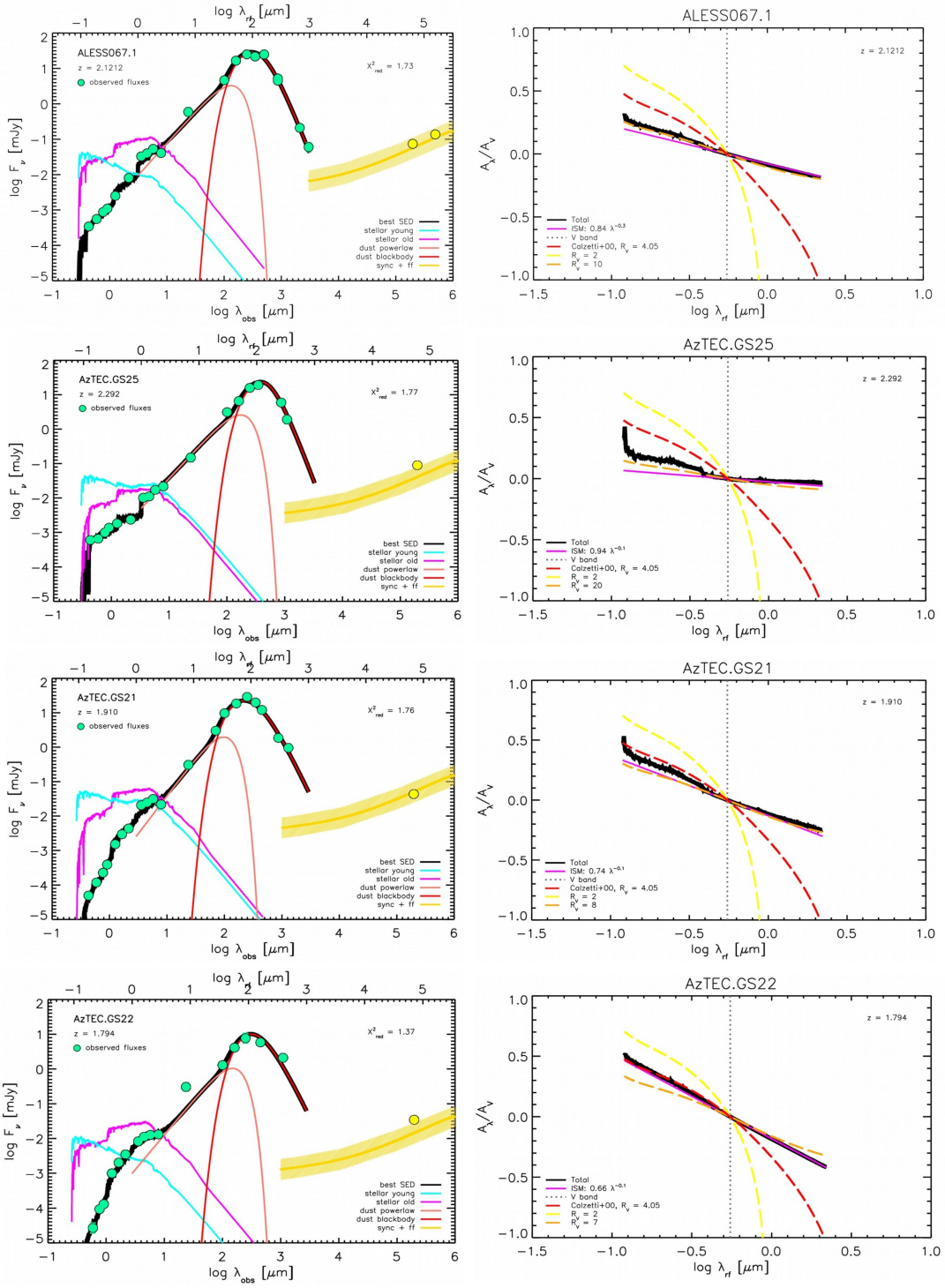
ALESS067.1
z = 2.1212
observed fluxes
X^2_{red} = 1.73
best SED
stellar young
stellar old
dust powerlaw
dust blackbody
sync + ff
log λ_obs [μm]
log λ_rf [μm]
log F_ν [mJy]
ALESS067.1
z = 2.1212
A_λ/A_V
Total
ISM: 0.84 λ^-0.3
V band
Calzetti+00, R_V = 4.05
R_V = 2
R_V = 10
AzTEC.GS25
z = 2.292
observed fluxes
X^2_{red} = 1.77
ISM: 0.94 λ^-0.1
R_V = 20
AzTEC.GS21
z = 1.910
observed fluxes
X^2_{red} = 1.76
ISM: 0.74 λ^-0.1
R_V = 8
AzTEC.GS22
z = 1.794
observed fluxes
X^2_{red} = 1.37
ISM: 0.66 λ^-0.1
R_V = 7

ID	$\alpha_{\rm dust}$	$\beta_{\rm dust}$	$T_{\rm dust}$ [K]	$L_{\rm dust}$ [$10^{12}\ L_\odot$]
UDF1	1.80 ± 0.09	2.0 ± 0.3	56 ± 3	3.5 ± 0.2
UDF3	2.2 ± 0.1	2.1 ± 0.3	73 ± 4	4.9 ± 0.3
UDF5	1.80 ± 0.09	2.3 ± 0.3	42 ± 3	0.77 ± 0.04
UDF8	1.60 ± 0.08	2.2 ± 0.3	52 ± 4	1.10 ± 0.06
UDF10	1.9 ± 0.1	2.1 ± 0.3	46 ± 7	0.41 ± 0.05
UDF11	2.2 ± 0.1	2.5 ± 0.2	69 ± 4	2.2 ± 0.2
UDF13	1.8 ± 0.1	2.3 ± 0.3	60 ± 3	1.2 ± 0.2
ALESS067.1	1.80 ± 0.09	2.2 ± 0.2	50 ± 3	5.4 ± 0.3
AzTEC.GS25	1.80 ± 0.09	2.3 ± 0.2	40 ± 2	3.9 ± 0.2
AzTEC.GS21	2.2 ± 0.1	1.8 ± 0.2	63 ± 3	3.9 ± 0.2
AzTEC.GS22	1.9 ± 0.1	1.8 ± 0.3	40 ± 2	1.01 ± 0.06

TABLE 3.6: CIGALE outputs from dust emission Bayesian analysis for the sources of the sample (ID in the first column). In the order, the table lists: MIR power-law spectral index ($\alpha_{\rm dust}$); FIR modified-BB spectral index ($\beta_{\rm dust}$); dust temperature ($T_{\rm dust}$) and dust luminosity ($L_{\rm dust}$) in units of $10^{12}\ L_\odot$.

CIGALE. By definition, the attenuation law is a function of wavelength normalized to attenuation in the V (photometric) band, i.e. A_λ/A_V. Namely, a non-transparent medium along the line-of-sight modify the source intrinsic monochromatic luminosity L^0_λ according to the law:

$$\frac{L_\lambda}{L^0_\lambda} = e^{-\tau_\lambda} \tag{3.6}$$

where τ_λ is the medium optical depth and L_λ is the attenuated luminosity, at a given wavelength λ. The attenuation at λ is then defined as:

$$A_\lambda = -2.5 \log_{10} \frac{L_\lambda}{L^0_\lambda}. \tag{3.7}$$

Comparing equations (3.6) and (3.7), it follows that $A_\lambda = 2.5 \log_{10}(e)\, \tau_\lambda = 1.086\, \tau_\lambda \simeq \tau_\lambda$. Notice that A_λ is actually a measure of the stellar luminosity that is absorbed by dust, i.e $\Delta L_\lambda = L^0_\lambda - L_\lambda$. In this work, the quantities $\Delta L^{\rm BC}_\lambda$, $\Delta L^{\rm ISM}_\lambda$ and $\Delta L^{\rm tot}_\lambda$ are provided by CIGALE, as outputs of SED fitting, along with the stellar intrinsic luminosities, thus:

$$A^{\rm i}_\lambda = -2.5 \log_{10} \frac{L^{0,i}_\lambda - \Delta L^{\rm i}_\lambda}{L^{0,i}_\lambda}. \tag{3.8}$$

where i = BC, ISM, tot.

Attenuations in V-band (A^i_V) are calculated from Eq. (3.8), by assuming $\lambda = 5500$ Å. Then, deriving the attenuation laws A^i_λ/A^i_V is straightforward.

Looking at the galaxy attenuation laws in Fig. 3.3, it is clear that the overall emerging stellar emission is mostly shaped by dust attenuation in the ISM ($\sim \lambda^{-\delta^{\rm ISM}}$, with $0.1 \leq \delta^{\rm ISM} \leq 0.7$; solid magenta line). Indeed, dust extinction in BCs has been modelled to absorb almost all the radiation from young stars that are enshrouded in very dense environments (cf. Sect. 3.2.1). A fraction of the light emitted by young stars emerges just at $\lambda_{\rm rest} \gtrsim 10\ \mu$m, where dust extinction is less effective.

Focusing on the total (i.e., ISM + BC) attenuation law ($A_\lambda/A_{\rm V}$), two main different

behaviours in λ clearly emerge. For the majority of the galaxies (seven out of eleven) the attenuation law is well described by a standard Calzetti et al. (2000, i.e. $R_V = A_V/E(B-V) \simeq 4.05 \pm 0.80$, dashed red line) at wavelengths bluer than $\lambda_V = 540$ nm, while it shows a flattening towards redder wavelengths, with a characteristic R_V ranging between 7 and 15 (cf. dashed orange line and dashed yellow line). The other five objects show a flatter attenuation law at every λ, with a $R_V \simeq 20$. This flattening of the attenuation law towards high-z may be caused by a more uniformly mixed geometry of the interstellar dust grains or may simply indicate the presence of dust grains with diverse geometries and distributions into the ISM, that are very difficult to be constrained at $z > 1$ (e.g., Salmon et al., 2016; Leja et al., 2017; Narayanan et al., 2018; Salim, Boquien, and Lee, 2018; Buat et al., 2019; Trayford and Schaye, 2019). Because of the smaller amount of reddening at NIR wavelengths, the standard Calzetti, constrained just in local Milky Way-like galaxies, is found to significantly lower SFR and stellar mass when applied to high-z dusty galaxies (e.g., Williams et al., 2019). Exploiting this attenuation law at high-z should be done with caution, in particular while dealing with the UV/optical-to-millimetre emission of DSFGs.

Dust mass

I have estimated the dust mass of each source using the dust temperature (from galaxy SED fitting; Tab. 3.6) and a measure of the dust flux in the rest-frame Rayleigh-Jeans regime. It is well known (e.g., Bianchi, 2013; Gilli et al., 2014; D'Amato et al., 2020; Pozzi et al., 2020) that galaxy dust mass M_{dust} can be calculated under the optically thin approximation ($\tau_\nu \ll 1$):

$$M_{dust} = \frac{S(\nu_{obs})\, d_L^2}{(1+z)\, k(\nu_{rest})\, B_{BB}(\nu_{rest}, T_{dust})} \tag{3.9}$$

where $S(\nu_{obs})$ is the observed flux such that $\nu_{rest} = \nu_{obs}(1+z)$ is in Rayleigh-Jeans regime; B_{BB} is the BB brightness computed at ν_{rest}, with T_{dust} being the dust equilibrium temperature derived by performing the single-T fit of the FIR SED; $k(\nu_{rest}) = 5.1\,(\nu_{rest}/1.2\,\mathrm{THz})^\beta$ cm^2 g^{-1} is the dust absorption coefficient per unit of mass (e.g., Magdis et al., 2012; Gilli et al., 2014); d_L^2 is the luminosity distance; $(1+z)$ takes into account the *k-correction* entering in the relation between flux and luminosity.

In order to obtain the most reliable estimate of dust mass I have exploited the reddest (sub-)mm observed flux for each source. In Tab. 3.7 I list the corresponding rest-frame wavelength, that lies to a good extent in the Rayleigh-Jeans regime. Errors on dust mass are calculated following the error propagation theory.

The dust masses derived from single-temperature modified-BB fit of the FIR SED are *luminosity-weighted*. As a consequence, the resulting dust temperature is typically slightly higher than the mean and the resulting dust mass tends to be underestimated. Magdis et al. (2012) attempted to quantify this effect, which turns out to shift downwards dust masses of a factor ~ 2 (cf. Sects. 3.2.1 and 3.2.2). I will take into consideration this correction in the following analysis.

Gas mass

CIGALE does not allow to derive galaxy gas mass directly from broad band fitting: gas masses computed by the stellar emission module consist solely of the gas fraction that is restituted to the medium by stellar evolution (i.e., M_R; see Tab. 3.5).

ID	d_L [Mpc]	λ_{dust}^{rest} [μm]	ν_{dust}^{rest} [GHz]	S_{dust} [mJy]	M_{dust} [$10^8\ M_\odot$]
UDF1	22886.4	353	850	0.924 ± 0.076^a	2.8 ± 1.0
UDF3	21294.4	367	817	0.863 ± 0.084^a	2.0 ± 0.8
UDF5	13553.1	471	637	0.311 ± 0.049^a	2.3 ± 1.1
UDF8	11588.6	510	588	0.208 ± 0.046^a	1.21 ± 0.67
UDF10	16711.9	421	712	0.184 ± 0.046^a	0.95 ± 0.67
UDF11	15833.4	434	691	0.186 ± 0.046^a	0.73 ± 0.33
UDF13	20825.4	372	806	0.174 ± 0.045^a	0.60 ± 0.34
ALESS067.1	17058.3	279	1075	4.5 ± 0.4^b	4.8 ± 1.8
AzTEC.GS25	18755.5	334	898	1.9 ± 0.6^c	6.8 ± 4.1
AzTEC.GS21	14997.8	445	674	0.954 ± 0.074^a	2.9 ± 0.7
AzTEC.GS22	13885.7	394	761	2.1 ± 0.6^c	7 ± 4

TABLE 3.7: For each source of the sample (ID in column 1) we list of the values for the quantities entering in Eq. 3.9 (values for β_{dust} and T_{dust} can be found in Tab. 3.6) and the resulting dust mass (M_{dust}; last column, in units of $10^8\ M_\odot$). In particular, ν_{dust}^{rest} ($\equiv \lambda_{dust}^{rest}$>200 μm) is the rest-frame frequency corresponding to the observed Rayleigh-Jeans flux $S_{dust} \equiv S(\nu_{obs})$: *a*) ALMA flux at $\lambda_{obs} = 1300$ μm ($\nu_{obs} = 230$ GHz); *b*) ALMA flux at $\lambda_{obs} = 870$ μm ($\nu_{obs} = 345$ GHz); *c*) AzTEC flux at $\lambda_{obs} = 1100$ μm ($\nu_{obs} = 273$ GHz). Units are reported between square brackets. Dust masses are not corrected by Magdis et al. (2012): a factor 2 must be added.

Gas masses of high-z dusty galaxies can be derived by relying either on CO line luminosities or on Rayleigh-Jeans dust continuum. Although CO lines require to assume a conversion factor α_{CO} (to convert the observed CO line luminosity into the galaxy molecular hydrogen mass, M_{H_2}) and an excitation ladder (in case of transitions with $J > 1$), they provide the most direct method to infer the molecular gas content in high-z DSFGs. However, observing CO lines at high-z is very expensive in terms of time-on-source ($\gtrsim$ a few hours) and so they are available just for a small number of DSFGs. Alternative methods are mainly based on the exploitation of dust FIR continuum, but they are affected by larger uncertainties since they need to assume a gas-to-dust ratio (GDR). Nevertheless, they are very convenient for dusty galaxies at high-z: indeed their dust continuum can be detected, e.g. by ALMA, in just a few minutes of observing time. The two most popular methods exploiting dust Rayleigh-Jeans continuum are developed and described in the articles by Leroy et al. (2011), Scoville et al. (2014), and Scoville et al. (2016), to which I refer for the following analysis. These two approaches have been recently combined in the work by Liu et al. (2019) on the A3 COSMOS[8] sample.

To derive the total gas mass, i.e. including both atomic and molecular hydrogen ($HI + H_2$), I made use of the local relation by Leroy et al. (2011, their Sect. 5.2):

$$\begin{aligned} \log_{10}(\mathrm{GDR}) &= \log_{10} \frac{M_{\mathrm{HI}} + M_{\mathrm{H_2}}}{M_{\mathrm{dust}}} \\ &= (9.4 \pm 1.1) - (0.85 \pm 0.13)[12 + \log_{10}(O/H)]. \end{aligned} \tag{3.10}$$

The dependence on gas metallicity allows to extend the result to $z \lesssim 3$. The gas metallicity for the $z \sim 2$ sample of DSFGs is calculated using the mass-metallicity

[8] https://sites.google.com/view/a3cosmos

ID	$\log M_{\rm gas,\,mol}$ $[M_\odot]$	$\log M_{\rm gas,\,tot}$ $[M_\odot]$	GDR	$Z_{\rm gas}$ 12+log(O/H)
UDF1	10.5	10.8	120	8.61
UDF3	10.6	10.7	119	8.62
UDF5	10.1	10.9	161	8.46
UDF8	10.0	10.5	126	8.59
UDF10	9.8	10.5	159	8.47
UDF11	9.8	10.3	127	8.58
UDF13	9.7	10.2	127	8.59
ALESS067.1	10.9	11.0	100	8.71
AzTEC.GS25	10.6	11.2	121	8.61
AzTEC.GS21	10.7	10.8	106	8.68
AzTEC.GS22	10.7	11.3	130	8.57

TABLE 3.8: Molecular gas mass $M_{\rm gas,\,mol}$ derived following the approach in Scoville et al. (2016); total (HI + H_2) gas mass $M_{\rm gas,\,tot}$ and gas metallicity $Z_{\rm gas}$ evaluated following Genzel et al. (2012) and Elbaz et al. (2018). Uncertainties have been omitted for clarity: they are ∼ 0.3 dex for molecular gas masses and ∼ 0.4 dex for total gas masses and gas metallicities.

relation by Genzel et al. (2012, their Sect. 2.2), following Elbaz et al. (2018, their Sect. 2.4):

$$12 + \log_{10}(O/H) = -4.51 + 2.18\,M_\star - 0.0896\,(\log_{10} M_\star)^2. \tag{3.11}$$

The rms dispersion of mass-metallicity relation at $z \sim 2$ is of about 0.09 dex. Systematic uncertainties between different metallicity indicators and calibrators can reach ∼ 0.3 dex (e.g., Kewley and Ellison, 2008) and clearly dominate over the statistical one. The outcomes are shown in Fig. 3.8. In order to derive the total gas mass (Eq. 3.10), I have used the SED-inferred dust masses (cf. Tab. 3.7) corrected following Magdis et al. (2012). As discussed in Sect. 3.2.2, this procedure brings into the total dust mass budget also the coldest interstellar dust, whose content is (on average) a factor ∼ 2 underestimated when a single-temperature modified-BB is used to fit the FIR interstellar dust thermal emission. The resulting total gas masses $M_{\rm gas,\,tot}$ are listed in Tab. 3.8. The uncertainty is of about 0.3 dex. It is important to note that metallicities could be even higher, in case of very compact FIR sources ($r_{\rm FIR} < 1$ kpc) and possibly dust thick. Actually, the inferred total gas masses strongly depend on the method and, in the case of this work, on the assumed mass-metallicity relation, shown in Eq. (3.11).

I have estimated the molecular ISM masses of the 11 DSFGs using the empirical calibration by Scoville et al. (2016, cf. their Fig. 1, right panel):

$$\frac{L_{\nu_{850\,\mu m}}}{M_{\rm gas,\,mol}} = 6.2 \times 10^{19} \left(\frac{L_{\nu_{850\,\mu m}}}{10^{31}}\right)^{0.07}. \tag{3.12}$$

The resulting molecular gas masses $M_{\rm gas,\,mol}$ are listed in Tab. 3.8. The corresponding uncertainty is of about 0.3 dex. The two estimates for gas mass (i.e., $M_{\rm gas,\,mol}$ and $M_{\rm gas,\,tot}$) are compatible within the errors.

X-ray properties

The X-ray emission in star-forming galaxies can be traced back to two main different processes: the star-formation itself, since massive, compact binaries can produce X-ray radiation (the so called *X-ray binaries*); the accretion of matter onto the central SMBH (if the AGN is *on*), since the infalling heated material radiate (also) in the X-ray band. Thus, the X-ray luminosity can provide a wealth of information on the possible presence of a central AGN and on its evolutionary stage.

As described in Chapter 3, nine sources of the sample out of eleven own a robust counterpart in the X-ray *Chandra* catalog by Luo et al. (2017), based on a ≈ 7 Ms map of the CDF-S. The two X-ray non-detections (UDF5 and AzTEC.GS22) lie in very deep regions of the *Chandra* map (equivalent exposure times are $\sim$ 6.22 Ms and $\sim$ 5.80 Ms, respectively), thus the hypothesis of totally obscured X-ray sources is the most probable.

Derivation of galaxy intrinsic 2-10 keV luminosity

For every X-ray source, Luo et al. (2017) provide the $0.5 - 7.0$ keV *intrinsic* luminosity, i.e. net of the Milky Way and X-ray source intrinsic absorption, the latter determined by the intrinsic column density $N_{\rm H,int}$.

In the following I convert the $0.5 - 7.0$ keV luminosity by Luo et al. (2017) to the corresponding $2 - 10$ keV luminosity, given that the latter is the most widely used in literature to investigate galaxy-BH co-evolution. I estimate the conversion factor with the X-ray simulator WebPIMMS[9], the same tool used by Luo et al. (2017) to obtain $N_{\rm H,int}$. To this aim I exploit the known intrinsic spectral index ($\equiv 1.8$ or greater; Luo et al., 2017) of the source. Intrinsic and effective[10] spectral indices ($\Gamma_{\rm int}$ and $\Gamma_{\rm eff}$), together with $L_{0.5-7\,\rm keV} - L_{2-10\,\rm keV}$ conversion factors and the derived $2 - 10$ keV intrinsic luminosities ($L_{2-10\,\rm keV}$) are listed in Tab. 3.9.

Then, I convert the $2 - 10$ keV luminosities to be consistent with the redshift adopted in this work (cf. Tab. 3.1), not always exactly coincident with Luo et al. (2017) ones. To this aim, I proceed as follows. In case both the intrinsic X-ray luminosity $L_{\nu/(1+z)}$ of a source at a given redshift z and the power-law describing its X-ray emission are known, it is possible to derive the corresponding observed flux $S_{\nu/(1+z)}$ applying the so-called *k-correction*. This correction is defined by the following equation:

$$S_{\nu/(1+z)} = (1+z)\,\frac{L_{\nu}}{L_{\nu/(1+z)}}\,\frac{L_{\nu/(1+z)}}{4\pi\, d_{\rm L}(z)^2} \tag{3.13}$$

Since $L_{\nu} \propto \nu^{-\alpha}$, with $\alpha > 0$ and $\Gamma = \alpha + 1 > 0$ (e.g., Ishibashi & Courvoisier 2010) (e.g., Ishibashi and Courvoisier, 2010) where Γ is the energy spectral index, one can write:

$$\frac{L_{\nu}}{L_{\nu/(1+z)}} = \left(\frac{\nu}{\nu/(1+z)}\right)^{-\alpha} = (1+z)^{-\alpha} = (1+z)^{1-\Gamma}$$

this result, together with equation (3.13), brings to:

$$S_{\nu/(1+z)} = (1+z)^{2-\Gamma_{\rm int}}\,\frac{L_{\nu/(1+z)}}{4\pi\, d_{\rm L}(z)^2} \tag{3.14}$$

[9] https://heasarc.gsfc.nasa.gov/cgi-bin/Tools/w3pimms/w3pimms.pl

[10] Note that the effective spectral index is actually almost coincident with the observed spectral index.

where Γ_{int} is the intrinsic energy spectral index, i.e. the one derived after the correction for an eventual intrinsic absorption. Specializing Eq. (3.14) to this case, one has:

$$S_{2-10\,\mathrm{keV}} = (1+z_\mathrm{L})^{2-\Gamma_\mathrm{int}} \frac{L_{2-10\,\mathrm{keV}}(z_\mathrm{L})}{4\pi\, d_\mathrm{L}(z_\mathrm{L})^2} \tag{3.15}$$

where z_L is the source redshift in Luo et al. (2017). Then, exploiting Eq. (3.15), it is possible to derive the observed flux $S_{2-10\,\mathrm{keV}}$ corresponding to the intrinsic luminosity $L_{2-10\,\mathrm{keV}}(z_\mathrm{L})$ provided by Luo et al. (2017). Now, it is sufficient to invert Eq. (3.14) with $S_{\nu/(1+z)} \equiv S_{2-10\,\mathrm{keV}}$ and from Eq. (3.15) it follows:

$$L_{X,\,\mathrm{int}} = (1+z_\mathrm{L})^{2-\Gamma_\mathrm{int}} \frac{L_{2-10\,\mathrm{keV}}(z_\mathrm{L})}{4\pi\, d_\mathrm{L}(z_\mathrm{L})^2} \frac{4\pi\, d_\mathrm{L}(z)^2}{(1+z)^{2-\Gamma_\mathrm{int}}}\,. \tag{3.16}$$

Intrinsic $2-10$ keV luminosities ($L_{2-10\mathrm{keV}}$) for the nine sources with an X-ray counterpart are listed in Tab. 3.10, along with the other quantities exploited to derive it.

X-ray dominant component

Luo et al. (2017) provide also a classification of the X-ray sources (i.e., AGN, galaxy or star), that is displayed in Tab. 3.10 (**classX** - Luo+17), for reference. They classified as *AGN* every X-ray source that shows at least one of the following evidences:

- $L_{X,\,\mathrm{int}} > 3\times10^{43}$ erg s^{-1} (*luminous* X-ray sources);
- $\Gamma_\mathrm{eff} \leq 1.0$ (*hard*-X sources);
- $\log(S_\mathrm{X}/S_\mathrm{R}) > -1$, where S_X is either the *full* X-ray band flux, the *soft* X-ray band flux, or the *hard* X-ray one (in order of priority), and S_R is the observed flux in R-band ;
- the source is spectroscopically classified as AGN;
- $\log(S_\mathrm{X}/S_{\mathrm{K_s}}) > -1.2$, where S_X is either the *full* X-ray band flux, the *soft* X-ray band flux, or the *hard* X-ray one (in order of priority), and $S_{\mathrm{K_s}}$ is the NIR flux observed in the filter K_s.

For a more detailed description of these criteria I refer the reader to Luo et al. (2017, their Sect. 4.5 and references therein).

However, even if the object is classified as *AGN*, it does not imply that the X-ray emission coming from the AGN actually prevails over the galactic one. To get a deeper insight on this topic, in Fig. 3.4 I compare the $2-10$ keV luminosity of the nine X-ray detected DSFGs with their IR luminosity (measure by fitting galaxy SED and listed in Tab. 3.6). In this thesis every object falling above the relation by Ranalli, Comastri, and Setti (2003) for star-forming galaxies (light grey solid line in Fig. 3.4) has been classified as *X-ray AGN*, meaning that its X-ray luminosity overwhelms the one coming from the host galaxy. In Fig. 3.4 these sources are marked with a blue circle. This result is still valid when the evolution of X-ray binaries luminosity with galaxy redshift, SFR and $M_\star$ is taken into consideration (e.g., Lehmer et al., 2016) (dark grey dotted line in Fig. 3.4). I further note that the two *X-ray AGN*s are also in the 3Ms XMM catalog by Ranalli et al. (2013).

Actually, many recent works have shown that the X-ray luminosity from the AGN (if present) begins to be comparable to the host galaxy one at $L_\mathrm{X} \approx 10^{42}$ erg s^{-1} (e.g., Bonzini et al., 2013; Padovani et al., 2015). Indeed, this value is commonly adopted

ID	ID_X	d [arcsec]	z	z_L	$L_{0.5-7\,keV}$ [10^{42} erg s^{-1}]	f_{conv}	$L_{2-10\,keV}$ [10^{42} erg s^{-1}]	Γ_{eff}	Γ_{int}
UDF1	805	0.69	2.688	2.69	64.0	0.63	40.3	1.96	1.96
UDF3	718	0.54	2.544	2.547	4.6	0.40	1.8	2.44	2.44
UDF8	748	0.07	1.549	1.552	50.7	0.72	36.5	1.32	1.8
UDF10	756	0.31	2.086	2.096	2.7	0.22	0.6	3.0	3.0
UDF11	751	0.29	1.996	1.998	2.4	0.72	1.7	1.74	1.8
UDF13	655	0.26	2.497	2.07	2.3	0.57	1.3	2.07	2.07
ALESS067.1	794	0.40	2.1212	2.122	8.5	0.45	3.8	2.33	2.33
AzTEC.GS25	844	0.71	2.292	2.292	8.5	0.72	6.1	1.2	1.8
AzTEC.GS21	852	0.36	1.91	1.91	2.3	0.72	1.7	1.4	1.8

TABLE 3.9: This table lists: counterparts IDs (ID: this work; ID_X: Luo et al. 2017) and their angular separation (d) in arcsec; redshifts adopted in this work (z) and the ones associated to X-ray sources in (Luo et al., 2017, z_L); intrinsic 0.5 – 7 keV luminosities from Luo et al. (2017, $L_{0.5-7keV}$); conversion factors (f_{conv}) from $L_{0.5-7\,keV}$ to $L_{2-10\,keV}$; 2 – 10 keV luminosities at redshift z_L ($L_{2-10\,keV}$); 2 – 10 keV intrinsic luminosities at redshift z (L_X); effective spectral indices (Γ_{eff}) and the intrinsic ones (Γ_{int}). In the last two columns are shown (in the order): the class (AGN or galaxy) associated to each source by Luo et al. (2017) and the X-ray dominant component (active nucleus or host galaxy) found by the analysis presented in this thesis.

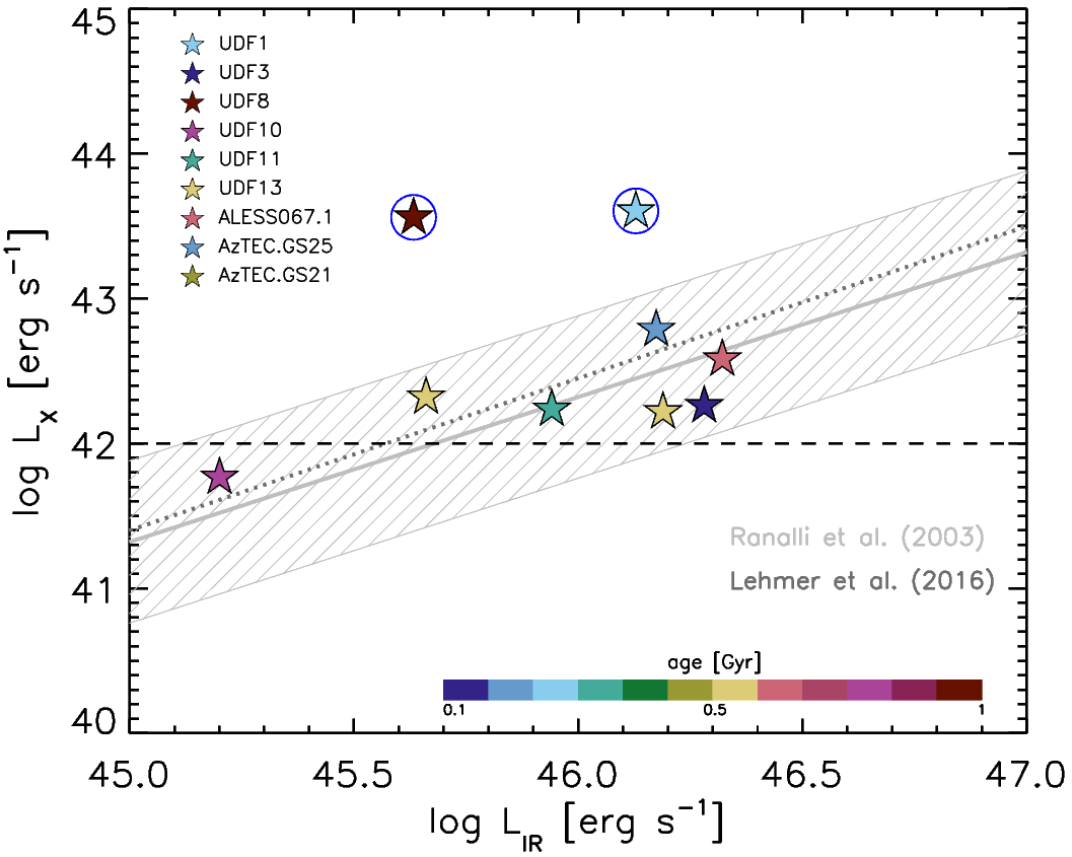

FIGURE 3.4: X-ray luminosity versus IR luminosity. Stars stand for the sources with an X-ray counterpart in the catalog by Luo et al. (2017). They are color-coded by age (i.e., $\tau_\star$). IR luminosities (8 – 1000 μm rest-frame) result from SED fitting. Gray line represents the correlation between X-ray and IR luminosity when they are ascribed to star formation solely by Ranalli, Comastri, and Setti (2003), with its 1σ scatter. Dark gray dotted line represents the trend followed by our objects when the evolution with galaxy z, $M_\star$ and SFR is taken into account in the relation by Lehmer et al. (2016). Its 1σ scatter (of about 0.4 dex) has not been plotted for clarity. The two outliers are highlighted with a blue circle. The dashed horizontal black line indicates the value at which X-ray luminosity from the central BH begins to be comparable to the one coming from star formation.

ID	ID_X	z	L_X [10^{42} erg s^{-1}]	class X Luo+17	X dominant component
UDF1	805	2.698	40.2	AGN	AGN
UDF3	718	2.544	1.8	AGN	galaxy
UDF8	748	1.549	36.3	AGN	AGN
UDF10	756	2.086	0.6	galaxy	galaxy
UDF11	751	1.996	1.7	galaxy	galaxy
UDF13	655	2.497	2.1	AGN	galaxy
ALESS067.1	794	2.1212	3.8	AGN	galaxy
AzTEC.GS25	844	2.292	6.1	AGN	galaxy
AzTEC.GS21	852	1.91	1.7	AGN	galaxy

TABLE 3.10: This table lists: counterparts IDs (ID: this work; ID_X: Luo et al. 2017); source redshifts (z); 2 – 10 keV intrinsic luminosities at redshift z (L_X); the class (AGN or galaxy) associated to each source by Luo et al. (2017) and the X-ray dominant component (active nucleus or host galaxy) found by our analysis.

to clearly discern the nuclear X-ray emission from that associated to star formation $L_{X,\,SFR} \approx 7\times10^{41}$ erg s^{-1} SFR/10^2 $M_\odot$ yr^{-1} (e.g., Vattakunnel et al., 2012). This threshold is indicated in Fig. 3.4 with a dashed black line. Almost all the sources with an X-ray counterpart lie above it, possibly indicating that a X-ray quasar is growing in the nuclear region of the host galaxy.

AGN fraction in the IR domain

I have exploited galaxy 2 – 10 keV luminosity (L_X) to infer the fraction of IR luminosity (i.e., integrated over 8 – 1000 μm) coming from the central AGN, in a way that is totally independent from SED fitting and avoids all the caveats related to parameter degeneracies (see Sect. 3.2.1). In particular, I have used the correlation by Mullaney et al. (2011, their Eq. 4):

$$\log\left(\frac{L_{IR}^{AGN}}{10^{43}\,\mathrm{erg\,s^{-1}}}\right) = (0.53 \pm 0.26) + (1.11 \pm 0.07)\,\log\left(\frac{L_X}{10^{43}\,\mathrm{erg\,s^{-1}}}\right) \tag{3.17}$$

to derive AGN IR luminosity and the corresponding AGN fraction (i.e., $f_{AGN}^{(1)} = L_{IR}^{AGN}/L_{IR}^{dust}$), that is listed in Tab. 3.11. The IR luminosities entering the above equation (also listed in Tab. 3.11) come from the SED fit with CIGALE and have been obtained following the approach by Casey (2012, Sect. 3.2.1).

The correlation by Mullaney et al. (2011) is based on a sample of 25 local (i.e., z < 0.1) AGNs from the Swift-BAT survey, with typical X-ray and IR properties (i.e., N_H, $L_{2-10\,keV}$ and L_{IR}) largely covering the same ranges as those z $\sim$ 2 AGNs and star-forming galaxies detected in *Chandra* (e.g., CDF-N and CDF-S; see Fig. 1 in Mullaney et al., 2011) and *Spitzer*/*Herschel* deep surveys (e.g. GOODS). Thus, it is possible to reasonably apply the result from Mullaney et al. (2011) to the sample of $z \sim 2$ DSFGs studied in this thesis. It follows that the central AGN contribution to the total infrared light of the nine X-ray detected DSFGs is negligible (i.e., consistent with 0 or a few per cent): it attains values $\lesssim 10\%$ once the 1σ scatter (i.e., ~ 0.5 dex) of Mullaney et al. correlation is considered. A similar result is found by Pozzi et al. (2012) analyzing a sample of ~ 30 *Herschel*-selected $z \sim 2$ LIRGs: just the $\sim 35\%$ of the sample show the presence of an AGN at the 3σ confidence level, but its contribution

ID	L_X [10^{43} erg s^{-1}]	L_{IR}^{dust} [10^{43} erg s^{-1}]	L_{IR}^{AGN} [10^{43} erg s^{-1}]	$f_{AGN}^{(1)}$ [%]	$f_{AGN}^{(2)}$ [%]
UDF1	4.0 ± 0.4	1345 ± 67	16 ± 13	1	6
UDF3	0.18 ± 0.02	1910 ± 114	0.5 ± 0.3	0.03	0.2
UDF8	3.6 ± 0.4	430 ± 21	14 ± 11	3	14
UDF10	0.060 ± 0.006	159 ± 19	0.15 ± 0.07	0.09	1
UDF11	0.17 ± 0.02	873 ± 59	0.5 ± 0.3	0.06	0.5
UDF13	0.21 ± 0.02	458 ± 75	0.6 ± 0.4	0.1	0.8
ALESS067.1	0.38 ± 0.04	2096 ± 105	1.2 ± 0.7	0.06	0.4
AzTEC.GS25	0.61 ± 0.06	1493 ± 75	2 ± 1	0.1	1
AzTEC.GS21	0.17 ± 0.2	1546 ± 77	0.5 ± 0.3	0.03	0.3

TABLE 3.11: This table lists: IDs of the sources; 2 − 10 keV luminosities (L_X); total infrared luminosities (8 − 1000 μm rest frame) obtained from SED fitting (L_{IR}^{dust}) as described in Sect. 3.2.1; infrared AGN luminosities and AGN fractions ($f_{AGN}^{(1)}$) inferred following (Mullaney et al., 2011, Eq. 3.17); AGN fraction inferred by using Asmus et al. (2015) MIR-X ray correlation ($f_{AGN}^{(2)}$).

to the IR emission accounts for only ∼ 5% of the energy budget.

I provide a further investigation on AGN fraction in the IR domain by referring to the relation between the nuclear 12 μm luminosity ($L_{12\,\mu m}^{nuc}$) and the intrinsic 2−10 keV luminosity by Asmus et al. (2015, their Eq. 1) found for a local sample but valid also at higher redshift (see also Gandhi et al., 2009). I have used the 2−10 keV luminosities (L_X; Tab. 3.11) to derive the expected rest-frame 12 μm nuclear luminosity of our sources. Comparing the outcome with the corresponding observed luminosity at $\lambda_{rest} = 12\,\mu$m, it is possible to derive the fraction coming from the nucleus $f_{AGN}^{(2)}$ (see the last column of Tab. 3.11). The MIR-X ray correlation scatter of 0.34 dex does not allow to precisely constrain AGN fraction, but still this analysis provides a qualitatively estimation of the impact of the AGN on the observed MIR emission. For the nine X-ray detected objects, the fraction of 12 μm luminosity coming from the nucleus attains to values $\lesssim$ 10% and for the majority of our sources (seven out of nine) it is $\lesssim$ 1%.

The two X-ray non-detected sources (UDF5 and AzTEC.GS22) do not appear also in the supplementary catalog at very low significance. This may indicate either that no (not very powerful) AGN is present or that it is highly obscured, i.e. *Compton-thick*, with $N_H \gtrsim 10^{24}$ cm^{-2}. However, it is not possible to provide an insight on this issue just basing on the (other) multi-wavelength data at our disposal.

Finally, I have cross-checked these results with the outcomes obtained by fitting the 11 DSFG SEDs once the modules by Draine and Li (2007) and Fritz, Franceschini, and Hatziminaoglou (2006) had been included in the CIGALE routine and the free parameters fixed to the values found in literature to better reproduce the high-z DSFG emission (see e.g., Małek et al., 2018; Donevski et al., 2020). The resulting AGN fraction f_{AGN} is still smaller than 10% for almost all the DSFGs in the sample. A similar result has been recently found by Barrufet et al. (2020) by analysing the IR SED of ∼ 200 DSFGs in the COSMOS field at $0.7 < z_{phot} < 5.6$. These evidences provide a further confirmation of the approach adopted here to model the MIR and FIR emission, as it is discussed in Sect. 3.2.1.

Radio properties

The radio emission in star-forming galaxies can be traced back to two different astrophysical processes: the star formation itself and the accretion of the central SMBH, that can eventually turn into an AGN emitting in the radio band (cf. Mancuso et al., 2017).

Radio emission associated with star formation comprises two components: free-free emission coming from HII regions, fully dominating at frequencies $\nu > 30$ GHz; synchrotron emission by relativistic electrons accelerated by supernova remnants. In the following I will consider both these contributions to provide a rough but realistic estimate of the stellar radio emission for each galaxy of the sample by using the SFR from the SED fitting (see Sect. 3.2.1). I adopt the classical free-free emission calibration with SFR at 33 GHz for a pure hydrogen plasma ($Z_i = 1$) with temperature $T = 10^4$ K by Murphy et al. (2012) :

$$L_{\rm ff} \approx 3.75 \times 10^{26}\,{\rm erg\,s^{-1}\,Hz^{-1}}\,\frac{SFR}{M_\odot\,{\rm yr^{-1}}}\left(\frac{T}{10^4\,{\rm K}}\right)^{0.3} \times g(\nu,\,T)\,e^{-h\nu/kT} \tag{3.18}$$

where $g(\nu, T)$ is the Gaunt factor: approximated according to Draine (2011). Synchrotron calibration with SFR is a bit controversial since it involves complex and poorly understood processes, such as the production and escaping rates of relativistic electrons and the magnetic field strength. Here, I exploit the calibration proposed by Murphy et al. (2011), Murphy et al. (2012), and Kennicutt and Evans (2012, for a review). Thus, the synchrotron luminosity ascribed to star formation can be written as follows:

$$\begin{aligned} L_{\rm sync} \approx 1.9 \times 10^{28}\,{\rm erg\,s^{-1}\,Hz^{-1}}\,\frac{SFR}{{\rm M_\odot\,yr^{-1}}}\left(\frac{\nu}{\rm GHz}\right)^{-\alpha_{\rm sync}} \times \\ \times \left[1+\left(\frac{\nu}{20\,{\rm GHz}}\right)^{0.5}\right]^{-1} \times \frac{1-e^{-\tau_{\rm sync}(\nu)}}{\tau_{\rm sync}(\nu)} \end{aligned} \tag{3.19}$$

where $\alpha_{\rm sync} \sim 0.75$ is the spectral index found for high-z DSFGs (e.g., Condon, 1992; Ibar et al., 2009; Ibar et al., 2010; Thomson et al., 2014), the term $(1 + \nu^{0.5})^{-1}$ renders spectral aging effects (see Banday and Wolfendale, 1991), and the latter factor takes into account synchrotron self-absorption in terms of the plasma optical depth (e.g., Kellermann, 1966; Tingay and de Kool, 2003).

I have compared these predictions with the observed radio fluxes (Tab. 3.12) in order to get some hints on the presence (or not) of an AGN. The observed radio fluxes are consistent with galaxy star formation for all the 11 DSFGs. In Fig. 3.3 radio data points lie within the scatter of free-free plus synchrotron radio emission, represented by the yellow shaded area. It is worth noticing, though, that this evidence does not exclude the presence of an AGN, whose radio emission could be simply too low to emerge from the stellar one. I pinpoint three possible scenarios: the galaxy does not host an AGN; the galaxy host an accreting central SMBH but it does not contribute to the observed emission in the radio band; an AGN is present but it is radio silent or radio quiet. In this respect I will provide a further analysis in Sect. 3.3.

ID	ν^{obs} [GHz]	F_{ff} [μJy]	F_{sync} [μJy]	F^{obs}_{radio} [μJy]
UDF1	5.25	4.0	7.6	9.0 ± 0.6
UDF3	5.25	4.5	0.6	12.1 ± 0.6
UDF5	5.25	2.0	3.8	6.3 ± 0.5
UDF8	5.25	3.0	5.7	7.2 ± 0.5
UDF10	5.25	0.7	1.4	< 0.7
UDF11	5.25	4.6	8.7	9.3 ± 0.7
UDF13	5.25	1.4	2.7	4.7 ± 0.5
ALESS067.1	1.5	9.4	47.3	74 ± 7
	0.61	10.1	100.3	137 ± 15
AzTEC.GS25	1.5	6.8	34.1	90 ± 6
AzTEC.GS21	1.5	8.4	42	44 ± 6
AzTEC.GS22	1.5	2.4	12.1	35 ± 7

TABLE 3.12: This table lists (in the order): IDs of the sources; the observed frequency in the radio band (ν^{obs}); the corresponding radio fluxes from free-free (F_{ff}) and synchrotron emission (F_{sync}) by using Eqs. (3.18) and (3.19), with a scatter of 0.3 dex; the observed radio fluxes (F^{obs}_{radio}) and their uncertainties. Units are given between square brackets.

3.3 Interpreting galaxy integral properties in the context of galaxy evolution

In this Section I give a possible characterization of the 11 DSFGs by exploiting the main results from SED fitting and the analysis of their broad-band emission in the X-rays and radio band, described in Sects. 3.2.1 and 3.2.2. Then, I place the objects in the broad context of galaxy evolution, both comparing with the most popular diagnostic plots (that are empirically derived, such as galaxy main-sequence; dust and gas masses vs. stellar mass; gas metallicity relation), and the predictions from theory discussed in Chapter 2. To this aim, I mainly refer to the *in-situ* galaxy-BH co-evolution scenario (e.g., Eke, Efstathiou, and Wright, 2000; Fall, 2002; Romanowsky and Fall, 2012; Mancuso et al., 2016b; Mancuso et al., 2016a; Mancuso et al., 2017; Shi et al., 2017; Lapi et al., 2018), as I have anticipated in previous chapters.

In Tab. 3.13 I list the median physical properties of the sample and the corresponding first and third quartiles. The 11 DSFGs are young (median $\tau_\star \sim 0.7$ Gyr) and forming stars at high rates, of the order of hundreds $M_\odot\, yr^{-1}$, leading to stellar masses of $\sim 10^{10} - 10^{11}\ M_\odot$. This very intense star formation activity is typically observed in the very central regions of the galaxies. Dusty (median $M_{dust} \sim 5 \times 10^8\ M_\odot$) and gas-rich (median total $M_{gas,\,tot} \sim 6 \times 10^{10}\, M_\odot$ and median molecular $M_{gas,\,mol} \sim 3 - 4 \times 10^{10}\, M_\odot$), these objects are the typical high-z (sub-)millimeter star-forming galaxies whose detections have been constantly growing since the advent of ALMA (see the review by Hodge and da Cunha, 2020). They are characterized by very high IR luminosities ($\sim$ a few $10^{12}\, L_\odot$), comparable to the typical values of the local ULIRGs and high-z DSFGs (see the review by Casey, Narayanan, and Cooray, 2014), revealing the aforementioned large interstellar dust content. The AGN fraction contributing to IR emission is negligible ($f_{AGN} = 1\%$ lies in the 75^{th} percentile): similar values are found in literature for high-z dusty galaxies (e.g., Elbaz et al., 2018; Barrufet et al., 2020). As to the ISM attenuation law, it results shallower (median $\delta_{ISM} \sim -0.5$) than the standard Calzetti et al. (2000), constrained in local

		Median	1st quartile	3rd quartile
z		2.086	1.794	2.497
SFR	$[M_\odot\, yr^{-1}]$	241	91	401
$\tau_\star$	[Myr]	746	334	917
$M_\star$	$[10^{10}\, M_\odot]$	6.5	5.7	9
$\delta_{\rm ISM}$		-0.5	-0.1	-0.7
$f_{\rm att}$	$[10^{-4}]$	2.5	1	3
$L_{\rm IR}$	$[10^{12}\, L_\odot]$	2.2	1.01	3.9
$M_{\rm dust}$	$[10^{8}\, M_\odot]$	4.6	1.9	10
$M_{\rm gas,\,tot}$	$[10^{10}\, M_\odot]$	6.3	3.2	10
$M_{\rm gas,\,mol}$	$[10^{10}\, M_\odot]$	4.0	0.6	5.8
$f_{\rm AGN}$	[%]	0.8	0.4	1

TABLE 3.13: Median, first and third quartiles of the following quantities (in the order): redshift (z), age of the burst ($\tau_\star$); SFR; stellar mass ($M_\star$); ISM attenuation spectral index ($\delta_{\rm ISM}$); IR luminosity ($L_{\rm IR}$); dust mass ($M_{\rm dust}$); gas mass ($M_{\rm gas}$: total and molecular); depletion time ($\tau_{\rm depl}$); AGN fraction in the IR domain ($f_{\rm AGN}$).

star-forming galaxies. These results, mainly derived from the SED fitting, basically reflect the selection performed on the FIR/millimeter catalogs in the GOODS-S field to build the sample (cf. Sect. 3.1.3).

In Fig. 3.5 the 11 galaxies of the sample are placed on the M$_\star$– SFR plane. SFRs, stellar masses and galaxy ages are derived from SED fitting, as described in Sect. 3.2.1. In the last decades, the majority of star-forming galaxies, from local to high-z Universe (at least out to $z \sim 4$), were found to follow an empirical relation between stellar mass and SFR, the *galaxy main-sequence* (e.g., Daddi et al., 2007; Noeske et al., 2007). In Fig. 3.5 I compare the position of the 11 DSFGs with the empirical determination of galaxy main-sequence by Speagle et al. (2014), at redshifts 1.7, 2, and 2.5 (color-coded), spanning the redshift range of the sample ($z_{\rm spec} \sim 1.5 - 3$): I note that the sources lie in correspondence or just above the relation at the corresponding redshift.

In Fig. 3.5 the solid black tracks represent the path onto M$_\star$– SFR plane followed by a high-z DSFG during its evolution, as predicted by the *in-situ* galaxy-BH co-evolution scenario. Time flow is indicated by the black arrows. The starting point of galaxy evolutionary track is determined by galaxy SFR when star formation ignites. During the early phase, star formation proceeds at an almost constant rate (i.e., SFR $\propto \tau^{1/2}$ and $M_\star \propto \tau^{2/3}$, which implies SFR $\propto M_\star^{1/3}$) and, increasing its stellar mass, the galaxy approaches the main-sequence of star-forming galaxies (Mancuso et al., 2016a, see their Eq. 7). Galaxy main-sequence emerges as a statistical *locus* in M$_\star$– SFR plane, where it is more probable to find star-forming galaxies because they spend in its vicinity most of their lifetime. Following the *in-situ* scenario, the less abundant population of star-forming galaxy that has been found to lie above the main-sequence (traditionally referred as *starbursts*; e.g., Rodighiero et al., 2011) is constituted by young galaxies that have still to accumulate most of their stellar mass. As soon as AGN feedback removes the fuel of star formation (effective for galaxies with $M_\star > 10^{10}\, M_\odot$), galaxy SFR is abruptly reduced and the object moves below the main-sequence, becoming a red and dead galaxy. Stars in Fig. 3.5 represent the 11 objects of the sample and are color-coded by galaxy age (i.e., $\tau_\star$), as obtained from SED fitting. Younger (i.e., bluer) objects lie to the upper-left side of the main-sequence at the corresponding redshift, while the elder (i.e., redder) lie in correspondence of

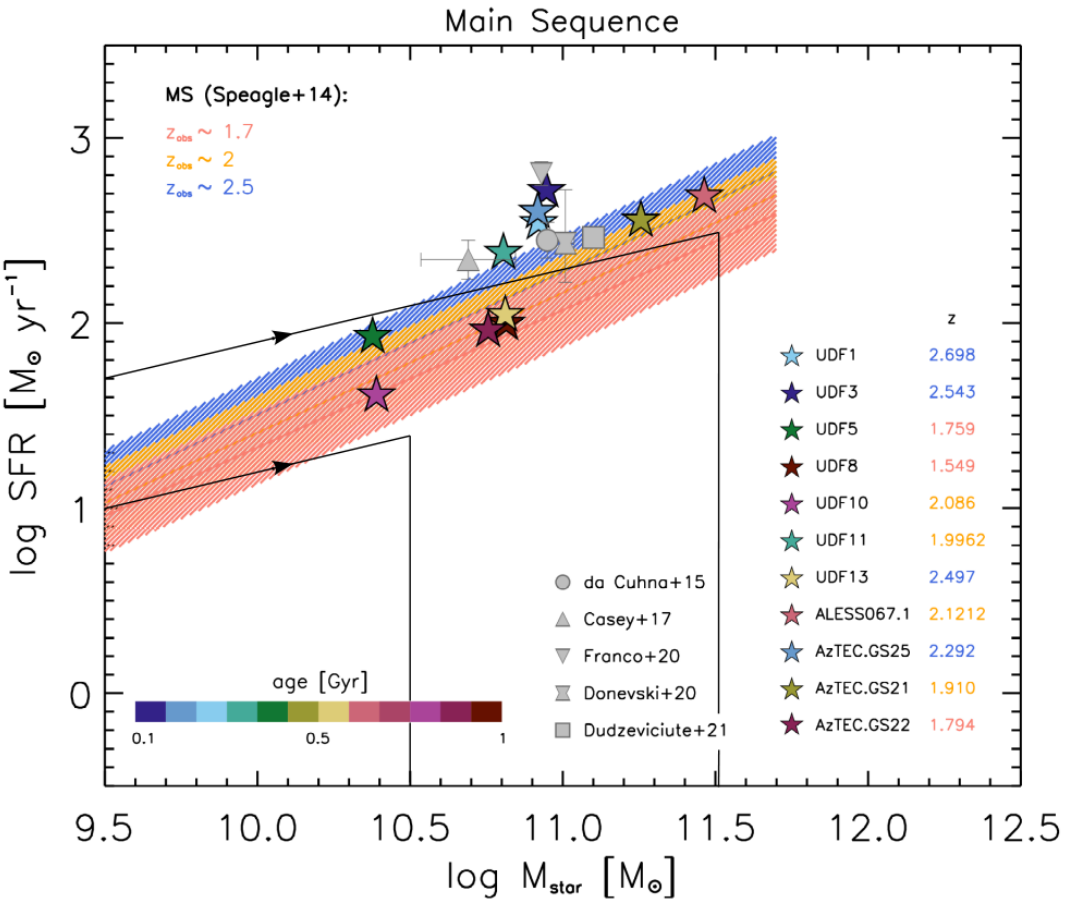

FIGURE 3.5: Empirical galaxy main-sequence of star-forming galaxies by Speagle et al. (2014) at different redshifts: $z \sim 1.5$ in red, $z \sim 2$ in orange, $z \sim 3.5$ in blue, with its 1σ scatter (~ 0.2 dex). Over-plotted stars stand for the galaxies of this work, considering the values of SFR and $M_\star$ derived from SED fitting. Symbols are color-coded by galaxy age (i.e., $\tau_\star$). Error bars are compatible with symbol size. Galaxy redshift is indicated in the legend next to galaxy ID and color-coded by the corresponding redshift bin. Grey symbols represent the median values obtained by some other existing samples of high-z DSFGs, as specified in legend. For reference, the evolutionary tracks predicted by the *in-situ* co-evolution scenario are displayed in black (solid lines; Mancuso et al., 2016a).

it, as predicted by the *in-situ* scenario. All in all, these galaxies are almost main-sequence objects and, as such, they should show some signatures indicating the presence of an obscured and/or accreting AGN, and possibly some evidences of its activity (i.e., outflows/winds). However, AGN contribution to the galaxy IR emission is negligible: the median value for our sample attains less than 1%.

The median values of stellar mass and SFR of the sample (i.e., median $M_\star \sim 6.5\times10^{10}\,M_\odot$ and median SFR$\sim 241\,M_\odot\,yr^{-1}$) are consistent (i.e., lie in the same area of $M_\star-$ SFR plane) with the median values found in many recent studies on high-z DSFGs exploiting SED fitting (e.g. da Cunha et al., 2015; Casey et al., 2017; Franco et al., 2020; Donevski et al., 2020; Dudzevičiūtė et al., 2021, grey symbols in Fig. 3.5), spanning the photometric redshift range $0.5 < z < 5$. These results refer to samples of different sizes, including large statistically significant samples of DSFGs selected in the FIR-mm domain (Donevski et al., 2020; Dudzevičiūtė et al., 2021), and smaller samples of a few tenths of objects, with different selection criteria.

Figs. 3.6, 3.7 and 3.8 show the statistical relationships derived in Chapter 2 for the population of high-z star-forming progenitors of massive quiescents, with their 1σ scatter, at redshifts 1.7, 2, and 2.5 (color-coded). Stars represent the 11 DSFGs and are color coded by galaxy age (i.e., $\tau_\star$). They match the model prediction within 2σ, again witnessing that the main drivers of the evolution of the 11 DSFGs can be traced back mostly to in-situ processes. The superimposed grey symbols represent the median values found by da Cunha et al. (2015), Casey et al. (2017), Franco et al. (2020), Donevski et al. (2020), and Dudzevičiūtė et al. (2021) as specified in the legend. The corresponding outcomes, found also for statistical samples of DSFGs in the photometric redshift range $0.5 < z_{\rm phot} < 5$ (see Donevski et al., 2020; Dudzevičiūtė et al., 2021), are in agreement with both the predictions by the analytic model and the corresponding median values of the sample, i.e. $M_{\rm dust} \sim 4.6\times10^8\,M_\odot$ and $M_{\rm gas,\,mol} \sim 3.2\times10^{10}\,M_\odot$ (cf. Tab. 3.13). It follows that the approach and selection criteria presented in here do not introduce any substantial bias and may be applied to statistical samples of spectroscopically confirmed DSFGs, as soon as they will be available. In the following I briefly comment on the outcomes, going into more details.

The dust masses of the 11 DSFGs, shown in Fig. 3.6, are derived as it is described in Sect. 3.2.2. All the galaxies have a very high content of interstellar dust ($M_{\rm dust} > 10^8\,M_\odot$), that is almost consistent with the relations obtained by applying the analytic model described in Chapter 2 to the dusty massive galaxy population at high-z. Indeed, the model predicts a very rapid ($\sim 10^7 - 10^8$ yr) pollution of the ambient by dust and metals. The interstellar dust content does not show any significant trend with galaxy age (i.e. the burst duration, $\tau_\star$). Four galaxies (UDF5, UDF10, AzTEC.GS25, AzTEC.GS22) are outliers (but still consistent with the statistical relation within 2σ): although they are very close to galaxy main-sequence at the corresponding redshift (cf. Fig. 3.5), they show a dust-to-stellar mass ratio very similar to that of ALMA starbursts in the sample studied by Donevski et al. (2020), i.e. $M_{\rm dust}/M_\star \gtrsim 0.01$. This evidence may indicate that they are experiencing a quicker growth of dust in their ISM (on timescales shorter than 10^8 yr), or that they are characterized by much longer dust destruction timescales, preserving larger grains longer (see Donevski et al., 2020, their Sect. 4).

In Fig. 3.7 I compare the molecular gas mass estimates for the 11 DSFGs (stars and circles, color coded by galaxy age, i.e., $\tau_\star$) with the predictions by the analytic model presented in Chapter 2 (colored shaded area, including their 1σ scatter), for three redshift bins spanning the sample redshift range and the median values recently found by some studies of high-z DSFGs exploiting SED fitting (i.e., Casey

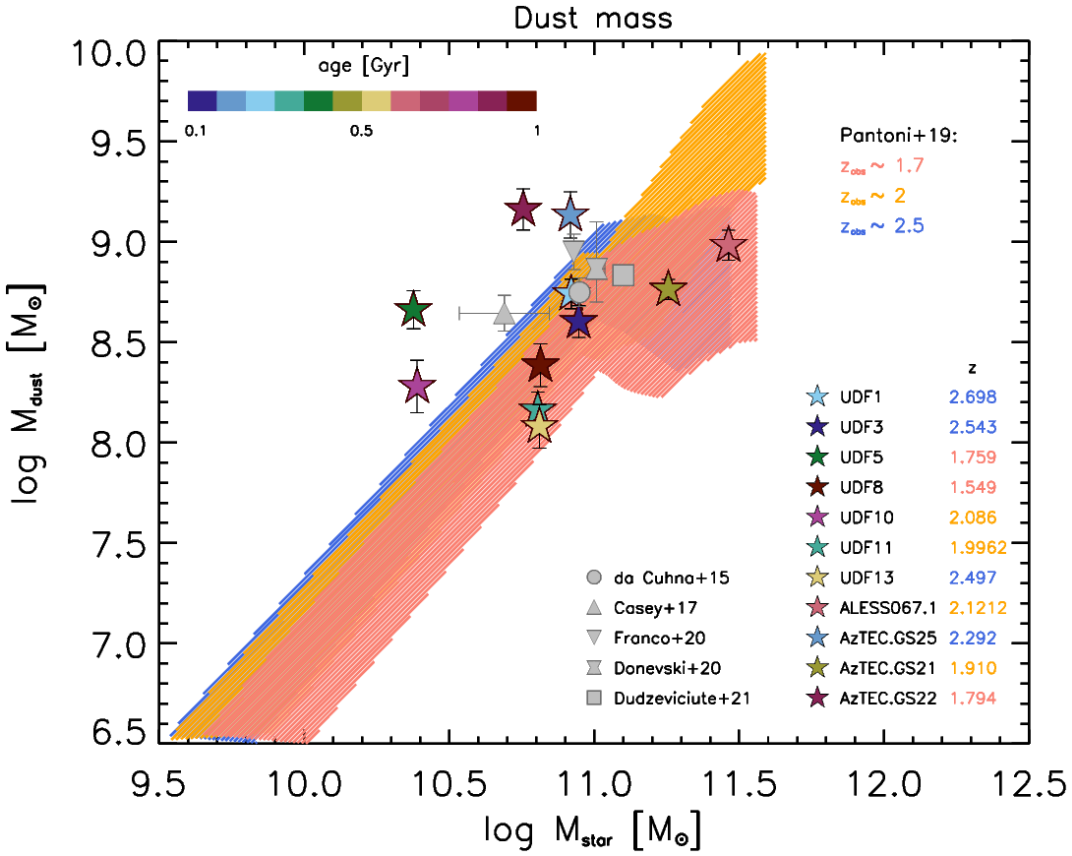

FIGURE 3.6: Statistical relationship between dust mass $M_{\rm dust}$ and stellar mass $M_\star$ for the high-z star-forming progenitors of ETGs by the analytic model described in Chapter 2 at three different observational redshifts: $z \sim 1.5$ (red), $z \sim 2$ (orange), $z \sim 2.5$ (blue), with its 1σ scatter (shaded area). Stars represent the outcomes for the 11 DSFGs of the sample derived from SED fitting as explained in Sect. 3.2.2 and corrected following Magdis et al. (2012). Symbols are color-coded by galaxy age (i.e., $\tau_\star$). Galaxy redshift is indicated in the legend next to galaxy ID and color-coded by the corresponding redshift bin. Grey symbols represent the median values obtained by some other existing samples of high-z DSFGs, as specified in legend.

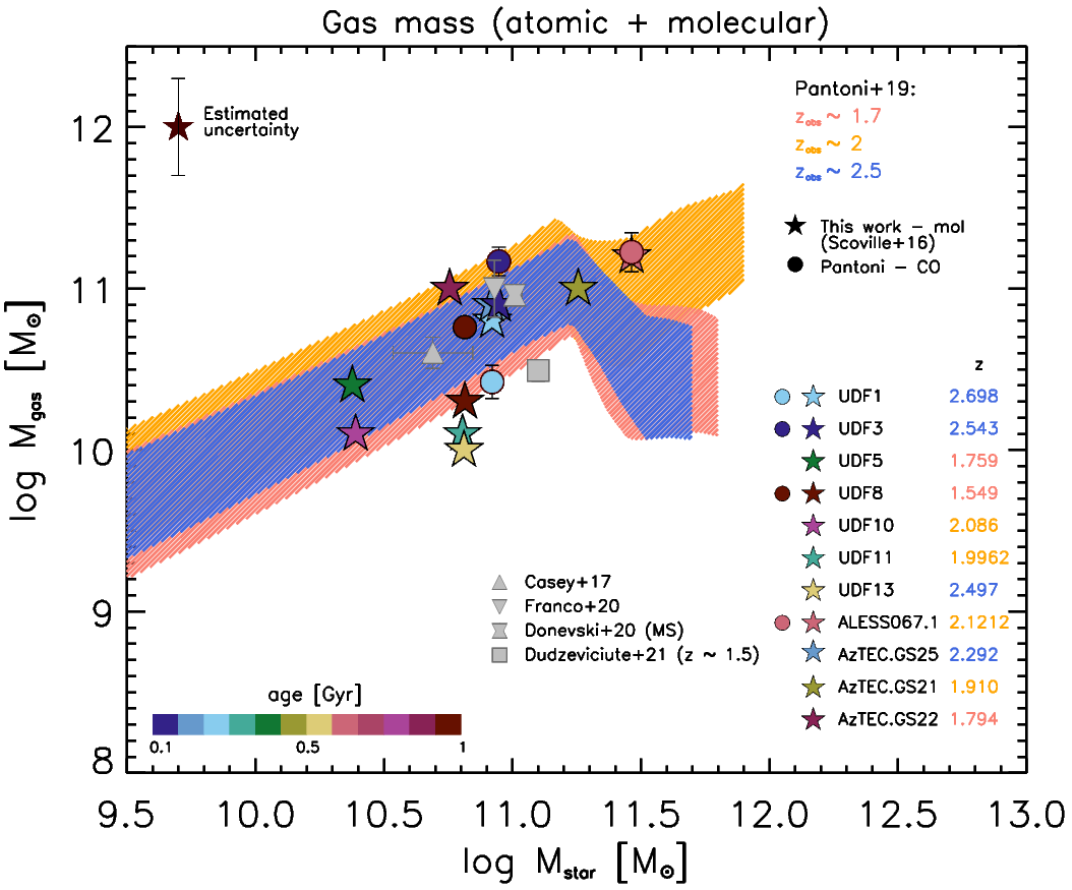

FIGURE 3.7: Statistical relationship between gas mass M_{gas} and stellar mass $M_\star$ for the high-z star-forming progenitors of ETGs by the analytic model presented in Chapter 2 at three different observational redshifts: $z \sim 1.5$ (red), $z \sim 2$ (orange), $z \sim 2.5$ (blue), with its 1σ scatter (shaded area). Stars represent the outcomes for the 11 DSFGs of our sample derived from SED fitting as explained in Sect. 3.2.2, following the approach by Scoville et al. (2016). The estimated uncertainty (~ 0.3 dex) is consistent with the 1σ scatter of the relation and is shown in the left top corner of the plot. Circles stand for the H_2 masses estimated from $J > 1$ CO lines in this work (see Chapter 4). Symbols are color-coded by galaxy age (i.e., $\tau_\star$). Galaxy redshift is indicated in the legend next to galaxy ID and color-coded by the corresponding redshift bin. Grey symbols represent the median values obtained by some other existing samples of high-z DSFGs, as specified in legend.

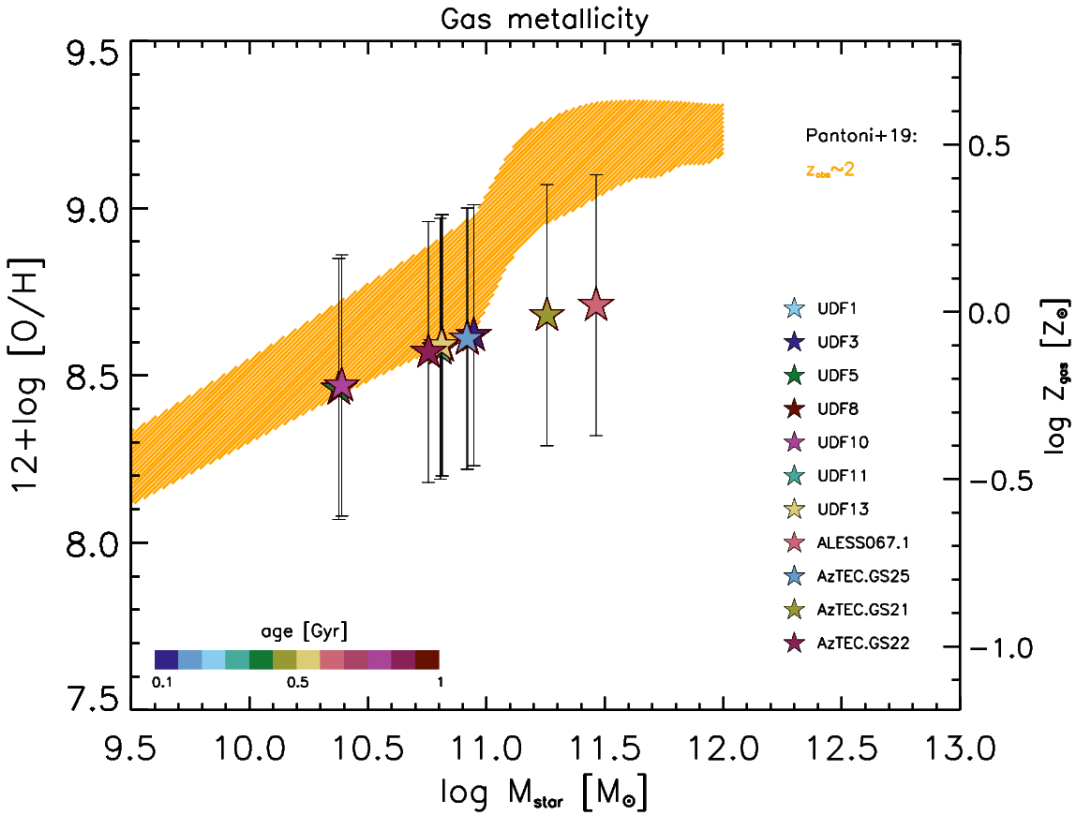

FIGURE 3.8: Statistical relationship between gas metallicity $Z_{\rm gas}$ and stellar mass $M_\star$ for high-z star-forming progenitors of ETGs derived from the analytic solutions presented in Chapter 2 at $z \sim 2$ (orange), with its 1σ scatter (shaded area). Stars represent the outcomes for the 11 DSFGs of the sample derived as explained in Sect. 3.2.2. Symbols are color-coded by galaxy age (i.e., $\tau_\star$).

et al., 2017; Franco et al., 2020; Donevski et al., 2020; Dudzevičiūtė et al., 2021, grey symbols). They are in great accordance, within the errors. No significant trend emerges, neither in redshift or galaxy age. Stars represent the molecular gas mass estimates that derived from dust FIR continuum following the approach by Scoville et al. (2016), as described in Sect. 3.2.2. Error bars, shown in the top left corner of Fig. 3.7, are comparable to the 1σ scatter of the statistical relationships that are obtained by applying the analytic model described in Chapter 2 to the high-z population of DSFGs. Even if the latter predicts the evolution of the total gas mass, i.e. $HI + H_2$, with galaxy stellar mass (at a given redshift), comparing the two is still valid since we expect the molecular phase to be definitely dominant for these objects. Circles represent the estimated hydrogen molecular mass derived from $J > 1$ CO lines (see Chapter 4), available for 4 galaxies, i.e. UDF1, UDF3, UDF8 and ALESS067.1. The H_2 masses are estimated by assuming an $\alpha_{\rm CO} = 3.6\ M_{\odot}$(K km s^{-1} pc^2)$^{-1}$, consistently with the approach followed by Scoville et al. (2016). The outcomes are almost in agreement within the error bars (the comparison is sensible as H_2 constitutes the large majority of the molecular gas content in galaxies: even when corrected for Helium mass by a factor 1.36, the estimations are still consistent). However, some differences can be traced back to the fact that dust and CO emission often sample diverse (more compact/extended) galaxy regions, respectively (see e.g., Carilli and Walter, 2013; Scoville et al., 2014; Scoville et al., 2016; Scoville et al., 2017; Elbaz et al., 2018).

All the galaxies have almost solar metallicities (even if error bars are huge; see Fig. 3.8), and do not show any significant trend with galaxy age. Gas metallicity is compared solely with the statistical relation at $z \sim 2$, since it does not show a significant evolution in redshift and gas metallicity of the 11 DSFGs is not strictly constrained due to the big uncertainties, i.e. ~ 0.4 dex.

The large content of cold gas ($10^{10} \lesssim {\rm M_{gas,mol}/M_{\odot}} \lesssim 10^{11}$), interstellar dust ($M_{\rm dust} > 10^8\ M_{\odot}$) and stars ($3\times10^{10} \lesssim {\rm M_{\star}/M_{\odot}} \lesssim 3\times10^{11}$), associated with relatively short depletion timescales (~ 200 Myr),suggest that the 11 DSFGs are the high-z star-forming progenitors of massive elliptical galaxies, caught in the *compaction phase*, i.e. a phase characterized by clump/gas migration toward the galaxy center, where the intense dust-enshrouded star formation takes place and most of the stellar mass is accumulated (see Lapi et al., 2018).

This statement is furthermore confirmed by the detection of an X-ray emitting AGN for the majority of DSFGs in the sample (Sect. 3.2.2), that does not emerge in the radio domain. Indeed, while the star formation ignites in the host galaxy, the *in-situ* scenario predicts the growth of the central BH to occur at mild super-Eddington rates so that rotational energy cannot be easily funnelled into jets to power radio emission: the AGN is expected to be radio silent and to shine as an X-ray source. This is possibly the case of the objects in the sample that are located to the left-upper side of galaxy main-sequence (cf. Fig. 3.5). Then, following the *in-situ* scenario, the AGN X-ray luminosity is expected to overwhelm that associated with star formation, becoming clearly detectable at luminosities $L_X \gtrsim 10^{42}$ erg s^{-1} (cf. Fig. 3.4: most of the X-ray detected DSFGs in the sample have $L_X > 10^{42}$). AGN power progressively increases to values similar to or even exceeding that of star formation in the host galaxy, originating outflows that can quench star formation in the host galaxy by heating and removing interstellar gas and dust from the ISM (i.e., AGN energy/momentum feedback). Still, these jets (that are driven by thin disk accretion) are rather ineffective in producing radio emission so that the AGN is radio quiet and does not emerge clearly from the host galaxy emission in the radio domain (see Mancuso et al., 2017, and references therein). This must be the case of the galaxies

that perfectly overlap galaxy main-sequence at the corresponding redshift (cf. Fig. 3.5). For a few objects the radio emission appears to be more extended than the FIR one, possibly being a signature of the forthcoming AGN feedback (e.g., UDF11; see Rujopakarn et al., 2016). Further analysis can be found in Chapter 4, where I discuss the evidences coming from multi-wavelength spatially-resolved images and CO spectral lines, in the framework of galaxy-BH co-evolution.

As a consequence of AGN feedback, star formation must be abruptly quenched in a few hundreds of Myr: afterwards stellar populations evolve passively and the galaxy must become a red and dead ETG.

3.4 Summary

I investigated the integral properties of 11 DSFGs at the peak of Cosmic SFH, that I selected in the (sub-)millimeter regime requiring the following criteria to be fulfilled for each galaxy: 3 or more detections in the optical domain ($\lambda_{\rm obs} = 0.3 - 1$ μm); 6 or more detections in the NIR+MIR bands ($\lambda_{\rm obs} = 1 - 25$ μm); 2 or more detections in the FIR band ($\lambda_{\rm obs} = 25 - 400$ μm); spectroscopically confirmed redshift in the range $1.5 < z_{\rm spec} < 3$; 1 or more detections and/or upper limits in the radio and X-ray regimes. The sources are located in one of the deepest multi-band field currently available, the GOODS-S.

I exploited the extensive multi-wavelength photometry of the GOODS-S field, from the X-rays to the radio band, to reliably reconstruct and precisely model galaxy SED with CIGALE, by using a physically-motivated recipe to describe stellar light attenuation by dust. By fitting galaxy SED, I extracted the main integral properties of the 11 DSFGs (i.e., SFR, stellar mass, stellar attenuation by dust, dust temperature, IR luminosity). I exploited the Rayleigh-Jeans dust continuum to estimate galaxy dust mass ($M_{\rm dust}$) and gas mass (total $M_{\rm gas,\,tot}$ and molecular $M_{\rm gas,\,mol}$). Finally, I took advantage of the X-ray and radio photometry to guess the presence of an AGN and its eventual contribution to IR light.

The 11 DSFGs of are (almost) main-sequence objects, with a median $M_\star = 6.5 \times 10^{10}\,M_\odot$ and SFR $\sim 250\,M_\odot\,{\rm yr}^{-1}$. They are experiencing an intense and dusty (median $L_{\rm IR} \sim 2 \times 10^{12}\,L_\odot$) burst of star formation, with typical duration $\tau_\star$ ranging between 0.2 and 1 Gyr. Although their young age, the interstellar dust content is high ($M_{\rm dust} > 10^8\,M_\odot$), possibly due to a very rapid enrichment of the ISM (on typical timescales of $10^7 - 10^8$ yr). The gas mass (median $M_{\rm gas,\,tot} \sim 6{\times}10^{10}\,M_\odot$ and $M_{\rm gas,\,mol} \sim 3{\times}10^{10}\,M_\odot$), fuelling the dusty star formation, will be rapidly depleted, over a median timescale $\tau_{\rm depl} \sim 200$ Myr. Nine objects out of eleven have an X-ray luminous ($L_{\rm 2-10keV} \gtrsim 10^{42}$ erg s^{-1}) counterpart in the *Chandra* $\simeq 7$ Ms catalog and two of them are clearly dominated by the active nucleus emission ($L_{\rm 2-10keV} \gtrsim 10^{43} - 10^{44}$ erg s^{-1}). The radio luminosity is consistent with the emission coming from galaxy star formation, suggesting that the AGN, if present, should be radio silent or quiet.

I gave a possible interpretation of the outcomes in light of the *in-situ* galaxy-BH co-evolution scenario (Mancuso et al., 2016a; Mancuso et al., 2016b; Shi et al., 2017; Mancuso et al., 2017; Lapi et al., 2018). In particular I compared the observational results with the predictions by the analytic model presented in Chapter 2. I found the results derived from SED fitting to match the model predictions within their 2σ scatter, suggesting that the main drivers of the 11 DSFGs evolution can be mostly traced back to local condensation processes. The majority of the 11 galaxies is caught in the compaction phase and I expect them to be quenched by the AGN feedback in $\lesssim 10^8$ yr. Their subsequent evolution must be passive, mainly driven by stellar

population aging and mass additions by dry merger events. Ultimately they should become compact quiescent galaxies or massive ETGs.

I compared the results obtained for the 11 spectroscopically confirmed $z \sim 2$ DSFGs with other recent good studies on high-z DSFGs, exploiting SED fitting. I found a great agreement between the median values of the main physical quantities estimated for these galaxies, such as stellar mass, gas mass and dust mass. I conclude that the approach and selection criteria described in this Chapter do not introduce any substantial bias and may be applied to statistical samples of spectroscopically-confirmed DSFGs, as soon as they will be available.

From the analysis it clearly emerges the importance of combining multi-band photometry, physically motivated prescription for SED fitting and self-consistent predictions from theory in order to characterize the role of high-z DSFGs in the context of galaxy formation and evolution, along with the impact of galaxy interactions and AGN feedback in determining galaxy evolution.

Chapter 4

The role of high-resolution imaging

In this Chapter I will complement the photometric analysis presented in Chapter 3 with the study of galaxy multi-wavelength continuum and CO emission lines at the best spatial resolution publicly available at the moment ($\Delta\theta \lesssim 1$ arcsec). The latter analysis, providing information on galaxy morphology, multi-band sizes and gas kinematics, is recognized to have a crucial role in gaining a deeper insight into dusty galaxy formation and evolution (see e.g., Barro et al., 2016b; Barro et al., 2017; Rujopakarn et al., 2016; Elbaz et al., 2018; Lapi et al., 2018; Rujopakarn et al., 2019; Kaasinen et al., 2020).

Spatially-resolved studies assume an essential role in this respect, since they may provide a precise description of the baryonic processes occurring inside galaxies, on (sub-)kpc scales, and may be used to determine their respective importance in driving DSFG evolution. Measuring and comparing galaxy sizes and morphologies in different spectral bands is informative of the processes that are driving the ongoing burst of star formation, the accretion of central BH and its eventual activity, and can be suggestive of the AGN action onto the whole host galaxy evolution. Indeed, galaxy morphology is determined by the combined effects of gas condensation and star formation along with eventual interactions with the surrounding ambient and/or companions (Lacey et al., 2016; Calura et al., 2017; Popping, Somerville, and Galametz, 2017; Lapi et al., 2018; Davé et al., 2019). All the astrophysical processes leading galaxy evolution reveal themselves in diverse spectral ranges. For example, optical rest-frame light samples the stellar component and, thus, the spatial distribution into galaxies of the most recent burst of star formation; rest-frame MIR and FIR emission samples the AGN torus and the interstellar dust; CO emission traces the molecular gas. As a consequence, galaxy size, computed at different wavelengths, provides a measure of the typical scales on which the diverse ongoing astrophysical processes are effective and gives an hint on their origin, their role in fuelling galaxy star formation and central BH accretion.

Furthermore, the detection of atomic and molecular spectral lines allow to investigate the gas phase properties, such as its dynamical status and kinematics (e.g., Tadaki et al., 2015; Talia et al., 2018; Chen et al., 2017; Hodge et al., 2019). In particular, molecular lines are essential to guess the presence of an AGN, through e.g. the identification of molecular outflows triggered by the central engine, that are expected to extend over a $\Delta v \gtrsim 500 - 1000$ km/s (e.g. Cicone et al., 2014; Fiore et al., 2017; Bischetti et al., 2019; Herrera-Camus et al., 2019). As such, molecular lines may be essential to characterize the AGN impact on the host galaxy (i.e., AGN *feeding & feedback* cycle; e.g., Bischetti et al., 2021) and, on a statistical basis, on DSFG evolution.

In the following Sections I will exploit ALMA continuum maps and data cubes at the highest spatial resolution currently available for the 11 DSFGs to get a deeper

insight into the processes driving dusty galaxy evolution. Then, I will combine the outcomes with galaxy multi-band spatially-resolved emission (mainly in the optical and radio bands), in order to sample the principal astrophysical processes occurring inside galaxies.

The final panchromatic view of the galaxy will combine the outcomes obtained from the accurate fit of its SED, as presented in Chapter 3 (Sect. 3.2.1), with multi-band continuum imaging and CO emission maps at high-resolution. I will show that this approach allows to unbiasedly extract information from galaxy multi-wavelength emission and shed light on the individual galaxy evolution.

4.1 Continuum emission

The (sub-)millimeter light of $z \sim 2$ star-forming galaxies traces the thermal emission coming from interstellar dust grains, that are heated by newly formed stars (e.g., Draine, 2003). Its size and the spatial distribution are essential to locate and characterize the dust-obscured star formation, that in high-z DSFGs occurs in the form of intense bursts (e.g. Casey, Narayanan, and Cooray, 2014). In this Section I will deal with the analysis of public ALMA archival continuum maps containing the 11 DSFGs in my sample, with the main scope of measuring the size of their (sub-)millimeter emission.

As first step, I selected the ALMA projects publicly available in the ALMA Archive with the best spatial resolution ($\Delta\theta \lesssim 1$ arcsec) in the wavelength range $\lambda_{\rm obs} \sim 500\,\mu$m $-$ 3 mm (corresponding to the frequency range $\nu_{\rm obs} \sim 100 - 600$ GHz). Almost all of the best spatially-resolved continuum maps are in ALMA B6 and B7 that, indeed, constitute a very good compromise between spatial resolution and the sampled wavelength. This allowed to provide the most homogeneous information on dust continuum emission. For AzTEC.GS22 it was possible to benefit of even better spatial resolution, offered by a B9 map. The code and member ous of the selected ALMA projects, along with the observational band and angular resolution, are listed in Tab. 4.1. In the same table, I list also the continuum flux densities (S_ν) and the corresponding sizes (θ_ν) of the 11 sources. I estimated the flux density errors as:

$$eS_\nu = \sqrt{(\mathrm{rms})^2 + (0.1 \times S_\nu)^2} \tag{4.1}$$

that is the quadratic sum of the ALMA continuum map rms and a conservative estimation of flux calibration accuracy, i.e. $\sim$ 10% for the ALMA bands of interest: B6, B7 and B9.

The source sizes (θ_ν) has been measured by performing a 2D Gaussian fit of the source emission on the ALMA map, using the task *imfit* embedded in the CASA viewer (CASA release 5.4.0-70). Some of the detections (six out of eleven) are not resolved in the corresponding ALMA map: in such a case the synthesized beam size (labelled with the apex *sb* in Tab. 4.1) provides an upper limit on the source size. I further note that in such cases the level of noise does not allow to extract the sizes from a fit in the visibility domains.

I derived the linear circularized size of galaxy (sub-)millimeter emission by using the following expression:

$$r_{\rm circ}(\nu)\,[\mathrm{kpc}] = \frac{a}{2}\,[\mathrm{arcsec}]\,\sqrt{\frac{b}{a}}\;c\,[\mathrm{kpc/arcsec}] \tag{4.2}$$

ID	**Project code**	**Member ous**	$\nu_{\mathbf{band}}$	$\Delta\theta = \mathbf{a}_{\Delta\theta} \times \mathbf{b}_{\Delta\theta}$ [arcsec × arcsec]	$\mathbf{S}_\nu$ [μJy]	$\theta_\nu = \mathbf{a}_\nu \times \mathbf{b}_\nu$ [arcsec × arcsec]
UDF1	2017.1.00001.S	A001/X1288/X4c3	B7	0.10×0.09	2900 ± 300	$0.123 \pm 0.006 \times 0.103 \pm 0.005$
UDF3	2017.1.00001.S	A001/X1288/X4c7	B7	0.08×0.07	1600 ± 200	$0.203 \pm 0.014 \times 0.111 \pm 0.009$
UDF5	2012.1.00173.S	A002/X5a9a13/X7e0	B6	0.62×0.52	311 ± 49^{D}	0.62×0.52^{sb}
UDF8	2012.1.00173.S	A002/X5a9a13/X7e0	B6	0.62×0.52	208 ± 46^{D}	$1.42 \pm 0.35 \times 0.66 \pm 0.19$
UDF10	2012.1.00173.S	A002/X5a9a13/X7e0	B6	0.62×0.52	184 ± 46^{D}	0.62×0.52^{sb}
UDF11	2012.1.00173.S	A002/X5a9a13/X7e0	B6	0.62×0.52	186 ± 46^{D}	$1.02 \pm 0.28 \times 0.61 \pm 0.21$
UDF13	2015.1.01074.S^{A}	A001/X2d8/Xfd	B7	0.17×0.15	910 ± 170	0.17×0.15^{sb}
ALESS067.1	2012.1.00307.S	A002/X7d1738/X103	B7	0.14×0.12	4500 ± 400	$0.35 \pm 0.05 \times 0.18 \pm 0.03$
AzTEC.GS25	2012.1.00983.S	A002/X7d1738/X169	B7	0.20×0.16	5900 ± 500	$0.38 \pm 0.03 \times 0.22 \pm 0.02$
AzTEC.GS21	2015.1.00098.S^{A}	A001/X2fe/Xaea	B6	0.18×0.16	954 ± 74	0.18×0.16^{sb}
AzTEC.GS22	2017.1.01347.S	A001/X12a3/X80e	B9	0.49×0.33	6400 ± 880	0.49×0.33^{sb}

TABLE 4.1: ALMA continuum observation settings and results. In the order: ID from literature; project code; member observing unit set ID; frequency band (ν_{band}); angular resolution (i.e., restoring beam, $\Delta\theta$); flux density (S_ν); FWHM of the Gaussian fit of the angular size deconvolved from beam (θ_ν). ALMA bands frequency range: B6 (211.21 – 231.20) GHz; B7 (335.50 – 351.48) GHz; B9 (662.53 – 685.56) GHz. For unresolved sources (labelled with ^{sb}) the synthesized beam size is reported and treated as an *upper limits* to the actual source size. ALMA observations labelled with the apex A have been re-imaged in the context of ARI-L project (https://almascience.eso.org/alma-data/aril; see also Massardi et al., 2021). Flux densities labelled with the apex D are taken from Dunlop et al. (2017).

ID	z	c [kpc/arcsec]	$a_{\rm ALMA}$ [arcsec]	$b_{\rm ALMA}$ [arcsec]	$r_{\rm ALMA}$ [kpc]	$a_{\rm H}$ [arcsec]	$b_{\rm H}$ [arcsec]	$r_{\rm H}$ [kpc]
UDF1	2.698	8.121	0.123 ± 0.006	0.103 ± 0.005	0.46	0.39 ± 0.02	(0.68 ± 0.02) *a*	2.6
UDF3	2.543	8.224	0.203 ± 0.014	0.111 ± 0.009	0.62	0.211 ± 0.001	(0.835 ± 0.005) *a*	1.6
UDF5	1.759	8.632	< 0.62	< 0.52	< 2.5	0.636 ± 0.003	(0.174 ± 0.002) *a*	2.3
UDF8	1.549	8.647	1.42 ± 0.35	0.66 ± 0.19	4.1	0.978 ± 0.004	(0.452 ± 0.002) *a*	5.7
UDF10	2.086	8.508	< 0.62	< 0.52	< 2.5	0.279 ± 0.002	(0.678 ± 0.004) *a*	2.0
UDF11	1.9962	8.551	1.02 ± 0.28	0.61 ± 0.21	3.4	0.601 ± 0.002	(0.766 ± 0.001) *a*	4.5
UDF13	2.497	8.256	< 0.17	< 0.15	< 0.65	0.182 ± 0.001	(0.604 ± 0.004) *a*	1.2
ALESS067.1	2.1212	8.489	0.35 ± 0.05	0.18 ± 0.03	1.1	0.88 ± 0.07	(0.758 ± 0.021) *a*	6.5
AzTEC.GS25	2.292	8.390	0.38 ± 0.03	0.22 ± 0.02	1.2	0.28 ± 0.03	(0.58 ± 0.04) *a*	1.8
AzTEC.GS21	1.910	8.586	< 0.18	< 0.16	< 0.7	0.48 ± 0.01	(0.80 ± 0.01) *a*	3.7
AzTEC.GS22	1.794	8.624	< 0.49	< 0.33	< 1.7	0.72 ± 0.02	(0.27 ± 0.02) *a*	3.2

TABLE 4.2: ALMA and H_{160} (HST/WFC3) circularized sizes. In the order: ID from literature; spectroscopic redshift (z); conversion factor angular-to-linear size (c); ALMA major projected axis ($a_{\rm ALMA}$); ALMA minor projected axis ($b_{\rm ALMA}$); ALMA linear circularized size ($r_{\rm ALMA}$); H_{160} (HST/WFC3) major projected axis ($a_{\rm H}$); H_{160} (HST/WFC3) minor projected axis ($b_{\rm H}$); H_{160} (HST/WFC3) linear circularized size ($r_{\rm H}$). Sizes labelled with the symbol "<" are just *upper limits* on the source size, that is given by the circularized synthesized beam in kpc. References and errors on source redshift can be found in Tab. 3.1.

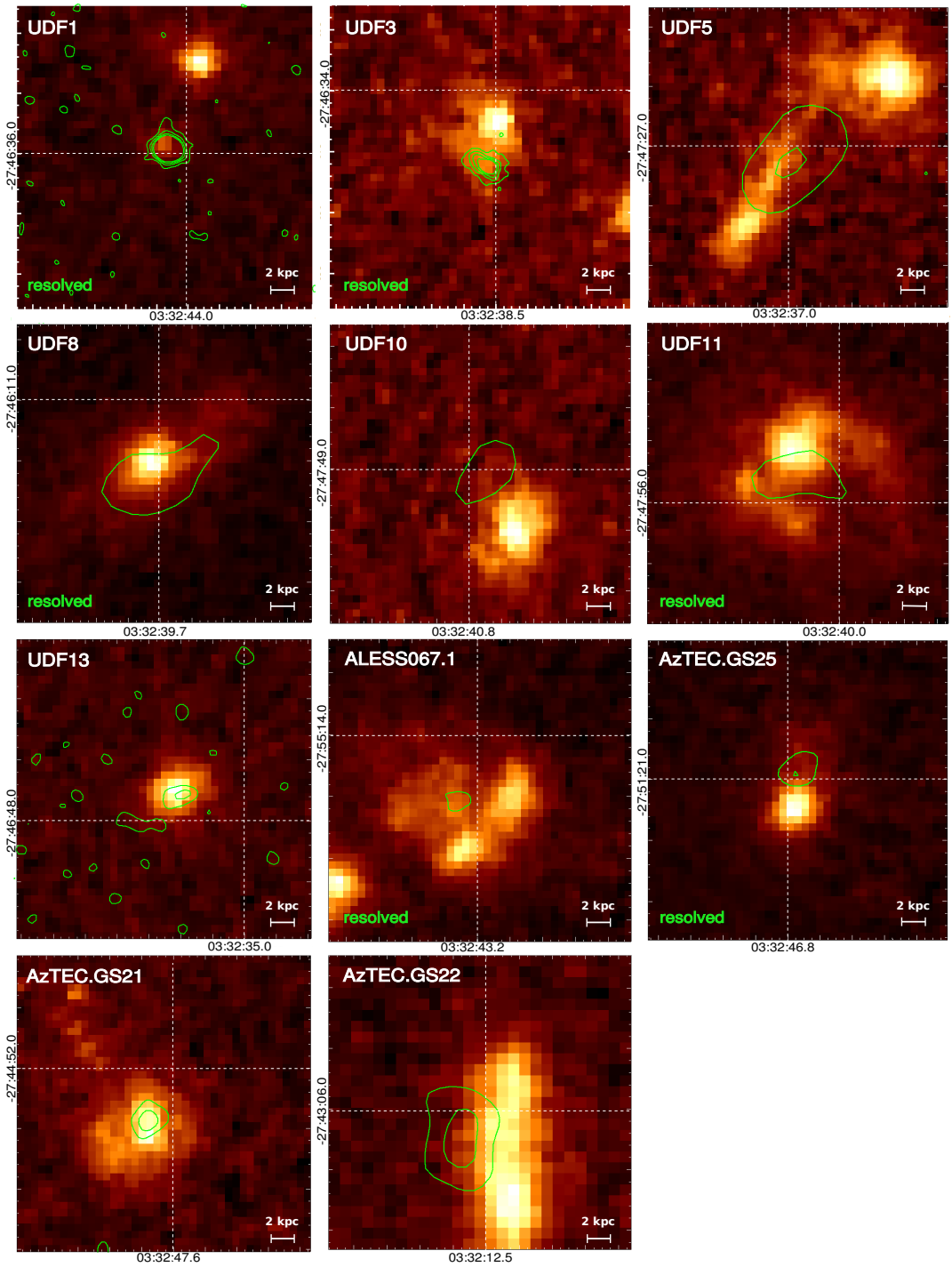

FIGURE 4.1: Postage stamps of 2.5 arcsec × 2.5 arcsec. ALMA continuum contours at $[1, 2, 3, 4] \times 2.5\sigma$ (green solid lines) are overlaid on F160W HST/WFC3 images (corrected for astrometry). Resolved ALMA sources are labelled as such in the bottom left corner of the panel. In the x-axis and y-axis I show the Right Ascension (RA) in h:m:s and the Declination (DEC) in deg:arcmin:arcsec, respectively, for a reference point on the map.

where a and b are the major and minor projected axes; c is the angular-to-linear conversion factor, which depends on redshift and cosmology[1]. a and b are listed in Tab. 4.2, along with the resulting circularized ALMA sizes ($r_{\rm ALMA}$, in kpc). When the source is not (entirely) resolved it is indicated just an upper limit on its size (labelled with the symbol "<"), given by the circularized synthesized beam in kpc. For reference I list also the circularized optical radii for the 11 DSFGs that are computed using the results by van der Wel et al. (2012) and Rujopakarn et al. (2019).

In Fig. 4.1 I show the ALMA continuum contours (at $[1, 2, 3, 4]\times2.5\sigma$) overlapping the HST ($H_{160}$) image of the galaxies. Due to the scarce spatial resolution of *Chandra* map (Luo et al., 2017), I do not show galaxy X-ray emission on the HST maps, but I note that its peak overlaps both the optical and (sub-)millimeter galaxy counterparts (this is valid for the nine galaxies that are detected in the x-rays; see Tab. 3.3). The HST astrometry is corrected using the position of Gaia sources (Gaia Collaboration et al., 2016) that are located in the same field of the 11 DSFGs. The mean error of $\sim [+2, -10]\times10^{-5}$ degrees ($\Delta_{\rm RA}\sim70$ mas, $\Delta_{\rm DEC}\sim-360$ mas), in agreement with the astrometric error between VLA and HST images shown by Rujopakarn et al. (2016), i.e. $\Delta_{\rm RA}=+80\pm110$ mas, $\Delta_{\rm DEC}=-260\pm130$ mas (see also e.g. Dunlop et al., 2017; Elbaz et al., 2018). The astrometric correction on AzTEC.GS22 HST H_{160} image is of $\sim [+15, +5]\times10^{-5}$ degrees, while no correction has been applied on AzTEC.GS25 optical coordinates. After that, the bulks of the stellar and dust emission coincide within the uncertainties of the astrometric correction ($\sim$ 100 mas) and the beam resolution, for most of the galaxies. An eventual remaining shift tells us that the peaks of optical and (sub-)millimeter emission are not exactly coincident, possibly due to dust obscuration of stellar light.

4.2 Spectroscopic emission

CO transitions can be used to trace the molecular gas phase inside galaxies and derive its mass, density and kinetic temperature (e.g. Yang et al., 2017; Joblin et al., 2018; Boogaard et al., 2020). A CO spectral line energy distribution (SLED) peaking at $J>3$ is typically considered an evidence of shocks and/or nuclear activity, originating from the so called X-ray Dominated Regions (XDRs, see Vallini et al., 2019), while the low-J lines are more commonly associated to star-formation (e.g. Pozzi et al., 2017; Mingozzi et al., 2018; Carniani et al., 2019), originating in the Photo-Dissociation Regions (PDRs, see Hollenbach and Tielens, 1999). Therefore, CO lines can be used to characterize both the ongoing star-forming burst (by measuring the SFR, see e.g. Bayet et al., 2009) and the impact of the activity of the central SMBH on the host galaxy (e.g., Cicone et al., 2014), giving some hints, in particular, on the possible connection between high-z SMGs and AGN hosts (e.g. Sharon et al., 2016), even if the CO SLED is not entirely sampled.

In the following I present five CO $J>1$ line detections for UDF1, UDF3, UDF8 and ALESS067.1 found in B3 and B4 data cubes publicly available in the ALMA Archive and listed in Tab. 4.3. Images native spectral resolution in most cases was too small to allow the CO line profile to be clearly detected. In such cases I performed a rebin (using the CASA task *imrebin*[2]) of the line channels. It consents to reduce the noise

[1] c is the number of proper kpc at the source redshift and it has been computed with the Ned Wright's Javascript Cosmology Calculator (http://www.astro.ucla.edu/~wright/CosmoCalc.html), assuming the standard flat ΛCDM cosmology (Planck Collaboration et al., 2020) with rounded parameter values, i.e. matter density $\Omega_{\rm M}=0.32$; dark energy density $\Omega_\Lambda=0.63$; baryon density $\Omega_{\rm b}=0.05$; Hubble constant $H_0=100\,h$ km s^{-1} Mpc^{-1} with $h=0.67$.

[2] In CASA, *imrebin* performs an average over the binned quantities, in this cases the spectral channels.

ID	Project code	Member ous	$\nu_{\rm band}$	Δv	$\Delta\theta = \mathbf{a}_\theta \times \mathbf{b}_\theta$	θ_ν	$\mathbf{r_{CO}}$
				[km/s]	[arcsec × arcsec]	[arcsec]	[kpc]
UDF1	2017.1.00270.S	A001/X1288/X484	B3	0.85	0.662×0.440	< 0.812	< 3.3
UDF3	2016.1.00324.L	A001/X87c/X20a	B3	59.4	1.34×1.171	0.326	1.35
UDF8	2016.1.00324.L	A001/X87c/X20e	B3	64.1	2.002×1.648	0.800	3.45
ALESS067.1	2016.1.00564.S	A001/X879/Xd9	B3	21.2	2.004×1.286	0.842	3.6
	2019.2.00246.S	A001/X14c3/Xaf4	B4	21.0	8.330×4.363	< 3	< 26

TABLE 4.3: ALMA observation settings and size of CO emission. In the order: ID from literature; project code; member ous ID; ALMA band ($\nu_{\rm band}$); velocity resolution (Δv); angular resolution (i.e., restoring beam, $\Delta\theta$); CO angular size (θ_ν); CO linear circularized size ($r_{\rm CO}$). Quantities preceded with a "<" are *upper limits*.

ID	$\mathbf{J^{up}}$	$\nu_{\rm obs}$	FWHM	$\mathbf{z_{CO}}$	$\mathbf{d_L}$	$\mathbf{I_{CO}}$	$\mathbf{L'_{CO}}$	$\mathbf{M_{H_2}}$
		[GHz]	[km/s]		[Mpc]	[mJy km s^{-1}]	[10^8 K km s^{-1} pc^2]	[10^{10} $M_\odot$]
UDF1	3	93.5	170	2.698 ± 0.005	22886.4	79.9 ± 7.4	31 ± 3	2.6 ± 0.7
UDF3	3	97.6	190; 390	$2.544^{+0.001}_{-0.002}$	21294.4	492 ± 28	170 ± 10	15 ± 3
UDF8	2	90.4	148; 379	$1.5510^{+0.0014}_{-0.0005}$	11588.4	378 ± 25	122 ± 9	5.8 ± 1.1
ALESS067.1	3	110.8	115; 314	$2.1212^{+0.0014}_{-0.0005}$	17058.3	774 ± 120	196 ± 31	16.8 ± 5.4
	6	221.6	45	″	17058.3	620 ± 70	123 ± 45	–

TABLE 4.4: CO spectral lines and molecular hydrogen masses. In the order: ID from literature; upper level of the CO transition ($J^{\rm up}$); FWHM; redshift from CO line ($z_{\rm CO}$); CO line intensity ($I_{\rm CO}$); $L_{\rm CO}$; and M_{H_2}, by assuming an $\alpha_{\rm CO}$ = 3.6 K km pc^2 s^{-1} $M_\odot^{-1}$. H_2 mass of ALESS067.1 is calculated by exploiting the transition with lower $J^{\rm up}$.

and boost the source signal by averaging among consecutive channels. I performed a ×15 rebin on UDF1 ALMA data cube and a ×5 rebin on ALESS067.1 ALMA (Project Code 2016.1.00564.S) data cube. I used instead data cubes of UDF3, UDF8 and ALESS067.1 ALMA (Project Code: 2019.2.00246.S) as available in the Archive, with clean spectral resolution as indicated in Tab. 4.3.

In Figs. 4.2, 4.3, 4.4 and 4.5, I show the observed spectral line profiles with their best Gaussian fits and the maps of spectral line distribution momenta (0, 1 and 2). CO intensity maps are overlapped by dust continuum contours. The angular and linear circularized sizes of CO emission (θ_ν and $r_{\rm CO}$) are listed in Tab. 4.3. Since they all appear unresolved to a 2D Gaussian fit, I provide: an upper limit on UDF1 CO emission size, given by the synthesized beam; a measure of UDF3, UDF8 and ALESS067.1 CO emission equal to the angular distance between the peaks of the two spectral line components. I performed the conversion from angular to linear size exploiting Eq. (4.2). Then, I measured the CO line intensity on mom0 maps: the corresponding values are listed in Tab. 4.4.

In Tab. 4.4 I also list the observed CO transition for each source and the observed central frequency $\nu_{\rm obs}$ that I used to compute the source redshift z (see also Tab. 3.1). I note that most of the lines (CO(3 − 2) for UDF3 and ALESS067.1; CO(2 − 1) for UDF8; see Figs. 4.2, 4.3, 4.4 and 4.5) show an asymmetric double-peaked CO line profile, that could suggest we are observing a tilted disc of rotating molecular gas or a molecular outflow produced by the central engine. Both the explanations are consistent with velocity maps (mom1), that are characterized by null central line (i.e., e.g. the rotation axis), and velocity dispersion maps (mom2), that are peaked along the same line. However, the width of the large components does not exceed 500 km/s, favouring the first scenario. Merging events seem to be less probable given the undisturbed appearance of the velocity dispersion on the mom2 maps. UDF1 CO line profile is very narrow (FWHM ∼ 170 km/s) and show just a peak: it means that the galaxy cold gas component is actually not rotating or that we are looking at the galaxy *face-on*. The latter interpretation is actually consistent with the velocity dispersion map, that is peaked in the centre. These evidences are confirmed also by the velocity range spanned by the CO component in the velocity maps: while for UDF3, UDF8 and ALESS067.1 the CO emission reaches velocities of the order of a few hundreds km/s, the CO velocity in UDF1 does not exceed 60 km/s, resembling the intrinsic chaotic motion of the cold gas phase (cf. Fig. 4.2).

Finally, I focus on the case of ALESS067.1 that has two CO lines detected ($J = 3$, $J = 6$; Tabs. 4.3 and 4.4). The velocity map of ALESS067.1 CO(3-2) (mom1; Fig. 4.5) does not show a clear null line, while the velocity dispersion map (mom2; Fig. 4.5) peaks in the centre and shows a tail towards the left upper corner. More likely this could be an indication of an early AGN driven molecular outflow or an evidence of interactions (e.g. Chen et al., 2017; Calistro Rivera et al., 2018; Targett et al., 2013, the latter claim that ALESS067.1 is actually the central dominant galaxy of a multiple system). However, in the latter scenario the momenta is expected to be much more disturbed. In case we are actually observing a AGN driven outflow, it should not affect significantly the galaxy properties and its current star formation activity, since the line FWHM is < 500 km/s. CO(6 − 5) maps are both null in the centre, while mom1 map shows a peak to the right upper corner, peaking at 80 km/s. This could trace either the warm star formation of the galaxy or the central engine activity. The low spatial resolution of the image does not allow to spatially compare the size of the two spectral emission, neither to understand the origin of the $J = 6$ line (a nuclear origin implies a very compact size of the CO emission, while a stellar one implies a more extended distribution). Imaging at higher spatial resolution and sensitivity

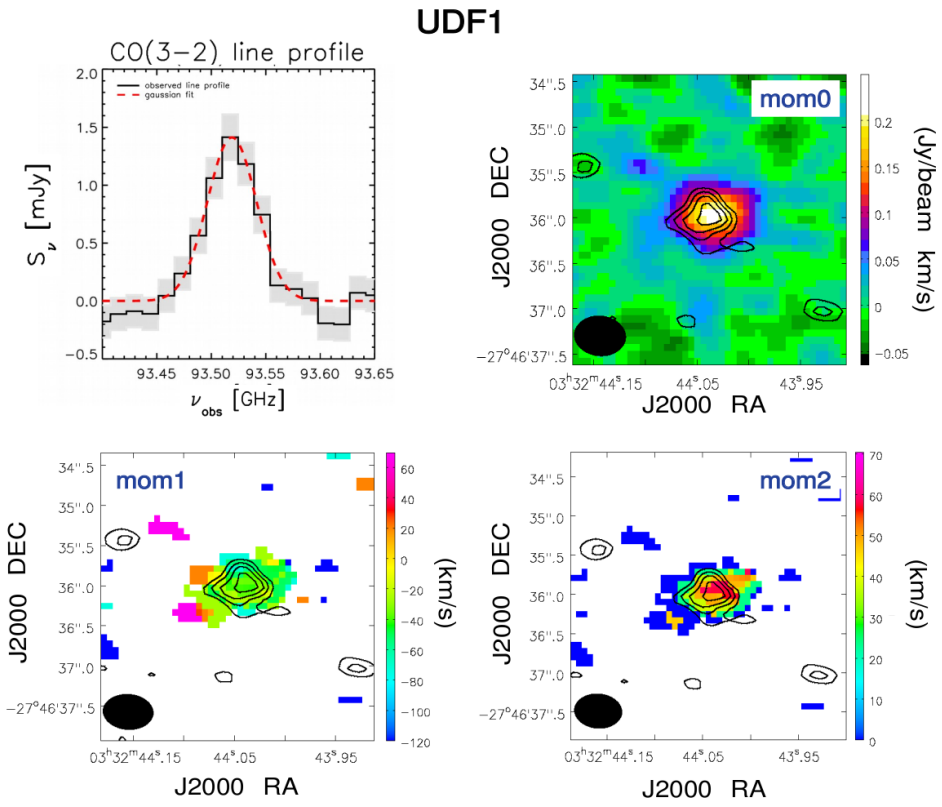

FIGURE 4.2: CO lines and spectral analysis for UDF1. The panels show: the observed spectral line profile (black solid line), the corresponding uncertainties on flux density (gray shaded area) and the best Gaussian fit (dashed red line); the maps of the spectral line distribution momenta (mom0, mom1 and mom2) overlapped by the continuum contours at $[2, 3, 4, 5] \times \sigma$ detected at the same frequency (ALMA B3). Black filled ellipse in the bottom left corners indicates the beam size.

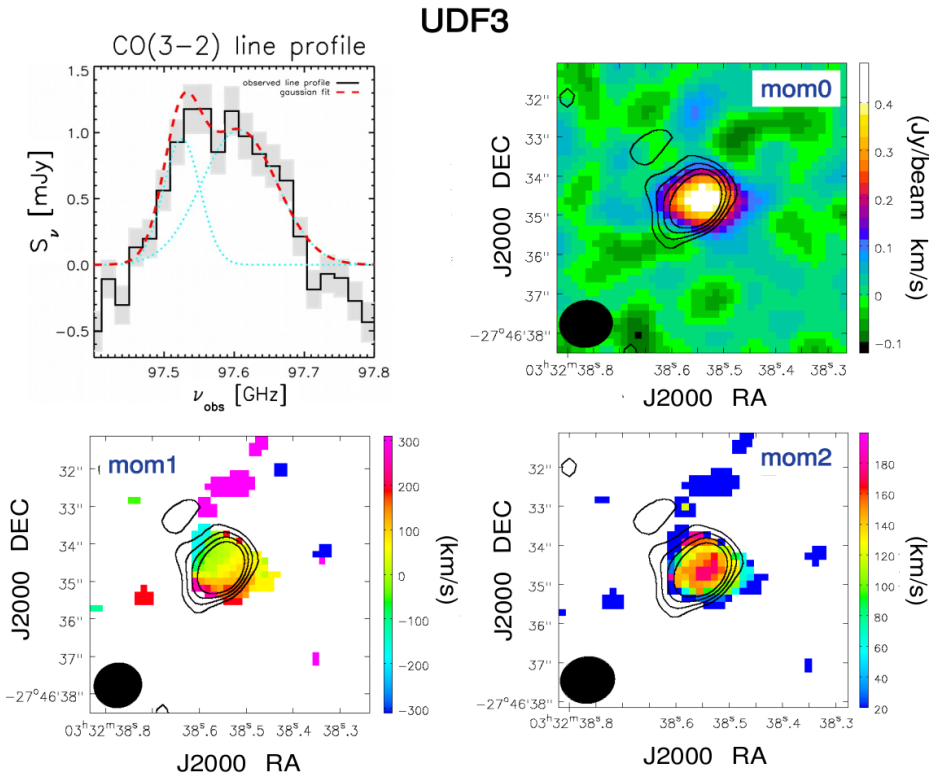

FIGURE 4.3: CO lines and spectral analysis for UDF3. The panels show: the observed spectral line profile (black solid line), the corresponding uncertainties on flux density (gray shaded area) and the total best Gaussian fit (dashed red line), modelled with a double peaked gaussian profile (the two components are in cyan); the maps of the spectral line distribution momenta (mom0, mom1 and mom2) overlapped by the continuum contours at $[2, 3, 4, 5] \times \sigma$ detected at the same frequency (ALMA B3). Black filled ellipse in the bottom left corners indicates the beam size.

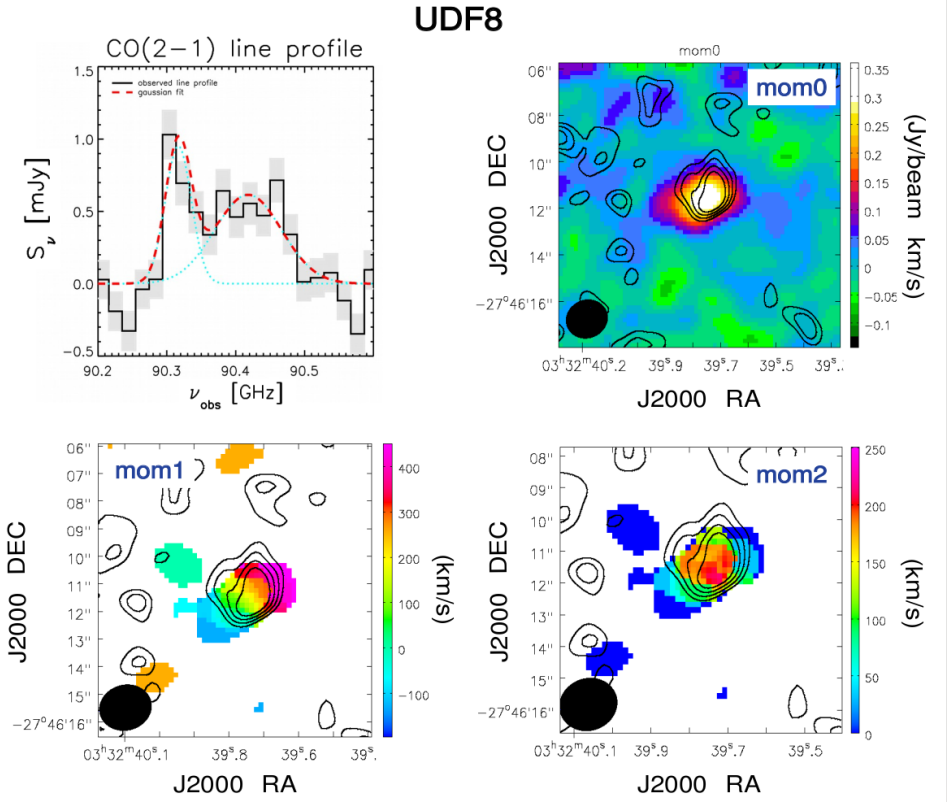

FIGURE 4.4: CO lines and spectral analysis for UDF8. The panels show: the same as Fig. 4.3.

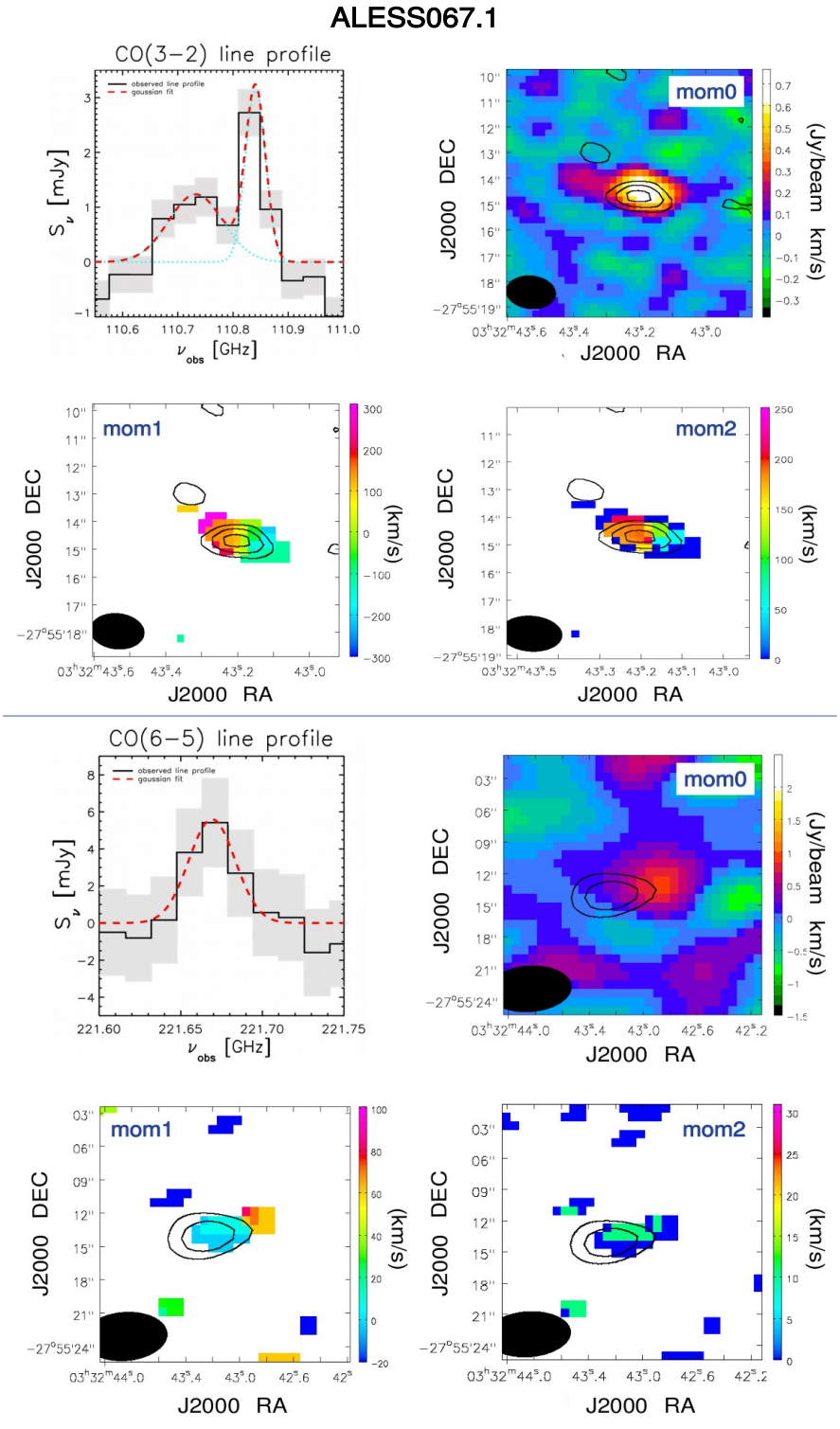

FIGURE 4.5: ALESS067.1 CO lines ($J = 3$ in the top; $J = 6$ in the bottom). The panels show: the observed spectral line profile (black solid line) with its uncertainty (gray shaded area) and the total best Gaussian fit (dashed red line - the two components are in cyan); the maps of distribution momenta (mom0, mom1 and mom2) overlapped by the continuum contours at $[2, 3, 4, 5] \times \sigma$ detected at the same frequency (ALMA B3 and ALMA B6). Black filled ellipse in the bottom left corners indicates the beam size.

are essential to definitively disentangle the diverse scenarios. Further details on ALESS067.1 CO spectral line emission along with a possible interpretation in the context of galaxy-BH co-evolution are described in Sect. 4.4.

4.2.1 Molecular gas mass

CO line intensity can be exploited to derive the molecular hydrogen mass content of UDF1, UDF3, UDF8 and ALESS067.1 as follows.

First, I derived the CO lines luminosity $L'_{\rm CO}$ from CO line intensity using the conversion by Solomon et al. (1997):

$$L'_{\rm CO}\,[{\rm K\,km\,s^{-1}\,pc}] = 3.27\times10^{7}\,I_{\rm CO}\,\nu_{\rm obs}^{-2}\,d_{\rm L}^{2}\,(1+z)^{-3} \tag{4.3}$$

where $I_{\rm CO}$ is measured in Jy km s^{-1}; $\nu_{\rm obs}$ is the observed central frequency of the line (measured in GHz) and z is the corresponding redshift. The luminosity distance $d_{\rm L}$ in Mpc depends on redshift and cosmology. All the quantities entering Eq. (4.3) are listed in Tab. 4.4. The associated uncertainties have been computed by using error propagation theory.

Then, I converted CO $J > 1$ line luminosity into the equivalent ground state luminosity $L'_{\rm CO(1-0)}$, by using the relation:

$$L'_{\rm CO(1-0)} = \frac{L'_{\rm CO(J-[J-1])}}{r_{\rm J1}} \tag{4.4}$$

and assuming the CO excitation ladder by Daddi et al. (2015), i.e. $r_{31} = 0.42 \pm 0.07$ and $r_{21} = 0.76 \pm 0.09$. Finally I derive the molecular hydrogen mass by using the relation:

$$M_{\rm H_2}[{\rm M_\odot}] = \alpha_{\rm CO}\,L'_{\rm CO(1-0)} \tag{4.5}$$

where $\alpha_{\rm CO}$ is the CO conversion factor in units of $M_\odot$ [K km s^{-1} pc^2]$^{-1}$. The assumed $\alpha_{\rm CO}$ factor is 3.6 $M_\odot$ [K km s^{-1} pc^2]$^{-1}$, following Daddi et al. (2015) and Decarli et al. (2016b). The resulting molecular hydrogen masses are listed in Tab. 4.4. Uncertainties have been computed with errors propagation theory.

The ALESS067.1 H_2 content ($M_{H_2} \sim 1.7\times10^{11}\,M_\odot$; see Tab. 4.4) is consistent with the molecular hydrogen mass derived from the CO(1 − 0) line luminosity measured with the Australian Telescope Compact Array (ATCA) by Huynh et al. (2017), i.e. $L'_{\rm CO(1-0)} = (9.9 \pm 1.8)^{10}$ K km s^{-1} pc^2, assuming an $\alpha_{\rm CO} = 1.8\ M_\odot$ [K km s^{-1} pc^2]$^{-1}$ (i.e. $M_{H_2} \sim 1.8\times10^{11}\,M_\odot$; see Chen et al., 2017). The latter conversion factor is often thought to be preferable for local ULIRGs and compact high-z SMGs (e.g. Chen et al., 2017; Elbaz et al., 2018; Carilli and Walter, 2013), but it is commonly thought to be inappropriate for the globally distributed molecular gas and more advisable for high-resolution observations which isolate the nuclear region (e.g., Scoville et al., 2016; Carilli and Walter, 2013, for a review). However, I note that Calistro Rivera et al. (2018) found an even smaller CO-to-H_2 conversion factor, i.e. $\alpha_{\rm CO} = 1.1^{+0.8}_{-0.7}$ $M_\odot$ [K km s^{-1} pc^2]$^{-1}$, that gives for ALESS067.1 a molecular hydrogen mass of $(1.0 \pm 0.2)\times10^{11}\,M_\odot$. Due to the large uncertainties on $\alpha_{\rm CO}$, I do not favour one or the other value and I suggest just to re-scale the resulting molecular gas in Tab. 4.4 by a factor 1.8/3.6 = 0.5.

The presence of the direct measurement of the CO(1 − 0) line luminosity for ALESS067.1 by Huynh et al. (2017) allowed to compute r_{31} and r_{61}. I calculated a line luminosity ratio of $r_{31} = L'_{\rm CO(3-2)}/L'_{\rm CO(1-0)} = 0.20 \pm 0.07$ and $r_{61} = L'_{\rm CO(6-5)}/L'_{\rm CO(1-0)} =$

0.12 ± 0.07. I note that the above r_{31} is smaller than the one measured by Daddi et al. (2015) and indicates a more excited CO SLED for ALESS067.1, if compared to the normal (near-IR selected BzK) star-forming disk galaxies at $z = 1.5$ studied by Daddi et al. (2015). Typical values of r_{61} are $\gtrsim 0.2$ for SMGs and even higher for QSOs (e.g., Bothwell et al., 2013; Carilli and Walter, 2013; Daddi et al., 2015, extrapolations from the latter two). The sightly lower value measured here for ALESS067.1 is probably due to both the sensitivity limit, that may imply the missing of the outskirts of the CO emission, and the low resolution, that causes the flux to be distributed on a larger image area while for high-J it is probably mostly concentrated in the central region.

4.3 Interpreting galaxy evolution from imaging at high resolution and spectral analyses

In this Section I will combine spatially-resolved and spectral analyses with the results obtained from galaxy SED fitting in Chapter 3 and additional information collected from literature and multi-wavelength images from public catalogs, in order to include the whole sample in a broad context of galaxy formation and evolution.

In Tabs. 4.5 and 4.6 I list the global astrophysical properties of the individual 11 DSFGs in the sample, while in Tab. 4.7 I show their median values, with the corresponding first and third quartiles. For reference I compared the outcomes with a well studied $z \sim 2$ DSFG (i.e. UDF2) that is not included in the sample, but presents a similar multi-band sampling of its SED and the same multi-wavelength spatially-resolved and spectral information (see e.g., Aravena et al., 2019; Boogaard et al., 2019; González-López et al., 2019; Rujopakarn et al., 2019; Boogaard et al., 2020; Kaasinen et al., 2020).

In Tab. 4.6 I compute the ratio between the optical (H_{160}) circularized radius and the ALMA size, i.e. $r_{\rm H}/r_{\rm ALMA}$: the optical size is typically equal or more extended than the (sub-)millimeter one. This trend is actually observed in many recent works on high-z SMGs (e.g., Barro et al., 2013; Barro et al., 2016b; Barro et al., 2016a; Ikarashi et al., 2015; Simpson et al., 2015; Talia et al., 2018; Tadaki et al., 2020; Massardi et al., 2018), and predicted by some theoretical models describing massive galaxy evolution, focusing in particular on the star-forming progenitors of $z < 1$ ETGs. In Fig. 4.6 I show the size-mass relation as it is predicted in the theoretical scenario by Lapi et al. (2018), in terms of two typical radii: the stability radius to gas fragmentation $R_{\rm Q}$ ($\sim$ a few kpc for ETG star-forming progenitors at $z > 1$), that is derived from the Toomre stability criterion (see Toomre, 1964; Lapi et al., 2018, their Eqs. 9 and 10); the rotational radius $R_{\rm rot}$ ($\sim$ 1 kpc for ETG star-forming progenitors at $z > 1$), for which the rotational support balances the gravitational pull of the inflowing gas (Lapi et al., 2018, their Eqs. 16 and 17). The scenario predicts that the star-forming progenitors of local ETGs experience, at high-z, a dusty burst of star formation in the very central region of the galaxy, at radii $\lesssim R_{\rm rot}$ (red solid line with its 1σ scatter in Fig. 4.6), that is traced by the size of dust continuum in the (sub-)millimeter band. At greater radii, i.e. $R_{\rm rot} \lesssim r \lesssim R_{\rm Q}$ (blue solid line with its 1σ scatter in Fig. 4.6) the star formation is less obscured by dust, so that UV/optical radiation from newly formed stars can partially emerge. This trend is present in all the six sources of the sample that are resolved both in the HST H_{160} (optical sizes; filled squares in Fig. 4.6) and ALMA continuum maps (millimeter sizes; filled stars in Fig. 4.6), i.e., UDF1, UDF3, UDF8, UDF11, ALESS067.1 and AzTEC.GS25, for which the optical size is more extended than the millimeter one. The median optical-to-millimeter radii ratio, i.e. $r_{\rm H}/r_{\rm ALMA} = 2.05$, may be just a lower limit of the real situation, since

ID	$\mathbf{z_{spec}}$	$\mathbf{M_\star}$ $[10^{10}\ M_\odot]$	**SFR** $[M_\odot\ \mathrm{yr}^{-1}]$	$\tau_\star$ [Myr]	$\mathbf{L_{IR}}$ $[10^{12}\ L_\odot]$	$\mathbf{f_{AGN}}^{(1)}$ [%]	$\mathbf{M_{dust}}^{(2)}$ $[10^8\ M_\odot]$	$\mathbf{M_{gas}}^{(3)}$ $[10^{10}\ M_\odot]$	$\tau_{\mathbf{depl}}$ [Myr]	$\mathbf{L_X}$ $[10^{42}\ \mathrm{erg\ s}^{-1}]$	**class X**	**AGN**
UDF1	2.698	8 ± 1	352 ± 18	334 ± 58	3.5 ± 0.2	6	5.6 ± 0.2	3^{+3}_{-1}	85	40.2	AGN	✓
UDF3	2.543	9 ± 1	519 ± 38	234 ± 47	4.9 ± 0.3	0.2	4.0 ± 1.6	4^{+4}_{-2}	77	1.8	galaxy	✓
UDF5	1.759	2.4 ± 0.3	85 ± 6	404 ± 85	0.77 ± 0.04	–	4.6 ± 2.2	$1.3^{+2.0}_{-0.4}$	153	–	–	*nd*
UDF8	1.549	6.5 ± 0.3	100 ± 5	992 ± 50	1.10 ± 0.06	14	2.4 ± 1.3	$1.0^{+1.0}_{-0.5}$	100	36.3	AGN	✓
UDF10	2.086	2.5 ± 0.3	41 ± 5	917 ± 137	0.41 ± 0.05	1	1.9 ± 1.3	$0.6^{+0.4}_{-0.3}$	146	0.6	galaxy	×
UDF11	1.9962	6.4 ± 0.9	241 ± 19	380 ± 82	2.2 ± 0.2	0.5	1.46 ± 0.66	$0.6^{+0.7}_{-0.3}$	25	1.7	galaxy	×
UDF13	2.497	6.5 ± 1.4	111 ± 17	879 ± 149	1.2 ± 0.2	0.8	1.20 ± 0.68	$0.5^{+0.5}_{-0.2}$	45	2.1	galaxy	✓
ALESS067.1	2.1212	29 ± 3	487 ± 24	903 ± 100	5.4 ± 0.3	0.4	10 ± 4	8^{+8}_{-4}	164	3.8	galaxy	✓
AzTEC.GS25	2.292	8 ± 2	401 ± 20	290 ± 88	3.9 ± 0.2	1	13.6 ± 8.2	4^{+4}_{-2}	100	6.1	galaxy	✓
AzTEC.GS21	1.910	18 ± 2	360 ± 18	746 ± 105	3.9 ± 0.2	0.3	5.8 ± 1.4	5^{+5}_{-2}	139	1.7	galaxy	✓
AzTEC.GS22	1.794	5.7 ± 0.5	91 ± 5	940 ± 74	1.01 ± 0.06	–	14 ± 8	5^{+5}_{-2}	550	–	–	*nd*
UDF2	$2.6961^{(a)}$	$13 \pm 3^{(a)}$	$187^{+35(a)}_{-16}$	–	–	–	$7.8^{+1.2(c)}_{1.0}$	Tab. 4.6	Tab. 4.6	–	–	**nd**

TABLE 4.5: Integral properties of the 11 DSFGs. I list (in the order): galaxy ID; spectroscopic redshift (references in Tab. 3.1); stellar mass ($M_\odot$); Star Formation Rate (SFR); burst age ($\tau_\star$); IR luminosity ($L_{\rm IR}$); AGN fraction in the IR ($f_{\rm AGN}$); dust mass ($M_{\rm dust}$); gas mass ($M_{\rm gas}$); gas depletion timescale ($\tau_{\rm depl}$); 2 – 10 keV luminosity ($L_{\rm X}$); X-ray dominant component (class X); presence of an AGN (AGN) by Luo et al. (2017). The AGN fractions (1) reported above are the ones inferred by using the MIR-X-ray correlation by Asmus et al. (2015). The dust masses (2) listed above include the correction by Magdis et al. (2012) of a factor ~ 2. Gas masses (3) are derived from the dust continuum flux at $\lambda = 850\,\mu$m, following Scoville et al. (2016, cf. their Fig. 1). In the column **AGN** any evidence of the presence of an AGNis consiedered, as reported by Luo et al. (2017): ✓ means that the galaxy has a signature of AGN; × means that the object is classified as a normal star-forming galaxy; *nd* stands for *not detected*. For reference I list the same available information for UDF2 by Boogaard et al. (2019)$^{(a)}$, Rujopakarn et al. (2019)$^{(b)}$ and Kaasinen et al. (2020)$^{(c)}$.

ID	z_{spec}	r_H [kpc]	r_{ALMA} [kpc]	r_{CO} [kpc]	r_H/r_{ALMA}	r_H/r_{CO}	r_{CO}/r_{ALMA}	morphology H_{160}	J^{up}	L_{CO} [10^8 K km s^{-1} pc^2]	M_{H_2} [10^{10} $M_\odot$]	τ_{depl} [Myr]
UDF1	2.698	2.6	0.46	< 3.3	5.7	–	–	isolated	3	31 ± 3	2.6 ± 0.7	74
UDF3	2.543	1.6	0.62	1.35	2.6	1.2	2.2	clumpy?	3	170 ± 10	15 ± 3	289
UDF5	1.759	2.3	< 2.5	–	–	–	–	clumpy	–	–	–	–
UDF8	1.549	5.7	4.1	3.45	1.4	1.7	0.9	isolated	2	122 ± 9	5.8 ± 1.1	580
UDF10	2.086	2.0	< 2.5	–	–	–	–	clumpy	–	–	–	–
UDF11	1.9962	4.5	3.4	–	1.3	–	–	clumpy	–	–	–	–
UDF13	2.497	1.2	< 0.65	–	–	–	–	isolated	–	–	–	–
ALESS067.1	2.1212	6.5	1.1	3.6	6.0	1.8	3.3	clumpy	3	196 ± 31	16.8 ± 5.4	345
									6	123 ± 45		
AzTEC.GS25	2.292	1.8	1.2	–	1.5	–	–	isolated	–	–	–	–
AzTEC.GS21	1.910	3.7	< 0.7	–	–	–	–	clumpy	–	–	–	–
AzTEC.GS22	1.794	3.2	< 1.7	–	–	–	–	clumpy	–	–	–	–
UDF2	2.6961[a]	2.5[b]	0.6[*]	2.6[c]	4.3	0.97	4.3	clumpy[b]	3[a]	279 ± 33[a]	23.9 ± 4.9[a]	1300[a]

TABLE 4.6: Spatially-resolved properties of the 11 DSFGs and information derived from CO emission lines. I list (in the order): galaxy ID; spectroscopic redshift (references in Tab. 3.1); optical (H_{160}) circularized radius (r_H); thermal dust circularized radius by ALMA continuum (r_{ALMA}); CO circularized radius (r_{CO}); optical-to-ALMA size ratio (r_H/r_{ALMA}); optical-to-CO size ratio (r_H/r_{CO}); HST morphology in the filter H_{160}; CO transition upper level (J^{up}); CO line luminosity (L_{CO}); H_2 mass (M_{H_2}); gas depletion timescale (τ_{depl}). For reference I list the same information for UDF2 by Boogaard et al. (2019)[a], Rujopakarn et al. (2019)[b] and Kaasinen et al. (2020)[c].
(*)Rujopakarn et al. (2019) find a core component of 0.3 kpc and a disk component of 1.2 kpc (circularized radii).

a significant part of the stellar emission could be lost, being completely absorbed by dust. Furthermore, the ratio $r_\star/r_{\rm dust}$ for the high-z objects studied here behaves differently than for local samples of similar stellar mass (e.g., Lang et al., 2019), being typically larger than 1 for the former and smaller than 1 for the latter.

For reference, in Fig. 4.6 I show the position of UDF2 (gray filled symbols), that was detected in the ALMA 1.3 mm survey by Dunlop et al. (2017) at $z_{\rm spec} = 2.6961$ (Aravena et al., 2019; Boogaard et al., 2019; González-López et al., 2019; Boogaard et al., 2020, source ID: ASPECS-LP.3mm.07). I stress that the source is not included in the pilot sample of this thesis since it has no counterpart in the GOODS-MUSIC catalog by Grazian et al. (2006), within the searching radius of 1 arcsec (see Sect. 3.1.3 for more details). Its physical properties are very similar to the 11 DSFGs. It has a stellar mass $M_\star = (1.3 \pm 0.3) \times 10^{11}\ M_\odot$ and it forms stars at a rate of SFR $= 187^{+35}_{-16}\ M_\odot\ {\rm yr}^{-1}$ (see Tab. 4.5 and Boogaard et al., 2019, source ID: ASPECS-LP.3mm.07). Its spatially-resolved continuum emission, both in the optical (H_{160}) and in the (sub-)millimeter (ALMA B7), is analysed in the details by Rujopakarn et al. (2019). For the sake of consistency and to compare with the results presented here, I measured the dust size on the same ALMA map (publicly available in the ALMA Archive; ALMA Project code: 2017.1.00001.S; Member ous: A001/X1288/X4c3) and calculated a circularized ALMA radius of $r_{\rm B7} \approx 0.6$ kpc, while Rujopakarn et al. (2019) I measured a core component of ≈ 0.3 kpc and a disc component of ≈ 1.2 kpc (circularized radii; see Tab. 4.6). The circularized H_{160} radius, i.e. $r_{\rm H} \approx 2.5$ kpc (Tab. 4.6), has been obtained from the effective radius by Rujopakarn et al. (2016), i.e. $r_e = 3.71 \pm 0.06$ kpc by assuming the axes ratio by van der Wel et al. (2012). As for the other sources in the sample, also the HST and ALMA sizes of UDF2 are in good agreement with the size-mass relation predicted by Lapi et al. (2018) and shown in Fig. 4.6.

On the one hand, this evidence further confirms that the panchromatic approach presented in this thesis may be applied to other high-z DSFGs with similar multi-band coverage of their SED and spectral information, in the case spatially-resolved images are available in the FIR and UV/optical rest-frame. On the other hand, it stresses again the great importance of multi-wavelength imaging at great spatial resolution in order to probe galaxy evolution.

More than half of the objects in the final sample (i.e., UDF5, UDF10, UDF11, ALESS067.1, AzTEC.GS21, AzTEC.GS22), as well as UDF2 (see Tab. 4.6), shows a clumpy morphology in the H_{160} image. This may be suggestive of interactions within a radius $\lesssim$ a few tens of kpc from the ALMA counterpart. However, the optical clumps may just indicate that some emitting areas in the star-forming regions are affected more than others by dust extinction (indeed they are often indicated as *star-forming clumps*). In order to discern the most likely scenario, it is essential to take into consideration galaxy multi-wavelength emission and its spatial distribution at comparable resolutions. In Sect. 4.4 I will provide an insight on this topic, for each galaxy of the sample.

Furthermore, atomic and molecular spectral lines provide essential information to investigate the mechanisms triggering star formation in galaxies and galaxy-BH co-evolution. CO lines are very well recognized as tracers of the cold (i.e., molecular) gas phase and the analysis of their resolved emission, both in space and frequency, allow to study gas kinematics and physical conditions and to measure its content in mass. Some differences can be identified by comparing the molecular gas masses estimated from the dust optically-thin continuum and CO lines, that obviously imply diverse depletion timescales $\tau_\star$ (cf. Tab. 4.5 and Tab. 4.6). These differences can be traced back to diverse dust and CO sizes, the latter being typically larger than the former and its emission almost optically thick (especially in case of low-J CO lines).

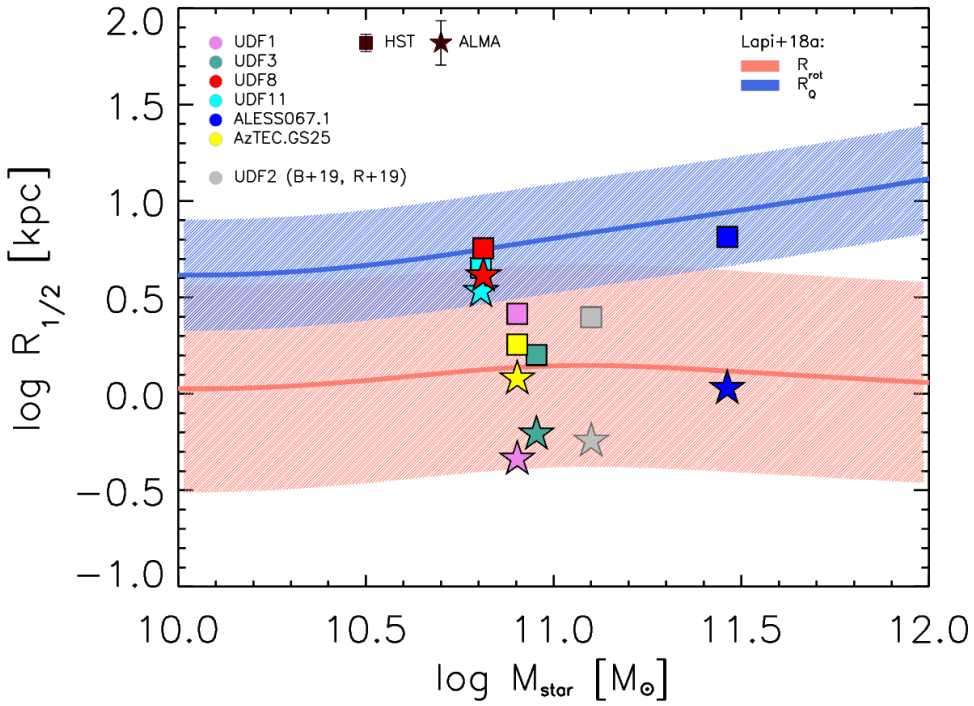

FIGURE 4.6: H_{160} HST sizes (filled squares) and ALMA continuum sizes (filled stars) for the six galaxy that are resolved in the continuum ALMA maps: UDF1 (lilac); UDF3 (green); UDF8 (red); UDF11 (cyan); ALESS067.1 (cyan); AzTEC.GS25 (yellow). Gray filled symbols stand for UDF2 by Boogaard et al. (2019, B+19) and Rujopakarn et al. (2019, R+19), that I show as an example of the typical outcomes from similar spatially-resolved and panchromatic studies on $z \sim 2$ dusty star-forming galaxies. Blue and red shaded areas represent the predicted behaviour (with its 1σ scatter) of $R_{\rm Q}$ and $R_{\rm rot}$ by the theoretical scenario presented in Lapi et al. (2018). Error bars, consistent with the scatter of the relations, have been omitted for clarity. Typical errors on HST and ALMA sizes are shown in the legend.

		Median	**1st quartile**	**3rd quartile**	**UDF2**
z		2.086	1.794	2.497	2.6961
SFR	$[M_\odot\ \mathrm{yr}^{-1}]$	241	91	401	187
$\tau_\star$	[Myr]	746	334	917	–
$M_\star$	$[10^{10}\ M_\odot]$	6.5	5.7	9	13
L_{IR}	$[10^{12}\ L_\odot]$	2.2	1.01	3.9	–
M_{dust}	$[10^{8}\ M_\odot]$	4.6	1.9	10	7.8
M_{gas}	$[10^{10}\ M_\odot]$	4.0	0.6	5.8	23.9
τ_{depl}	[Myr]	146	74	345	1300
f_{AGN}	[%]	0.8	0.4	1	–
L_{X}	$[10^{42}\ \mathrm{erg\ s}^{-1}]$	1.7	2.1	6.1	nd
r_{H}	[kpc]	2.6	1.8	4.5	2.5
r_{ALMA}	[kpc]	1.15	0.6	3.4	0.6
r_{CO}	[kpc]	3.45	1.35	3.6	2.6
$r_{\mathrm{H}}/r_{\mathrm{ALMA}}$		2.05	1.4	5.7	4.3
$r_{\mathrm{H}}/r_{\mathrm{CO}}$		1.7	1.2	1.8	0.97
$r_{\mathrm{CO}}/r_{\mathrm{ALMA}}$		2.2	0.9	3.3	4.3

TABLE 4.7: Median, first and third quartiles of the following quantities (in the order): redshift (z), age of the burst ($\tau_\star$); SFR; stellar mass ($M_\star$); IR luminosity (L_{IR}); dust mass (M_{dust}); molecular gas mass (M_{gas}); depletion time (τ_{depl}); AGN fraction in the IR domain (f_{AGN}); $2-10$ keV luminosity (L_{X}); HST, ALMA and CO sizes (r_{H}, r_{ALMA} and r_{CO}); optical-to-ALMA size ratio ($r_{\mathrm{H}}/r_{\mathrm{ALMA}}$); optical-to-CO size ratio ($r_{\mathrm{H}}/r_{\mathrm{CO}}$); CO-to-ALMA size ratio ($r_{\mathrm{CO}}/r_{\mathrm{ALMA}}$). For reference, in the last column I list the values measured for UDF2 byBoogaard et al. (2019)$^{(a)}$, Rujopakarn et al. (2019)$^{(b)}$ and Kaasinen et al. (2020)$^{(c)}$. To compute the gas mass value reported above I preferred the measurements from CO spectral lines (Tabs. 4.4 and 4.6) rather than the ones from dust continuum (Tab. 4.5).

As such, gas masses inferred from these measurements may sample different regions or components in the galaxy (e.g., Riechers et al., 2011; Hodge et al., 2015; Spilker et al., 2015; Decarli et al., 2016b).

For the four sources with detected CO lines (i.e., UDF1, UDF3, UDF8, ALESS067.1), and also for UDF2, the cold gas emission is equally or more extended then the ALMA B7 and B6 continuum (typically $r_{CO}/r_{ALMA} \gtrsim 1$), while it is equal or more compact than the optical emission (see Tab. 4.6). This is consistent with the size evolution scenario presented in Lapi et al. (2018) according to which the CO emission traces the rotating cold gas phase that, while inflowing towards the central regions of the galaxy, fuels both the mildly-obscured star formation at larger radii (traced by the emission in the optical) and the highly-obscured star formation in the innermost regions (sampled by the dust continuum in the (sub-)millimeter).

Furthermore, multi-wavelength observations at high spectral and spatial resolution can reveal the presence of nuclear activity. In particular, structure in the CO emission may trace molecular outflows associated with AGN feedback. For example, the X-ray emission properties combined with the double peak CO line profile of UDF8, are strongly suggestive of the presence of nuclear driven ouflows. This interpretation is also consistent with the age of UDF8 and its SFR (i.e., $\tau_\star \sim 1$ Gyr and SFR $\sim 100\ M_\odot\ \mathrm{yr}^{-1}$; cf. Tab. 4.5), in the galaxy-BH co-evolution scenario by Mancuso et al., 2016a; Mancuso et al., 2017. A more detailed analysis for UDF8 is given in Sect. 4.4.

4.4 An insight into individual galaxy evolution

The multi-band analysis presented in Chapter 3 and here enriched, by the analysis of multi-wavelength spatially-resolved emission and CO spectral lines, allows to provide a self-consistent characterization of the 11 DSFGs, that includes their role in the framework of galaxy formation and evolution. In this Section I will put together all the observational evidences and give an insight on the possible evolutionary scenario for the individual galaxies that are in the final sample.

While characterizing galaxy cold gas phase, I will use, preferentially, the gas mass measurements from CO spectral lines (when available; see Tabs. 4.4 and 4.6) rather than the ones from dust continuum (Tab. 4.5), since the latter can miss the gas distributed over scales larger than the dust continuum size (e.g., Riechers et al., 2011; Hodge et al., 2015; Spilker et al., 2015; Decarli et al., 2016b).

Finally, I note to the reader that all the multi-wavelength radii and sizes presented in the following are circularized (see Eq. (4.2)).

4.4.1 UDF1 (J033244.01-274635.2)

UDF1 is a DSFG at $z_{spec} = 2.698 \pm 0.005$ (see Tab. 4.5). I measured its spectroscopic redshift from a CO(3-2) line (Tab. 4.4) that is consistent, within the errors, with the redshift of the C[II] emission line at 8600Å (2330Å rest frame) by Szokoly et al. (2004, HII region-type spectrum). UDF1 was detected in the ALMA B6 ($\lambda \sim 1.3$ mm) survey by Dunlop et al. (2017) and more recently by Franco et al. (2018) at $\lambda \sim 1.1$ mm (source ID: AGS6). Rujopakarn et al. (2016) detected its radio counterpart with the VLA at 6 GHz. The corresponding fluxes are $S_{1.3\,mm} = 924 \pm 76\ \mu$Jy, $S_{1.1\,mm} = 1.26 \pm 0.16$ mJy and $S_{6\,GHz} = 9.02 \pm 0.57\ \mu$Jy. In the ALMA archival continuum map at the best spatial resolution currently available for UDF1 (Project code: 2017.1.00001.S, ALMA B7; see Tab. 4.1), the source is detected at a significance level $> 5\sigma$. I measure a flux $S_{1\,mm} = 2900 \pm 300\,\mu$Jy (Tab. 4.1). This flux is consistent with the 850 μm ALMA

B7 flux measured by Cowie et al. (2018), i.e. $S_{850\,\mu m} = 3.38 \pm 0.32$ mJy (source ID: no. 22; name ALMA033244-274635), and by Rujopakarn et al. (2019) on the same ALMA map, i.e. $S_{B7} = 3407 \pm 226$ μJy. In the B7 ALMA map the source is resolved: I measure a circularized radius $r_{ALMA} \simeq 0.46$ kpc, where the dusty star-formation is expected to be located. Rujopakarn et al. (2016) find the 6 GHz radio flux to be compatible with the star formation activity of the ALMA source, confirming the outcome obtained from the analysis of galaxy SED presented in Chapter 3 (see also Pantoni et al., 2021b). The radio emission, that samples also the mildly obscured and un-obscured star-formation of the galaxy, extends over a larger region: $r_{VLA} \sim 2.7$ kpc (FWHM; Rujopakarn et al., 2016). From the CO(3-2) line luminosity I estimate the molecular hydrogen content of the galaxy to be $M_{H_2} = (2.6 \pm 0.7) \times 10^{10}$ $M_\odot$. From its velocity and velocity dispersion maps one can claim that the galaxy cold gas component is probably a *faced-on* rotating disk that extends over a radius $\lesssim 3$ kpc (see Tab. 4.3). Its spatial distribution samples the galaxy star formation, both obscured and un-obscured, as well as the aforementioned radio emission, that extends over a region of a similar size.

The peak of dust radiation matches pretty well that of stellar emission (the HST/WFC3 emission map in the filter H_{160}, overlapped by ALMA contours, is shown in Fig. 4.1). The optical size ($r_H \sim 2.6$ kpc; Rujopakarn et al., 2019, see Tab. 4.2) extends over a radius that is more than a factor 5 larger than the ALMA size, reported above and in Tab 4.1. These evidences can be easily ascribed to a very rapid condensation and compaction of the gas towards the centre of the galaxy (over a typical timescale of $\tau \sim 10^6$ yr), where the bulk of dusty star formation takes place ($M_{dust} \sim 6 \times 10^8$ $M_\odot$, see Tab. 4.5 and 4.5).

From the analysis presented in Pantoni et al. (2021b), UDF1 is almost approaching the galaxy main-sequence (see e.g. Speagle et al., 2014) at the corresponding redshift (it is a factor $\sim 2\times$ above) with a stellar mass $M_\star = (8\pm1)\times10^{10}$ $M_\odot$ and $SFR = 352\pm18$ $M_\odot$ yr^{-1}. Probably it is experiencing the last phase of dusty star formation before the intervention of the AGN feedback. Indeed, even if the optical counterpart has been historically classified as a normal star-forming galaxy (the presence of an AGN cannot be established from the optical data alone), it has a very powerful counterpart in the X-ray, suggesting the presence of an accreting central SMBH. In the $\simeq 7$ Ms CDFS catalog by Luo et al. (2017), the X-ray source (IDX 850) is classified as *AGN* (see Tabs. 4.5 and 4.5). The intrinsic absorption column density[3] $N_H \sim 1.2 \times 10^{22}$ cm^{-2} gives an absorption-corrected intrinsic $2-10$ keV luminosity of $\sim 4 \times 10^{43}$ erg s^{-1} (see Tab. 4.5). Rujopakarn et al. (2016) suggest that the VLA size of UDF1 can be somehow more extended than the ALMA one due to the central AGN, even if the 6 GHz radio flux does not appear to be enhanced, when compared to the one expected from star formation alone. Relying on the prescriptions of the *in-situ* scenario for galaxy evolution (see Mancuso et al., 2017), the nucleus radio emission is expected to emerge from the one associated to star formation only at later times.

Gas and dust rich, with a typical depletion timescale $\tau_{depl} \sim 75$ Myr, UDF1 very compact and intense star formation must have triggered a rapid growth of the central SMBH, whose power in the X-ray clearly overwhelms the host galaxy one, as explained in Chapter 3 (see also Pantoni et al., 2021b). This galaxy should overlap the galaxy main-sequence in a few hundreds of Myr and then to be quenched by the central AGN.

[3]The column density N_H (reported here, but also for other sources in the sample, in the following Sections) is derived on the basis of flux ratios in the hard and soft X-ray bands, by assuming a classical AGN slope of 1.8.

4.4.2 UDF3 (J033238.53-274634.6)

UDF3 is a DSFG at $z_{\rm spec} = 2.544^{+0.001}_{-0.002}$ (Tab. 4.4), that I measured from a CO(3-2) line detected in a ALMA B3 ($\nu_{\rm obs} \simeq 97.6$ GHz; see Tabs. 4.3 and 4.4). Our measurement is consistent, within the errors, with the one by Decarli et al. (2016b), based on the blind detection of three CO transitions (ASPECS 3 mm.1, 1 mm.1, 1 mm.2; Decarli et al., 2016a), i.e. $z_{\rm spec} = 2.543$ (see also Tacconi et al., 2018). Another measurement, consistent with ours, comes from the MUSE HUDF project, i.e. $z_{\rm spec} = 2.541$ (Bacon et al., 2017). Finally, Momcheva et al. (2016) report a grism redshift $z_{\rm spec} \sim 2.561$, based on the detection of the [O II] line in the 3D-HST data, that is in accordance with the aforementioned spectroscopic determinations of the source redshift to the second decimal digit.

UDF3 was detected both in the B6 ($\sim$ 1.3 mm) ALMA continuum and 6 GHz VLA maps of the HUDF by Dunlop et al. (2017) and Rujopakarn et al. (2016). The corresponding fluxes are $S_{1.3\,\rm mm} = 863 \pm 84$ μJy and $S_{6\,\rm GHz} = 12.06 \pm 0.55$ μJy. I found a $> 5\sigma$ continuum detection for this source in the ALMA B7 (Project code: 2017.1.00001.S, Tab. 4.1) and I measured a flux $S_{1\,\rm mm} = 1600 \pm 200\,\mu$Jy. This flux is in accordance with the 850 μm ALMA flux measured by Cowie et al. (2018), i.e. $S_{850\,\mu\rm m} = 2000 \pm 400\,\mu$Jy (source ID: no. 48; name ALMA033238-274634), and the 1.1 mm ALMA flux measured by Franco et al. (2018), i.e. $S_{1.1\,\mu\rm m} = 1130 \pm 105\,\mu$Jy (source ID: AGS12). Rujopakarn et al. (2016) found the 6 GHz radio flux of UDF 3 to be solely compatible with the star formation activity of the galaxy, in agreement with the outcome from the SED analysis (Pantoni et al., 2021b). However, they claim that the possible presence of a central AGN, could have an impact on the radio size, i.e. $r_{\rm VLA} = 1.5 \pm 0.1$ kpc (FWHM; Rujopakarn et al., 2016). The ALMA (and VLA) source has an X-ray counterpart (IDX 718) in the $\simeq$ 7 Ms CDFS survey catalog by Luo et al. (2017). The source $2-10$ keV luminosity is 1.8×10^{42} erg s^{-1}. All these evidences suggest that the central BH could be accreting material in the host galaxy nucleus, even if its emission do not clearly overwhelms the X-ray light coming from star formation at the moment (Pantoni et al., 2021b).

The rest-frame UV/optical morphology is unclear and may be clumpy/disturbed (see Fig. 4.1 and Tab. 4.6). However, no clear evidence of interactions are observed. The starlight emission is compact ($r_{\rm H} \sim 1.6$ kpc; van der Wel et al., 2012, see Tab. 4.2) and its peak appears to be shifted when compared to the ALMA B7 continuum emission, possibly due to dust obscuration of stellar light. (Fig. 4.1). The absence of interactions is confirmed by the velocity and dispersion velocity maps of CO$(3-2)$ molecular line, that are smooth (i.e., not disturbed) and consistent with a rotating disc of molecular gas (confirmed by the double-peaked profile of the spectral line; see Figs. 4.2, 4.3, 4.4) extending over a radius of $\sim$ 1.4 kpc. The (sub-)millimeter source is resolved in the ALMA B7 continuum map: I measure a circularized radius of $r_{\rm ALMA} \sim 0.6$ kpc (Tab. 4.1). However, to confirm this scenario multi-wavelength images at higher spatial resolution are definitely needed.

In the analysis presented in Chapter 3 (see also Pantoni et al., 2021b), UDF3 resulted a very young object (age $\sim 200-300$ Myr), forming stars at a rate $SFR \sim 500$ $M_\odot$ yr^{-1} ($sSFR \sim 5.8$ Gyr^{-1}). Fuelled by the large amount of gas and dust ($M_{H_2} = (1.5 \pm 0.3) \times 10^{11}$ $M_\odot$ and $M_{\rm dust} \sim 4 \times 10^8$ $M_\odot$; Tabs. 4.4 and 4.5), its intense burst of star formation (depletion timescale $\tau_{\rm depl} \lesssim 100$ Myr) must trigger the growth of the central BH, that is expected to become active and quench star formation in a few 10^8 yr. In the $SFR - M_\star$ plot, UDF3 lies to the top-left side of the main-sequence at the corresponding redshift (even if it is still consistent with the 2σ scatter of the relation;

see Speagle et al., 2014; Pantoni et al., 2021b). A similar result was found by Elbaz et al. (2018), who classify UDF3 as a starburst galaxy.

4.4.3 UDF5 (J033236.94-274726.8)

UDF5 is a DSFG detected both in the B6 ($\sim$ 1.3 mm) ALMA and 6 GHz VLA maps of the HUDF by Dunlop et al. (2017) and Rujopakarn et al. (2016). The corresponding fluxes are $S_{1.3\,\mathrm{mm}} = 311 \pm 49$ μJy and $S_{6\,\mathrm{GHz}} = 6.26 \pm 0.46$ μJy.

As to the source redshift, Momcheva et al. (2016) report a $z_{\mathrm{spec}} = 1.759$, basing on 3D-HST spectroscopy (Tab. 3.1).

For this millimeter source no X-ray counterpart is found in the literature, neither by the association with the $\simeq$ 7 Ms X-ray catalogue by Luo et al. (2017) or in the supplementary catalog at very low significance. This may indicate either that no (i.e. not very powerful) AGN is present or that it is highly obscured (i.e. Compton-thick, with $N_{\mathrm{H}} \gtrsim 10^{24}$ cm^{-2}). Since the source lies in a very deep region of the *Chandra* map (equivalent exposure time of about 6.22 Ms), it is reasonable to think that the latter is the most probable hypothesis to explain the non-detection. Following the *in-situ* scenario predictions, the central BH must have just started to accrete material from the surroundings; as such, no signature of its activity on the source morphology is expected. Both ALMA and VLA sizes can provide a good measure of the region where the bulk of star formation is occurring, i.e. very compact, $\sim$ 2 kpc ($r_{\mathrm{ALMA}} < 2.5$ kpc; $r_{\mathrm{VLA}} \sim 1.5$ kpc; see Tab. 4.1 and Rujopakarn et al., 2016). Rujopakarn et al. (2016) claim that the 6 GHz VLA flux is solely compatible with the star formation activity of the galaxy, confirming the result by Pantoni et al. (2021b).

The HST/WFC3 H_{160} circularized radius of UDF5 is $r_{\mathrm{H}} \sim 2.3$ kpc, slightly larger than the radio one and consistent with the upper limit on the ALMA B6 size. The rest-frame optical morphology is clumpy/disturbed (Fig. 4.1 and Tab. 4.6). Since no clear evidence of interactions and/or AGN feedback has been observed, the galaxy multi-band morphology must be ascribed to both the dust enshrouded star formation occurring at radii $\lesssim$ 2 kpc and the gas compaction towards the central region.

From the analysis by Pantoni et al. (2021b), UDF5 is in the vicinity of the main-sequence at the corresponding redshift. This young galaxy (age $\sim$ 400 Myr) shows a more moderate SFR ($\sim 80 - 90$ $M_{\odot}$ yr^{-1}) and a more modest stellar mass (a few 10^{10} $M_{\odot}$) compared to the other galaxies in the sample (cf. Tab. 4.5). The depletion timescale is $\tau_{\mathrm{depl}} \lesssim 900$ Myr and the dust content is quite high ($M_{\mathrm{dust}} \sim 4 \times 10^{10}$ $M_{\odot}$). Following the *in-situ* scenario, the star-formation should last longer than what is seen for the bulk of high-z DSFGs ($\tau_{\mathrm{burst}} \sim$ a few 10^9 yr). This picture can explain there is no evidence of an active nucleus: less intense burst of star formation implies a slower BH Accretion History and at the current galaxy age (i.e., $\sim$ 400 Myr) the central BH is highly obscured in the X-ray and the emission is still dominated by star formation.

4.4.4 UDF8 (J033239.74-274611.4)

UDF8 is a DSFG at $z_{\mathrm{spec}} \sim 1.6$. The slit redshift $z_{\mathrm{spec}} = 1.552$ by Kurk et al. (2013) matches the CO line detection by Decarli et al. (2016b, source ID: ASPECS3mm.2) and the measurement from the CO(2 – 1) spectral line detected in the ALMA B3 data cube, i.e. $z_{\mathrm{spec}} = 1.5510^{+0.0014}_{-0.0005}$ (Tab 4.4), that I used in the analysis.

UDF8 was detected both in the B6 ($\sim$ 1.3 mm) ALMA and 6 GHz VLA maps of the HUDF by Dunlop et al. (2017) and Rujopakarn et al. (2016). The corresponding fluxes are $S_{\mathrm{B6}} = 208 \pm 46$ μJy and $S_{6\,\mathrm{GHz}} = 7.21 \pm 0.47$ μJy. The source is resolved both in ALMA and VLA maps and the corresponding radii are $r_{\mathrm{ALMA}} \sim 4.1$ kpc (Tab. 4.1)

and $r_{\rm VLA} \sim 2.1$ kpc. This dusty galaxy, still compact, is however more extended in the millimeter than the bulk of high-z DSFGs (typical ALMA radius is found to be $\lesssim 1-2$ kpc).

In the rest-frame UV/optical the galaxy appears to be isolated (see Fig. 4.1 and Tab. 4.6), suggesting that the bulk of star formation can be traced back to local, *in-situ* condensation processes. The galaxy is more extended in the optical ($r_{\rm H} \sim 5.7$ kpc) than in the millimeter continuum, consistently with what is expected during the gas compaction evolutionary phase. This is confirmed by the double-peaked spectral profile of its CO(2 − 1) line and the velocity and velocity dispersion maps (Figs. 4.2, 4.3, 4.4), that suggest we are observing a rotating disc of molecular gas extending over an area of radius $r_{,\rm CO} \sim 3.5$ kpc. From the CO line luminosity I derived a molecular hydrogen mass $M_{H_2} = (5.8 \pm 1.1) \times 10^{10}\ M_\odot$ that is consistent within the uncertainties with the one estimated by Decarli et al. (2016b), i.e. $M_{H_2} \sim 6.5 \times 10^{10}\ M_\odot$, under the assumption of the same $\alpha_{\rm CO} = 3.6$ K km pc^2 s^{-1} $M_\odot^{-1}$.

UDF8 is detected with *Chandra*. Its X-ray counterpart (IDX 748) is in the $\simeq 7$ Ms CDFS survey catalog by Luo et al. (2017). The source 2 − 10 keV luminosity is 3.5×10^{43} erg s^{-1}, suggesting that UDF8 hosts an active galactic nucleus (see Tab. 4.5), which dominates over the X-ray emission of the host galaxy (Pantoni et al., 2021b). Even if the galaxy hosts an X-ray AGN, Rujopakarn et al. (2016) claim that its contribution to the radio emission is negligible. They find the radio flux at 6 GHz to be solely consistent with galaxy star formation, as to the radio morphology. I note that I obtained the same outcome from the analysis of galaxy SED in Chapter 3 (see also Pantoni et al., 2021b).

UDF8 is a main-sequence galaxy of age ~ 1 Gyr, forming stars at a rate $SFR \sim 100\ M_\odot$ yr^{-1}, with a $sSFR \sim 1.5$ Gyr^{-1} (Pantoni et al., 2021b). AGN quenching must be very close: eventually, its effect could be already seen under the shape of outflows and winds that can affect the multi-band sizes of UDF8 and broaden its CO(2 − 1) spectral line profile (with respect to pure disc rotation). To confirm this scenario multi-band images at higher spatial resolution of the galaxy nuclear region are definitely needed.

4.4.5 UDF10 (J033240.73-274749.4)

UDF10 is a DSFG at $z_{\rm spec} = 2.086$ (grism redshift by Momcheva et al., 2016, based on the detection of an optical rest-frame line in the 3D-HST data, Tab. 3.1).

The galaxy was detected at 3.6σ in the ALMA B6 ($S_{\rm B6} = 184 \pm 46\ \mu$m) in the blind-survey of the HUDF by Dunlop et al. (2017). In the radio (6 GHz VLA Rujopakarn et al., 2016) it is detected at a significance level $< 3\sigma$, thus only an upper limit of the 6 GHz radio flux of the source is available, i.e. $S_{6\,\rm GHz} \lesssim 0.70\ \mu$Jy. The source is not resolved in the ALMA map, but its size must be < 2.5 kpc (Tab. 4.1). After the astrometric corrections, the ALMA centroid emission appears to be shifted of ~ 10 mas from the optical peak (Fig. 4.1; see also Dunlop et al., 2017). UDF10 optical radius is $r_{\rm H} \sim 2.0$ kpc (Tab. 4.2), that is comparable with the upper limit on ALMA size.

UDF10 is detected with *Chandra* (IDX 756) in the $\simeq 7$ Ms CDFS catalog by Luo et al. (2017). The source 2 − 10 keV luminosity is then 6×10^{41} erg s^{-1}. Luo et al. (2017) classified the source to be a normal galaxy (Tab. 4.5).

Putting together these evidences with the outcomes from the galaxy SED analysis presented in Pantoni et al. (2021b), UDF10 is a $z \sim 2$ main-sequence galaxy, since it overlaps the corresponding relation by Speagle et al. (2014). Quite old (age ~ 1 Gyr) when compared to the other sources of the sample, it is characterized by a less intense burst of star formation, with $SFR \sim 40\ M_\odot$ yr^{-1} and $sSFR \sim 1 - 2$ Gyr^{-1}.

With a slightly smaller dust content ($M_{\rm dust} \sim 2\times10^8\ M_\odot$) than the majority of DSFGs, possibly its star formation has not triggered yet the activity of the central nucleus, whose power is still too low to have any kind of impact on the host galaxy. Indeed, the emission coming from star formation dominates both the radio and the X-rays (Rujopakarn et al., 2016; Pantoni et al., 2021b). However, multi-wavelength images at higher spatial resolution and sensitivity are crucial to confirm (or reject) this scenario.

4.4.6 UDF11 (J033240.06-274755.5)

UDF11 is a DSFG at $z_{\rm spec} \sim 2$. The most recent redshift measurement comes from the MUSE HUDF project, i.e. $z_{\rm spec} = 1.9962 \pm 0.0014$ (Bacon et al., 2017; Dunlop et al., 2017), in total agreement with the previous deep-spectroscopy by Kurk et al. (2013), who exploited the red-sensitive optical spectrograph FORS2 installed at the Very Large Telescope.

UDF11 was detected both in the B6 ($\sim$ 1.3 mm) ALMA and 6 GHz VLA maps of the HUDF by Dunlop et al. (2017) and Rujopakarn et al. (2016). The corresponding fluxes are $S_{1.3\,\rm mm} = 186 \pm 46\ \mu$Jy and $S_{6\,\rm GHz} = 9.34 \pm 0.74\ \mu$Jy.

The galaxy is resolved both in ALMA and VLA maps. In the millimeter it results to be more extended ($r_{\rm ALMA} \sim 3.4$ kpc; see Tab. 4.1) than the bulk of high-z DSFGs (typical ALMA radius is found to be $\lesssim 1-2$ kpc). The radio morphology is well reproduced by a two-components fit: one is spatially coincident with the central ALMA emission ($r_{\rm VLA} \sim 3.4$ kpc); the other, more compact ($r_{\rm VLA} \sim 0.7$ kpc) but shifted to the sides of the central millimeter emission, could indicate the presence of two radio lobes/hot spots, suggesting the presence of a central radio AGN (Rujopakarn et al., 2016). The radio flux at 6 GHz is solely consistent with the ongoing star formation in the host galaxy, as it is confirmed by the SED analysis presented in Pantoni et al. (2021b). Basing on these results one can assert that the central nucleus is experiencing the Radio Quiet (RQ) phase, producing jets that are still not dominant in the radio band. This is partially confirmed by the properties of the X-ray source counterpart (IDX 751) in the *Chandra* 7 Ms catalog by Luo et al. (2017). The intrinsic absorption column density $N_H \sim 3.79 \times 10^{21}$ cm^{-2} gives an absorption-corrected intrinsic $2-10$ keV luminosity of 1.7×10^{42} erg s^{-1}. Luo et al. (2017) do not find any clear evidence to classify the source as *AGN* (see Tab. 4.5). However, an X-ray luminosity $> 10^{42}$ erg s^{-1} could indicate that a (small) fraction of the emission may be traced back to the central engine. The galaxy should host a RQ AGN, still accreting material.

Also the HST/WFC3 H_{160} radius is more extended ($r_{\rm H} \sim 4.5$ kpc; see Tab. 4.2) than the aforementioned ALMA and VLA sizes. The rest-frame optical morphology is clearly clumpy/disturbed (Fig. 4.1). This evidence could be traced back to some interactions with the ambient, replenishing with gas the galaxy at large radii and fuelling the star formation (that is still ongoing, even if a signature of AGN feedback is observed in the radio band). Alternatively, the optical clumpy morphology could be simply ascribed to the combination of quenching and host galaxy star formation. Note that AGN driven winds and outflows can locally have a positive impact on star formation, compressing the gas phase and increasing its density at large radii, i.e. r $\gtrsim$ 1 kpc (e.g., Cresci and Maiolino, 2018; Shin et al., 2019). This may have affected the SED derived age of the galaxy (which appears younger) and could justify the still high SFR. Multi-wavelength imaging at higher resolution are crucial to shed light on this respect.

From the SED analysis by Pantoni et al. (2021b), the ongoing star formation burst in UDF11 has an age $\sim$ 400 Myr and it is forming stars at a rate $SFR \sim 250\ M_\odot$

yr^{-1}, with a $sSFR \sim 4$ Gyr^{-1}. Showing a more modest gas and dust content (i.e., $M_{gas} \sim 6 \times 10^9$ $M_\odot$ and $M_{dust} \sim (1.5 \times 10^8$ $M_\odot$) than the majority of the 11 DSFGs, UDF11 is characterized by a depletion timescale of $\tau_{depl} \sim 25$ Myr. AGN quenching must be close, as it is also confirmed by the extended radio size of the galaxy and the disturbed morphology in the optical, that may be affected by the energetic of the central nucleus. Indeed, in the $SFR - M_\star$ plot, UDF11 is indeed almost on the main-sequence at the corresponding redshift.

4.4.7 UDF13 (J033235.07-274647.6)

UDF13 is a DSFG at redshift $z_{spec} = 2.497 \pm 0.008$ grism redshift by Momcheva et al., 2016, based on the 3D-HST spectroscopy, see Tab. 3.1.

UDF13 was detected both in the B6 ($\sim$ 1.3 mm) ALMA and 6 GHz VLA maps of the HUDF by Dunlop et al. (2017) and Rujopakarn et al. (2016). The corresponding fluxes are $S_{1.3\,mm} = 174 \pm 45$ μJy and $S_{6\,GHz} = 4.67 \pm 0.53$ μJy. I measure an ALMA B7 continuum flux of $S_{B7} = 910 \pm 170$ μJy and give an upper limit on the ALMA size, i.e. < 0.65 kpc (Tab. 4.1). I note that the optical radius ($r_H \sim 1.2$ kpc; Tab. 4.2) is more extended than the upper limit on the millimeter size. In the UV/optical rest-frame (Fig. 4.1) UDF13 appears as an isolated object with a smooth (i.e. undisturbed) morphology.

UDF13 has a X-ray counterpart (IDX 655) in the 7 Ms *Chandra* catalog by Luo et al. (2017) with a $2-10$ keV luminosity of 1.3×10^{42} erg s^{-1}. Luo et al. classify it as *AGN* (Tab. 4.5). From the mutual analysis of FIR and radio fluxes of the source, Rujopakarn et al. (2016) found the radio emission to be enhanced by the central AGN detected in the X-ray. This conclusion is derived comparing the observed $S_{5\,cm}/S_{1.3\,mm}$ flux ratio with the one predicted by the Rieke et al. (2009) IR SED libraries, that are calibrated on local ULIRGs. This calibration on local Universe dusty galaxies along with the SED libraries intrinsic uncertainties might alter significantly the analysis. From the SED fitting and radio analysis presented in Pantoni et al. (2021b), the VLA flux is instead consistent with the ongoing star formation in the host galaxy.

The analysis presented in Pantoni et al. (2021b) classifies UDF13 a main-sequence galaxy, confirming the outcome by Elbaz et al. (2018). Quite old (age $\sim$ 900 Myr) when compared to the other sources of the sample, UDF13 forms stars at a rate $SFR \sim 100$ $M_\odot$ yr^{-1}, with a $sSFR \sim 1.7$ Gyr^{-1}. Showing a more modest modest gas and dust content ($M_{gas} \sim 5 \times 10^9$ $M_\odot$ and $M_{dust} \sim 1.2 \times 10^8$ $M_\odot$) than the majority of the 11 DSFGs, UDF13 is characterized by a depletion timescale of $\tau_{depl} \sim 45$ Myr. This galaxy should be quenched soon by the central AGN and subsequently it will become a red and dead galaxy.

4.4.8 ALESS067.1 (J033243.19-275514.3)

ALESS067.1 is a DSFG at redshift $z_{spec} = 2.1212^{+0.0014}_{-0.0005}$ (this work from CO(3 − 2) spectral line, see Tab. 4.4). It is consistent with the one measured from a H_α line with the Gemini Near-Infrared Spectrograph (GNIRS) by (Kriek et al., 2007), i.e. $z_{spec} = 2.122$.

The galaxy (sub-)millimeter counterpart was firstly observed by LABOCA (LESS; Weiß et al., 2009) and then by ALMA as a part of the ALESS project (Smail and Walter, 2014). It is a compact millimeter source, characterized by a radius of $r_{ALMA} \sim 1.1$ kpc (Tab. 4.1; but see also Thomson et al., 2014; Fujimoto et al., 2017). I found two continuum detection in ALMA B3 and B4 (Project Code: 2016.1.00564.S and 2015.1.00948.S) and I measure the fluxes $S_{B3} = 60 \pm 20$ μJy and $S_{B4} = 190 \pm 70$ μJy.

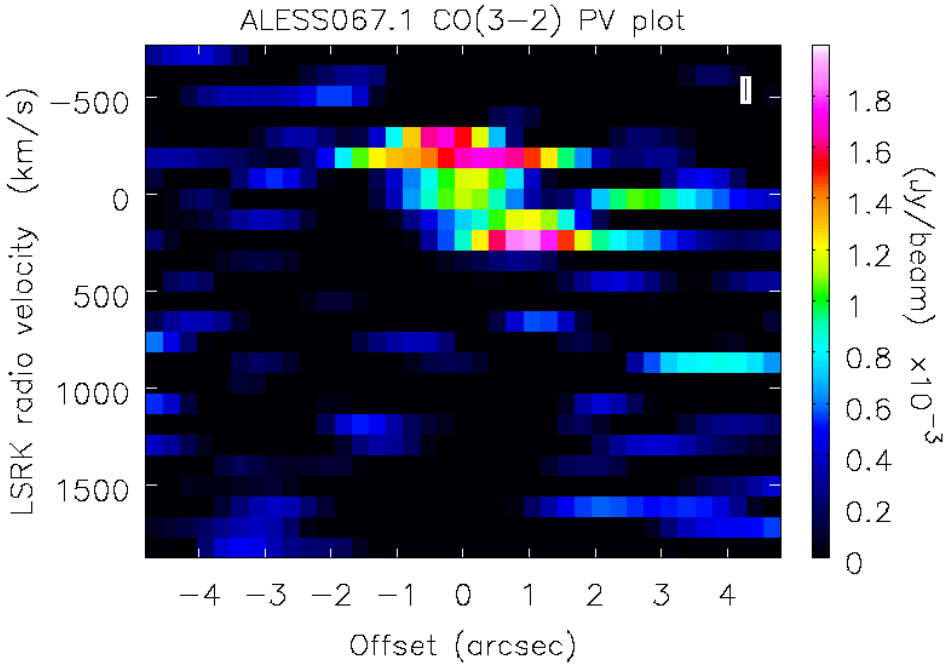

FIGURE 4.7: Position-velocity diagram for ALESS067.1 CO(3-2) molecular emission line.

In the HST/WFC3 H_{160} image (Fig. 4.1) the galaxy shows an extended (i.e. $r_{\rm H} \sim 6.5$ kpc; Tab. 4.2) and disturbed/clumpy morphology (Targett et al., 2013; van der Wel et al., 2012), that could be interpreted either as a signature of an ongoing heavily obscured and intense star formation episode, or as a possible indication of some companions (Targett et al., 2013, claim it is the dominant galaxy of a multiple system). It is possible to gain some indications on the overall picture by analysing the two CO $J > 0$ emission lines detected for ALESS067.1 (see Tab. 4.3 and Fig. 4.5). The velocity map (mom1) of the CO$(3-2)$ line show a clear velocity gradient that could indicate the presence of a rotating disc of molecular gas. However, the velocity dispersion map (mom2) shows an evident central peak with a high-velocity tail towards the upper left corner, that could indicate the presence of an outflow, possibly due to a central AGN. Similarly, the double-peaked line profile (Fig. 4.5) could be ascribed either to the inclination of the rotation plane with respect to the line of sight or to the presence of a double outflow powered by the active nucleus, where one jet is receding and the other is approaching the observer. Other hints can be gained by the analysis of the position-velocity (pv) diagram (Fig. 4.7); reference axis go through the centre and follows the velocity gradient in the velocity map with an inclination of ~ 70 degrees). The asymmetric and disturbed appearance of the pv plot may confirm the presence of a double AGN-driven molecular outflow, with a $|v| \simeq 400$ km s^{-1} and a peak of $v \simeq 900$ km s^{-1} (light cyan structure, that actually, might be just noise). A clear interpretation requires higher spectral and spatial resolution in the ALMA cube, that would have allowed to model the CO$(3-2)$ kinematics, exploiting e.g., 3D-Barolo (Di Teodoro and Fraternali, 2015), a tool for fitting 3D tilted-ring models to emission-line data cubes that takes into account the effect of beam smearing. However, I note that the presence of a molecular outflow triggered by a central engine is consistent also with the CO$(6-5)$ velocity map (mom1; Fig. 4.5), that shows a peak at higher velocities (i.e. ~ 100 km/s) in the orthogonal

direction with respect the CO(3 – 2) peak in the mom1 map. I further note that another possible interpretation is the one suggested by Calistro Rivera et al. (2018), who gave the preference to the scenario in which the CO(3 – 2) line is originated by two sources (one of them is ALESS067.1) possibly in an early stage of merger event (see also Chen et al., 2017).

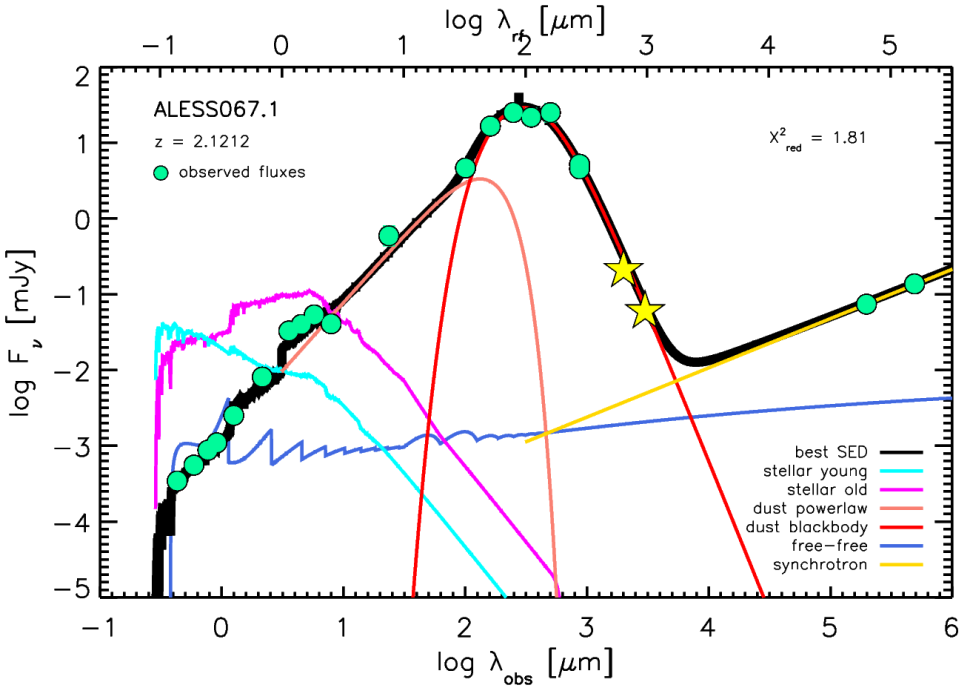

FIGURE 4.8: UV-radio best SED for ALESS067.1. Yellow filled stars stand for the ALMA B4 and B3 fluxes measured in this work (see B3 continuum contours in Fig. 4.5) and are not included in the SED fitting. Green filled circles represent the multi-band available photometry. Error bars are omitted when comparable to symbol size.

ALESS067.1 was detected in the X-ray by Luo et al. (2017). Its intrinsic 2 – 10 keV luminosity is $L_{2-10\,\mathrm{keV}} \simeq 3.8 \times 10^{42}$ erg s^{-1}, once corrected for obscuration. In Chapter 3 I have already noted that the X-ray luminosity is mostly dominated by the host galaxy star formation (see also Wang et al., 2013), however it does not exclude the presence of a central accreting nucleus at early stage (cf. Mancuso et al., 2017), whose activity could have an impact on the unclear galaxy morphology, even if at this point the nucleus emission does not emerge significantly neither in the radio or IR domains (Thomson et al., 2014).

In Fig. 4.8 I show the full SED of ALESS067.1, already presented in Chapter 3 (Pantoni et al., 2021b, see also). I note that here the modelling includes the two galaxy radio fluxes available for the source (cf. their Tab. 2 Pantoni et al., 2021b) in the SED fitting, thanks to the exploitation of the CIGALE modules for synchrotron and free-free emission in the radio band. The resulting stellar mass $M_\star = (2.9 \pm 0.3) \times 10^{11}$ $M_\odot$ and star formation rate $SFR = 485 \pm 24$ $M_\odot$ yr^{-1} place the source on the main-sequence of star-forming galaxies at the corresponding redshift (e.g. Speagle et al., 2014). An almost constant SFH (e.g. Mancuso et al., 2016a) leads to a burst age of $\simeq 0.9$ Gyr. The quite huge dust content ($M_{\mathrm{dust}} \sim 1 \times 10^9$ $M_\odot$; Tab. 4.5) is consistent both with predictions from theory (e.g. Popping, Somerville, and Galametz, 2017; Pantoni et al., 2019) and measurements on statistical sample of DSFGs (e.g. Magdis

et al., 2012). I find a radio spectral index $\alpha = 0.7 \pm 0.1$ and a FIR/radio flux ratio $q_{\rm IR} = 2.5 \pm 0.1$, in total agreement with the findings by Ibar et al. (2009) and Ibar et al. (2010) and Thomson et al. (2014) for statistical samples of SMGs.

I derived ALESS067.1 molecular hydrogen mass from the CO(3−2) line luminosity as described in Sect. 4.2.1, i.e. $M_{\rm H_2} = (1.68 \pm 0.5) \times 10^{11}\ M_{\odot}$. The depletion timescale is $\tau_{\rm depl} \sim 350$ Myr, in agreement with typical values found in literature for high-z DSFGs Casey, Narayanan, and Cooray (2014, e.g.).

Multiple evidences (such as its X-ray 2 − 10 keV luminosity, that is $> 10^{42}$ erg s^{-1}, and the eventual molecular outflow observed in the B3 ALMA map, mentioned before) suggest a forthcoming quenching of star formation in the host galaxy by the AGN.

In order to surely identify (eventual) interactions with minor companions and/or the surrounding ambient and to understand their role and the role of the active nucleus in shaping ALESS067.1 evolution, multi-wavelength images at higher sensitivity and spatial/spectral resolution are definitely needed. However, even if one accepts the scenario in which the clumpy morphology of the galaxy in the optical is an evidence of an interacting multiple system, the presented picture must not change significantly, since ALESS067.1 is thought to be by far the dominant object (Targett et al., 2013).

4.4.9 AzTEC.GS25 (J033246.83-275120.9)

AzTEC.GS25 is a DSFG galaxy firstly detected at 1.1 mm with AzTEC/ASTE ($S_{1.1\,\rm mm} = 1.9 \pm 0.6$ mJy). For this source, Popesso et al. (2009) report a grism redshift $z_{\rm spec} = 2.292 \pm 0.001$ (Tab. 3.1), based on the detection of rest-frame optical line by the VLT/VIMOS spectroscopy.

An ALMA counterpart of the AzTEC source is in the DANCING ALMA catalogue by Fujimoto et al. (2017, source ID: 661). They measured a total flux in the ALMA B7 of $S_{1\,\rm mm} = 5.9 \pm 0.5$ mJy (Tab. 4.1), in total accordance with the ALMA Band 7 flux by Cowie et al. (2018), i.e. $S_{850\,\mu\rm m} = 5.9 \pm 0.18$ mJy (source ID: no. 6; name ALMA033246-275120). Both the millimeter and optical counterparts are resolved and compact. The ALMA radius is $r_{\rm ALMA} \sim 1.2$ kpc, while the optical radius is slightly larger, i.e. $r_{\rm H} \sim 1.8$ kpc (tabs. 4.2 and 4.1). The smooth morphology of ALMA continuum and optical emission of the galaxy suggest that this object must be isolated. These evidences support the scenario in which the bulk of star formation can be traced back to local, *in-situ* condensation processes.

AzTEC.GS25 has a X-ray counterpart (IDX 844) in the $\simeq 7$ Ms *Chandra* catalog by Luo et al. (2017). The intrinsic column density $N_H \sim 8.2 \times 10^{22}$ cm^{-2} gives an absorption-corrected intrinsic 2 − 10 keV luminosity of 6×10^{42} erg s^{-1}. From the analysis of its X-ray emission, Luo et al. (2017) classified the source as *AGN* (Tab. 4.5).

Yun et al. (2012) found a radio (unresolved) counterpart of the AzTEC source in the deep ($\sigma \sim 8\ \mu$Jy) VLA 1.4 GHz imaging survey by Kellermann et al. (2008) and Miller et al. (2013). The corresponding radio flux is $S_{1.4\,GHz} = 89.5 \pm 6.2\ \mu$Jy, and it is consistent with the host galaxy star formation activity. The red IRAC/MIPS source associated with radio emission GS25a is located only 6.8 arcsec away from the AzTEC centroid position and Magnelli et al. (2013) assumed it as the NIR counterpart of the millimeter source. The 870 μm LABOCA source LESS J033246.7-275120 ($S_8 70\ \mu$m $= 5.9 \pm 0.5\ \mu$Jy) is well centred on GS25a, and Biggs et al. (2011) also identify the same galaxy as the robust LABOCA counterpart. In Chapter 3 see also Pantoni et al., 2021b, I used the flux coming from these multi-wavelength counterparts to build the galaxy SED. From the SED analysis, AzTEC.GS25 resulted a young object (age $\sim$ 300 Myr),

forming stars at a rate SFR $\sim 400\ M_\odot\ \mathrm{yr}^{-1}$, with a sSFR $\sim 3.8\ \mathrm{Gyr}^{-1}$ ($M_\star \sim 8\times10^{10}\ M_\odot$). Gas and dust rich ($M_{\rm gas} \sim 4\times10^{10}\ M_\odot$; $M_{\rm dust} \sim 1.4\times10^{9}\ M_\odot$), with a typical depletion timescale $\tau_{\rm depl} \sim 100$ Myr, its very intense burst of star formation must trigger a rapid growth of the central AGN.

4.4.10 AzTEC.GS21 (J033247.59-274452.3)

AzTEC.GS21 is a DSFG galaxy at $z_{\rm spec} = 1.910 \pm 0.001$ (grism redshift by Vanzella et al., 2008, measured with the FORS2 spectrograph (ESO/VLT), ESO/GOODS spectroscopic campaign program in the GOODS-S field). It was firstly detected at 1.1 mm with AzTEC/ASTE ($S_{1.1\,\rm mm} = 2.7^{+0.6}_{-0.7}\ \mu$Jy). This photometric data was not included in the SED analysis by Pantoni et al. (2021b) since this flux is probably contaminated by other (sub-)millimeter sources in the neighborhood. Indeed, the H_{160} image of its optical counterpart is disturbed (Fig. 4.1) and Targett et al. (2013) claim that AzTEC.GS21 is the primary dominant component of a multiple system. The authors measure an effective H_{160} radius of $r_{\rm H} \sim 2.6$ kpc and a Sérsic index $n_H \simeq 1.3$ (close to a disk-like profile). A more recent analysis on the HST image was performed by van der Wel et al. (2012), who find a circularized H_{160} radius $r_{\rm H} \sim 3.7$ kpc. In this work I have exploited the latter result.

The source was detected by ALMA in B7 (at $\lambda = 850\,\mu$m) by Cowie et al. (2018), measuring a flux $S_{850\,\mu m} = 3.6 \pm 0.3$ mJy (source ID: no. 20; name ALMA033247-274452). Hatsukade et al. (2018) measured the source flux in the ALMA B6, reporting the value $S_{\rm B6} = 1.86 \pm 0.32$ mJy. I found a $> 5\sigma$ continuum detection for this source in the ALMA B9 ($\lambda = 400 - 500\ \mu$m), measuring a flux $S_{\rm B9} = 12 \pm 1$ mJy (Tab. 4.1). AzTEC.GS21 is not resolved in the ALMA maps. For this reason I chose the map with the best spatial resolution available in the ALMA Archive in order to give at least an upper limit on its size, i.e. $r_{\rm ALMA} < 0.7$ kpc, that I use to trace the bulk of dusty star formation occurring in the galaxy.

The AzTEC source has a radio (unresolved) counterpart (GS21a) in the deep ($\sigma \sim 8\ \mu$Jy) VLA map at 1.4 GHz by Kellermann et al. (2008) and Miller et al. (2013). The corresponding radio flux is $S_{1.4\,\rm GHz} = 43.6 \pm 6.3\ \mu$Jy, that is consistent with the radio emission coming from the host galaxy star formation (see Chapter 3 and Pantoni et al., 2021b).

The AzTEC source has a X-ray counterpart (IDX 852) in the catalog by Luo et al. (2017). The intrinsic absorption column density $N_H \sim 2.27\times10^{22}\ \mathrm{cm}^{-2}$ gives an absorption-corrected intrinsic $2-10$ keV luminosity of 1.7×10^{42} erg s^{-1}. Luo et al. (2017) classified the source as *AGN* (Tab. 4.5, even if its X-ray luminosity do not clearly emerge from the host galaxy one (Pantoni et al., 2021b).

The SED analysis by Pantoni et al. (2021b) presents AzTEC.GS21 as a main-sequence galaxy. The galaxy is forming stars at a rate SFR $\sim 350\ M_\odot\ \mathrm{yr}^{-1}$, with a sSFR $\sim 2\,\mathrm{Gyr}^{-1}$. Massive ($M_\star \sim 2\times10^{11}\ M_\odot$), gas and dust rich ($M_{\rm gas} \sim 5\times10^{10}\ M_\odot$; $M_{\rm dust} \sim 6\times10^{8}\ M_\odot$), AzTEC.GS21 is characterized by a depletion timescale of $\tau_{\rm depl} \sim 140$ Myr. Notice that its star formation could be fuelled (also) by interactions with some objects in the vicinity, since some works indicate it to be the central, dominant component of a multiple system (Targett et al., 2013). However, the clumpy/disturbed morphology of the source in the optical band may also trace the condensation process of the gas phase toward the centre of the galaxy where the dusty star formation is occurring on a radius < 0.7 kpc. Even accounting the former scenario, eventual interactions should not have an important impact on the galaxy subsequent evolution, except for prolonging the star-formation, since AzTEC.GS21 dominates by far the gravitational potential of the system (Targett et al., 2013). The galaxy must be quenched by the

central AGN in some hundreds of Myr and subsequently become a red and dead galaxy. Clearly, to confirm the right scenario for the evolution of AzTEC.GS21 deeper multi-wavelength images and at higher resolution are necessary.

4.4.11 AzTEC.GS22 (J033212.55-274306.1)

AzTEC.GS22 is a DSFG galaxy firstly detected at 1.1 mm with AzTEC/ASTE ($S_{1.1\,\mathrm{mm}}$ = 2.1 ± 0.6 mJy). Yun et al. (2012) found a red IRAC/MIPS counterpart for the AzTEC source, with a spectroscopic redshift of $z_{\mathrm{spec}} = 1.794 \pm 0.005$ (Tab. 3.1 Wuyts et al., 2009; Targett et al., 2013), that I adopt in this work.

I found a $> 5\sigma$ continuum detection for AzTEC.GS22 in the ALMA B9 (λ = 400 − 500 μm) and I measured a flux $S_{0.45\,mm} = 5.8 \pm 0.8$ mJy (Tab. 4.1), that was essential to constrain the dusty peak of galaxy SED in Pantoni et al. (2021b), since the lack of the Herschel 500 μm photometric point. The ALMA source is not resolved in the continuum B9 thus I provide just an upper limit on its size, i.e. $r_{\mathrm{ALMA}} < 1.7$ kpc, tracing the bulk of dusty star formation.

The most recent analysis of the optical emission of AzTEC.GS22 was performed by van der Wel et al. (2012), who measured an optical size of $r_{\mathrm{H}} \sim 3.2$ kpc, that is more extended than the dust continuum emission (at least of a factor 2).

The faint radio source GS22a, located 7.8 arcsec away from the AzTEC centroid, is adopted in literature as the most likely counterpart at 1.4 GHz (Yun et al., 2012; Dunlop et al., 2017). Moreover in Chapter 3 (see also Pantoni et al., 2021b) I found that the VLA flux at 1.4 GHz ($S_{1.4\,\mathrm{GHz}} = 34.6 \pm 6.5$ μJy) can be traced back solely to galaxy star formation.

From the SED analysis of AzTEC.GS22 (cf. Tab. 4.5), the object resulted a main sequence galaxy. The burst of ongoing star formation in this object is almost 1 Gyr old (age $\sim 900-1000$ Myr) and it is forming stars at a rate $\sim 90-100\ M_{\odot}\ \mathrm{yr}^{-1}$. Massive ($M_{\star} \sim 6 \times 10^{10}\ M_{\odot}$), gas and dust rich ($M_{\mathrm{gas}} \sim 5 \times 10^{10}\ M_{\odot}$; $M_{\mathrm{dust}} \sim 1.4 \times 10^{9}\ M_{\odot}$), AzTEC.GS22 is characterized by a depletion timescale of $\tau_{\mathrm{depl}} \sim 550$ Myr. The huge content of gas and dust could be ascribed simply to its past star formation activity and/or to some kind of interactions (e.g., gas stripping/harassment) with possible companions observed in the optical by Targett et al. (2013). These interactions should not have a huge impact on the galaxy, since it must dominate the potential well of the multiple system. To confirm this scenario multi-wavelength imaging at higher resolution are necessary. Indeed, the clumpy/disturbed optical morphology, extending over a radius of a few kpcs, could also be interpreted as a signature of the intense dusty star formation of the galaxy.

In the literature no X-ray counterpart is found for the millimeter source, neither in the deep X-ray catalogue by Luo et al. (2017). Since the source lies in a very deep region of the *Chandra* map (equivalent exposure times of $\gtrsim 5$ Ms), the most probable hypothesis to explain the non-detection is that the source is totally obscured in the X-ray. Again, to confirm this interpretation spatially-resolved images of the system are needed, at least in the radio and millimeter bands, together with a deeper follow-up in the X-ray.

4.5 Summary

In this Chapter I derived the ALMA continuum size of the 11 DSFGs by using the ALMA continuum maps at higher spatial resolution currently available in the ALMA Archive. To this aim I performed a 2D Gaussian fitting of each source on the image, using the task *imfit* embedded in the CASA viewer. More than half of the sources

(six out of eleven) are resolved and the median physical size is 1.15 kpc. I interpreted this radius as a measure of the region where the bulk of dusty star formation occurs. It results to be very compact and always < 5 kpc.

I compared the ALMA continuum sizes with the HST/WFC3 H_{160} radii (van der Wel et al., 2012; Rujopakarn et al., 2019). The H_{160} filter samples the optical rest-frame emission from stars, and traces the star formation of the galaxy that is mildly obscured by dust or unobscured. I found a median ratio between HST and ALMA sizes of $r_{\rm H}/r_{\rm ALMA} = 2.05$ and it is always > 1, in accordance with the prediction by the *in-situ* scenario for the evolution of high-z massive star-forming galaxies (see Lapi et al., 2018) and with other recent works on high-z DSFGs (e.g. Barro et al., 2013; Barro et al., 2016b; Barro et al., 2016a; Ikarashi et al., 2015; Simpson et al., 2015; Talia et al., 2018; Tadaki et al., 2020; Massardi et al., 2018). After correcting for the astrometric shift between HST maps and ALMA maps, the bulks of the stellar and dust emission coincide within the uncertainties of the astrometric correction ($\sim$ 100 mas) and the beam resolution, for most of the galaxies. An eventual remaining shift tells us that the peaks of optical and (sub-)millimeter emission are not exactly coincident and it is possible due to the obscuration of stellar light by dust.

I analysed the five CO emission lines that were found for four of the 11 DSFGs, i.e. UDF1, UDF3, UDF8 and ALESS067.1, and derived the (sub-)millimeter redshift of the sources. The double-peaked spectral line profile of three CO lines, along with their velocity and velocity dispersion maps, are consistent with both a rotating disc of molecular gas and an AGN outflow. In particular, the first and second momenta of ALESS067.1 may suggest the presence of an outflow, even if the associated velocity (that is < 500 km/s) does not allow us to confirm this scenario. ALESS067.1 CO(6-5) line is narrow and could trace also the warm star formation in the galaxy (to confirm this interpretation it is necessary to reconstruct the CO SLED). The narrow single-peaked CO(3-2) line of UDF1 is consistent with a *faced-on* rotating molecular gas disc.

I derived the molecular gas mass of UDF1, UDF3, UDF8 and ALESS067.1 from the lower-J CO emission line luminosity, by assuming the CO excitation ladder by Daddi et al. (2015). The median molecular hydrogen gas mass is $M_{H_2} \sim 1.4 \times 10^{11}$ $M_\odot$. I measured the CO emission size from the distance between the two components peaks (in case of a double peaked profile) or I gave just an upper limit on it, since the sources are not resolved in the mom0 maps. The median CO size is of 3.5 kpc. The CO emission extends over an area greater or equal to the dust continuum size.

I complemented these results by exploiting multi-wavelength images from public catalogs, that allowed to include in the final interpretation every signature of galaxy merging/interactions and AGN feedback. The compact FIR and radio sizes ($\lesssim$ a few kpc) of the DSFGs, together with their optical radii ($\sim 2-7$ kpc), suggest that the bulk of their star formation can be traced back to *in-situ* condensation processes. Almost half of the sources shows an optical isolated morphology, while six galaxies (UDF5, UDF10, UDF11, ALESS067.1, AzTEC.GS21, AzTEC.GS22) have more complex (i.e., clumpy or disturbed) morphologies, but still on scales $\sim 5-10$ kpc. They may indicate the presence of minor interactions - that can prolong the star formation in the dominant galaxy by refuelling it with gas - or may be just a signature of the ongoing dusty star formation.

Most of the galaxies in the pilot sample are caught in the *gas compaction* phase and models predict that they should be quenched by the AGN feedback in $\sim 10^8$ yr. Three objects show some features that can be interpreted as signatures of nuclear activity by the detection of possible AGN-driven molecular outflows (UDF3, UDF8, ALESS067.1). After quenching, galaxy evolution should be mainly driven by stellar

populations aging and mass additions by dry merger events. Ultimately, the 11 DSFGs are expected to become compact quiescent galaxies or massive ETGs.

More sensitive multi-wavelength maps and higher spatial and spectral resolution images in the diverse spectral bands are needed to definitely clarify the relative impact of *in-situ* processes, galaxy interactions and AGN feedback in determining massive star-forming galaxy evolution at high-z and their morphological transformation.

Chapter 5

Conclusions and future perspectives

In this Chapter I will summarize the main results of this work and give some indications on possible future plans for research.

5.1 Main results

The goal of this thesis is to characterize the early stages of DSFG evolution by investigating the spectral multi-band traces of the ongoing astrophysical processes. I used, as test-bench, a sample of 11 DSFG spectroscopically confirmed to be at the peak of cosmic SFH ($z \sim 2$). I exploited a panchromatic approach, that encompasses the analysis of galaxy integral properties, through SED fitting, and the information coming from galaxy spatially-resolved and spectral multi-wavelength emission. This approach allowed me to provide valuable insights into the principal astrophysical processes that mostly account for massive galaxy evolution at high-z, such as gas condensation, star formation, central BH accretion and feedback, galaxy interactions.

I provided a consistent and physically motivated picture of the main mechanisms that are effective on (sub-)galactic scales (i.e., gas cooling, star formation and stellar feedback, dust production and destruction, pollution of the ISM by metals from SN II and SN Ia explosions) by developing a simple but effective analytic model that describes the time evolution of galaxy baryonic components: stars, warm and cold gas, metals and interstellar dust in the ISM (see also Pantoni et al., 2019).

Then, by comparing my model prediction with the observational measurements of the selected sample, I demonstrated how the multiple information coming from photometry, spectroscopy and imaging at high-resolution, when put together, constitute a fundamental instrument to give a complete interpretative picture of galaxy evolution. My analysis confirmed that the in-situ scenario for galaxy-BH co-evolution is suitable to provide a possible physical explanation of massive galaxy formation and evolution (see Lapi et al., 2014; Mancuso et al., 2016b; Mancuso et al., 2016a; Mancuso et al., 2017; Shi et al., 2017; Lapi et al., 2018).

In the following I summarize the principal outcomes of this work and outline my conclusions.

- I have presented a set of new analytic solutions aimed at describing the spatially-averaged evolution of the gas/stellar/dust mass and metal content in a star-forming galaxy hosted within a dark halo of given mass and formation redshift. The analytic solutions were applied to describe the formation of ETGs and the evolution of their star-forming progenitors at high-z using specific prescriptions for parameter setting, inspired by the *in-situ* galaxy-BH co-evolution scenarios

for ETG formation. Then, I derived a bunch of fundamental relationships involving spatially-averaged quantities as a function of the observed stellar mass (i.e., star formation efficiency, SFR, gas mass, dust mass, gas metallicity, stellar metallicity and [α/Fe] ratio, and out-flowing gas metallicity), that resulted in a pleasant overall agreement when compared with observational data on local ETGs and their high-z star-forming progenitors. I remark that a major value of this approach is to reproduce, with a unique set of physically motivated parameters, a wealth of observables concerning ETGs and their progenitors.

- By using the predictions of the aforementioned model, I have investigated the astrophysical properties of 11 (sub-)millimeter selected DSFGs in the GOODS-S field. All of them have a spectroscopic measurement of redshift and a complete sampling of their broad-band emission, from the X-rays to the radio band. The extensive multi-wavelength photometry of the GOODS-S field was essential to reliably reconstruct and precisely model galaxy SED with CIGALE, by using a physically-motivated recipe to describe stellar light attenuation by dust. In such a way I was able to extracted the main integral properties of the 11 DSFGs (i.e., SFR, stellar mass, stellar attenuation by dust, dust temperature, IR luminosity, dust mass). Finally, I took advantage of the X-ray and radio photometry to guess the presence of an AGN and its eventual contribution to IR light.

- I analyzed the most recent ALMA continuum maps and spectroscopic images of the pilot sample of DSFGs, choosing the ones with the highest spatial and spectral resolution publicly available in the ALMA Archive. I derived the dust emission size (or just an upper limit in case of scarce spatial resolution) of the 11 DSFGs. I modelled the CO $J > 1$ emission lines found in the ALMA data cubes for four of the galaxies (i.e. UDF1, UDF3, UDF8, ALESS067.1) and derived the molecular hydrogen mass. The outcomes in the (sub-)millimeter regime were compared with the galaxy emission in the other spectral bands, such as optical, X-ray and radio. Finally, I could easily and successfully include my findings in the perspectives presented by the *in-situ* galaxy-BH co-evolution scenario (e.g., Mancuso et al., 2016b; Mancuso et al., 2016a; Mancuso et al., 2017; Lapi et al., 2018; Pantoni et al., 2019) to identify the evolutionary status of each galaxy and describe its observed features in a more general framework.

- The 11 DSFGs of are (almost) main-sequence objects, with a median $M_\star = 6.5 \times 10^{10}\ M_\odot$ and $SFR \sim 250\ M_\odot\ \mathrm{yr}^{-1}$. They are experiencing an intense and dusty (median $L_{\rm IR} \sim 2 \times 10^{12}\ L_\odot$) burst of star formation, with typical duration $\tau_\star$ ranging between 0.2 and 1 Gyr. Although their young age, the interstellar dust content is high ($M_{\rm dust} > 10^8\ M_\odot$), possibly due to a very rapid enrichment of the ISM (on typical timescales of $10^7 - 10^8$ yr). The gas mass (median $M_{\rm gas,\,tot} \sim 6 \times 10^{10}\ M_\odot$ and $M_{\rm gas,\,mol} \sim 3 \times 10^{10}\ M_\odot$)[1], fuelling the dusty star formation, will be rapidly depleted, over a median timescale $\tau_{\rm depl} \sim 200$ Myr. Nine objects out of eleven have an X-ray luminous ($L_{2-10\rm keV} \gtrsim 10^{42}\ \mathrm{erg\,s^{-1}}$) counterpart in the *Chandra* 7 Ms catalog and two of them are clearly dominated by the active nucleus emission ($L_{2-10\rm keV} \gtrsim 10^{43} - 10^{44}\ \mathrm{erg\ s^{-1}}$). The radio luminosity is consistent with the emission coming from galaxy star formation, suggesting that the AGN, if present, should be radio silent or quiet.

[1]The median molecular hydrogen gas mass derived from the CO line luminosity of 4 galaxy of the sample is $M_{H_2} \sim 1.4 \times 10^{11}\ M_\odot$

- I give a possible interpretation of the outcomes in light of the *in-situ* galaxy-BH co-evolution scenario (Mancuso et al., 2016a; Mancuso et al., 2016b; Shi et al., 2017; Mancuso et al., 2017; Lapi et al., 2018). I found the results derived from SED fitting to match the model predictions within their 2σ scatter, suggesting that the main drivers of the 11 DSFGs evolution can be mostly traced back to local condensation processes.

- I compared the ALMA continuum sizes with the HST/WFC3 H_{160} radii (van der Wel et al., 2012; Rujopakarn et al., 2019). The H_{160} filter samples the optical rest-frame emission from stars, and traces the star formation of the galaxy that is mildly obscured by dust or unobscured. I found a median ratio between HST and ALMA sizes of $r_{\rm H}/r_{\rm ALMA} = 2.05$ and it is always > 1, while the median CO size is of 3.5 kpc and it extends over an area greater or equal to the dust continuum size. These observational results are in accordance with the prediction by the *in-situ* scenario for the evolution of high-z massive star-forming galaxies (see Lapi et al., 2018) and with other recent works on high-z DSFGs (e.g. Barro et al., 2013; Barro et al., 2016b; Barro et al., 2016a; Ikarashi et al., 2015; Simpson et al., 2015; Talia et al., 2018; Tadaki et al., 2020; Massardi et al., 2018).

- Multi-wavelength images from public catalogs allowed to include in the final interpretation every signature of galaxy merging/interactions and AGN feedback. The compact FIR and radio sizes ($\lesssim$ a few kpc) of the DSFGs, together with their optical radii ($\sim 2-7$ kpc), suggest that the bulk of their star formation can be traced back to *in-situ* condensation processes. Almost half of the sources shows an optical isolated morphology, while six galaxies (UDF5, UDF10, UDF11, ALESS067.1, AzTEC.GS21, AzTEC.GS22) have more complex (i.e., clumpy or disturbed) morphologies, but still on scales $\sim 5-10$ kpc. They may indicate the presence of minor interactions - that can prolong the star formation in the dominant galaxy by refuelling it with gas - or may be just a signature of the ongoing dusty star formation.

- Most of the galaxies in the pilot sample are caught in the *gas compaction* phase and models predict that they should be quenched by the AGN feedback in $\sim 10^8$ yr. Three objects show some features that can be interpreted as signatures of nuclear activity by the detection of possible AGN-driven molecular outflows (UDF3, UDF8, ALESS067.1). However, the double-peaked spectral line profile of their CO lines, along with their velocity and velocity dispersion maps, are consistent also with rotating disk of molecular gas. More sensitive multi-wavelength maps and higher spatial and spectral resolution images in the diverse spectral bands are needed to definitely clarify the picture. After quenching, galaxy evolution should be mainly driven by stellar populations aging and mass additions by dry merger events. Ultimately, the 11 DSFGs are expected to become compact quiescent galaxies or massive ETGs.

5.2 Future prospects

The method presented in this thesis applies easily to small sample of galaxies and, as such, the first straightforward future plan consists in extending the analysis to other fields, such as COSMOS and H-ATLAS, that ensure both a complete sampling of galaxy SED and multi-wavelength continuum and spectral information at similar

resolution, even if just on a limited number of spectroscopically-confirmed objects (e.g., Neri et al., 2020). As soon as big samples of spectroscopically-confirmed high-z DSFGs become available (see e.g. the ongoing z-GAL NOEMA Large Program[2]; PIs: P. Cox; T.Bakx; H.Dannerbauer), it will be possible to exploit the approach presented here for constraining, on a statistical basis, the evolution of the whole galaxy population, its final contribution to the Cosmic stellar mass assembly, the actual impact of the central nucleus on the host galaxy and its role in the formation of massive spheroids.

As I have already underlined in Chapter 3 (cf. in particular Sect. 3.1.3), the study presented here could be somehow biased towards the sub-population of high-z DSFGs that are observed in the UV/optical rest-frame, even if the magnitude limits of the optical/NIR photometric filters exploited in the HUDF survey[3] allow to detect also sources that are very faint in this wavelength range. The requirement of 3 detections (at least) in the optical domain, that is essential to constrain galaxy stellar mass and interstellar dust attenuation by fitting galaxy SED, implies the loss of all the dusty galaxies that are totally dark in the UV/optical rest-frame, namely more than 20% of the total population (e.g., Chen et al., 2015). As such, another important future application to study DSFGs evolution consists in including also these objects in the analysis, e.g. by the development of new recipes to model the total absorption of stellar light by dust.

A great improvement of the results presented in this thesis can be achieved by the study of gravitationally-lensed millimeter sources. This is particularly true at the Cosmic Noon (i.e., the peak of Cosmic SFH at $z \sim 2$) where the cosmological trend of angular distance disfavour at most the conversion to physical scales (Hogg, 1999). Gravitational lensing, on the one hand, magnifies the source flux without modifying its colors, on the other hand, it increases the source angular dimension, easing the study of processes occurring on sub-galactic scales. In selecting the sample of $z \sim 2$ dusty galaxies, I discarded four millimeter sources showing some peculiarities that may indicate these objects to be lensed by a foreground source. For the sake of completeness, the cases of these four galaxies are illustrated in Appendix A, along with the main issues related to lensing.

Finally, the approach described in this thesis can be interestingly applied to local star-forming galaxies, that are spatially resolved. Indeed, the analytic model presented in Chapter 2 may be easily specialized to the diverse local galaxy environments, simply by changing the values of the main parameters entering the analytic solutions, and thus exploited to characterize the ISM and the dust-cycle. Of course, other processes must be taken into consideration while studying local disc-dominated/Milky Way-like star-forming galaxies, such as the refurnishing of reprocessed, metal-enriched gas by stellar evolution, that can be traced back e.g. to the so-called *galactic fountain* mechanism. For the sake of completeness, in Appendix B I suggest a possible generalization of the analytic solutions to the case of LTGs, that includes a simple but effective description of wind recycling and galactic fountains, with the aim of self-consistently investigating the spatially-averaged time evolution of LTG gas, stellar, metal, and dust content.

[2]http://www.iram.fr/ z-gal/Home.htm

[3]Magnitude limits of the optical/NIR filters in the GOODS-MUSIC (HUDF) $m_{AB}(B) = 27.5$ mag; $m_{AB}(V) = 27.5$ mag; $m_{AB}(i) = 26.5$ mag; $m_{AB}(z) = 26.0$ mag; $m_{AB}(J) = 24.5$ mag; $m_{AB}(H) = 24.3$, $m_{AB}(K_s) = 23.8$ (Grazian et al., 2006).

Appendix A

A view on four peculiar DSFGs at $z \sim 2$

In this Appendix I will provide an insight into the cases of four millimeter sources, firstly detected by AzTEC (see Yun et al., 2012), that were not included in the pilot sample analysed in this thesis because showing some peculiarities in their multi-wavelength emission. In the following I will briefly present the cases of these four objects, and suggest a possible operative method to address the analysis.

Three AzTEC sources, i.e. AzTEC.GS2, AzTEC.GS11, AzTEC.GS24, were discarded because they possibly are lensed candidate. The common character of these millimeter sources is that the multi-band association reveals multiple counterparts within the AzTEC beam at very diverse redshifts, both in the high-z Universe ($z \sim 1.5 - 3.5$) and in the local Universe ($z \sim 0.2 - 0.7$). A slightly different case is the one of AzTEC.GS28 (that I will address at last), since in the literature I did not find the same great variety in redshift of the millimeter source multi-wavelength counterparts. However, AzTEC.GS28 was finally discarded because it was not possible to reliably reconstruct its multi-wavelength emission.

An informative future analysis on these objects can be performed by targeting the AzTEC sources with ALMA B6/B7 and/or B3/B4 observations at high-resolution in order to investigate the lensed nature of the millimeter sources and eventually apply the panchromatic method presented in this thesis to constrain galaxy properties and gain some insights into their evolution. Specifically, in the case of AzTEC.GS28 an ALMA follow-up at high-resolution may be important to understand whether we are observing e.g., an optically-dark ALMA source (since HST and ALMA positions are mismatched, as I will later address) or e.g., a lensed millimeter source by an evolved foreground object.

I further note that similar approaches are in development, e.g., on samples of DSFGs selected in H-ATLAS (see Giulietti et al. submitted to *MNRAS*) with analog criteria to the ones used in this thesis but with the additional requirements exploited by Negrello et al. (e.g. 2014), so that the most luminous sources at 500 μm are most likely lensed.

A.1 AzTEC.GS2.1 (J033219.06-275214.6)

AzTEC.GS2.1 (J033219.06-275214.6)[1] has two optical counterparts in the GOODS-MUSIC by Grazian et al. (2006), i.e. GOODS-CDFS-MUSIC 04107 (RA 03h32m19.032s DEC -27d52m13.99s), showing a separation from the AzTEC centroid of $d \sim 5.3$ arcsec; and GOODS-CDFS-MUSIC 04099 (RA 03h32m19.037s DEC -27d52m14.83s),

[1]The IAU position refers to the radio (VLA at 1.4 GHz) counterpart (GS2.1a) by Yun et al. (2012), that show a separation of 4.7 arcsec from AzTEC centroid, but still inside its beam.

showing a separation from the AzTEC centroid of $d \sim 5.9$ arcsec. GOODS-CDFS-MUSIC 04107 appears also in the CANDELS GOODS-S catalog by Cappelluti et al. (2016, CANDELS J033219.03-275213.9), who measured a spectroscopic redshift of $z_{\rm spec} = 0.696$ for the HST source. The latter is found to be the most probable optical counterpart for the X-ray source detected in the 7 Ms catalog by Luo et al. (2017, CDFS 0342), that is located within 1 arcsec from the AzTEC centroid. The accepted redshift for CDFS 0342 by Luo et al. (2017) is $z_{\rm phot} = 0.76$. However, Bonzini et al. (2012) claim that the most probable optical/infrared counterpart of the *Chandra* source (CDFS 0342) is at $z_{\rm phot} = 1.98$. While GOODS-CDFS-MUSIC 04107 has no *Herschel* counterpart, GOODS-CDFS-MUSIC 04099 is in the *Herschel* catalog by Magnelli et al. (2013). The multi-band photometry available for the latter optical source allow to perform the SED fitting and derive its photometric redshift, i.e. $z_{\rm phot} = 2.44$ (Santini et al., 2009) and $z_{\rm phot} = 2.13$ (Grazian et al., 2006), consistent with the measurement by Bonzini et al. (2012).

In the radio band (VLA map at 1.4 GHz), Yun et al. (2012) found two most probable counterparts of the millimeter source, i.e. GS2.1a and GS2.1b. They claim that GS2.1a constitutes a robust identification, with a p-value $P_{1.4\,\rm GHz} = 0.001$. GS2.1a is also characterized by a red IRAC colour, i.e. [3.6 μm] − [4.5 μm] = +0.38. In addition, they note that there is a third potential radio counterpart, GS2.1c, identified by a MIPS 24 μm detection, that is only 3.9 arcsec from the AzTEC centroid. However, they state that it is likely a foreground object, due to its a blue IRAC color, i.e. [3.6 μm] − [4.5 μm] = −0.32. GS2.1c spectroscopic redshift is $z = 0.644$ (that is interestingly consistent with the measurements for GOODS-CDFS-MUSIC 04107 and CDFS 0342).

I further note that Yun et al. (2012) derived from the optical/NIR SED (see their Sect. 3.1) a $z_{\rm phot} = 2.13 \pm 0.60$ for AzTEC.GS2.1, while from the radio and AzTEC photometry (see their Sect. 3.2) a $z_{\rm phot} = 3.20^{+0.60}_{-1.10}$.

All the aforementioned multi-wavelength sources fall within the AzTEC beam and possibly contaminate the millimeter flux and/or magnify the background source through gravitational lensing. The presence of multi-band sources at $z \sim 0.6 - 0.7$, that are almost perfectly aligned with AzTEC.GS2.1, supports the thesis of having a foreground object that may act as a lens for the background AzTEC source. In addition, $z \sim 0.6 - 0.7$ falls into the redshift range that maximize the probability of the gravitational-lensing of background sources at $z \sim 2$ (where the millimeter source should lie).

A.2 AzTEC.GS11 (J033215.79-275036.8)

AzTEC.GS11 (J033215.79-275036.8)[2] has just one association with the GOODS-MUSIC by Grazian et al. (2006), when it is matched with the Magnelli et al. (2013) catalog, i.e. GOODS-CDFS-MUSIC 05744 (RA 53.063641 deg DEC -27.844280 deg), with a separation $d \sim 7.3$ arcsec. However, this optical source has a spectroscopic redshift $z_{\rm spec} = 0.246$ (Grazian et al., 2006), that is consistent with the most accredited measurements in the literature (Wolf et al., 2004; Szokoly et al., 2004; Wuyts et al., 2009; Santini et al., 2009; Conselice et al., 2011, e.g.). The photometric redshift measured by Yun et al. (2012) from the AzTEC 1.1 mm flux, i.e. $z_{\rm phot} = 2.5^{+0.52}_{-0.88}$, is completely inconsistent with the identification above, as well as the photometric redshift calculated by Targett et al. (2013), i.e. $z_{\rm phot} = 1.69$ (1σ uncertainty interval: 1.50 − 1.95).

Yun et al. (2012) found a single tentative VLA radio counterpart for this source that is located 6.5 arcsec from the AzTEC centroid, and it is also a *Chandra* X-ray

[2]The IAU position refers to the AzTEC centroid position by Targett et al. (2013).

source. Its IRAC/MIPS counterpart (GS11.a) is actually a blend of an optically bright foreground source at $z = 0.246$ (the same of GOODS-CDFS-MUSIC 05744) and an optically faint source second source, which is the radio source mentioned at first (Retzlaff et al., 2010).

It is clear that the foreground source may work as a lens and magnify the millimeter flux of the AzTEC source. However, multi-band follow-ups at higher spatial resolution are needed to confirm this hypothesis. I further note that the CANDELS counterpart for AzTEC.GS11 by Targett et al. (2013) was recently found to have a spectroscopic redshift $z_{\rm spec} = 3.911$ (Cappelluti et al., 2016), that renders the picture more complex. The redshifts that are found in the literature for this CANDELS source span the range $z \sim 0.2 - 4$ (e.g. Bonzini et al., 2012; Weigel et al., 2015; Luo et al., 2017), possibly supporting the scenario in which we are observing a lensed millimeter source.

A.3 AzTEC.GS24 (J033234.76-274943.1)

AzTEC.GS24 (J033234.76-274943.1)[3] has just one association with the GOODS-MUSIC by Grazian et al. (2006), when it is matched with the Magnelli et al. (2013) catalog, i.e. GOODS-CDFS-MUSIC 07280 (RA 53.1428833 deg DEC -27.8279305 deg), with a separation $d \sim 6.7$ arcsec. The optical counterpart redshift is not well constrained since in the literature it spans the range $z_{\rm phot} = 0.16 - 3.6$ (see e.g. Grazian et al., 2006; Santini et al., 2009; Xue et al., 2011; Targett et al., 2013; Cappelluti et al., 2016; Luo et al., 2017). The most recent measurement comes from the MUSE-Wide survey in the CANDELS/Deep area of the CDFS by Herenz et al. (2017), who associate ($d \sim 0.12$ arcsec) to GOODS-CDFS-MUSIC 07280 the CANDELS source J033234.28-274940.4 (IAU ID), measuring a spectroscopic redshift $z_{\rm spec} = 0.543769 \pm 0.000025$. However, I note that at a separation of $d \sim 5$ arcsec (still in the AzTEC beam) is found another CANDELS source (IAU ID J033234.23-274935.5), whose spectroscopic redshift is $z_{\rm spec} = 3.5705 \pm 0.0001$ (Herenz et al., 2017).

Yun et al. (2012) found just a single tentative association with a faint radio source within 12.2 arcsec, i.e. GS24.a. The BLAST source 104 (at $\lambda = 250\,\mu$m Eales et al., 2009) straddles GS24.a together with the type 2 QSO J033235.78-274916.82 at $z_{\rm spec} = 2.578$ (Rigopoulou et al., 2009, also detected at MIPS 70 μm)): both these sources likely contribute to the 250 μm continuum. Basing on the P-value statistics, Dunlop et al. (2010) identified for the BLAST source 104 a radio counterpart at $z_{\rm spec} = 0.547$, that is located at the edge of the AzTEC and BLAST beam. No nearby source is found in the 870 μm LABOCA catalog, but the LABOCA map shows a $S/N \sim 3$ emission peak near the $z_{\rm spec} = 2.578$ type 2 QSO J033235.78-274916.82 and a secondary $S/N \sim 2$ emission peak near GS24.a (Yun et al., 2012).

I further note that Yun et al. (2012) derived for AzTEC.GS24 a $z_{\rm phot} = 1.94 \pm 0.5$ from the optical/NIR SED (see their Sect. 3.1), while from the radio and AzTEC photometry (see their Sect. 3.2) a $z_{\rm phot} = 3.04^{+0.74}_{-1.10}$. Targett et al. (2013) measured a photometric redshift $z_{\rm phot} = 2.18$ (1σ uncertainty range: $2.07 - 2.27$) from the SED fitting to the optical–MIR photometry that they associated to the AzTEC source (cf. their Sect. 4.4).

All these evidences clearly indicate that multiple sources must fall into the AzTEC beam. In fact, Yun et al. (2012) note that the AzTEC contours are elongated in the north–south direction, and claim that this may indicate a case of blended source. As noted also for AzTEC.GS2, the presence of multi-band sources at $z \sim 0.5$ that are

[3]The IAU position refers to the AzTEC centroid position by Targett et al. (2013).

almost aligned with AzTEC.GS24 supports the thesis of having a foreground object that may act as a lens for the background millimeter galaxy.

A.4 AzTEC.GS28 (J033242.71-275206.8)

AzTEC.GS28 (J033242.71-275206.8)[4] has an optical counterpart in the GOODS-MUSIC by Grazian et al. (2006), i.e. GOODS-CDFS-MUSIC 04302, with a $z_{\rm spec} = 3.607$ (from both Hβ and [OIII] emission line Straughn et al., 2009). This optical source was detected also in the CANDELS, i.e. CANDELS J033241.85-275202.4, and was chosen by (Yun et al., 2012) to be the AzTEC.GS28 optical counterpart. Every measurements of the optical source redshift available in the literature (both spectroscopic and photometric; e.g. Wolf et al., 2004; Balestra et al., 2010; Xue et al., 2010; Iwasawa et al., 2012; Cappelluti et al., 2016) agree in indicating the source redshift to be $z \sim 3.4-3.6$.

Yun et al. (2012) do not find any VLA ($\nu = 1.4$ GHz) detection within a radius of 13 arcsec. However, the authors indicate two most likely IRAC red counterparts for the millimeter source, referred as GS28.a and GS28.b. By assuming GS28.a to be the IRAC counterpart of AzTEC.GS28, Yun et al. (2012) measured a photometric redshift $z_{\rm phot} = 3.29 \pm 0.65$. The preferred (photometric) redshifts in the literature for the two IRAC sources are $z_{\rm a} = 3.92$ (Santini et al., 2009) for GS28.a, and $z_{\rm b} = 0.13$ (Wolf et al., 2004), $z_{\rm b} = 2.77$ (Santini et al., 2009) for GS28.b. No nearby source is found in the 870 μm LABOCA catalog, but the LABOCA map shows an extended source with a $S/N \sim 3.0$ emission peak near the AzTEC source position, and this may constitute an indication of blended source.

The latter hypothesis is supported by the search for an ALMA B7/B6 counterpart in the ALMA Archive[5]. In correspondence of the CANDELS position no source has been found in the ALMA B7 map (Project Code: 2015.1.00242.S), even if a detection was expected instead, given the ALMA B7 rms of 0.15 mJy (*Herschel* fluxes associated to the optical source by Magnelli et al. (2013) are in the range $\sim 3-10$ mJy and the AzTEC flux at 1.1 mm is $S_{1.1\,\rm mm} = 2.1^{+0.6}_{-0.6}$ mJy). However, at a separation $d \sim 19.5$ arcsec from the optical source there is an ALMA B7 detection, with a flux $S_{\rm B7} \sim 3.5$ mJy (source ID scuba2-016; RA 03:32:42.803 DEC -27:52:12.813), that falls into the AzTEC beam (of ~ 30 arcsec) and possibly also in the *Herschel* cameras' ones (respectively of about 18, 24 and 36 arcsec). The *Herschel* fluxes in the catalog by Magnelli et al. (2013) are consistent with the *Spitzer*, AzTEC and ALMA (meaning scuba2-016) ones, even if there is an intrinsic inconsistency between them: they are not monotonically increasing as it is expected from the typical FIR SED shape: $S_{250} \simeq 7 \pm 3$; $S_{350} \simeq 4 \pm 3$; $S_{500} \simeq 10 \pm 5$).

I further note that the scuba2-016 closest counterpart in the GOODS-MUSIC by Grazian et al. (2006) is GOODS-CDFS-MUSIC 04350, that is at a distance of 13.6 arcsec with $z_{\rm spec} = 1.12$. Notice that this 13.6 arcsec correspond to ~ 100 kpc given a scale of ~ 8 kpc/arcsec (valid at $z \sim 2$). By performing a sky match with a 15 arcsec searching radius from the AzTEC centroid, I found 3 sources of the Magnelli et al. (2013) catalog, that have also a GOODS-MUSIC counterpart, to fall into the AzTEC beam. In order to untangle this complex picture, other multi-band follow-ups at higher spatial resolution are definitely needed.

[4] The IAU position refers to the AzTEC centroid position by Targett et al. (2013).

[5] https://almascience.nrao.edu

Appendix B

Application to LTGs

Basing on Lapi et al. (2020), here I illustrate a possible generalization of the analytic solution presented in Chapter 2 to the case of $z < 1$ disk-dominated Late Type Galaxies (LTGs), like the Milky Way. To this aim, a simple yet effective description of wind recycling and galactic fountains is included. In such a way, the model allows to carry out a self-consistent investigation of the spatially-averaged time evolution of galaxy baryonic components, i.e. gas, stars, metals and dust.

In Lapi et al. (2020) it is shown that, when supplemented with specific prescriptions for parameter setting and halo accretion rates from $N-$body simulations, the analytic solutions can reproduce the main statistical relationships followed by local LTGs. In particular, these involve, as a function of the stellar mass, the star formation efficiency, the gas mass fraction, the gas/stellar metallicity, the dust mass, the star formation rate, the specific angular momentum, and the overall mass/metal budget.

I would stress that the model can be exploited to disentangle the diverse role of the main physical processes ruling galaxy formation in LTGs. In particular, wind recycling and galactic fountains result to be crucial in efficiently refurnishing the gas mass, extending the star formation timescale in LTGs, and boosting the metal enrichment in gaseous and stellar components. As such, the analytic solutions constitute a transparent, handy, and fast tool and, as such, they provide a basis for improving the (sub-grid) physical recipes implemented in more sophisticated semi-analytic models and numerical simulations. Moreover, they offer a benchmark for interpreting and forecasting current and future spatially-averaged observations of $z < 1$ LTGs.

In the following Sections, I present the solutions for an individual LTG, that is described as a one-zone system with three interlinked mass components: the infalling gas mass $M_{\rm inf}$, the cold gas mass $M_{\rm cold}$, and the stellar mass $M_\star$. For future reference, the gas mass is defined as $M_{\rm gas} \equiv M_{\rm inf} + M_{\rm cold}$.

B.1 Gas and stars

The evolution of gas and stars as a function of the galactic age τ is described by the following system of ordinary differential equations:

$$\begin{cases} \dot{M}_{\rm inf} = -\frac{M_{\rm inf}}{\tau_{\rm cond}} + \alpha_{\rm GF}\,\epsilon_{\rm out}\,\frac{M_{\rm cold}}{\tau_\star}\ , \\ \dot{M}_{\rm cold} = \frac{M_{\rm inf}}{\tau_{\rm cond}} - (1-\mathcal{R})\,\frac{M_{\rm cold}}{\tau_\star} - \epsilon_{\rm out}\,\frac{M_{\rm cold}}{\tau_\star}\ , \\ \dot{M}_\star = (1-\mathcal{R})\,\frac{M_{\rm cold}}{\tau_\star}\ . \end{cases} \tag{B.1}$$

These equations prescribe that the infalling gas mass $M_{\rm inf}$ condenses into the cold gas phase $M_{\rm cold}$ over a characteristic timescale $\tau_{\rm cond}$; then the stellar mass $M_\star$ is formed from the cold mass $M_{\rm cold}$ at a rate $M_{\rm cold}/\tau_\star$ over a characteristic timescale $\tau_\star$; the cold gas mass is further replenished at a rate $\mathcal{R}\,M_{\rm cold}/\tau_\star$ by stellar recycling, where $\mathcal{R}$ is the return fraction of gaseous material from stellar evolution, and it is removed at a rate $\epsilon_{\rm out}\,M_{\rm cold}/\tau_\star$ by SN II driven outflows and stellar winds, where $\epsilon_{\rm out}$ is the mass loading factor of the outflow; finally, a fraction $\alpha_{\rm GF}$ of this out-flowing gas mass returns back to the infalling gas and becomes again available for condensation, in the way of establishing a galactic fountain. In the above Eqs. (B.1) the quantity $M_\star$ represents the true relic stellar mass after the loss due to stellar evolution. The IMF ($\phi(m_\star)$) is uniform in space and constant in time. The exploited approximations of instantaneous mixing (gas is well mixed at anytime) and instantaneous recycling (stars with mass $m_\star \gtrsim 1\,M_\odot$ die as soon as they form, while those with $m_\star \lesssim 1\,M_\odot$ live forever) imply a recycled fraction (fraction of a stellar population not locked into long-living dark remnants):

$$\mathcal{R} \equiv \int_{1\,M_\odot}^{100\,M_\odot} \mathrm{d}m_\star\,(m_\star - m_{\rm rem})\,\phi(m_\star) \tag{B.2}$$

where $m_{\rm rem}(m_\star)$ is the mass of the remnants. The recycling fraction amounts to $\mathcal{R} \approx 0.45$, for the fiducial Chabrier (2003) and Chabrier (2005) IMF and the Romano et al. (2010) stellar yield models. Standard initial conditions for the above system of equations read $M_{\rm inf}(0) = f_{\rm inf}\,M_{\rm b}$ and $M_{\rm cold}(0) = M_\star(0) = 0$, where $M_{\rm b} = f_{\rm b}\,M_{\rm H}$ is the baryonic mass originally present in the host halo with mass $M_{\rm H}$, while $f_{\rm inf} = M_{\rm inf}/f_{\rm b}\,M_{\rm H}$ is the fraction of such a mass that can effectively cool fast and inflow toward the inner regions of the halo over the timescale $\tau_{\rm cond}$.

I note that the above equations are very similar to those included in many semi-analytic models (SAMs), and in particular in the `GALFORM` implementation (see Cole et al., 2000; Lacey et al., 2016; Lagos et al., 2018, for a review of different SAMs), though typically these codes solve the equations over infinitesimal time-steps (see Appendix B in Cole et al., 2000), since the halo and infall gas masses are continuously updated due to merging events along DM merger trees. The model presented here, instead, provides a global time solution for any finite galactic age, since the latest $N-$body simulations have shown that, when depurated from pseudo-evolution, the mass additions to the baryonic content after formation are minor and occur on rather long timescales so they can be included *a posteriori*. Furthermore, in Eqs. (B.1) the mechanisms of fountain-driven accretion (see Marinacci et al., 2010; Marinacci et al., 2011; Fraternali et al., 2015; Pezzulli and Fraternali, 2016) has been neglected. It envisaging that a significant portion of the CGM that constitutes the hot galactic corona can be induced to condense and fall onto the disk due to the interaction with the ejected gas clouds in the fountain. An attempt to include such an effect is implemented in Lapi et al. (2020, their Appendix).

The above system of coupled first order linear differential equations can be solved by writing the first two equations in vectorial form and diagonalising the related coefficients matrix. The resulting eigenvalues read

$$\begin{cases} \lambda_+ = \frac{s\gamma+1+\Lambda}{2} \\ \\ \lambda_- = \frac{s\gamma+1-\Lambda}{2} \end{cases} \tag{B.3}$$

where $s \equiv \tau_{\rm cond}/\tau_\star$, $\gamma = 1 - \mathcal{R} + \epsilon_{\rm out}$, and $\Lambda = [(s\gamma-1)^2 + 4\,\alpha_{\rm GF}\,s\,\epsilon_{\rm out}]^{1/2} = \lambda_+ - \lambda_-$.

With these definitions, note for future reference that $\lambda_+ \lambda_- = s\,[1 - \mathcal{R} + \epsilon_{\rm out}\,(1 - \alpha_{\rm GF})]$ and $(1 - \lambda_-)\,(\lambda_+ - 1) = s\,\epsilon_{\rm out}\,\alpha_{\rm GF}$. The solution can be written as

$$\begin{cases} M_{\rm inf}(\tau) = \frac{f_{\rm inf}\,M_{\rm b}}{\lambda_+ - \lambda_-}\,\left[(\lambda_+ - 1)\,e^{-\lambda_-\,x} + (1 - \lambda_-)\,e^{-\lambda_+\,x}\right]\,, \\ M_{\rm cold}(\tau) = \frac{f_{\rm inf}\,M_{\rm b}}{\lambda_+ - \lambda_-}\,\left[e^{-\lambda_-\,x} - e^{-\lambda_+\,x}\right]\,, \\ M_\star(\tau) = (1 - \mathcal{R})\,\frac{s\,f_{\rm inf}\,M_{\rm b}}{\lambda_+ - \lambda_-}\,\left[\frac{1 - e^{-\lambda_-\,x}}{\lambda_-} - \frac{1 - e^{-\lambda_+\,x}}{\lambda_+}\right]\,, \end{cases} \tag{B.4}$$

where $x \equiv \tau/\tau_{\rm cond}$ is a dimensionless time variable normalized to the condensation timescale. Note that the above solution is physically meaningful (i.e., the cold and stellar masses are non-negative for any x) whenever $s\gamma > 1$, which in turn implies that $0 < \lambda_- \leq 1 \leq \lambda_+$.

It is instructive to examine the initial behavior of the solutions for $\tau \ll \tau_{\rm cond}$, that reads

$$\begin{cases} M_{\rm inf} \simeq f_{\rm inf}\,M_{\rm b}\,\left(1 - \frac{\tau}{\tau_{\rm cond}}\right)\,, \\ M_{\rm cold} \simeq f_{\rm inf}\,M_{\rm b}\,\left(\frac{\tau}{\tau_{\rm cond}}\right)\,, \\ M_\star \simeq (1 - \mathcal{R})\,\frac{s\,f_{\rm inf}\,M_{\rm b}}{2}\,\left(\frac{\tau}{\tau_{\rm cond}}\right)^2\,. \end{cases} \tag{B.5}$$

I note that the infall and cold gas mass are depleted and enhanced linearly, while the stellar mass rises quadratically, since it has to wait the cold gas reservoir to set up. For $\tau \gg \tau_{\rm cond}$ the solutions behave as

$$\begin{cases} M_{\rm inf} \simeq f_{\rm inf}\,M_{\rm b}\,\frac{\lambda_+ - 1}{\lambda_+ - \lambda_-}\,e^{-\lambda_-\,\tau/\tau_{\rm cond}}\,, \\ M_{\rm cold} \simeq \frac{f_{\rm inf}\,M_{\rm b}}{\lambda_+ - \lambda_-}\,e^{-\lambda_-\,\tau/\tau_{\rm cond}}\,, \\ M_\star \simeq (1 - \mathcal{R})\,\frac{s\,f_{\rm inf}\,M_{\rm b}}{\lambda_+\,\lambda_-}\,\left[1 - \frac{\lambda_+}{\lambda_+ - \lambda_-}\,e^{-\lambda_-\,\tau/\tau_{\rm cond}}\right]\,. \end{cases} \tag{B.6}$$

Notice that the infall and cold gas masses decline exponentially while the stellar mass converges to the relic value $\bar{M}_\star \simeq (1 - \mathcal{R})\,s\,f_{\rm inf}\,M_{\rm b}/\lambda_+\lambda_- = (1 - \mathcal{R})\,f_{\rm inf}\,M_{\rm b}/[1 - \mathcal{R} + \epsilon_{\rm out}\,(1 - \alpha_{\rm GF})]$. Rising for early times and declining at late times, the cold gas mass (and hence the SFR) features a maximum value

$$M_{\rm cold}(\tau_{\rm max}) \simeq \frac{f_{\rm inf}\,M_{\rm b}}{\lambda_-}\,\left(\frac{\lambda_+}{\lambda_-}\right)^{-\lambda_+/(\lambda_+ - \lambda_-)}\,. \tag{B.7}$$

occurring at a time

$$\tau_{\rm max} = \tau_{\rm cond}\,\ln\left[\left(\frac{\lambda_+}{\lambda_-}\right)^{1/(\lambda_+ - \lambda_-)}\right]\,. \tag{B.8}$$

Instead, the star formation efficiency $f_\star \equiv \bar{M}_\star/M_{\rm b}$, i.e. the amount of the original baryon content in the halo at formation converted into stars, reads

$$f_\star = \frac{1 - \mathcal{R}}{1 - \mathcal{R} + \epsilon_{\rm out}\,(1 - \alpha_{\rm GF})}\,f_{\rm inf}\,.$$

I firstly remark that all the available (infalling) baryons would be converted into stars ($f_\star \simeq f_{\rm inf}$) in absence of any outflows $\epsilon_{\rm out} \approx 0$, or for a maximally efficient wind recycling $\alpha_{\rm GF} \approx 1$. Second, in presence of fountains the value of the efficiency is generally higher, and its dependence on halo mass, that is encoded mainly in $\epsilon_{\rm out}$, is mitigated somewhat. This could be at the origin of the slightly different $f_\star$ measured in halos of the same mass but hosting an LTG or an ETG.

B.2 Metals

Here I present and discuss the time evolution of the metallicity in gas and stars, that can be described by the following system of coupled equations:

$$\begin{cases} {\rm d}_\tau [M_{\rm inf}\, Z_{\rm inf}] = -\frac{M_{\rm inf}}{\tau_{\rm cond}}\, Z_{\rm inf} + \alpha_{\rm GF}\, \epsilon_{\rm out}\, \frac{M_{\rm cold}}{\tau_\star}\, Z_{\rm cold}\ , \\ {\rm d}_\tau [M_{\rm cold}\, Z_{\rm cold}] = +\frac{M_{\rm inf}}{\tau_{\rm cond}}\, Z_{\rm inf} - \gamma\, \frac{M_{\rm cold}}{\tau_\star}\, Z_{\rm cold} + y_Z\, (1-\mathcal{R})\, \frac{M_{\rm cold}}{\tau_\star}\ , \\ {\rm d}_\tau [M_\star\, Z_\star] = (1-\mathcal{R})\, \frac{M_{\rm cold}}{\tau_\star}\, Z_{\rm cold}\ . \end{cases} \tag{B.9}$$

The equations above prescribe: the mass of metals in cold gas ($M_{\rm cold}\, Z_{\rm cold}$) to evolve (because of dilution) at a rate $M_{\rm inf}\, Z_{\rm inf}/\tau_{\rm cond}$ instantaneous metal production at a rate $y_Z\, (1-\mathcal{R})\, M_{\rm cold}/\tau_\star$; outflow depletion at a rate $\epsilon_{\rm out}\, M_{\rm cold}\, Z_{\rm cold}/\tau_\star$; astration (i.e., metal mass locking into stellar remnants) at a rate $(1-\mathcal{R})\, M_{\rm cold}\, Z_{\rm cold}/\tau_\star$. The mass of the metals in the infalling gas varies because of condensation at a rate $M_{\rm inf}\, Z_{\rm inf}/\tau_{\rm cond}$ and enrichment due to wind recycling at a rate $\alpha_{\rm GF}\, \epsilon_{\rm out}\, M_{\rm cold}\, Z_{\rm cold}/\tau_\star$.

The above, is a basic framework apt for describing analytically the overall metallicity evolution. In order to follow the evolution of individual elements it is necessary to relax the instantaneous recycling/mixing approximations and to include the chemical enrichment from SNe Ia, possibly according to a specific delay-time distribution (see Matteucci, 2012). Other complications may arise from the presence of differential/selective winds, in which different metals are subject to different feedback efficiencies (e.g., Recchi et al., 2008), or when considering the delayed mixing of gas and metals due to the non-negligible time taken by fountains to orbit around and fall back onto the galaxy (e.g., Spitoni et al., 2009).

Under the instantaneous mixing and recycling approximation, the metal production yield is given by

$$y_Z \equiv \frac{1}{1-\mathcal{R}} \int_{1\, M_\odot}^{100\, M_\odot} {\rm d}m_\star\, m_\star\, p_{Z,\star}\, \phi(m_\star) \tag{B.10}$$

where $p_{Z,\star}$ is the mass-fraction of newly synthesized metals by the star of initial mass $m_\star$. With this definition relative to $1-\mathcal{R}$, the yield y_Z represents the ratio between the mass of heavy elements ejected by a stellar generation and the mass locked up in remnants.

Using Eqs. (B.1) the system of the first two equations above can be recast into the form

$$\begin{cases} \dot{Z}_{\rm inf} = \alpha_{\rm GF}\, s\, \epsilon_{\rm out}\, \frac{M_{\rm cold}}{M_{\rm inf}}\, \frac{Z_{\rm cold}-Z_{\rm inf}}{\tau_{\rm cond}}\ , \\ \dot{Z}_{\rm cold} = -\frac{M_{\rm inf}}{M_{\rm cold}}\, \frac{Z_{\rm cold}-Z_{\rm inf}}{\tau_{\rm cond}} + \frac{s\, y_Z\, (1-\mathcal{R})}{\tau_{\rm cond}}\ , \end{cases} \tag{B.11}$$

with initial conditions $Z_{\rm inf}(0) = Z_{\rm cold}(0) = 0$. In many previous analytic models, to solve the chemical evolution equation an empirical shape of the SFR is adopted. Here, instead, the self-consistent solutions for time evolution of gas masses are used, in particular their ratio that is

$$\frac{M_{\rm inf}}{M_{\rm cold}} = \frac{\lambda_+ - 1 + (1-\lambda_-)\, e^{-(\lambda_+ - \lambda_-)\, x}}{1 - e^{-(\lambda_+ - \lambda_-)\, x}} \tag{B.12}$$

entering Eqs. (B.11). The latter are coupled non-linear differential equations, whose solution is generally nontrivial. However, in this particular instance it can be worked out rather easily by taking their difference and obtaining a first order equation for $Z_{\rm cold} - Z_{\rm inf}$, whose solution is trivial; then the latter must be put back on the right hand sides of Eqs. (B.11), and a further integration allows to solve analytically for the infalling and cold gas metallicity.

The corresponding analytic solutions read

$$\begin{cases} Z_{\rm inf}(\tau) = \bar{Z}_{\rm gas} \left\{ (1-\lambda_-)\, x - 2\, \frac{1-\lambda_-}{\lambda_+ - \lambda_-} \left[1 - \frac{(\lambda_+ - \lambda_-)\, (1 + \frac{\lambda_+ + \lambda_- - 2}{2}\, x)}{1 - \lambda_- + (\lambda_+ - 1)\, e^{(\lambda_+ - \lambda_-)\, x}} \right] \right\} , \\ Z_{\rm cold}(\tau) = \bar{Z}_{\rm gas} \left\{ (1-\lambda_-)\, x + \frac{\lambda_+ + \lambda_- - 2}{\lambda_+ - \lambda_-} \left[1 - \frac{(\lambda_+ - \lambda_-)\, x}{e^{(\lambda_+ - \lambda_-)\, x} - 1} \right] \right\} . \end{cases} \tag{B.13}$$

Here

$$\bar{Z}_{\rm gas} = \frac{s\, y_Z\, (1 - \mathcal{R})}{\lambda_+ - \lambda_-} \tag{B.14}$$

represents the asymptotic value for $\tau \gg \tau_{\rm cond}$ of the difference $Z_{\rm cold} - Z_{\rm inf}$, which is finite since individually $Z_{\rm cold}$ and $Z_{\rm inf}$ diverge linearly in the same manner. However, such a divergence is not an issue, because the masses in metals $M\, Z$ for both the infall and the cold gas components are always finite and exponentially suppressed at late-times.

It is also worth looking at the initial behavior of the gas metallicities for $\tau \ll \tau_{\rm cond}$, that reads

$$\begin{cases} Z_{\rm inf} \simeq \frac{s\, y_Z\, (1-\mathcal{R})}{6}\, s\, \epsilon_{\rm out}\, \alpha_{\rm GF} \left(\frac{\tau}{\tau_{\rm cond}} \right)^3 , \\ Z_{\rm cold} \simeq \frac{s\, y_Z\, (1-\mathcal{R})}{2}\, \frac{\tau}{\tau_{\rm cond}} . \end{cases} \tag{B.15}$$

The cold gas metallicity increases almost linearly with galactic age, while the infalling gas metallicity evolution is cubic; this is because at early times the cold gas is rapidly enriched by direct production from stars, while the infalling gas has to wait the galactic fountain process to bring some metals from the cold gas into it.

The last of Eqs. (B.9) implies that the metallicity $Z_\star$ in the stellar component is the average of the cold gas one over the star formation history:

$$Z_\star(\tau) = \frac{1}{M_\star(\tau)} \int_0^\tau {\rm d}\tau'\, Z_{\rm cold}(\tau')\, \dot{M}_\star(\tau') . \tag{B.16}$$

Using the self-consistent solutions for $Z_{\rm cold}$ and $M_{\rm cold}$, one obtains

$$Z_\star = \bar{Z}_\star \left\{ 1 - \frac{\lambda_+ \lambda_-}{(\lambda_+ - \lambda_-)\left[\lambda_+ \left(1 - e^{-\lambda_- x}\right) - \lambda_- \left(1 - e^{-\lambda_+ x}\right)\right]} \left[\frac{2\,\lambda_+\lambda_- - \lambda_+ - \lambda_-}{\lambda_+ - \lambda_-} \right.\right.$$

$$\left.\left. \times \left(e^{-\lambda_- x} - e^{-\lambda_+ x}\right) + (1 - \lambda_-)\,\lambda_+\, x\, e^{-\lambda_- x} - (\lambda_+ - 1)\,\lambda_-\, x\, e^{-\lambda_+ x} \right] \right\} ,$$

where the limiting value for $\tau \gg \tau_{\rm cond}$ writes

$$\bar{Z}_\star = \frac{s\, y_Z\,(1 - \mathcal{R})}{\lambda_+\,\lambda_-} = \frac{y_Z\,(1 - \mathcal{R})}{1 - \mathcal{R} + \epsilon_{\rm out}\,(1 - \alpha_{\rm GF})} \,. \tag{B.17}$$

The analytic solutions predict that the asymptotic stellar metallicity $\bar{Z}_\star \simeq \bar{Z}_{\rm gas}\,(\lambda_+ - \lambda_-)/\lambda_+\lambda_-$ is not equal, but rather somewhat lower, than the gas one. The early-time behavior of $Z_\star$ for $\tau \ll \tau_{\rm cond}$ reads

$$Z_\star \simeq \frac{s\, y_Z\,(1 - \mathcal{R})}{3}\, \frac{\tau}{\tau_{\rm cond}} \,, \tag{B.18}$$

so that, initially, $Z_\star(\tau) \simeq 2\, Z_{\rm cold}(\tau)/3$, i.e., the stellar and cold gas metallicity evolve in parallel.

Finally, it is worth noticing that Eqs. (B.9) and (B.17) imply a direct connection among the infalling gas fraction $f_{\rm inf}$, the asymptotic stellar metallicity $\bar{Z}_\star$ and the star formation efficiency $f_\star$, in the form

$$f_{\rm inf} = \frac{y_Z\, f_\star}{\bar{Z}_\star} \,;$$

this has indeed been used by Shi et al. (2017) and Lapi et al. (2018) (cf. Sect. 1.2.1, Chapter 1) to infer the infall fraction $f_{\rm inf}$ via observations of $f_\star$ (from photometric/dynamical modeling and weak lensing data) and $\bar{Z}_\star$ (from stellar archeology).

B.3 Dust

In the following I will deal with the global evolution of dust mass and dust-to-gas mass ratio, taking up the basic analytic modeling adopted by many previous studies (e.g., Dwek, 1998; Hirashita, 2000; Edmunds, 2001; Inoue, 2003; Asano et al., 2013; Feldmann, 2015; Mancini et al., 2015). Specifically, dust is assumed to consist of two interlinked components,i.e. a refractory *core* and a volatile *mantle*, subject to the

evolution equations[1]

$$\begin{cases} \mathrm{d}_\tau[M_{\rm cold}\, D_{\rm core}] = -\gamma\, \dot{M}_\star\, D_{\rm core} - \kappa_{\rm SN}\, \dot{M}_\star\, D_{\rm core} + y_D\, (1-\mathcal{R})\, \dot{M}_\star\ , \\ \mathrm{d}_\tau[M_{\rm cold}\, D_{\rm mantle}] = -\gamma\, \dot{M}_\star\, D_{\rm mantle} - \kappa_{\rm SN}\, \dot{M}_\star\, D_{\rm mantle} + \\ \qquad\qquad + \epsilon_{\rm acc}\, \dot{M}_\star\, D_{\rm core}\, (Z_{\rm cold} - D_{\rm mantle})\ . \end{cases} \tag{B.19}$$

The first equation prescribes that the evolution of the mass in grain cores $M_{\rm cold}\, D_{\rm core}$ results from the competition of various processes: production due to stellar evolution at a rate $y_D\, (1-\mathcal{R})\, \dot{M}_\star$ with an average yield y_D; astration by star formation and ejection from galactic outflows, that combine in the rate term $-\gamma\, \dot{M}_\star\, D_{\rm core}$; dust sputtering, spallation and destruction via SN shock-waves at a rate $\kappa_{\rm SN}\, \dot{M}_\star\, D_{\rm core}$ with a strength parameter $\kappa_{\rm SN}$. The second equation describes the evolution of the mass in dust mantles, which differs from the previous one for the production term: mantle growth is assumed to be driven by accretion of metals onto pre-existing grain cores at a rate $\epsilon_{\rm acc}\, \dot{M}_\star\, D_{\rm core}\, (Z - D_{\rm mantle})$ with an efficiency $\epsilon_{\rm acc}$.

Eqs. (B.19) can be recast in terms of the dust-to-gas mass ratios:

$$\begin{cases} \dot{D}_{\rm core} = -\frac{D_{\rm core}}{\tau_{\rm cond}} \left[s\, \kappa_{\rm SN} + \frac{M_{\rm inf}}{M_{\rm cold}} \right] + \frac{y_D\, (1-\mathcal{R})\, s}{\tau_{\rm cond}}\ ; \\ \dot{D}_{\rm mantle} = -\frac{D_{\rm mantle}}{\tau_{\rm cond}} \left[s\, \kappa_{\rm SN} + s\, \epsilon_{\rm acc}\, D_{\rm core} + \frac{M_{\rm inf}}{M_{\rm cold}} \right] + \frac{s\, \epsilon_{\rm acc}\, D_{\rm core}}{\tau_{\rm cond}}\, Z_{\rm cold}\ . \end{cases} \tag{B.20}$$

with initial conditions $D_{\rm core}(0) = D_{\rm mantle}(0) = 0$; in the above both $M_{\rm inf}/M_{\rm cold}$ and $Z_{\rm cold}$ depend on τ (or x) as expressed by Eqs. (B.12) and (B.19), respectively.

The corresponding analytic solution for grain cores is

$$D_{\rm core} = \bar{D}_{\rm core} \left[1 - \frac{\lambda_+ - \lambda_-}{e^{(\lambda_+ - \lambda_-)\, x} - 1}\, \frac{1 - e^{-(s\, \kappa_{\rm SN} + \lambda_- - 1)\, x}}{s\, \kappa_{\rm SN} + \lambda_- - 1} \right]\ , \tag{B.21}$$

where the asymptotic value for $\tau \gg \tau_{\rm cond}$ reads

$$\bar{D}_{\rm core} = \frac{s\, y_D\, (1-\mathcal{R})}{s\, \kappa_{\rm SN} + \lambda_+ - 1}\ . \tag{B.22}$$

In solving the equation for the mantle, the core fraction $D_{\rm core}$ is assumed to be fixed at its asymptotic value $\bar{D}_{\rm core} \ll \bar{Z}_{\rm cold}$, since from Eq. (B.21) this is seen to be attained quite rapidly after a time $\tau \gtrsim \tau_{\rm cond}/s\, \kappa_{\rm SN}$. Then,

$$D_{\rm mantle} = \bar{D}_{\rm mantle} \left\{ \frac{1}{d_\pm}\, \frac{(1-\lambda_-)\, x}{1 - e^{-(\lambda_+ - \lambda_-)\, x}} + 1 - \frac{1}{d_\pm}\, \frac{s\tilde{\epsilon}}{s\tilde{\epsilon} + \lambda_- - 1}\, \frac{(\lambda_+ - 1)\, x}{e^{(\lambda_+ - \lambda_-)\, x} - 1} \right.$$

$$\left. \times \left[1 + \frac{\lambda_+ - 1}{s\tilde{\epsilon}} \left(1 - \frac{(\lambda_+ - \lambda_-)^2}{(\lambda_+ - 1)^2}\, \frac{s\, \tilde{\epsilon} + \lambda_+ + \lambda_- - 2}{s\, \tilde{\epsilon} + \lambda_+ - 1}\, \frac{1 - e^{-(s\, \tilde{\epsilon} + \lambda_- - 1)\, x}}{(s\, \tilde{\epsilon} + \lambda_- - 1)\, x} \right) \right] \right\}$$

[1] In principle, a negative term describing gas mass and metal locking into dust should be added on the right hand side of the differential equations for $\mathrm{d}_\tau M_{\rm cold}$ and $\mathrm{d}_\tau[M_{\rm cold}\, Z_{\rm cold}]$; however, these terms are usually neglected since they are proportional to the dust mass and this is always a small fraction of the gas one.

where $\tilde{\epsilon} \equiv \kappa_{\rm SN} + \epsilon_{\rm acc}\,\bar{D}_{\rm core}$ and we have defined the two auxiliary quantities

$$\bar{D}_{\rm mantle} = \frac{s\,\epsilon_{\rm acc}\,\bar{D}_{\rm core}\,\bar{Z}_{\rm gas}}{s\,\tilde{\epsilon} + \lambda_+ - 1}\,d_\pm \tag{B.23}$$

and

$$d_\pm \equiv \frac{\lambda_+ + \lambda_- - 2}{\lambda_+ - \lambda_-} - \frac{1-\lambda_-}{s\,\tilde{\epsilon} + \lambda_+ - 1}\,. \tag{B.24}$$

I note that in case of a very efficient accretion process, Eq. (B.23) implies that the final dust fraction behaves like the gas metallicity.

The early-time behavior for $\tau \ll \tau_{\rm cond}$ writes

$$\begin{cases} D_{\rm core}(\tau) \simeq \frac{s\,y_D\,(1-\mathcal{R})}{2}\,\frac{\tau}{\tau_{\rm cond}}\,, \\ \\ D_{\rm mantle}(\tau) \simeq \frac{s^3}{6}\,\frac{\epsilon_{\rm acc}\,y_D\,y_Z\,(1-\mathcal{R})^2}{s\,(\gamma+\kappa_{\rm SN})-1}\,\left(\frac{\tau}{\tau_{\rm cond}}\right)^2\,, \end{cases} \tag{B.25}$$

so that the mantle component overwhelms the core one soon after dust production has started. The second equation above is strictly valid for times $\tau_{\rm cond}/s\kappa_{\rm SN} \lesssim \tau \lesssim \tau_{\rm cond}$ when $D_{\rm core}$ has already saturated to its asymptotic value $\bar{D}_{\rm core}$.

It is worth stressing that total dust production and enrichment (core plus mantle) are in general very rapid with respect to the condensation timescale, of order a few $10^{-1}\,\tau_{\rm cond}$.

B.4 Evolution of stars, gas and dust in an individual Late Type Galaxy

In Fig. B.1 I show the evolution with galactic age τ of the relevant spatially-averaged quantities described by the analytic solutions: infalling gas mass, cold gas mass, stellar mass, dust mass and stellar metallicity. The trends refer to a LTG formed at redshift $z_{\rm form} \approx 1.5$ and are illustrated for representative galaxies with halo masses $M_{\rm H} = 10^{11} - 10^{12} - 10^{13}\,M_\odot$ at formation (first, second and third column respectively).

Parameter settings inspired by the *in-situ* scenario are included, along with external halo and baryonic accretion, though when depurated from pseudo-evolution their contribution is minor, especially toward higher $z_{\rm form}$. For the detailed description of the typical timescales prescribed by the *in-situ* scenario for LTGs evolution and the inclusion of mergers and smooth accretion from the cosmic web into the evolutionary picture I refer the reader to Lapi et al. (2020, their Sects. 3.1.1 and 4). As to the parameters concerning feedback by SN II and wind recycling, the adopted fiducial value of the wind recycling fraction is $\alpha_{\rm GF} \approx 0.75$, consistent with the outcomes of several numerical simulations including wind recycling and galactic fountains (e.g., Oppenheimer et al., 2010; Übler et al., 2014; Nelson et al., 2015; Christensen et al., 2016; Anglés-Alcázar et al., 2017; Grand et al., 2019; Tollet et al., 2019), while the value of SN II feedback efficiency is set to $\epsilon_{\rm SN} \approx 0.2$: in such a way, the effective efficiency , i.e. $\epsilon_{\rm SN}(1-\alpha_{\rm GF}) \approx 0.05$, assumes the standard value (e.g., Hopkins, Quataert, and Murray, 2012). Furthermore, the adopted Chabrier (2003) and Chabrier (2005) IMF, along with the Romano et al. (2010) stellar yield models, imply an instantaneous recycling fraction $\mathcal{R} \approx 0.45$, an average yield of instantaneously produced metals $y_Z \approx 0.06$ and an yield of oxygen $y_O \approx 0.04$ (see Krumholz, Dekel, and McKee, 2012; Nomoto, Kobayashi, and Tominaga, 2013; Feldmann, 2015; Vincenzo et al., 2016). In the treatment of dust production, the adopted dust yield is $y_D \approx 7 \times 10^{-4}$ (see

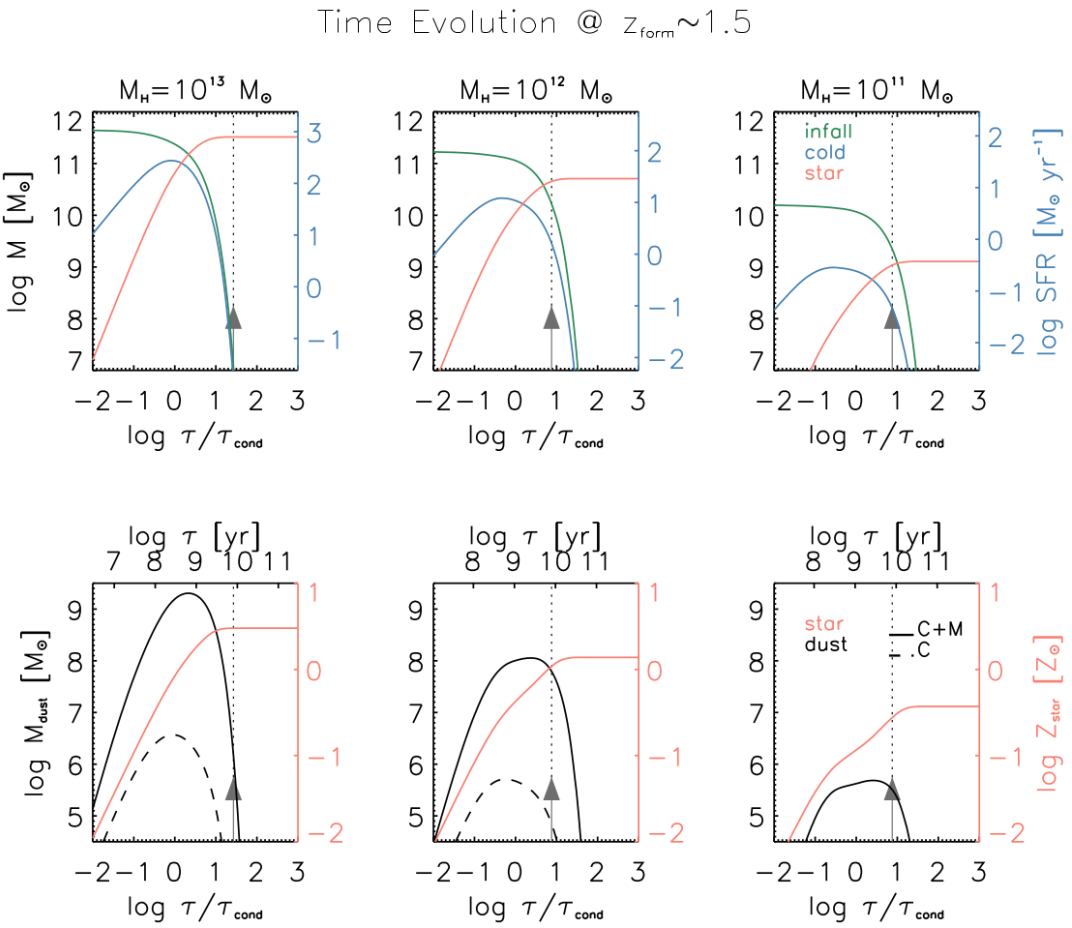

FIGURE B.1: Time evolution of baryonic components of an individual LTG by Lapi et al. (2020). Top panels: evolution of the infall (green), cold (blue), and stellar (orange) masses as a function of galactic age τ (normalized to the condensation timescale $\tau_{\rm cond}$ or in absolute units of yr) for galaxies hosted in halos with mass $M_{\rm H} = 10^{13}\,M_\odot$ (left panels), $M_{\rm H} = 10^{12}\,M_\odot$ (middle panels), and $M_{\rm H} = 10^{11}\,M_\odot$ (right panels) at a formation redshift $z_{\rm form} = 1.5$; the right $y-$axis reports the SFR (in log-scale) and refers to the cyan line. Bottom panels: evolution of the dust mass (black, refers to the left $y-$axis; dashed line is for the core and solid for core plus mantles) and of the stellar metallicity (orange, refers to the right $y-$axis). In all panels, the vertical arrow and dotted line indicates the present time $t(z = 0) - t(z_{\rm form})$.

Bianchi and Schneider, 2007; Zhukovska, Gail, and Trieloff, 2008; Feldmann, 2015), while the strength parameter for dust spallation by SN winds is $\kappa_{\rm SN} \approx 10$ (see e.g., de Bennassuti et al., 2014), and the efficiency for dust accretion $\epsilon_{\rm acc} \approx 10^6$ (see Hirashita, 2000; Asano et al., 2013; Feldmann, 2015). I note that these parameters are rather uncertain, and mainly set basing on previous literature and on obtaining a good match to the dust vs. stellar mass relationship at $z \sim 0 - 1$.

Looking at Fig. B.1, one can appreciate that the infalling gas mass decreases almost exponentially with the galactic age as it condenses in the cold gas component, though it is partially refurnished by wind recycling; the cold gas then feeds star formation and is affected by stellar feedback. The balance of these processes makes the cold gas mass (hence the SFR) to slowly grow at early times, to attain a maximum and then to decrease almost exponentially. Correspondingly, the stellar component increases almost linearly and then saturates. In less massive halos stellar feedback is more efficient, the initial gas reservoir is smaller, and the molecular fraction is lower (hence the star formation timescales are longer).At the same time, wind recycling is more effective in refurnishing the infall gas reservoir and thus extending the duration of the star formation. The stellar metallicity rises almost linearly at early times, then slows down because of the balance between dilution, feedback and the recycling of enriched gas by the fountain, and then saturates to an asymptotic value reflecting the effective stellar yield. Moving toward lower mass halos the saturation values are progressively smaller since more metals are ejected by the action of stellar feedback. The dust mass features a behavior similar to the cold gas phase, with an extended maximum attained as soon as metals are available for accretion onto the grain cores, and then decreases as the gas mass gets exhausted.

For a typical Milky-Way sized galaxy with halo mass $M_{\rm H} \approx 10^{12}\,M_\odot$ formed at $z \lesssim 1.5$ it is expected a present day stellar mass of $M_\star \approx$ some $10^{10}\,M_\odot$, a current SFR ≈a few $M_\odot$ yr^{-1} and a stellar metallicity $Z_\star \approx Z_\odot$. For smaller galaxies like the Large Magellanic Cloud (LMC) with halo masses $M_{\rm H} \approx 10^{11}\,M_\odot$ formed at $z \gtrsim 1.5$ a $M_\star \lesssim 10^9\,M_\odot$, SFR $\lesssim 10^{-1}\,M_\odot$ yr^{-1} and $Z_\star \approx 0.3\,Z_\odot$ are predicted. Notice that very massive halos with $M_{\rm H} \approx 10^{13}\,M_\odot$ and $z_{\rm form} \gtrsim 1.5$ feature present-day stellar masses $M_\star \gtrsim 10^{11}\,M_\odot$ but tend to be caught in the exponentially declining phase of their SFH. In the *in-situ* framework for galaxy formation and evolution, such very large halos rarely host a local star-forming LTGs and can do so only if formed relatively recently at $z_{\rm form} \lesssim 1$, as suggested by indications from weak lensing measurements (see e.g., Velander et al., 2014; Hudson et al., 2015; Mandelbaum et al., 2016).

B.5 Limit of no galactic fountain

When wind recycling and galactic fountains are negligible, it is straightforward to demonstrate that the solutions above converge to the ones already presented in Chapter 2 (see also Pantoni et al., 2019). In fact, posing $\alpha_{\rm GF} \simeq 0$ in Eqs. (B.3) implies $\lambda_+ \simeq s\,\gamma$ and $\lambda_- \simeq 1$. Thus the solutions for the gas and stellar masses become

$$\begin{cases} M_{\rm inf}(\tau) = f_{\rm inf}\,M_{\rm b}\,e^{-x}\ , \\ M_{\rm cold}(\tau) = \frac{f_{\rm inf}\,M_{\rm b}}{s\,\gamma-1}\,\left[e^{-x} - e^{-s\,\gamma\,x}\right]\ , \\ M_\star(\tau) = (1-\mathcal{R})\,\frac{s\,f_{\rm inf}\,M_{\rm b}}{s\,\gamma-1}\,\left[1 - e^{-x} - \frac{1}{s\,\gamma}\,(1-e^{-s\,\gamma\,x})\right]\ , \end{cases} \tag{B.26}$$

and those for the gas and stellar metallicities turn into

$$\begin{cases} Z_{\rm inf} \simeq 0 \,, \\ Z_{\rm cold} \simeq \bar{Z}_{\rm gas} \left[1 - \frac{(s\,\gamma - 1)\,x}{e^{(s\,\gamma-1)\,x} - 1} \right] \,, \\ Z_{\star} \simeq \bar{Z}_{\star} \left[1 - \frac{s\,\gamma}{s\,\gamma - 1} \, \frac{e^{-x} - e^{-s\,\gamma\,x}\,[1 + (s\,\gamma - 1)\,x]}{s\gamma - 1 + e^{-s\,\gamma\,x} - s\gamma\,e^{-x}} \right] \,, \end{cases} \tag{B.27}$$

where now the asymptotic values read $\bar{Z}_{\rm gas} = s\,y_Z\,(1 - \mathcal{R})/(s\gamma - 1)$ and $\bar{Z}_{\star} = y_Z\,(1 - \mathcal{R})/\gamma$.

As for the dust evolution, consider that the auxiliary quantity $d_{\pm}$ defined in Eq. (B.24) tends to 1 and hence the solutions become

$$\begin{cases} D_{\rm core} \simeq \bar{D}_{\rm core} \left[1 - \frac{s\,\gamma - 1}{e^{(s\,\gamma-1)\,x} - 1} \, \frac{1 - e^{-s\,\kappa_{\rm SN}\,x}}{s\,\kappa_{\rm SN}} \right] \,, \\ D_{\rm mantle} \simeq \bar{D}_{\rm mantle} \left\{ 1 - \frac{(s\,\gamma - 1)\,x}{e^{(s\,\gamma-1)\,x} - 1} \left[1 + \frac{s\,\gamma - 1}{s\,\tilde{\epsilon}} \left(1 - \frac{1 - e^{-s\,\tilde{\epsilon}\,x}}{s\,\tilde{\epsilon}\,x} \right) \right] \right\} \,, \end{cases} \tag{B.28}$$

in terms of the quantity $\tilde{\epsilon} \equiv \kappa_{\rm SN} + \epsilon_{\rm acc}\,\bar{D}_{\rm core}$ and of the asymptotic values $\bar{D}_{\rm core} \simeq s\,y_D\,(1 - \mathcal{R})/[s\,(\gamma + \kappa_{\rm SN}) - 1]$ and $\bar{D}_{\rm mantle} \simeq s\,\epsilon_{\rm acc}\,\bar{D}_{\rm core}\,\bar{Z}_{\rm cold}/[s\,(\gamma + \tilde{\epsilon}) - 1]$.

All in all, these are the solutions provided in Chapter 2 (Pantoni et al., 2019).

Bibliography

Aird, J. et al. (Feb. 2010). "The evolution of the hard X-ray luminosity function of AGN". In: *Monthly Notices of the Royal Astronomical Society* 401.4, pp. 2531–2551. DOI: 10.1111/j.1365-2966.2009.15829.x. arXiv: 0910.1141 [astro-ph.CO].

Andrews, Brett H. et al. (Feb. 2017). "Inflow, Outflow, Yields, and Stellar Population Mixing in Chemical Evolution Models". In: *The Astrophysical Journal* 835.2, 224, p. 224. DOI: 10.3847/1538-4357/835/2/224. arXiv: 1604.08613 [astro-ph.GA].

Anglés-Alcázar, Daniel et al. (Oct. 2017). "The cosmic baryon cycle and galaxy mass assembly in the FIRE simulations". In: *Monthly Notices of the Royal Astronomical Society* 470.4, pp. 4698–4719. DOI: 10.1093/mnras/stx1517. arXiv: 1610.08523 [astro-ph.GA].

Aoyama, Shohei et al. (Apr. 2017). "Galaxy simulation with dust formation and destruction". In: *Monthly Notices of the Royal Astronomical Society* 466.1, pp. 105–121. DOI: 10.1093/mnras/stw3061. arXiv: 1609.07547 [astro-ph.GA].

Aoyama, Shohei et al. (Aug. 2018). "Cosmological simulation with dust formation and destruction". In: *Monthly Notices of the Royal Astronomical Society* 478.4, pp. 4905–4921. DOI: 10.1093/mnras/sty1431. arXiv: 1802.04027 [astro-ph.GA].

Aravena, Manuel et al. (Sept. 2019). "The ALMA Spectroscopic Survey in the Hubble Ultra Deep Field: Evolution of the Molecular Gas in CO-selected Galaxies". In: *The Astrophysical Journal* 882.2, 136, p. 136. DOI: 10.3847/1538-4357/ab30df. arXiv: 1903.09162 [astro-ph.GA].

Arrigoni, Matías et al. (Feb. 2010). "Galactic chemical evolution in hierarchical formation models - I. Early-type galaxies in the local Universe". In: *Monthly Notices of the Royal Astronomical Society* 402.1, pp. 173–190. DOI: 10.1111/j.1365-2966.2009.15924.x. arXiv: 0905.4189 [astro-ph.CO].

Asano, Ryosuke S. et al. (Mar. 2013). "Dust formation history of galaxies: A critical role of metallicity for the dust mass growth by accreting materials in the interstellar medium". In: *Earth, Planets, and Space* 65.3, pp. 213–222. DOI: 10.5047/eps.2012.04.014. arXiv: 1206.0817 [astro-ph.GA].

Asmus, D. et al. (Nov. 2015). "The subarcsecond mid-infrared view of local active galactic nuclei - II. The mid-infrared-X-ray correlation". In: *Monthly Notices of the Royal Astronomical Society* 454.1, pp. 766–803. DOI: 10.1093/mnras/stv1950. arXiv: 1508.05065 [astro-ph.GA].

Athey, Alex E. and Joel N. Bregman (May 2009). "Oxygen Metallicity Determinations from Optical Emission Lines in Early-Type Galaxies". In: *The Astrophysical Journal* 696.1, pp. 681–689. DOI: 10.1088/0004-637X/696/1/681. arXiv: 0903.4197 [astro-ph.CO].

Aversa, R. et al. (Sept. 2015). "Black Hole and Galaxy Coevolution from Continuity Equation and Abundance Matching". In: *The Astrophysical Journal* 810.1, 74, p. 74. DOI: 10.1088/0004-637X/810/1/74. arXiv: 1507.07318 [astro-ph.GA].

Bacon, Roland et al. (Dec. 2017). "The MUSE Hubble Ultra Deep Field Survey. I. Survey description, data reduction, and source detection". In: *Astronomy and Astrophysics* 608, A1, A1. DOI: 10.1051/0004-6361/201730833. arXiv: 1710.03002 [astro-ph.GA].

Balestra, I. et al. (Mar. 2010). "The Great Observatories Origins Deep Survey. VLT/VIMOS spectroscopy in the GOODS-south field: Part II". In: *Astronomy and Astrophysics* 512, A12, A12. DOI: 10.1051/0004-6361/200913626. arXiv: 1001.1115 [astro-ph.CO].

Banday, A. J. and A. W. Wolfendale (Feb. 1991). "Fluctuations in the galactic synchrotron radiation. I - Implications for searches for fluctuations of cosmological origin". In: *Monthly Notices of the Royal Astronomical Society* 248, pp. 705–714. DOI: 10.1093/mnras/248.4.705.

Barnes, Joshua and George Efstathiou (Aug. 1987). "Angular Momentum from Tidal Torques". In: *The Astrophysical Journal* 319, p. 575. DOI: 10.1086/165480.

Barro, G. et al. (Aug. 2016a). "Sub-kiloparsec ALMA Imaging of Compact Star-forming Galaxies at z ∼2.5: Revealing the Formation of Dense Galactic Cores in the Progenitors of Compact Quiescent Galaxies". In: *The Astrophysical Journall* 827.2, L32, p. L32. DOI: 10.3847/2041-8205/827/2/L32. arXiv: 1607.01011 [astro-ph.GA].

Barro, G. et al. (Dec. 2017). "Spatially Resolved Kinematics in the Central 1 kpc of a Compact Star-forming Galaxy at z ∼2.3 from ALMA CO Observations". In: *The Astrophysical Journal, Letters* 851.2, L40, p. L40. DOI: 10.3847/2041-8213/aa9f0d. arXiv: 1712.01283 [astro-ph.GA].

Barro, Guillermo et al. (Mar. 2013). "CANDELS: The Progenitors of Compact Quiescent Galaxies at z ∼2". In: *The Astrophysical Journal* 765.2, 104, p. 104. DOI: 10.1088/0004-637X/765/2/104. arXiv: 1206.5000 [astro-ph.CO].

Barro, Guillermo et al. (Apr. 2016b). "Caught in the Act: Gas and Stellar Velocity Dispersions in a Fast Quenching Compact Star-Forming Galaxy at z∼1.7". In: *The Astrophysical Journal* 820.2, 120, p. 120. DOI: 10.3847/0004-637X/820/2/120. arXiv: 1503.07164 [astro-ph.GA].

Barrufet, L. et al. (Sept. 2020). "A high redshift population of galaxies at the North Ecliptic Pole. Unveiling the main sequence of dusty galaxies". In: *Astronomy and Astrophysics* 641, A129, A129. DOI: 10.1051/0004-6361/202037838. arXiv: 2007.07992 [astro-ph.GA].

Battisti, A. J. et al. (Sept. 2019). "MAGPHYS+photo-z: Constraining the Physical Properties of Galaxies with Unknown Redshifts". In: *The Astrophysical Journal* 882.1, 61, p. 61. DOI: 10.3847/1538-4357/ab345d. arXiv: 1908.00771 [astro-ph.GA].

Bayet, E. et al. (Oct. 2009). "Are ^{12}CO lines good indicators of the star formation rate in galaxies?" In: *Monthly Notices of the Royal Astronomical Society* 399.1, pp. 264–272. DOI: 10.1111/j.1365-2966.2009.15258.x. arXiv: 0906.2975 [astro-ph.CO].

Beckwith, Steven V. W. et al. (Nov. 2006). "The Hubble Ultra Deep Field". In: *Astronomical Journal* 132.5, pp. 1729–1755. DOI: 10.1086/507302. arXiv: astro-ph/0607632 [astro-ph].

Behroozi, Peter S., Risa H. Wechsler, and Charlie Conroy (June 2013). "The Average Star Formation Histories of Galaxies in Dark Matter Halos from z = 0-8". In: *The Astrophysical Journal* 770.1, 57, p. 57. DOI: 10.1088/0004-637X/770/1/57. arXiv: 1207.6105 [astro-ph.CO].

Bekki, Kenji (Dec. 2013). "Simulating galaxy evolution with a non-universal stellar initial mass function". In: *Monthly Notices of the Royal Astronomical Society* 436.3, pp. 2254–2275. DOI: 10.1093/mnras/stt1735. arXiv: 1309.3878 [astro-ph.CO].

— (May 2015). "Dust-regulated galaxy formation and evolution: a new chemodynamical model with live dust particles". In: *Monthly Notices of the Royal Astronomical Society* 449.2, pp. 1625–1649. DOI: 10.1093/mnras/stv165. arXiv: 1501.05459 [astro-ph.GA].

Bell, Eric F. et al. (Dec. 2003). "The Optical and Near-Infrared Properties of Galaxies. I. Luminosity and Stellar Mass Functions". In: *The Astrophysical Journal, Supplement* 149.2, pp. 289–312. DOI: 10.1086/378847. arXiv: astro-ph/0302543 [astro-ph].

Belli, Sirio, Andrew B. Newman, and Richard S. Ellis (Jan. 2017). "MOSFIRE Spectroscopy of Quiescent Galaxies at 1.5 < z < 2.5. I. Evolution of Structural and Dynamical Properties". In: *The Astrophysical Journal* 834.1, 18, p. 18. DOI: 10.3847/1538-4357/834/1/18. arXiv: 1608.00608 [astro-ph.GA].

Benson, Andrew J. (Feb. 2012). "G ALACTICUS: A semi-analytic model of galaxy formation". In: *New Astronomy* 17.2, pp. 175–197. DOI: 10.1016/j.newast.2011.07.004. arXiv: 1008.1786 [astro-ph.CO].

Bernstein, Rebecca A., Wendy L. Freedman, and Barry F. Madore (May 2002). "The First Detections of the Extragalactic Background Light at 3000, 5500, and 8000 Å. I. Results". In: *The Astrophysical Journal* 571.1, pp. 56–84. DOI: 10.1086/339422. arXiv: astro-ph/0112153 [astro-ph].

Berta, S. et al. (Mar. 2016). "Measures of galaxy dust and gas mass with Herschel photometry and prospects for ALMA". In: *Astronomy and Astrophysics* 587, A73, A73. DOI: 10.1051/0004-6361/201527746. arXiv: 1511.05147 [astro-ph.GA].

Béthermin, Matthieu et al. (July 2014). "Clustering, host halos, and environment of z ∼2 galaxies as a function of their physical properties". In: *Astronomy and Astrophysics* 567, A103, A103. DOI: 10.1051/0004-6361/201423451. arXiv: 1405.0492 [astro-ph.GA].

Béthermin, Matthieu et al. (Nov. 2017). "The impact of clustering and angular resolution on far-infrared and millimeter continuum observations". In: *Astronomy and Astrophysics* 607, A89, A89. DOI: 10.1051/0004-6361/201730866. arXiv: 1703.08795 [astro-ph.GA].

Bianchi, S. (Apr. 2013). "Vindicating single-T modified blackbody fits to Herschel SEDs". In: *Astronomy and Astrophysics* 552, A89, A89. DOI: 10.1051/0004-6361/201220866. arXiv: 1302.5699 [astro-ph.CO].

Bianchi, Simone and Raffaella Schneider (July 2007). "Dust formation and survival in supernova ejecta". In: *Monthly Notices of the Royal Astronomical Society* 378.3, pp. 973–982. DOI: 10.1111/j.1365-2966.2007.11829.x. arXiv: 0704.0586 [astro-ph].

Bianchini, Federico et al. (Feb. 2019). "Broadband Spectral Energy Distributions of SDSS-selected Quasars and of Their Host Galaxies: Intense Activity at the Onset of AGN Feedback". In: *The Astrophysical Journal* 871.2, 136, p. 136. DOI: 10.3847/1538-4357/aaf86b. arXiv: 1806.06516 [astro-ph.GA].

Biggs, A. D. et al. (June 2011). "The LABOCA survey of the Extended Chandra Deep Field-South - radio and mid-infrared counterparts to submillimetre galaxies". In: *Monthly Notices of the Royal Astronomical Society* 413.4, pp. 2314–2338. DOI: 10.1111/j.1365-2966.2010.18132.x. arXiv: 1012.0305 [astro-ph.CO].

Bigiel, F. et al. (Dec. 2008). "The Star Formation Law in Nearby Galaxies on Sub-Kpc Scales". In: *Astronomical Journal* 136.6, pp. 2846–2871. DOI: 10.1088/0004-6256/136/6/2846. arXiv: 0810.2541 [astro-ph].

Bischetti, M. et al. (Oct. 2019). "Widespread QSO-driven outflows in the early Universe". In: *Astronomy and Astrophysics* 630, A59, A59. DOI: 10.1051/0004-6361/201833557. arXiv: 1806.00786 [astro-ph.GA].

Bischetti, M. et al. (Jan. 2021). "The WISSH quasars project. IX. Cold gas content and environment of luminous QSOs at z ~ 2.4-4.7". In: *Astronomy and Astrophysics* 645, A33, A33. DOI: 10.1051/0004-6361/202039057. arXiv: 2009.01112 [astro-ph.GA].

Blain, Andrew W. et al. (Oct. 2002). "Submillimeter galaxies". In: *Physics Reports* 369.2, pp. 111–176. DOI: 10.1016/S0370-1573(02)00134-5. arXiv: astro-ph/0202228 [astro-ph].

Bocquet, Sebastian et al. (Mar. 2016). "Halo mass function: baryon impact, fitting formulae, and implications for cluster cosmology". In: *Monthly Notices of the Royal Astronomical Society* 456.3, pp. 2361–2373. DOI: 10.1093/mnras/stv2657. arXiv: 1502.07357 [astro-ph.CO].

Bonzini, M. et al. (Nov. 2012). "The Sub-mJy Radio Population of the E-CDFS: Optical and Infrared Counterpart Identification". In: *The Astrophysical Journal, Supplement* 203.1, 15, p. 15. DOI: 10.1088/0067-0049/203/1/15. arXiv: 1209.4176 [astro-ph.CO].

Bonzini, M. et al. (Dec. 2013). "The sub-mJy radio sky in the Extended Chandra Deep Field-South: source population". In: *Monthly Notices of the Royal Astronomical Society* 436.4, pp. 3759–3771. DOI: 10.1093/mnras/stt1879. arXiv: 1310.1248 [astro-ph.CO].

Boogaard, Leindert A. et al. (Sept. 2019). "The ALMA Spectroscopic Survey in the HUDF: Nature and Physical Properties of Gas-mass Selected Galaxies Using MUSE Spectroscopy". In: *The Astrophysical Journal* 882.2, 140, p. 140. DOI: 10.3847/1538-4357/ab3102. arXiv: 1903.09167 [astro-ph.GA].

Boogaard, Leindert A. et al. (Oct. 2020). "The ALMA Spectroscopic Survey in the Hubble Ultra Deep Field: CO Excitation and Atomic Carbon in Star-forming Galaxies at z = 1-3". In: *The Astrophysical Journal* 902.2, 109, p. 109. DOI: 10.3847/1538-4357/abb82f. arXiv: 2009.04348 [astro-ph.GA].

Boquien, M. et al. (Feb. 2019). "CIGALE: a python Code Investigating GALaxy Emission". In: *Astronomy and Astrophysics* 622, A103, A103. DOI: 10.1051/0004-6361/201834156. arXiv: 1811.03094 [astro-ph.GA].

Bothwell, M. S. et al. (Mar. 2013). "A survey of molecular gas in luminous sub-millimetre galaxies". In: *Monthly Notices of the Royal Astronomical Society* 429.4, pp. 3047–3067. DOI: 10.1093/mnras/sts562. arXiv: 1205.1511 [astro-ph.CO].

Bouché, N. et al. (Aug. 2010). "The Impact of Cold Gas Accretion Above a Mass Floor on Galaxy Scaling Relations". In: *The Astrophysical Journal* 718.2, pp. 1001–1018. DOI: 10.1088/0004-637X/718/2/1001. arXiv: 0912.1858 [astro-ph.CO].

Bournaud, Frédéric et al. (Nov. 2011). "Black Hole Growth and Active Galactic Nuclei Obscuration by Instability-driven Inflows in High-redshift Disk Galaxies Fed by Cold Streams". In: *Astrophysical Journal, Letters* 741.2, L33, p. L33. DOI: 10.1088/2041-8205/741/2/L33. arXiv: 1107.1483 [astro-ph.CO].

Bouwens, R. J. et al. (Apr. 2015). "UV Luminosity Functions at Redshifts z ~ 4 to z ~ 10: 10,000 Galaxies from HST Legacy Fields". In: *The Astrophysical Journal* 803.1, 34, p. 34. DOI: 10.1088/0004-637X/803/1/34. arXiv: 1403.4295 [astro-ph.CO].

Bregman, J. N. (Mar. 1980). "The galactic fountain of high-velocity clouds." In: *The Astrophysical Journal* 236, pp. 577–591. DOI: 10.1086/157776.

Bruzual, G. and S. Charlot (Oct. 2003). "Stellar population synthesis at the resolution of 2003". In: *Monthly Notices of the Royal Astronomical Society* 344.4, pp. 1000–1028. DOI: 10.1046/j.1365-8711.2003.06897.x. arXiv: astro-ph/0309134 [astro-ph].

Buat, V. et al. (Dec. 2019). "Cold dust and stellar emissions in dust-rich galaxies observed with ALMA: a challenge for SED-fitting techniques". In: *Astronomy and Astrophysics* 632, A79, A79. DOI: 10.1051/0004-6361/201936643.

Bullock, J. S. et al. (July 2001). "A Universal Angular Momentum Profile for Galactic Halos". In: *The Astrophysical Journal* 555.1, pp. 240–257. DOI: 10.1086/321477. arXiv: astro-ph/0011001 [astro-ph].

Burkert, A. et al. (Aug. 2016). "The Angular Momentum Distribution and Baryon Content of Star-forming Galaxies at z ~ 1-3". In: *The Astrophysical Journal* 826.2, 214, p. 214. DOI: 10.3847/0004-637X/826/2/214. arXiv: 1510.03262 [astro-ph.GA].

Calistro Rivera, Gabriela et al. (Aug. 2018). "Resolving the ISM at the Peak of Cosmic Star Formation with ALMA: The Distribution of CO and Dust Continuum in z ~ 2.5 Submillimeter Galaxies". In: *The Astrophysical Journal* 863.1, 56, p. 56. DOI: 10.3847/1538-4357/aacffa. arXiv: 1804.06852 [astro-ph.GA].

Calura, F. et al. (Feb. 2017). "The dust-to-stellar mass ratio as a valuable tool to probe the evolution of local and distant star-forming galaxies". In: *Monthly Notices of the Royal Astronomical Society* 465.1, pp. 54–67. DOI: 10.1093/mnras/stw2749. arXiv: 1610.08979 [astro-ph.GA].

Calzetti, Daniela et al. (Apr. 2000). "The Dust Content and Opacity of Actively Star-forming Galaxies". In: *The Astrophysical Journal* 533.2, pp. 682–695. DOI: 10.1086/308692. arXiv: astro-ph/9911459 [astro-ph].

Caon, Nicola, Duccio Macchetto, and Miriani Pastoriza (Mar. 2000). "A Survey of the Interstellar Medium in Early-Type Galaxies. III. Stellar and Gas Kinematics". In: *The Astrophysical Journal, Supplement* 127.1, pp. 39–58. DOI: 10.1086/313315.

Cappellari, Michele et al. (July 2013). "The ATLAS^{3D} project - XX. Mass-size and mass-σ distributions of early-type galaxies: bulge fraction drives kinematics, mass-to-light ratio, molecular gas fraction and stellar initial mass function". In: *Monthly Notices of the Royal Astronomical Society* 432.3, pp. 1862–1893. DOI: 10.1093/mnras/stt644. arXiv: 1208.3523 [astro-ph.CO].

Cappelluti, N. et al. (June 2016). "Chandra Counterparts of CANDELS GOODS-S Sources". In: *The Astrophysical Journal* 823.2, 95, p. 95. DOI: 10.3847/0004-637X/823/2/95. arXiv: 1512.00510 [astro-ph.HE].

Carilli, C. L. and F. Walter (Aug. 2013). "Cool Gas in High-Redshift Galaxies". In: *Annual Review of Astronomy and Astrophysics* 51.1, pp. 105–161. DOI: 10.1146/annurev-astro-082812-140953. arXiv: 1301.0371 [astro-ph.CO].

Carniani, S. et al. (Nov. 2019). "Constraints on high-J CO emission lines in z ~ 6 quasars". In: *Monthly Notices of the Royal Astronomical Society* 489.3, pp. 3939–3952. DOI: 10.1093/mnras/stz2410. arXiv: 1902.01413 [astro-ph.GA].

Casey, C. M. et al. (Mar. 2011). "Spectroscopic characterization of 250-μm-selected hyper-luminous star-forming galaxies". In: *Monthly Notices of the Royal Astronomical Society* 411.4, pp. 2739–2749. DOI: 10.1111/j.1365-2966.2010.17876.x. arXiv: 1009.5709 [astro-ph.CO].

Casey, Caitlin M. (Oct. 2012). "Far-infrared spectral energy distribution fitting for galaxies near and far". In: *Monthly Notices of the Royal Astronomical Society* 425.4, pp. 3094–3103. DOI: 10.1111/j.1365-2966.2012.21455.x. arXiv: 1206.1595 [astro-ph.CO].

Casey, Caitlin M., Desika Narayanan, and Asantha Cooray (Aug. 2014). "Dusty star-forming galaxies at high redshift". In: *Physics Reports* 541.2, pp. 45–161. DOI: 10.1016/j.physrep.2014.02.009. arXiv: 1402.1456 [astro-ph.CO].

Casey, Caitlin M. et al. (May 2017). "Near-infrared MOSFIRE Spectra of Dusty Star-forming Galaxies at 0.2 < z < 4". In: *The Astrophysical Journal* 840.2, 101, p. 101. DOI: 10.3847/1538-4357/aa6cb1. arXiv: 1703.10168 [astro-ph.GA].

Casey, Caitlin M. et al. (July 2018). "The Brightest Galaxies in the Dark Ages: Galaxies' Dust Continuum Emission during the Reionization Era". In: *The Astrophysical Journal* 862.1, 77, p. 77. DOI: 10.3847/1538-4357/aac82d. arXiv: 1805.10301 [astro-ph.GA].

Cassarà, L. P. et al. (Aug. 2016). "Effect of the star formation histories on the SFR-M_* relation at $z \geq 2$". In: *Astronomy and Astrophysics* 593, A9, A9. DOI: 10.1051/0004-6361/201526505. arXiv: 1606.04823 [astro-ph.GA].

Cattaneo, A. et al. (July 2009). "The role of black holes in galaxy formation and evolution". In: *Nature* 460.7252, pp. 213–219. DOI: 10.1038/nature08135. arXiv: 0907.1608 [astro-ph.CO].

Ceverino, Daniel, Avishai Dekel, and Frederic Bournaud (June 2010). "High-redshift clumpy discs and bulges in cosmological simulations". In: *Monthly Notices of the Royal Astronomical Society* 404.4, pp. 2151–2169. DOI: 10.1111/j.1365-2966.2010.16433.x. arXiv: 0907.3271 [astro-ph.CO].

Chabrier, Gilles (July 2003). "Galactic Stellar and Substellar Initial Mass Function". In: *Publications of the Astronomical Society of the Pacific* 115.809, pp. 763–795. DOI: 10.1086/376392. arXiv: astro-ph/0304382 [astro-ph].

— (2005). "The Initial Mass Function: From Salpeter 1955 to 2005". In: *The Initial Mass Function 50 Years Later*. Ed. by E. Corbelli, F. Palla, and H. Zinnecker. Vol. 327, p. 41. DOI: 10.1007/978-1-4020-3407-7_5.

Chapin, Edward L. et al. (Feb. 2011). "A joint analysis of BLAST 250-500 μm and LABOCA 870 μm observations in the Extended Chandra Deep Field-South". In: *Monthly Notices of the Royal Astronomical Society* 411.1, pp. 505–549. DOI: 10.1111/j.1365-2966.2010.17697.x. arXiv: 1003.2647 [astro-ph.CO].

Chapman, S. C. et al. (Dec. 2003). "Hubble Space Telescope Images of Submillimeter Sources: Large Irregular Galaxies at High Redshift". In: *The Astrophysical Journal* 599.1, pp. 92–104. DOI: 10.1086/379120. arXiv: astro-ph/0308197 [astro-ph].

Chapman, S. C. et al. (Apr. 2005). "A Redshift Survey of the Submillimeter Galaxy Population". In: *The Astrophysical Journal* 622.2, pp. 772–796. DOI: 10.1086/428082. arXiv: astro-ph/0412573 [astro-ph].

Chary, R. and D. Elbaz (Aug. 2001). "Interpreting the Cosmic Infrared Background: Constraints on the Evolution of the Dust-enshrouded Star Formation Rate". In: *The Astrophysical Journal* 556.2, pp. 562–581. DOI: 10.1086/321609. arXiv: astro-ph/0103067 [astro-ph].

Chen, C.-C. et al. (Feb. 2015). "An ALMA survey of submillimeter galaxies in the Extended Chandra Deep Field South : near-infrared morphologies and stellar sizes." In: *The Astrophysical Journal*. Astronomy Group 799.2, p. 194. URL: http://dro.dur.ac.uk/15094/.

Chen, Chian-Chou et al. (Sept. 2017). "A Spatially Resolved Study of Cold Dust, Molecular Gas, H II Regions, and Stars in the z = 2.12 Submillimeter Galaxy ALESS67.1". In: *The Astrophysical Journal* 846.2, 108, p. 108. DOI: 10.3847/1538-4357/aa863a. arXiv: 1708.08937 [astro-ph.GA].

Chiappini, Cristina, Francesca Matteucci, and Donatella Romano (June 2001). "Abundance Gradients and the Formation of the Milky Way". In: *The Astrophysical Journal* 554.2, pp. 1044–1058. DOI: 10.1086/321427. arXiv: astro-ph/0102134 [astro-ph].

Chiosi, C. (Mar. 1980). "Chemical evolution of the galactic disk: the inflow problem." In: *Astronomy and Astrophysics* 83, pp. 206–216.

Christensen, Charlotte R. et al. (June 2016). "In-N-Out: The Gas Cycle from Dwarfs to Spiral Galaxies". In: *The Astrophysical Journal* 824.1, 57, p. 57. DOI: 10.3847/0004-637X/824/1/57. arXiv: 1508.00007 [astro-ph.GA].

Cicone, C. et al. (Feb. 2014). "Massive molecular outflows and evidence for AGN feedback from CO observations". In: *Astronomy and Astrophysics* 562, A21, A21. DOI: 10.1051/0004-6361/201322464. arXiv: 1311.2595 [astro-ph.CO].

Ciesla, L., D. Elbaz, and J. Fensch (Dec. 2017). "The SFR-M_* main sequence archetypal star-formation history and analytical models". In: *Astronomy and Astrophysics* 608, A41, A41. DOI: 10.1051/0004-6361/201731036. arXiv: 1706.08531 [astro-ph.GA].

Cimatti, A. et al. (Apr. 2008). "GMASS ultradeep spectroscopy of galaxies at z ~2. II. Superdense passive galaxies: how did they form and evolve?" In: *Astronomy and Astrophysics* 482.1, pp. 21–42. DOI: 10.1051/0004-6361:20078739. arXiv: 0801.1184 [astro-ph].

Citro, Annalisa et al. (July 2016). "Inferring the star-formation histories of the most massive and passive early-type galaxies at z < 0.3". In: *Astronomy and Astrophysics* 592, A19, A19. DOI: 10.1051/0004-6361/201527772. arXiv: 1604.07826 [astro-ph.GA].

Cole, Shaun et al. (Nov. 2000). "Hierarchical galaxy formation". In: *Monthly Notices of the Royal Astronomical Society* 319.1, pp. 168–204. DOI: 10.1046/j.1365-8711.2000.03879.x. arXiv: astro-ph/0007281 [astro-ph].

Collacchioni, Florencia et al. (Nov. 2018). "Semi-analytic galaxies - III. The impact of supernova feedback on the mass-metallicity relation". In: *Monthly Notices of the Royal Astronomical Society* 481.1, pp. 954–969. DOI: 10.1093/mnras/sty2347. arXiv: 1808.09089 [astro-ph.GA].

Comparat, Johan et al. (Aug. 2017). "Accurate mass and velocity functions of dark matter haloes". In: *Monthly Notices of the Royal Astronomical Society* 469.4, pp. 4157–4174. DOI: 10.1093/mnras/stx1183. arXiv: 1702.01628 [astro-ph.CO].

— (Feb. 2019). "Erratum: Accurate mass and velocity functions of dark matter halos". In: *Monthly Notices of the Royal Astronomical Society* 483.2, pp. 2561–2562. DOI: 10.1093/mnras/sty3296.

Condon, J. J. (Jan. 1992). "Radio emission from normal galaxies." In: *Annual Review of Astronomy and Astrophysics* 30, pp. 575–611. DOI: 10.1146/annurev.aa.30.090192.003043.

Conley, A. et al. (May 2011). "Discovery of a Multiply Lensed Submillimeter Galaxy in Early HerMES Herschel/SPIRE Data". In: *The Astrophysical Journal, Letters* 732.2, L35, p. L35. DOI: 10.1088/2041-8205/732/2/L35. arXiv: 1104.4113 [astro-ph.CO].

Conroy, Charlie (Aug. 2013). "Modeling the Panchromatic Spectral Energy Distributions of Galaxies". In: *Annual Review of Astronomy and Astrophysics* 51.1, pp. 393–455. DOI: 10.1146/annurev-astro-082812-141017. arXiv: 1301.7095 [astro-ph.CO].

Conselice, C. J. et al. (May 2011). "The Hubble Space Telescope GOODS NICMOS Survey: overview and the evolution of massive galaxies at 1.5< z< 3". In: *Monthly Notices of the Royal Astronomical Society* 413.1, pp. 80–100. DOI: 10.1111/j.1365-2966.2010.18113.x. arXiv: 1010.1164 [astro-ph.CO].

Cooray, Asantha et al. (July 2014). "HerMES: The Rest-frame UV Emission and a Lensing Model for the z = 6.34 Luminous Dusty Starburst Galaxy HFLS3". In: *The Astrophysical Journal* 790.1, 40, p. 40. DOI: 10.1088/0004-637X/790/1/40. arXiv: 1404.1378 [astro-ph.GA].

Cousin, M. et al. (May 2016). "Metal enrichment in a semi-analytical model, fundamental scaling relations, and the case of Milky Way galaxies". In: *Astronomy and Astrophysics* 589, A109, A109. DOI: 10.1051/0004-6361/201527734. arXiv: 1602.07908 [astro-ph.GA].

Cowie, L. L. et al. (Oct. 2018). "A Submillimeter Perspective on the GOODS Fields (SUPER GOODS). III. A Large Sample of ALMA Sources in the GOODS-S". In: *The Astrophysical Journal* 865.2, 106, p. 106. DOI: 10.3847/1538-4357/aadc63. arXiv: 1805.09424 [astro-ph.GA].

Cresci, Giovanni and Roberto Maiolino (Feb. 2018). "Observing positive and negative AGN feedback". In: *Nature Astronomy* 2, pp. 179–180. DOI: 10.1038/s41550-018-0404-5. arXiv: 1802.10305 [astro-ph.GA].

Croton, Darren J. et al. (Jan. 2006). "The many lives of active galactic nuclei: cooling flows, black holes and the luminosities and colours of galaxies". In: *Monthly Notices of the Royal Astronomical Society* 365.1, pp. 11–28. DOI: 10.1111/j.1365-2966.2005.09675.x. arXiv: astro-ph/0508046 [astro-ph].

da Cunha, E. et al. (June 2015). "An ALMA Survey of Sub-millimeter Galaxies in the Extended Chandra Deep Field South: Physical Properties Derived from Ultraviolet-to-radio Modeling". In: *The Astrophysical Journal* 806.1, 110, p. 110. DOI: 10.1088/0004-637X/806/1/110. arXiv: 1504.04376 [astro-ph.GA].

da Cunha, Elisabete, Stéphane Charlot, and David Elbaz (Aug. 2008). "A simple model to interpret the ultraviolet, optical and infrared emission from galaxies". In: *Monthly Notices of the Royal Astronomical Society* 388.4, pp. 1595–1617. DOI: 10.1111/j.1365-2966.2008.13535.x. arXiv: 0806.1020 [astro-ph].

Daddi, E. et al. (Nov. 2007). "Multiwavelength Study of Massive Galaxies at z$\sim$2. I. Star Formation and Galaxy Growth". In: *The Astrophysical Journal* 670.1, pp. 156–172. DOI: 10.1086/521818. arXiv: 0705.2831 [astro-ph].

Daddi, E. et al. (May 2015). "CO excitation of normal star-forming galaxies out to z = 1.5 as regulated by the properties of their interstellar medium". In: *Astronomy and Astrophysics* 577, A46, A46. DOI: 10.1051/0004-6361/201425043. arXiv: 1409.8158 [astro-ph.GA].

Dale, D. A. et al. (Jan. 2012). "Herschel Far-infrared and Submillimeter Photometry for the KINGFISH Sample of nearby Galaxies". In: *The Astrophysical Journal* 745.1, 95, p. 95. DOI: 10.1088/0004-637X/745/1/95. arXiv: 1112.1093 [astro-ph.CO].

Dale, Daniel A. and George Helou (Sept. 2002). "The Infrared Spectral Energy Distribution of Normal Star-forming Galaxies: Calibration at Far-Infrared and Submillimeter Wavelengths". In: *The Astrophysical Journal* 576.1, pp. 159–168. DOI: 10.1086/341632. arXiv: astro-ph/0205085 [astro-ph].

Dale, Daniel A. et al. (Mar. 2001). "The Infrared Spectral Energy Distribution of Normal Star-forming Galaxies". In: *The Astrophysical Journal* 549.1, pp. 215–227. DOI: 10.1086/319077.

D'Amato, Q. et al. (Apr. 2020). "Dust and gas content of high-redshift galaxies hosting obscured AGN in the Chandra Deep Field-South". In: *Astronomy and Astrophysics* 636, A37, A37. DOI: 10.1051/0004-6361/201936175. arXiv: 2003.08631 [astro-ph.GA].

Danovich, Mark et al. (May 2015). "Four phases of angular-momentum buildup in high-z galaxies: from cosmic-web streams through an extended ring to disc and bulge". In: *Monthly Notices of the Royal Astronomical Society* 449.2, pp. 2087–2111. DOI: 10.1093/mnras/stv270. arXiv: 1407.7129 [astro-ph.GA].

Davé, Romeel, Kristian Finlator, and Benjamin D. Oppenheimer (Mar. 2012). "An analytic model for the evolution of the stellar, gas and metal content of galaxies". In: *Monthly Notices of the Royal Astronomical Society* 421.1, pp. 98–107. DOI: 10.1111/j.1365-2966.2011.20148.x. arXiv: 1108.0426 [astro-ph.CO].

Davé, Romeel et al. (June 2019). "SIMBA: Cosmological simulations with black hole growth and feedback". In: *Monthly Notices of the Royal Astronomical Society* 486.2, pp. 2827–2849. DOI: 10.1093/mnras/stz937. arXiv: 1901.10203 [astro-ph.GA].

de Bennassuti, Matteo et al. (Dec. 2014). "Decoding the stellar fossils of the dusty Milky Way progenitors". In: *Monthly Notices of the Royal Astronomical Society* 445.3, pp. 3039–3054. DOI: 10.1093/mnras/stu1962. arXiv: 1409.5798 [astro-ph.GA].

de los Reyes, Mithi A. et al. (Feb. 2015). "The Relationship between Stellar Mass, Gas Metallicity, and Star Formation Rate for Hα-Selected Galaxies at z $\approx$ 0.8 from the NewHα Survey". In: *Astronomical Journal* 149.2, 79, p. 79. DOI: 10.1088/0004-6256/149/2/79. arXiv: 1410.1551 [astro-ph.GA].

De Lucia, Gabriella, Fabio Fontanot, and Michaela Hirschmann (Mar. 2017). "AGN feedback and the origin of the α enhancement in early-type galaxies - insights from the GAEA model". In: *Monthly Notices of the Royal Astronomical Society* 466.1, pp. L88–L92. DOI: 10.1093/mnrasl/slw242. arXiv: 1611.04597 [astro-ph.GA].

De Lucia, Gabriella et al. (Nov. 2014). "Elemental abundances in Milky Way-like galaxies from a hierarchical galaxy formation model". In: *Monthly Notices of the Royal Astronomical Society* 445.1, pp. 970–987. DOI: 10.1093/mnras/stu1752. arXiv: 1407.7867 [astro-ph.GA].

De Rossi, María Emilia and Volker Bromm (Oct. 2019). "Redshift Horizon for Detecting the First Galaxies in Far-infrared Surveys". In: *The Astrophysical Journal* 883.2, 113, p. 113. DOI: 10.3847/1538-4357/ab3e0b. arXiv: 1903.02512 [astro-ph.GA].

Decarli, Roberto et al. (Dec. 2016a). "ALMA Spectroscopic Survey in the Hubble Ultra Deep Field: CO Luminosity Functions and the Evolution of the Cosmic Density of Molecular Gas". In: *The Astrophysical Journal* 833.1, 69, p. 69. DOI: 10.3847/1538-4357/833/1/69. arXiv: 1607.06770 [astro-ph.GA].

Decarli, Roberto et al. (Dec. 2016b). "The ALMA Spectroscopic Survey in the Hubble Ultra Deep Field: Molecular Gas Reservoirs in High-redshift Galaxies". In: *The Astrophysical Journal* 833.1, 70, p. 70. DOI: 10.3847/1538-4357/833/1/70. arXiv: 1607.06771 [astro-ph.GA].

DeGraf, C. et al. (Apr. 2017). "Black hole growth and AGN feedback under clumpy accretion". In: *Monthly Notices of the Royal Astronomical Society* 466.2, pp. 1462–1476. DOI: 10.1093/mnras/stw2777. arXiv: 1412.3819 [astro-ph.GA].

Dekel, A. et al. (Jan. 2009). "Cold streams in early massive hot haloes as the main mode of galaxy formation". In: *Nature Astronomy* 457.7228, pp. 451–454. DOI: 10.1038/nature07648. arXiv: 0808.0553 [astro-ph].

Dekel, Avishai and Nir Mandelker (Nov. 2014). "An analytic solution for the minimal bathtub toy model: challenges in the star formation history of high-z galaxies". In: *Monthly Notices of the Royal Astronomical Society* 444.3, pp. 2071–2084. DOI: 10.1093/mnras/stu1427. arXiv: 1402.2283 [astro-ph.CO].

Dekel, Avishai et al. (Oct. 2019). "The global star formation law by supernova feedback". In: *Monthly Notices of the Royal Astronomical Society* 488.4, pp. 4753–4778. DOI: 10.1093/mnras/stz1919. arXiv: 1903.00962 [astro-ph.GA].

Delvecchio, I. et al. (Apr. 2014). "Tracing the cosmic growth of supermassive black holes to z $\sim$ 3 with Herschel". In: *Monthly Notices of the Royal Astronomical Society* 439.3, pp. 2736–2754. DOI: 10.1093/mnras/stu130. arXiv: 1401.4503 [astro-ph.GA].

Di Teodoro, E. M. and F. Fraternali (Aug. 2015). "^{3D} BAROLO: a new 3D algorithm to derive rotation curves of galaxies". In: *Monthly Notices of the Royal Astronomical Society* 451.3, pp. 3021–3033. DOI: 10.1093/mnras/stv1213. arXiv: 1505.07834 [astro-ph.GA].

Dickinson, M. and GOODS Legacy Team (May 2001). "The Great Observatories Origins Deep Survey (GOODS)". In: *American Astronomical Society Meeting Abstracts #198*. Vol. 198. American Astronomical Society Meeting Abstracts, p. 25.01.

Diemand, Jürg, Michael Kuhlen, and Piero Madau (Oct. 2007). "Formation and Evolution of Galaxy Dark Matter Halos and Their Substructure". In: *The Astrophysical Journal* 667.2, pp. 859–877. DOI: 10.1086/520573. arXiv: astro-ph/0703337 [astro-ph].

Donevski, D. et al. (June 2018). "Towards a census of high-redshift dusty galaxies with Herschel. A selection of "500 μm-risers"". In: *Astronomy and Astrophysics* 614, A33, A33. DOI: 10.1051/0004-6361/201731888. arXiv: 1709.00942 [astro-ph.GA].

Donevski, D. et al. (Dec. 2020). "In pursuit of giants. I. The evolution of the dust-to-stellar mass ratio in distant dusty galaxies". In: *Astronomy and Astrophysics* 644, A144, A144. DOI: 10.1051/0004-6361/202038405. arXiv: 2008.09995 [astro-ph.GA].

Dopita, Michael A. et al. (Feb. 2005). "Modeling the Pan-Spectral Energy Distribution of Starburst Galaxies. I. The Role of ISM Pressure and the Molecular Cloud Dissipation Timescale". In: *The Astrophysical Journal* 619.2, pp. 755–778. DOI: 10.1086/423948. arXiv: astro-ph/0407008 [astro-ph].

Draine, B. T. (Jan. 2003). "Interstellar Dust Grains". In: *Annual Review of Astronomy and Astrophysics* 41, pp. 241–289. DOI: 10.1146/annurev.astro.41.011802.094840. arXiv: astro-ph/0304489 [astro-ph].

Draine, B. T. and Aigen Li (Mar. 2007). "Infrared Emission from Interstellar Dust. IV. The Silicate-Graphite-PAH Model in the Post-Spitzer Era". In: *The Astrophysical Journal* 657.2, pp. 810–837. DOI: 10.1086/511055. arXiv: astro-ph/0608003 [astro-ph].

Draine, Bruce T. (2011). *Physics of the Interstellar and Intergalactic Medium*.

Dubois, Y. et al. (Aug. 2014). "Dancing in the dark: galactic properties trace spin swings along the cosmic web". In: *Monthly Notices of the Royal Astronomical Society* 444.2, pp. 1453–1468. ISSN: 0035-8711. DOI: 10.1093/mnras/stu1227. eprint: https://academic.oup.com/mnras/article-pdf/444/2/1453/24039446/stu1227.pdf. URL: https://doi.org/10.1093/mnras/stu1227.

Dubois, Yohan et al. (Sept. 2016). "The Horizon-AGN simulation: morphological diversity of galaxies promoted by AGN feedback". In: *Monthly Notices of the Royal Astronomical Society* 463.4, pp. 3948–3964. ISSN: 0035-8711. DOI: 10.1093/mnras/stw2265. eprint: https://academic.oup.com/mnras/article-pdf/463/4/3948/18515487/stw2265.pdf. URL: https://doi.org/10.1093/mnras/stw2265.

Dudzevičiūtė, U. et al. (May 2020). "An ALMA survey of the SCUBA-2 CLS UDS field: physical properties of 707 sub-millimetre galaxies". In: *Monthly Notices of the Royal Astronomical Society* 494.3, pp. 3828–3860. DOI: 10.1093/mnras/staa769. arXiv: 1910.07524 [astro-ph.GA].

Dudzevičiūtė, U. et al. (Jan. 2021). "Tracing the evolution of dust-obscured activity using sub-millimetre galaxy populations from STUDIES and AS2UDS". In: *Monthly Notices of the Royal Astronomical Society* 500.1, pp. 942–961. DOI: 10.1093/mnras/staa3285. arXiv: 2010.06605 [astro-ph.GA].

Dunlop, J. S. et al. (Nov. 2010). "The BLAST 250 μm-selected galaxy population in GOODS-South". In: *Monthly Notices of the Royal Astronomical Society* 408.4, pp. 2022–2050. DOI: 10.1111/j.1365-2966.2010.17278.x. arXiv: 0910.3642 [astro-ph.CO].

Dunlop, J. S. et al. (Apr. 2017). "A deep ALMA image of the Hubble Ultra Deep Field". In: *Monthly Notices of the Royal Astronomical Society* 466.1, pp. 861–883. DOI: 10.1093/mnras/stw3088. arXiv: 1606.00227 [astro-ph.GA].

Dunne, Loretta and Stephen A. Eales (Nov. 2001). "The SCUBA Local Universe Galaxy Survey - II. 450-μm data: evidence for cold dust in bright IRAS galaxies". In: *Monthly Notices of the Royal Astronomical Society* 327.3, pp. 697–714. DOI: 10.1046/j.1365-8711.2001.04789.x. arXiv: astro-ph/0106362 [astro-ph].

Dwek, Eli (July 1998). "The Evolution of the Elemental Abundances in the Gas and Dust Phases of the Galaxy". In: *The Astrophysical Journal* 501, p. 643. DOI: 10.1086/305829. arXiv: astro-ph/9707024 [astro-ph].

Dwek, Eli and Isabelle Cherchneff (Feb. 2011). "The Origin of Dust in the Early Universe: Probing the Star Formation History of Galaxies by Their Dust Content". In: *The Astrophysical Journal* 727.2, 63, p. 63. DOI: 10.1088/0004-637X/727/2/63. arXiv: 1011.1303 [astro-ph.CO].

Dye, S. et al. (Sept. 2015). "Revealing the complex nature of the strong gravitationally lensed system H-ATLAS J090311.6+003906 using ALMA". In: *Monthly Notices of the Royal Astronomical Society* 452.3, pp. 2258–2268. DOI: 10.1093/mnras/stv1442. arXiv: 1503.08720 [astro-ph.GA].

Eales, S. et al. (May 2010). "The Herschel ATLAS". In: *Publications of the Astronomical Society of the Pacific* 122.891, p. 499. DOI: 10.1086/653086. arXiv: 0910.4279 [astro-ph.CO].

Eales, Stephen et al. (Dec. 2009). "BLAST: The Redshift Survey". In: *The Astrophysical Journal* 707.2, pp. 1779–1808. DOI: 10.1088/0004-637X/707/2/1779. arXiv: 0907.4156 [astro-ph.CO].

Edmunds, M. G. (Oct. 1990). "General Constraints on the Effect of Gas Flows in the Chemical Evolution of Galaxies". In: *Monthly Notices of the Royal Astronomical Society* 246, p. 678.

— (Nov. 2001). "An elementary model for the dust cycle in galaxies". In: *Monthly Notices of the Royal Astronomical Society* 328.1, pp. 223–236. DOI: 10.1046/j.1365-8711.2001.04859.x.

Eke, Vincent, George Efstathiou, and Lisa Wright (June 2000). "The cosmological dependence of galactic specific angular momenta". In: *Monthly Notices of the Royal Astronomical Society* 315.2, pp. L18–L22. DOI: 10.1046/j.1365-8711.2000.03632.x. arXiv: astro-ph/9908294 [astro-ph].

Elbaz, D. et al. (June 2007). "The reversal of the star formation-density relation in the distant universe". In: *Astronomy and Astrophysics* 468.1, pp. 33–48. DOI: 10.1051/0004-6361:20077525. arXiv: astro-ph/0703653 [astro-ph].

Elbaz, D. et al. (Aug. 2018). "Starbursts in and out of the star-formation main sequence". In: *Astronomy and Astrophysics* 616, A110, A110. DOI: 10.1051/0004-6361/201732370. arXiv: 1711.10047 [astro-ph.GA].

Elmegreen, Debra Meloy, Bruce G. Elmegreen, and Thomas E. Ferguson (Apr. 2005). "Central Blue Clumps in Elliptical Galaxies of the Hubble Ultra Deep Field". In: *The Astrophysical Journal, Letters* 623.2, pp. L71–L74. DOI: 10.1086/430141. arXiv: astro-ph/0504033 [astro-ph].

Elmegreen, Debra Meloy et al. (Apr. 2007). "Resolved Galaxies in the Hubble Ultra Deep Field: Star Formation in Disks at High Redshift". In: *The Astrophysical Journal* 658.2, pp. 763–777. DOI: 10.1086/511667. arXiv: astro-ph/0701121 [astro-ph].

Erb, Dawn K. (Feb. 2008). "A Model for Star Formation, Gas Flows, and Chemical Evolution in Galaxies at High Redshifts". In: *The Astrophysical Journal* 674.1, pp. 151–156. DOI: 10.1086/524727. arXiv: 0710.4146 [astro-ph].

Erb, Dawn K. et al. (June 2006). "The Mass-Metallicity Relation at z>∼2". In: *The Astrophysical Journal* 644.2, pp. 813–828. DOI: 10.1086/503623. arXiv: astro-ph/0602473 [astro-ph].

Fabian, A. C. (Oct. 1999). "The obscured growth of massive black holes". In: *Monthly Notices of the Royal Astronomical Society* 308.4, pp. L39–L43. DOI: 10.1046/j.1365-8711.1999.03017.x. arXiv: astro-ph/9908064 [astro-ph].

Faisst, A. L. et al. (May 2016). "Rest-UV Absorption Lines as Metallicity Estimator: The Metal Content of Star-forming Galaxies at z ∼5". In: *The Astrophysical Journal* 822.1, 29, p. 29. DOI: 10.3847/0004-637X/822/1/29. arXiv: 1512.00018 [astro-ph.GA].

Fakhouri, Onsi and Chung-Pei Ma (May 2008). "The nearly universal merger rate of dark matter haloes in ΛCDM cosmology". In: *Monthly Notices of the Royal*

Astronomical Society 386.2, pp. 577–592. DOI: 10.1111/j.1365-2966.2008.13075.x. arXiv: 0710.4567 [astro-ph].

Fakhouri, Onsi, Chung-Pei Ma, and Michael Boylan-Kolchin (Aug. 2010). "The merger rates and mass assembly histories of dark matter haloes in the two Millennium simulations". In: *Monthly Notices of the Royal Astronomical Society* 406.4, pp. 2267–2278. DOI: 10.1111/j.1365-2966.2010.16859.x. arXiv: 1001.2304 [astro-ph.CO].

Fall, S. M. (Dec. 2002). "Origin of Galactic Disks". In: *Disks of Galaxies: Kinematics, Dynamics and Peturbations*. Ed. by E. Athanassoula, A. Bosma, and R. Mujica. Vol. 275. Astronomical Society of the Pacific Conference Series, pp. 389–396.

Feldmann, Robert (May 2015). "The equilibrium view on dust and metals in galaxies: Galactic outflows drive low dust-to-metal ratios in dwarf galaxies". In: *Monthly Notices of the Royal Astronomical Society* 449.3, pp. 3274–3292. DOI: 10.1093/mnras/stv552. arXiv: 1412.2755 [astro-ph.GA].

Feltre, A. et al. (Oct. 2012). "Smooth and clumpy dust distributions in AGN: a direct comparison of two commonly explored infrared emission models". In: *Monthly Notices of the Royal Astronomical Society* 426.1, pp. 120–127. DOI: 10.1111/j.1365-2966.2012.21695.x. arXiv: 1207.2668 [astro-ph.CO].

Ferrari, F. et al. (July 2002). "Survey of the ISM in early-type galaxies. IV. The hot dust component". In: *Astronomy and Astrophysics* 389, pp. 355–366. DOI: 10.1051/0004-6361:20020582. arXiv: astro-ph/0204318 [astro-ph].

Finkelstein, Keely D. et al. (Nov. 2015). "Probing the Physical Properties of z = 4.5 Lyman Alpha Emitters with Spitzer". In: *The Astrophysical Journal* 813.1, 78, p. 78. DOI: 10.1088/0004-637X/813/1/78. arXiv: 1509.06381 [astro-ph.GA].

Finlator, Kristian et al. (Dec. 2012). "Gas clumping in self-consistent reionization models". In: *Monthly Notices of the Royal Astronomical Society* 427.3, pp. 2464–2479. DOI: 10.1111/j.1365-2966.2012.22114.x. arXiv: 1209.2489 [astro-ph.CO].

Fiore, F. et al. (May 2017). "AGN wind scaling relations and the co-evolution of black holes and galaxies". In: *Astronomy and Astrophysics* 601, A143, A143. DOI: 10.1051/0004-6361/201629478. arXiv: 1702.04507 [astro-ph.GA].

Fontanot, Fabio et al. (Feb. 2017). "Variations of the stellar initial mass function in semi-analytical models: implications for the mass assembly and the chemical enrichment of galaxies in the GAEA model". In: *Monthly Notices of the Royal Astronomical Society* 464.4, pp. 3812–3824. DOI: 10.1093/mnras/stw2612. arXiv: 1606.01908 [astro-ph.GA].

Forbes, John C., Mark R. Krumholz, and Joshua S. Speagle (Aug. 2019). "Towards a radially resolved semi-analytic model for the evolution of disc galaxies tuned with machine learning". In: *Monthly Notices of the Royal Astronomical Society* 487.3, pp. 3581–3606. DOI: 10.1093/mnras/stz1473. arXiv: 1810.12919 [astro-ph.GA].

Forbes, John C. et al. (July 2014). "On the origin of the fundamental metallicity relation and the scatter in galaxy scaling relations". In: *Monthly Notices of the Royal Astronomical Society* 443.1, pp. 168–185. ISSN: 0035-8711. DOI: 10.1093/mnras/stu1142. eprint: https://academic.oup.com/mnras/article-pdf/443/1/168/4301291/stu1142.pdf. URL: https://doi.org/10.1093/mnras/stu1142.

Forrest, Ben et al. (Aug. 2018). "ZFOURGE: Using Composite Spectral Energy Distributions to Characterize Galaxy Populations at 1 < z < 4". In: *The Astrophysical Journal* 863.2, 131, p. 131. DOI: 10.3847/1538-4357/aad232. arXiv: 1807.03785 [astro-ph.GA].

Förster Schreiber, N. M. et al. (July 2006). "SINFONI Integral Field Spectroscopy of z ∼2 UV-selected Galaxies: Rotation Curves and Dynamical Evolution". In: *The*

Astrophysical Journal 645.2, pp. 1062–1075. DOI: 10.1086/504403. arXiv: astro-ph/0603559 [astro-ph].

Förster Schreiber, N. M. et al. (Sept. 2011). "Constraints on the Assembly and Dynamics of Galaxies. II. Properties of Kiloparsec-scale Clumps in Rest-frame Optical Emission of z ∼2 Star-forming Galaxies". In: *The Astrophysical Journal* 739.1, 45, p. 45. DOI: 10.1088/0004-637X/739/1/45. arXiv: 1104.0248 [astro-ph.CO].

Franco, M. et al. (Dec. 2018). "GOODS-ALMA: 1.1 mm galaxy survey. I. Source catalog and optically dark galaxies". In: *Astronomy and Astrophysics* 620, A152, A152. DOI: 10.1051/0004-6361/201832928. arXiv: 1803.00157 [astro-ph.GA].

Franco, M. et al. (Nov. 2020). "GOODS-ALMA: The slow downfall of star formation in z = 2-3 massive galaxies". In: *Astronomy and Astrophysics* 643, A30, A30. DOI: 10.1051/0004-6361/202038312. arXiv: 2005.03043 [astro-ph.GA].

Fraternali, F. et al. (Feb. 2015). "Galactic hail: the origin of the high-velocity cloud complex C." In: *Monthly Notices of the Royal Astronomical Society* 447, pp. L70–L74. DOI: 10.1093/mnrasl/slu182. arXiv: 1411.4050 [astro-ph.GA].

Fraternali, F. et al. (Mar. 2021). "Fast rotating and low-turbulence discs at z 4.5: Dynamical evidence of their evolution into local early-type galaxies". In: *Astronomy and Astrophysics* 647, A194, A194. DOI: 10.1051/0004-6361/202039807. arXiv: 2011.05340 [astro-ph.GA].

Fritz, J., A. Franceschini, and E. Hatziminaoglou (Mar. 2006). "Revisiting the infrared spectra of active galactic nuclei with a new torus emission model". In: *Monthly Notices of the Royal Astronomical Society* 366.3, pp. 767–786. DOI: 10.1111/j.1365-2966.2006.09866.x. arXiv: astro-ph/0511428 [astro-ph].

Fu, Jian et al. (Sept. 2013). "Star formation and metallicity gradients in semi-analytic models of disc galaxy formation". In: *Monthly Notices of the Royal Astronomical Society* 434.2, pp. 1531–1548. DOI: 10.1093/mnras/stt1117. arXiv: 1303.5586 [astro-ph.CO].

Fujimoto, Seiji et al. (Nov. 2017). "Demonstrating a New Census of Infrared Galaxies with ALMA (DANCING-ALMA). I. FIR Size and Luminosity Relation at z = 0-6 Revealed with 1034 ALMA Sources". In: *The Astrophysical Journal* 850.1, 83, p. 83. DOI: 10.3847/1538-4357/aa93e6. arXiv: 1703.02138 [astro-ph.GA].

Gabor, J. M. and Frédéric Bournaud (Sept. 2013). "Simulations of supermassive black hole growth in high-redshift disc galaxies". In: *Monthly Notices of the Royal Astronomical Society* 434.1, pp. 606–620. DOI: 10.1093/mnras/stt1046. arXiv: 1306.2954 [astro-ph.CO].

Gaia Collaboration et al. (Nov. 2016). "Gaia Data Release 1. Summary of the astrometric, photometric, and survey properties". In: *Astronomy and Astrophysics* 595, A2, A2. DOI: 10.1051/0004-6361/201629512. arXiv: 1609.04172 [astro-ph.IM].

Gallazzi, Anna et al. (Aug. 2006). "Ages and metallicities of early-type galaxies in the Sloan Digital Sky Survey: new insight into the physical origin of the colour-magnitude and the Mg_2-σ_V relations". In: *Monthly Notices of the Royal Astronomical Society* 370.3, pp. 1106–1124. DOI: 10.1111/j.1365-2966.2006.10548.x. arXiv: astro-ph/0605300 [astro-ph].

Gallazzi, Anna et al. (June 2014). "Charting the Evolution of the Ages and Metallicities of Massive Galaxies since z = 0.7". In: *The Astrophysical Journal* 788.1, 72, p. 72. DOI: 10.1088/0004-637X/788/1/72. arXiv: 1404.5624 [astro-ph.GA].

Gandhi, P. et al. (Aug. 2009). "Resolving the mid-infrared cores of local Seyferts". In: *Astronomy and Astrophysics* 502.2, pp. 457–472. DOI: 10.1051/0004-6361/200811368. arXiv: 0902.2777 [astro-ph.GA].

Genel, Shy et al. (Aug. 2010). "The Growth of Dark Matter Halos: Evidence for Significant Smooth Accretion". In: *The Astrophysical Journal* 719.1, pp. 229–239. DOI: 10.1088/0004-637X/719/1/229. arXiv: 1005.4058 [astro-ph.CO].

Genel, Shy et al. (Sept. 2014). "Introducing the Illustris project: the evolution of galaxy populations across cosmic time". In: *Monthly Notices of the Royal Astronomical Society* 445.1, pp. 175–200. ISSN: 0035-8711. DOI: 10.1093/mnras/stu1654. eprint: https://academic.oup.com/mnras/article-pdf/445/1/175/18471627/stu1654.pdf. URL: https://doi.org/10.1093/mnras/stu1654.

Genzel, R. et al. (June 2011). "The Sins Survey of z ~2 Galaxy Kinematics: Properties of the Giant Star-forming Clumps". In: *The Astrophysical Journal* 733.2, 101, p. 101. DOI: 10.1088/0004-637X/733/2/101. arXiv: 1011.5360 [astro-ph.CO].

Genzel, R. et al. (Feb. 2012). "The Metallicity Dependence of the CO → H_2 Conversion Factor in z >= 1 Star-forming Galaxies". In: *The Astrophysical Journal* 746.1, 69, p. 69. DOI: 10.1088/0004-637X/746/1/69. arXiv: 1106.2098 [astro-ph.CO].

Genzel, R. et al. (Mar. 2017). "Strongly baryon-dominated disk galaxies at the peak of galaxy formation ten billion years ago". In: *Nature* 543.7645, pp. 397–401. DOI: 10.1038/nature21685. arXiv: 1703.04310 [astro-ph.GA].

Giavalisco, M. et al. (Jan. 2004). "The Great Observatories Origins Deep Survey: Initial Results from Optical and Near-Infrared Imaging". In: *The Astrophysical Journal* 600.2, pp. L93–L98. DOI: 10.1086/379232. arXiv: astro-ph/0309105 [astro-ph].

Gilli, R. et al. (Feb. 2014). "ALMA reveals a warm and compact starburst around a heavily obscured supermassive black hole at z = 4.75". In: *Astronomy and Astrophysics* 562, A67, A67. DOI: 10.1051/0004-6361/201322892. arXiv: 1312.1248 [astro-ph.GA].

Gioannini, L. et al. (Jan. 2017). "A new galactic chemical evolution model with dust: results for dwarf irregular galaxies and DLA systems". In: *Monthly Notices of the Royal Astronomical Society* 464.1, pp. 985–1002. DOI: 10.1093/mnras/stw2343. arXiv: 1609.03833 [astro-ph.GA].

Giocoli, Carlo, Giuseppe Tormen, and Ravi K. Sheth (May 2012). "Formation times, mass growth histories and concentrations of dark matter haloes". In: *Monthly Notices of the Royal Astronomical Society* 422.1, pp. 185–198. DOI: 10.1111/j.1365-2966.2012.20594.x. arXiv: 1111.6977 [astro-ph.CO].

Glazebrook, Karl et al. (Apr. 2017). "A massive, quiescent galaxy at a redshift of 3.717". In: *Nature* 544.7648, pp. 71–74. DOI: 10.1038/nature21680. arXiv: 1702.01751 [astro-ph.GA].

Gómez-Guijarro, C. et al. (Apr. 2018). "Starburst to Quiescent from HST/ALMA: Stars and Dust Unveil Minor Mergers in Submillimeter Galaxies at z ~ 4.5". In: *The Astrophysical Journal* 856.2, 121, p. 121. DOI: 10.3847/1538-4357/aab206. arXiv: 1802.07751 [astro-ph.GA].

González-López, Jorge et al. (Sept. 2019). "The Atacama Large Millimeter/submillimeter Array Spectroscopic Survey in the Hubble Ultra Deep Field: CO Emission Lines and 3 mm Continuum Sources". In: *The Astrophysical Journal* 882.2, 139, p. 139. DOI: 10.3847/1538-4357/ab3105. arXiv: 1903.09161 [astro-ph.GA].

Granato, Gian Luigi et al. (Jan. 2004). "A Physical Model for the Coevolution of QSOs and Their Spheroidal Hosts". In: *The Astrophysical Journal* 600.2, pp. 580–594. DOI: 10.1086/379875. arXiv: astro-ph/0307202 [astro-ph].

Grand, Robert J. J. et al. (Dec. 2019). "Gas accretion and galactic fountain flows in the Auriga cosmological simulations: angular momentum and metal redistribution". In: *Monthly Notices of the Royal Astronomical Society* 490.4, pp. 4786–4803. DOI: 10.1093/mnras/stz2928. arXiv: 1909.04038 [astro-ph.GA].

Grazian, A. et al. (Apr. 2006). "The GOODS-MUSIC sample: a multicolour catalog of near-IR selected galaxies in the GOODS-South field". In: *Astronomy and Astrophysics* 449.3, pp. 951–968. DOI: 10.1051/0004-6361:20053979. arXiv: astro-ph/0603094 [astro-ph].

Greggio, L. (Oct. 2005). "The rates of type Ia supernovae. I. Analytical formulations". In: *Astronomy and Astrophysics* 441.3, pp. 1055–1078. DOI: 10.1051/0004-6361:20052926. arXiv: astro-ph/0504376 [astro-ph].

Grisoni, V., E. Spitoni, and F. Matteucci (Dec. 2018). "Abundance gradients along the Galactic disc from chemical evolution models". In: *Monthly Notices of the Royal Astronomical Society* 481.2, pp. 2570–2580. DOI: 10.1093/mnras/sty2444. arXiv: 1805.11415 [astro-ph.GA].

Gruppioni, C. et al. (June 2013). "The Herschel PEP/HerMES luminosity function - I. Probing the evolution of PACS selected Galaxies to z 4". In: *Monthly Notices of the Royal Astronomical Society* 432.1, pp. 23–52. DOI: 10.1093/mnras/stt308. arXiv: 1302.5209 [astro-ph.CO].

Gruppioni, C. et al. (Aug. 2015). "Star formation in Herschel's Monsters versus semi-analytic models". In: *Monthly Notices of the Royal Astronomical Society* 451.4, pp. 3419–3426. DOI: 10.1093/mnras/stv1204. arXiv: 1506.01518 [astro-ph.GA].

Gruppioni, C. et al. (Nov. 2020). "The ALPINE-ALMA [CII] survey. The nature, luminosity function, and star formation history of dusty galaxies up to z 6". In: *Astronomy and Astrophysics* 643, A8, A8. DOI: 10.1051/0004-6361/202038487. arXiv: 2006.04974 [astro-ph.GA].

Guo, Yicheng et al. (Feb. 2018). "Clumpy Galaxies in CANDELS. II. Physical Properties of UV-bright Clumps at $0.5 \leq z < 3$". In: *The Astrophysical Journal* 853.2, 108, p. 108. DOI: 10.3847/1538-4357/aaa018. arXiv: 1712.01858 [astro-ph.GA].

Halliday, C. et al. (Feb. 2008). "GMASS ultradeep spectroscopy of galaxies at z $\sim$2 . I. The stellar metallicity". In: *Astronomy and Astrophysics* 479.2, pp. 417–425. DOI: 10.1051/0004-6361:20078673. arXiv: 0801.1193 [astro-ph].

Hartwick, F. D. A. (Oct. 1976). "The Chemical Evolution of the Galactic Halo". In: *The Astrophysical Journal* 209, pp. 418–423. DOI: 10.1086/154735.

Hatsukade, Bunyo et al. (Dec. 2018). "ALMA twenty-six arcmin^2 survey of GOODS-S at one millimeter (ASAGAO): Source catalog and number counts". In: *Publications of the Astronomical Society of Japan* 70.6, 105, p. 105. DOI: 10.1093/pasj/psy104. arXiv: 1808.04502 [astro-ph.GA].

Herenz, Edmund Christian et al. (Sept. 2017). "The MUSE-Wide survey: A first catalogue of 831 emission line galaxies". In: *Astronomy and Astrophysics* 606, A12, A12. DOI: 10.1051/0004-6361/201731055. arXiv: 1705.08215 [astro-ph.GA].

Herrera-Camus, R. et al. (Jan. 2019). "Molecular and Ionized Gas Phases of an AGN-driven Outflow in a Typical Massive Galaxy at $z \approx 2$". In: *The Astrophysical Journal* 871.1, 37, p. 37. DOI: 10.3847/1538-4357/aaf6a7. arXiv: 1807.07074 [astro-ph.GA].

Hildebrand, R. H. (Sept. 1983). "The determination of cloud masses and dust characteristics from submillimetre thermal emission." In: *Quarterly Journal of the RAS* 24, pp. 267–282.

Hill, Ryley et al. (June 2018). "High-resolution SMA imaging of bright submillimetre sources from the SCUBA-2 Cosmology Legacy Survey". In: *Monthly Notices of the Royal Astronomical Society* 477.2, pp. 2042–2067. DOI: 10.1093/mnras/sty746. arXiv: 1710.02231 [astro-ph.GA].

Hirashita, Hiroyuki (Aug. 2000). "Dust Growth Timescale and Mass Function of Molecular Clouds in the Galaxy". In: *Publications of the ASJ* 52, pp. 585–588. DOI: 10.1093/pasj/52.4.585.

Hirashita, Hiroyuki et al. (Dec. 2015). "Dust processing in elliptical galaxies". In: *Monthly Notices of the Royal Astronomical Society* 454.2, pp. 1620–1633. DOI: 10.1093/mnras/stv2095. arXiv: 1509.03978 [astro-ph.GA].

Hirschmann, Michaela, Gabriella De Lucia, and Fabio Fontanot (Sept. 2016). "Galaxy assembly, stellar feedback and metal enrichment: the view from the GAEA model". In: *Monthly Notices of the Royal Astronomical Society* 461.2, pp. 1760–1785. DOI: 10.1093/mnras/stw1318. arXiv: 1512.04531 [astro-ph.GA].

Hodge, J. A. and E. da Cunha (Dec. 2020). "High-redshift star formation in the Atacama large millimetre/submillimetre array era". In: *Royal Society Open Science* 7.12, 200556, p. 200556. DOI: 10.1098/rsos.200556. arXiv: 2004.00934 [astro-ph.GA].

Hodge, J. A. et al. (May 2013). "An ALMA Survey of Submillimeter Galaxies in the Extended Chandra Deep Field South: Source Catalog and Multiplicity". In: *The Astrophysical Journal* 768.1, 91, p. 91. DOI: 10.1088/0004-637X/768/1/91. arXiv: 1304.4266 [astro-ph.CO].

Hodge, J. A. et al. (Jan. 2015). "The Kiloparsec-scale Star Formation Law at Redshift 4: Widespread, Highly Efficient Star Formation in the Dust-obscured Starburst Galaxy GN20". In: *The Astrophysical Journall* 798.1, L18, p. L18. DOI: 10.1088/2041-8205/798/1/L18. arXiv: 1412.2132 [astro-ph.GA].

Hodge, J. A. et al. (Dec. 2016). "Kiloparsec-scale Dust Disks in High-redshift Luminous Submillimeter Galaxies". In: *The Astrophysical Journal* 833.1, 103, p. 103. DOI: 10.3847/1538-4357/833/1/103. arXiv: 1609.09649 [astro-ph.GA].

Hodge, J. A. et al. (May 2019). "ALMA Reveals Potential Evidence for Spiral Arms, Bars, and Rings in High-redshift Submillimeter Galaxies". In: *The Astrophysical Journal* 876.2, 130, p. 130. DOI: 10.3847/1538-4357/ab1846. arXiv: 1810.12307 [astro-ph.GA].

Hogg, David W. (May 1999). "Distance measures in cosmology". In: *arXiv e-prints*, astro-ph/9905116, astro–ph/9905116. arXiv: astro-ph/9905116 [astro-ph].

Hollenbach, D. J. and A. G. G. M. Tielens (Jan. 1999). "Photodissociation regions in the interstellar medium of galaxies". In: *Reviews of Modern Physics* 71.1, pp. 173–230. DOI: 10.1103/RevModPhys.71.173.

Hopkins, Philip F. and Lars Hernquist (Feb. 2010). "A new empirical method to infer the starburst history of the Universe from local galaxy properties". In: *Monthly Notices of the Royal Astronomical Society* 402.2, pp. 985–1004. DOI: 10.1111/j.1365-2966.2009.15933.x. arXiv: 0910.4582 [astro-ph.CO].

Hopkins, Philip F., Eliot Quataert, and Norman Murray (Apr. 2012). "Stellar feedback in galaxies and the origin of galaxy-scale winds". In: *Monthly Notices of the Royal Astronomical Society* 421.4, pp. 3522–3537. DOI: 10.1111/j.1365-2966.2012.20593.x. arXiv: 1110.4638 [astro-ph.CO].

Hopkins, Philip F. et al. (Dec. 2006). "The Relation between Quasar and Merging Galaxy Luminosity Functions and the Merger-driven Star Formation History of the Universe". In: *The Astrophysical Journal* 652.2, pp. 864–888. DOI: 10.1086/508503. arXiv: astro-ph/0602290 [astro-ph].

Hopkins, Philip F. et al. (Sept. 2014). "Galaxies on FIRE (Feedback In Realistic Environments): stellar feedback explains cosmologically inefficient star formation". In: *Monthly Notices of the Royal Astronomical Society* 445.1, pp. 581–603. ISSN: 0035-8711. DOI: 10.1093/mnras/stu1738. eprint: https://academic.oup.com/mnras/article-pdf/445/1/581/18473138/stu1738.pdf. URL: https://doi.org/10.1093/mnras/stu1738.

Hopkins, Philip F et al. (June 2018). "FIRE-2 simulations: physics versus numerics in galaxy formation". In: *Monthly Notices of the Royal Astronomical Society* 480.1,

pp. 800–863. ISSN: 0035-8711. DOI: 10.1093/mnras/sty1690. eprint: https://academic.oup.com/mnras/article-pdf/480/1/800/25368704/sty1690.pdf. URL: https://doi.org/10.1093/mnras/sty1690.

Hudson, Michael J. et al. (Feb. 2015). "CFHTLenS: co-evolution of galaxies and their dark matter haloes". In: *Monthly Notices of the Royal Astronomical Society* 447.1, pp. 298–314. DOI: 10.1093/mnras/stu2367. arXiv: 1310.6784 [astro-ph.CO].

Huertas-Company, M. et al. (Aug. 2015). "The Morphologies of Massive Galaxies from z ∼3—Witnessing the Two Channels of Bulge Growth". In: *The Astrophysical Journal* 809.1, 95, p. 95. DOI: 10.1088/0004-637X/809/1/95. arXiv: 1506.03084 [astro-ph.GA].

Humphrey, Philip J. and David A. Buote (Mar. 2006). "A Chandra Survey of Early-Type Galaxies. I. Metal Enrichment in the Interstellar Medium". In: *The Astrophysical Journal* 639.1, pp. 136–156. DOI: 10.1086/499323. arXiv: astro-ph/0504008 [astro-ph].

Huynh, Minh T. et al. (May 2017). "The AT-LESS CO(1-0) survey of submillimetre galaxies in the Extended Chandra Deep Field South: First results on cold molecular gas in galaxies at z ∼ 2". In: *Monthly Notices of the Royal Astronomical Society* 467.1, pp. 1222–1230. DOI: 10.1093/mnras/stx156. arXiv: 1701.05698 [astro-ph.GA].

Ibar, Edo et al. (July 2009). "Deep multi-frequency radio imaging in the Lockman Hole using the GMRT and VLA - I. The nature of the sub-mJy radio population". In: *Monthly Notices of the Royal Astronomical Society* 397.1, pp. 281–298. DOI: 10.1111/j.1365-2966.2009.14866.x. arXiv: 0903.3600 [astro-ph.CO].

Ibar, Edo et al. (Jan. 2010). "Deep multi-frequency radio imaging in the Lockman Hole - II. The spectral index of submillimetre galaxies". In: *Monthly Notices of the Royal Astronomical Society* 401.1, pp. L53–L57. DOI: 10.1111/j.1745-3933.2009.00786.x. arXiv: 0911.1954 [astro-ph.CO].

Ikarashi, Soh et al. (Sept. 2015). "Compact Starbursts in z ∼ 3-6 Submillimeter Galaxies Revealed by ALMA". In: *The Astrophysical Journal* 810.2, 133, p. 133. DOI: 10.1088/0004-637X/810/2/133. arXiv: 1411.5038 [astro-ph.GA].

Iliev, Ilian T. et al. (Apr. 2007). "Self-regulated reionization". In: *Monthly Notices of the Royal Astronomical Society* 376.2, pp. 534–548. DOI: 10.1111/j.1365-2966.2007.11482.x. arXiv: astro-ph/0607517 [astro-ph].

Imara, Nia et al. (Feb. 2018). "A Model Connecting Galaxy Masses, Star Formation Rates, and Dust Temperatures across Cosmic Time". In: *The Astrophysical Journal* 854.1, 36, p. 36. DOI: 10.3847/1538-4357/aaa3f0. arXiv: 1801.01499 [astro-ph.GA].

Inoue, Akio K. (Oct. 2003). "Evolution of Dust-to-Metal Ratio in Galaxies". In: *Publications of the ASJ* 55, pp. 901–909. DOI: 10.1093/pasj/55.5.901. arXiv: astro-ph/0308204 [astro-ph].

Ishibashi, W. and T. J. L. Courvoisier (Mar. 2010). "X-ray power law spectra in active galactic nuclei". In: *Astronomy and Astrophysics* 512, A58, A58. DOI: 10.1051/0004-6361/200913587. arXiv: 1001.4176 [astro-ph.CO].

Iwasawa, K. et al. (Oct. 2012). "The XMM deep survey in the CDF-S. II. A 9-20 keV selection of heavily obscured active galaxies at z > 1.7". In: *Astronomy and Astrophysics* 546, A84, A84. DOI: 10.1051/0004-6361/201220036. arXiv: 1209.0916 [astro-ph.CO].

Joblin, C. et al. (July 2018). "Structure of photodissociation fronts in star-forming regions revealed by Herschel observations of high-J CO emission lines". In: *Astronomy and Astrophysics* 615, A129, A129. DOI: 10.1051/0004-6361/201832611. arXiv: 1801.03893 [astro-ph.GA].

Johansson, Jonas, Daniel Thomas, and Claudia Maraston (Apr. 2012). "Chemical element ratios of Sloan Digital Sky Survey early-type galaxies". In: *Monthly Notices of the Royal Astronomical Society* 421.3, pp. 1908–1926. DOI: 10.1111/j.1365-2966.2011.20316.x. arXiv: 1112.0322 [astro-ph.CO].

Kaasinen, Melanie et al. (Aug. 2020). "A Comparison of the Stellar, CO, and Dust-continuum Emission from Three Star-forming HUDF Galaxies at z ∼ 2". In: *The Astrophysical Journal* 899.1, 37, p. 37. DOI: 10.3847/1538-4357/aba438. arXiv: 2007.03697 [astro-ph.GA].

Karim, A. et al. (June 2013). "An ALMA survey of submillimetre galaxies in the Extended Chandra Deep Field South: high-resolution 870 μm source counts". In: *Monthly Notices of the Royal Astronomical Society* 432.1, pp. 2–9. DOI: 10.1093/mnras/stt196. arXiv: 1210.0249 [astro-ph.CO].

Kauffmann, G., S. D. M. White, and B. Guiderdoni (Sept. 1993). "The formation and evolution of galaxies within merging dark matter haloes." In: *Monthly Notices of the Royal Astronomical Society* 264, pp. 201–218. DOI: 10.1093/mnras/264.1.201.

Kellermann, K. I. (Dec. 1966). "On the Interpretation of Radio-Source Spectra and the Evolution of Radio Galaxies and Quasi-Stellar Sources". In: *The Astrophysical Journal* 146, p. 621. DOI: 10.1086/148940.

Kellermann, K. I. et al. (Nov. 2008). "The VLA Survey of the Chandra Deep Field-South. I. Overview and the Radio Data". In: *The Astrophysical Journal Supplement Series* 179.1, pp. 71–94. DOI: 10.1086/591055. arXiv: 0806.0843 [astro-ph].

Kennicutt Robert C., Jr. (May 1998). "The Global Schmidt Law in Star-forming Galaxies". In: *The Astrophysical Journal* 498.2, pp. 541–552. DOI: 10.1086/305588. arXiv: astro-ph/9712213 [astro-ph].

Kennicutt, Robert C. and Neal J. Evans (Sept. 2012). "Star Formation in the Milky Way and Nearby Galaxies". In: *Annual Review of Astronomy and Astrophysics* 50, pp. 531–608. DOI: 10.1146/annurev-astro-081811-125610. arXiv: 1204.3552 [astro-ph.GA].

Kewley, Lisa J. and Sara L. Ellison (July 2008). "Metallicity Calibrations and the Mass-Metallicity Relation for Star-forming Galaxies". In: *The Astrophysical Journal* 681.2, pp. 1183–1204. DOI: 10.1086/587500. arXiv: 0801.1849 [astro-ph].

King, Andrew (Oct. 2003). "Black Holes, Galaxy Formation, and the M_{BH}-σ Relation". In: *The Astrophysical Journal, Letters* 596.1, pp. L27–L29. DOI: 10.1086/379143. arXiv: astro-ph/0308342 [astro-ph].

— (Sept. 2014). "The Supermassive Black Hole—Galaxy Connection". In: *Space Science Reviews* 183.1-4, pp. 427–451. DOI: 10.1007/s11214-013-0018-2.

King, Andrew and Ken Pounds (2015). "Powerful Outflows and Feedback from Active Galactic Nuclei". In: *Annual Review of Astronomy and Astrophysics* 53.1, pp. 115–154. DOI: 10.1146/annurev-astro-082214-122316. eprint: https://doi.org/10.1146/annurev-astro-082214-122316. URL: https://doi.org/10.1146/annurev-astro-082214-122316.

Kitayama, Tetsu and Yasushi Suto (May 1996). "Formation rate of gravitational structures and the cosmic X-ray background radiation". In: *Monthly Notices of the Royal Astronomical Society* 280, p. 638. DOI: 10.1093/mnras/280.3.638. arXiv: astro-ph/9602076 [astro-ph].

Koprowski, M. P. et al. (June 2016). "The SCUBA-2 Cosmology Legacy Survey: galaxies in the deep 850 μm survey, and the star-forming 'main sequence'". In: *Monthly Notices of the Royal Astronomical Society* 458.4, pp. 4321–4344. DOI: 10.1093/mnras/stw564. arXiv: 1509.07144 [astro-ph.GA].

Kravtsov, A. V., A. A. Vikhlinin, and A. V. Meshcheryakov (Jan. 2018). "Stellar Mass—Halo Mass Relation and Star Formation Efficiency in High-Mass Halos".

In: *Astronomy Letters* 44.1, pp. 8–34. DOI: 10.1134/S1063773717120015. arXiv: 1401.7329 [astro-ph.CO].

Kriek, Mariska et al. (Oct. 2006). "Spectroscopic Identification of Massive Galaxies at z ~2.3 with Strongly Suppressed Star Formation". In: *The Astrophysical Journall* 649.2, pp. L71–L74. DOI: 10.1086/508371. arXiv: astro-ph/0608446 [astro-ph].

Kriek, Mariska et al. (Nov. 2007). "The Origin of Line Emission in Massive z ~2.3 Galaxies: Evidence for Cosmic Downsizing of AGN Host Galaxies". In: *The Astrophysical Journal* 669.2, pp. 776–790. DOI: 10.1086/520789. arXiv: astro-ph/0611724 [astro-ph].

Kriek, Mariska et al. (Dec. 2016). "A massive, quiescent, population II galaxy at a redshift of 2.1". In: *Nature* 540.7632, pp. 248–251. DOI: 10.1038/nature20570. arXiv: 1612.02001 [astro-ph.GA].

Krumholz, Mark R., Avishai Dekel, and Christopher F. McKee (Jan. 2012). "A Universal, Local Star Formation Law in Galactic Clouds, nearby Galaxies, High-redshift Disks, and Starbursts". In: *The Astrophysical Journal* 745.1, 69, p. 69. DOI: 10.1088/0004-637X/745/1/69. arXiv: 1109.4150 [astro-ph.CO].

Kubryk, M., N. Prantzos, and E. Athanassoula (Aug. 2015). "Evolution of the Milky Way with radial motions of stars and gas. I. The solar neighbourhood and the thin and thick disks". In: *Astronomy and Astrophysics* 580, A126, A126. DOI: 10.1051/0004-6361/201424171. arXiv: 1412.0585 [astro-ph.GA].

Kurk, J. et al. (Jan. 2013). "GMASS ultradeep spectroscopy of galaxies at z ~2. VII. Sample selection and spectroscopy". In: *Astronomy and Astrophysics* 549, A63, A63. DOI: 10.1051/0004-6361/201117847. arXiv: 1209.1561 [astro-ph.CO].

Lacey, C. G. and S. M. Fall (Mar. 1985). "Chemical evolution of the galactic disk with radial gas flows." In: *The Astrophysical Journal* 290, pp. 154–170. DOI: 10.1086/162970.

Lacey, Cedric and Shaun Cole (June 1993). "Merger rates in hierarchical models of galaxy formation". In: *Monthly Notices of the Royal Astronomical Society* 262.3, pp. 627–649. DOI: 10.1093/mnras/262.3.627.

Lacey, Cedric G. et al. (Nov. 2016). "A unified multiwavelength model of galaxy formation". In: *Monthly Notices of the Royal Astronomical Society* 462.4, pp. 3854–3911. DOI: 10.1093/mnras/stw1888. arXiv: 1509.08473 [astro-ph.GA].

Lada, Charles J., Marco Lombardi, and João F. Alves (Nov. 2010). "On the Star Formation Rates in Molecular Clouds". In: *The Astrophysical Journal* 724.1, pp. 687–693. DOI: 10.1088/0004-637X/724/1/687. arXiv: 1009.2985 [astro-ph.GA].

Lagos, Claudia del P. et al. (Dec. 2018). "Shark: introducing an open source, free, and flexible semi-analytic model of galaxy formation". In: *Monthly Notices of the Royal Astronomical Society* 481.3, pp. 3573–3603. DOI: 10.1093/mnras/sty2440. arXiv: 1807.11180 [astro-ph.GA].

Lang, Philipp et al. (July 2019). "Revealing the Stellar Mass and Dust Distributions of Submillimeter Galaxies at Redshift 2". In: *The Astrophysical Journal* 879.1, 54, p. 54. DOI: 10.3847/1538-4357/ab1f77. arXiv: 1905.06960 [astro-ph.GA].

Lapi, A., P. Salucci, and L. Danese (Aug. 2013). "Statistics of Dark Matter Halos from the Excursion Set Approach". In: *The Astrophysical Journal* 772.2, 85, p. 85. DOI: 10.1088/0004-637X/772/2/85. arXiv: 1305.7382 [astro-ph.CO].

Lapi, A. et al. (Oct. 2006). "Quasar Luminosity Functions from Joint Evolution of Black Holes and Host Galaxies". In: *The Astrophysical Journal* 650.1, pp. 42–56. DOI: 10.1086/507122. arXiv: astro-ph/0603819 [astro-ph].

Lapi, A. et al. (Nov. 2011). "Herschel-ATLAS Galaxy Counts and High-redshift Luminosity Functions: The Formation of Massive Early-type Galaxies". In: *The Astrophysical Journal* 742.1, 24, p. 24. DOI: 10.1088/0004-637X/742/1/24. arXiv: 1108.3911 [astro-ph.CO].

Lapi, A. et al. (Jan. 2014). "THE COEVOLUTION OF SUPERMASSIVE BLACK HOLES AND MASSIVE GALAXIES AT HIGH REDSHIFT". In: *The Astrophysical Journal* 782.2, p. 69. DOI: 10.1088/0004-637x/782/2/69. URL: https://doi.org/10.1088/0004-637x/782/2/69.

Lapi, A. et al. (Sept. 2017). "Stellar Mass Function of Active and Quiescent Galaxies via the Continuity Equation". In: *The Astrophysical Journal* 847.1, 13, p. 13. DOI: 10.3847/1538-4357/aa88c9. arXiv: 1708.07643 [astro-ph.GA].

Lapi, A. et al. (Apr. 2018). "The Dramatic Size and Kinematic Evolution of Massive Early-type Galaxies". In: *The Astrophysical Journal* 857.1, 22, p. 22. DOI: 10.3847/1538-4357/aab6af. arXiv: 1803.04734 [astro-ph.GA].

Lapi, A. et al. (July 2020). "New Analytic Solutions for Galaxy Evolution. II. Wind Recycling, Galactic Fountains, and Late-type Galaxies". In: *The Astrophysical Journal* 897.1, 81, p. 81. DOI: 10.3847/1538-4357/ab9812. arXiv: 2006.01643 [astro-ph.GA].

Lara-López, Maritza A., Ángel R. López-Sánchez, and Andrew M. Hopkins (Feb. 2013). "On the Three-dimensional Structure of the Mass, Metallicity, and Star Formation Rate Space for Star-forming Galaxies". In: *The Astrophysical Journal* 764.2, 178, p. 178. DOI: 10.1088/0004-637X/764/2/178. arXiv: 1207.0950 [astro-ph.CO].

Law, David R. et al. (June 2009). "The Kiloparsec-scale Kinematics of High-redshift Star-forming Galaxies". In: *The Astrophysical Journal* 697.2, pp. 2057–2082. DOI: 10.1088/0004-637X/697/2/2057. arXiv: 0901.2930 [astro-ph.GA].

Lehmer, B. D. et al. (July 2016). "The Evolution of Normal Galaxy X-Ray Emission through Cosmic History: Constraints from the 6 MS Chandra Deep Field-South". In: *The Astrophysical Journal* 825.1, 7, p. 7. DOI: 10.3847/0004-637X/825/1/7. arXiv: 1604.06461 [astro-ph.GA].

Leja, Joel et al. (Mar. 2017). "Deriving Physical Properties from Broadband Photometry with Prospector: Description of the Model and a Demonstration of its Accuracy Using 129 Galaxies in the Local Universe". In: *The Astrophysical Journal* 837.2, 170, p. 170. DOI: 10.3847/1538-4357/aa5ffe. arXiv: 1609.09073 [astro-ph.GA].

Lelli, Federico et al. (Feb. 2021). "A massive stellar bulge in a regularly rotating galaxy 1.2 billion years after the Big Bang". In: *Science* 371.6530, pp. 713–716. DOI: 10.1126/science.abc1893. arXiv: 2102.05957 [astro-ph.GA].

Leroy, Adam K. et al. (Aug. 2011). "The CO-to-H_2 Conversion Factor from Infrared Dust Emission across the Local Group". In: *The Astrophysical Journal* 737.1, 12, p. 12. DOI: 10.1088/0004-637X/737/1/12. arXiv: 1102.4618 [astro-ph.CO].

Li, Aigen and Ingrid Mann (2012). "Nanodust in the Interstellar Medium in Comparison to the Solar System". In: *Nanodust in the Solar System: Discoveries and Interpretations*. Ed. by Ingrid Mann, Nicole Meyer-Vernet, and Andrzej Czechowski. Vol. 385, p. 5. DOI: 10.1007/978-3-642-27543-2_2.

Liang, Lichen et al. (Oct. 2019). "On the dust temperatures of high-redshift galaxies". In: *Monthly Notices of the Royal Astronomical Society* 489.1, pp. 1397–1422. DOI: 10.1093/mnras/stz2134. arXiv: 1902.10727 [astro-ph.GA].

Lilly, Simon J. et al. (Aug. 2013). "Gas Regulation of Galaxies: The Evolution of the Cosmic Specific Star Formation Rate, the Metallicity-Mass-Star-formation Rate Relation, and the Stellar Content of Halos". In: *The Astrophysical Journal* 772.2, 119, p. 119. DOI: 10.1088/0004-637X/772/2/119. arXiv: 1303.5059 [astro-ph.CO].

Liu, Daizhong et al. (Oct. 2019). "Automated Mining of the ALMA Archive in the COSMOS Field (A^{3}COSMOS). I. Robust ALMA Continuum Photometry Catalogs and Stellar Mass and Star Formation Properties for ~700 Galaxies at z = 0.5-6". In: *The Astrophysical Journal Supplement Series* 244.2, 40, p. 40. DOI: 10.3847/1538-4365/ab42da. arXiv: 1910.12872 [astro-ph.GA].

Lo Faro, B. et al. (Dec. 2017). "Characterizing the UV-to-NIR shape of the dust attenuation curve of IR luminous galaxies up to z ~ 2". In: *Monthly Notices of the Royal Astronomical Society* 472.2, pp. 1372–1391. DOI: 10.1093/mnras/stx1901. arXiv: 1707.09805 [astro-ph.GA].

Loewenstein, Michael and William G. Mathews (June 1991). "Hot Gas Metallicity and the History of Supernova Activity in Elliptical Galaxies". In: *The Astrophysical Journal* 373, p. 445. DOI: 10.1086/170063.

Luo, B. et al. (Jan. 2017). "The Chandra Deep Field-South Survey: 7 Ms Source Catalogs". In: *The Astrophysical Journal Supplement Series* 228.1, 2, p. 2. DOI: 10.3847/1538-4365/228/1/2. arXiv: 1611.03501 [astro-ph.GA].

Lutz, D. et al. (Aug. 2011). "PACS Evolutionary Probe (PEP) - A Herschel key program". In: *Astronomy and Astrophysics* 532, A90, A90. DOI: 10.1051/0004-6361/201117107. arXiv: 1106.3285 [astro-ph.CO].

Ma, Brian et al. (Nov. 2015). "Spitzer Imaging of Strongly lensed Herschel-selected Dusty Star-forming Galaxies". In: *The Astrophysical Journal* 814.1, 17, p. 17. DOI: 10.1088/0004-637X/814/1/17. arXiv: 1504.05254 [astro-ph.GA].

Ma, Jingzhe et al. (Dec. 2016). "SPT0346-52: Negligible AGN Activity in a Compact, Hyper-starburst Galaxy at z = 5.7". In: *The Astrophysical Journal* 832.2, 114, p. 114. DOI: 10.3847/0004-637X/832/2/114. arXiv: 1609.08553 [astro-ph.GA].

Mac Low, Mordecai-Mark and Andrea Ferrara (Mar. 1999). "Starburst-driven Mass Loss from Dwarf Galaxies: Efficiency and Metal Ejection". In: *The Astrophysical Journal* 513.1, pp. 142–155. DOI: 10.1086/306832. arXiv: astro-ph/9801237 [astro-ph].

Macciò, Andrea V. et al. (June 2007). "Concentration, spin and shape of dark matter haloes: scatter and the dependence on mass and environment". In: *Monthly Notices of the Royal Astronomical Society* 378.1, pp. 55–71. DOI: 10.1111/j.1365-2966.2007.11720.x. arXiv: astro-ph/0608157 [astro-ph].

Madau, Piero and Mark Dickinson (Aug. 2014). "Cosmic Star-Formation History". In: *Annual Review of Astronomy and Astrophysics* 52, pp. 415–486. DOI: 10.1146/annurev-astro-081811-125615. arXiv: 1403.0007 [astro-ph.CO].

Magdis, Georgios E. et al. (Nov. 2012). "The Evolving Interstellar Medium of Star-forming Galaxies since z = 2 as Probed by Their Infrared Spectral Energy Distributions". In: *The Astrophysical Journal* 760.1, 6, p. 6. DOI: 10.1088/0004-637X/760/1/6. arXiv: 1210.1035 [astro-ph.CO].

Magnelli, B. et al. (Apr. 2011). "Evolution of the dusty infrared luminosity function from z = 0 to z = 2.3 using observations from Spitzer". In: *Astronomy and Astrophysics* 528, A35, A35. DOI: 10.1051/0004-6361/200913941. arXiv: 1101.2467 [astro-ph.CO].

Magnelli, B. et al. (May 2013). "The deepest Herschel-PACS far-infrared survey: number counts and infrared luminosity functions from combined PEP/GOODS-H observations". In: *Astronomy and Astrophysics* 553, A132, A132. DOI: 10.1051/0004-6361/201321371. arXiv: 1303.4436 [astro-ph.CO].

Maiolino, R. and F. Mannucci (Feb. 2019). "De re metallica: the cosmic chemical evolution of galaxies". In: *Astronomy and Astrophysicsr* 27.1, 3, p. 3. DOI: 10.1007/s00159-018-0112-2. arXiv: 1811.09642 [astro-ph.GA].

Maiolino, R. et al. (Sept. 2005). "First detection of [CII]158 μm at high redshift: vigorous star formation in the early universe". In: *Astronomy and Astrophysics* 440.2, pp. L51–L54. DOI: 10.1051/0004-6361:200500165. arXiv: astro-ph/0508064 [astro-ph].

Maiolino, R. et al. (Sept. 2008). "AMAZE. I. The evolution of the mass-metallicity relation at z > 3". In: *Astronomy and Astrophysics* 488.2, pp. 463–479. DOI: 10.1051/0004-6361:200809678. arXiv: 0806.2410 [astro-ph].

Małek, K. et al. (Nov. 2018). "HELP: modelling the spectral energy distributions of Herschel detected galaxies in the ELAIS N1 field". In: *Astronomy and Astrophysics* 620, A50, A50. DOI: 10.1051/0004-6361/201833131. arXiv: 1809.00529 [astro-ph.GA].

Man, Allison W. S. et al. (Mar. 2016). "Confirming the Existence of a Quiescent Galaxy Population out to z=3: A Stacking Analysis of Mid-, Far-Infrared and Radio Data". In: *The Astrophysical Journal* 820.1, 11, p. 11. DOI: 10.3847/0004-637X/820/1/11. arXiv: 1411.2870 [astro-ph.GA].

Mancini, M. et al. (July 2015). "The dust mass in z > 6 normal star-forming galaxies." In: *Monthly Notices of the Royal Astronomical Society* 451, pp. L70–L74. DOI: 10.1093/mnrasl/slv070. arXiv: 1505.01841 [astro-ph.GA].

Mancuso, C. et al. (Dec. 2016a). "The Main Sequences of Star-forming Galaxies and Active Galactic Nuclei at High Redshift". In: *The Astrophysical Journal* 833.2, 152, p. 152. DOI: 10.3847/1538-4357/833/2/152. arXiv: 1610.05910 [astro-ph.GA].

Mancuso, C. et al. (June 2016b). "The Quest for Dusty Star-forming Galaxies at High Redshift z $\gtrsim$ 4". In: *The Astrophysical Journal* 823.2, 128, p. 128. DOI: 10.3847/0004-637X/823/2/128. arXiv: 1604.02507 [astro-ph.GA].

Mancuso, C. et al. (June 2017). "Galaxy Evolution in the Radio Band: The Role of Star-forming Galaxies and Active Galactic Nuclei". In: *The Astrophysical Journal* 842.2, 95, p. 95. DOI: 10.3847/1538-4357/aa745d. arXiv: 1705.06539 [astro-ph.GA].

Mandelbaum, Rachel et al. (Apr. 2016). "Strong bimodality in the host halo mass of central galaxies from galaxy-galaxy lensing". In: *Monthly Notices of the Royal Astronomical Society* 457.3, pp. 3200–3218. DOI: 10.1093/mnras/stw188. arXiv: 1509.06762 [astro-ph.GA].

Mandelker, Nir et al. (Oct. 2014). "The population of giant clumps in simulated high-z galaxies: in situ and ex situ migration and survival". In: *Monthly Notices of the Royal Astronomical Society* 443.4, pp. 3675–3702. DOI: 10.1093/mnras/stu1340. arXiv: 1311.0013 [astro-ph.CO].

Mandelker, Nir et al. (Jan. 2017). "Giant clumps in simulated high- z Galaxies: properties, evolution and dependence on feedback". In: *Monthly Notices of the Royal Astronomical Society* 464.1, pp. 635–665. DOI: 10.1093/mnras/stw2358. arXiv: 1512.08791 [astro-ph.GA].

Mannucci, F., M. Della Valle, and N. Panagia (Aug. 2006). "Two populations of progenitors for Type Ia supernovae?" In: *Monthly Notices of the Royal Astronomical Society* 370.2, pp. 773–783. DOI: 10.1111/j.1365-2966.2006.10501.x. arXiv: astro-ph/0510315 [astro-ph].

Mannucci, F. et al. (Nov. 2010). "A fundamental relation between mass, star formation rate and metallicity in local and high-redshift galaxies". In: *Monthly Notices of the Royal Astronomical Society* 408.4, pp. 2115–2127. DOI: 10.1111/j.1365-2966.2010.17291.x. arXiv: 1005.0006 [astro-ph.CO].

Maoz, Dan and Or Graur (Oct. 2017). "Star Formation, Supernovae, Iron, and α: Consistent Cosmic and Galactic Histories". In: *The Astrophysical Journal* 848.1, 25, p. 25. DOI: 10.3847/1538-4357/aa8b6e. arXiv: 1703.04540 [astro-ph.HE].

Maoz, Dan, Filippo Mannucci, and Gijs Nelemans (Aug. 2014). "Observational Clues to the Progenitors of Type Ia Supernovae". In: *Annual Review of Astron and Astrophys* 52, pp. 107–170. DOI: 10.1146/annurev-astro-082812-141031. arXiv: 1312.0628 [astro-ph.CO].

Marconi, G., F. Matteucci, and M. Tosi (Sept. 1994). "Element abundances in blue compact galaxies." In: *Monthly Notices of the Royal Astronomical Society* 270, pp. 35–45. DOI: 10.1093/mnras/270.1.35.

Marinacci, Federico et al. (May 2010). "The mode of gas accretion on to star-forming galaxies". In: *Monthly Notices of the Royal Astronomical Society* 404.3, pp. 1464–1474. DOI: 10.1111/j.1365-2966.2010.16352.x. arXiv: 1001.2446 [astro-ph.GA].

Marinacci, Federico et al. (Aug. 2011). "Galactic fountains and the rotation of disc-galaxy coronae". In: *Monthly Notices of the Royal Astronomical Society* 415.2, pp. 1534–1542. DOI: 10.1111/j.1365-2966.2011.18810.x. arXiv: 1103.5358 [astro-ph.GA].

Martín-Navarro, Ignacio et al. (Apr. 2018). "Timing the formation and assembly of early-type galaxies via spatially resolved stellar populations analysis". In: *Monthly Notices of the Royal Astronomical Society* 475.3, pp. 3700–3729. DOI: 10.1093/mnras/stx3346. arXiv: 1801.05486 [astro-ph.GA].

Martis, Nicholas S. et al. (Sept. 2019). "Stellar and Dust Properties of a Complete Sample of Massive Dusty Galaxies at $1 \leq z \leq 4$ from MAGPHYS Modeling of UltraVISTA DR3 and Herschel Photometry". In: *The Astrophysical Journal* 882.1, 65, p. 65. DOI: 10.3847/1538-4357/ab32f1. arXiv: 1907.08152 [astro-ph.GA].

Massardi, M. et al. (Feb. 2018). "Chandra and ALMA observations of the nuclear activity in two strongly lensed star-forming galaxies". In: *Astronomy and Astrophysics* 610, A53, A53. DOI: 10.1051/0004-6361/201731751. arXiv: 1709.10427 [astro-ph.GA].

Massardi, M. et al. (July 2021). "The Additional Representative Images for Legacy (ARI-L) project for the ALMA Science Archive". In: *arXiv e-prints*, arXiv:2107.11071, arXiv:2107.11071. arXiv: 2107.11071 [astro-ph.IM].

Mathews, William G. and Fabrizio Brighenti (Jan. 2003). "Hot Gas in and around Elliptical Galaxies". In: *Annual Review of Astron and Astrophys* 41, pp. 191–239. DOI: 10.1146/annurev.astro.41.090401.094542. arXiv: astro-ph/0309553 [astro-ph].

Matteucci, F. and C. Chiosi (July 1983). "Stochastic star formation and chemical evolution of dwarf irregular galaxies." In: *Astronomy and Astrophysics* 123, pp. 121–134.

Matteucci, F. and L. Greggio (Jan. 1986). "Relative roles of type I and II supernovae in the chemical enrichment of the interstellar gas". In: *Astronomy and Astrophysics* 154.1-2, pp. 279–287.

Matteucci, Francesca (2012). *Chemical Evolution of Galaxies*. DOI: 10.1007/978-3-642-22491-1.

McAlpine, S. et al. (Apr. 2016). "The EAGLE simulations of galaxy formation: Public release of halo and galaxy catalogues". In: *Astronomy and Computing* 15, pp. 72–89. DOI: 10.1016/j.ascom.2016.02.004. arXiv: 1510.01320 [astro-ph.GA].

McAlpine, Stuart et al. (Sept. 2019). "The nature of submillimetre and highly star-forming galaxies in the EAGLE simulation". In: *Monthly Notices of the Royal Astronomical Society* 488.2, pp. 2440–2454. DOI: 10.1093/mnras/stz1692. arXiv: 1901.05467 [astro-ph.GA].

McKinnon, Ryan et al. (June 2017). "Simulating the dust content of galaxies: successes and failures". In: *Monthly Notices of the Royal Astronomical Society* 468.2, pp. 1505–1521. DOI: 10.1093/mnras/stx467. arXiv: 1606.02714 [astro-ph.GA].

McKinnon, Ryan et al. (Aug. 2018). "Simulating galactic dust grain evolution on a moving mesh". In: *Monthly Notices of the Royal Astronomical Society* 478.3, pp. 2851–2886. DOI: 10.1093/mnras/sty1248. arXiv: 1805.04521 [astro-ph.GA].

Michałowski, M., J. Hjorth, and D. Watson (May 2010). "Cosmic evolution of submillimeter galaxies and their contribution to stellar mass assembly". In: *Astronomy and Astrophysics* 514, A67, A67. DOI: 10.1051/0004-6361/200913634. arXiv: 0905.4499 [astro-ph.CO].

Michałowski, Michał J. (May 2015). "Dust production 680-850 million years after the Big Bang". In: *Astronomy and Astrophysics* 577, A80, A80. DOI: 10.1051/0004-6361/201525644. arXiv: 1503.08210 [astro-ph.GA].

Miettinen, O. et al. (May 2015). "(Sub)millimetre interferometric imaging of a sample of COSMOS/AzTEC submillimetre galaxies. I. Multiwavelength identifications and redshift distribution". In: *Astronomy and Astrophysics* 577, A29, A29. DOI: 10.1051/0004-6361/201425032. arXiv: 1502.05854 [astro-ph.GA].

Miller, Neal A. et al. (Apr. 2013). "The Very Large Array 1.4 GHz Survey of the Extended Chandra Deep Field South: Second Data Release". In: *The Astrophysical Journal Supplement Series* 205.2, 13, p. 13. DOI: 10.1088/0067-0049/205/2/13. arXiv: 1301.7004 [astro-ph.CO].

Mingozzi, M. et al. (Mar. 2018). "CO excitation in the Seyfert galaxy NGC 34: stars, shock or AGN driven?" In: *Monthly Notices of the Royal Astronomical Society* 474.3, pp. 3640–3648. DOI: 10.1093/mnras/stx3011. arXiv: 1711.07995 [astro-ph.GA].

Mo, H. J. and Shude Mao (Sept. 2004). "Galaxy formation in pre-processed dark haloes". In: *Monthly Notices of the Royal Astronomical Society* 353.3, pp. 829–840. DOI: 10.1111/j.1365-2966.2004.08114.x. arXiv: astro-ph/0311459 [astro-ph].

Mo, H. J., Shude Mao, and Simon D. M. White (Apr. 1998). "The formation of galactic discs". In: *Monthly Notices of the Royal Astronomical Society* 295.2, pp. 319–336. DOI: 10.1046/j.1365-8711.1998.01227.x. arXiv: astro-ph/9707093 [astro-ph].

Mo, Houjun, Frank C. van den Bosch, and Simon White (2010). *Galaxy Formation and Evolution*.

Mollá, Mercedes et al. (Aug. 2015). "Galactic chemical evolution: stellar yields and the initial mass function". In: *Monthly Notices of the Royal Astronomical Society* 451.4, pp. 3693–3708. DOI: 10.1093/mnras/stv1102. arXiv: 1505.03341 [astro-ph.GA].

Momcheva, Ivelina G. et al. (Aug. 2016). "The 3D-HST Survey: Hubble Space Telescope WFC3/G141 Grism Spectra, Redshifts, and Emission Line Measurements for ~100,000 Galaxies". In: *The Astrophysical Journal Supplement Series* 225.2, 27, p. 27. DOI: 10.3847/0067-0049/225/2/27. arXiv: 1510.02106 [astro-ph.GA].

Mor, Rivay et al. (Apr. 2012). "Extreme Star Formation in the Host Galaxies of the Fastest Growing Supermassive Black Holes at z = 4.8". In: *The Astrophysical Journall* 749.2, L25, p. L25. DOI: 10.1088/2041-8205/749/2/L25. arXiv: 1203.1613 [astro-ph.CO].

More, Surhud et al. (Jan. 2011). "Satellite kinematics - III. Halo masses of central galaxies in SDSS". In: *Monthly Notices of the Royal Astronomical Society* 410.1, pp. 210–226. DOI: 10.1111/j.1365-2966.2010.17436.x. arXiv: 1003.3203 [astro-ph.CO].

Moreno, Jorge, Carlo Giocoli, and Ravi K. Sheth (July 2009). "Dark matter halo creation in moving barrier models". In: *Monthly Notices of the Royal Astronomical Society* 397.1, pp. 299–310. DOI: 10.1111/j.1365-2966.2009.14871.x. arXiv: 0712.4100 [astro-ph].

Moster, Benjamin P., Thorsten Naab, and Simon D. M. White (Feb. 2013). "Galactic star formation and accretion histories from matching galaxies to dark matter haloes". In: *Monthly Notices of the Royal Astronomical Society* 428.4, pp. 3121–3138. DOI: 10.1093/mnras/sts261. arXiv: 1205.5807 [astro-ph.CO].

Moustakas, John et al. (Apr. 2013). "PRIMUS: Constraints on Star Formation Quenching and Galaxy Merging, and the Evolution of the Stellar Mass Function from z = 0-1". In: *The Astrophysical Journal* 767.1, 50, p. 50. DOI: 10.1088/0004-637X/767/1/50. arXiv: 1301.1688 [astro-ph.CO].

Mullaney, J. R. et al. (June 2011). "Defining the intrinsic AGN infrared spectral energy distribution and measuring its contribution to the infrared output of composite galaxies". In: *Monthly Notices of the Royal Astronomical Society* 414.2, pp. 1082–1110. DOI: 10.1111/j.1365-2966.2011.18448.x. arXiv: 1102.1425 [astro-ph.CO].

Mullaney, J. R. et al. (Jan. 2012). "GOODS-Herschel: the far-infrared view of star formation in active galactic nucleus host galaxies since z ≈ 3". In: *Monthly Notices of the Royal Astronomical Society* 419.1, pp. 95–115. DOI: 10.1111/j.1365-2966.2011.19675.x. arXiv: 1106.4284 [astro-ph.CO].

Murphy, E. J. et al. (Aug. 2011). "Calibrating Extinction-free Star Formation Rate Diagnostics with 33 GHz Free-free Emission in NGC 6946". In: *The Astrophysical Journal* 737.2, 67, p. 67. DOI: 10.1088/0004-637X/737/2/67. arXiv: 1105.4877 [astro-ph.CO].

Murphy, E. J. et al. (Dec. 2012). "The Star Formation in Radio Survey: GBT 33 GHz Observations of Nearby Galaxy Nuclei and Extranuclear Star-forming Regions". In: *The Astrophysical Journal* 761.2, 97, p. 97. DOI: 10.1088/0004-637X/761/2/97. arXiv: 1210.3360 [astro-ph.CO].

Murray, Norman, Eliot Quataert, and Todd A. Thompson (Jan. 2005). "On the Maximum Luminosity of Galaxies and Their Central Black Holes: Feedback from Momentum-driven Winds". In: *The Astrophysical Journal* 618.2, pp. 569–585. DOI: 10.1086/426067. arXiv: astro-ph/0406070 [astro-ph].

Naab, Thorsten and Jeremiah P. Ostriker (Mar. 2006). "A simple model for the evolution of disc galaxies: the Milky Way". In: *Monthly Notices of the Royal Astronomical Society* 366.3, pp. 899–917. DOI: 10.1111/j.1365-2966.2005.09807.x. arXiv: astro-ph/0505594 [astro-ph].

Naab, Thorsten and Jeremiah P. Ostriker (2017). "Theoretical Challenges in Galaxy Formation". In: *Annual Review of Astronomy and Astrophysics* 55.1, pp. 59–109. DOI: 10.1146/annurev-astro-081913-040019. eprint: https://doi.org/10.1146/annurev-astro-081913-040019. URL: https://doi.org/10.1146/annurev-astro-081913-040019.

Narayanan, Desika et al. (Sept. 2015). "The formation of submillimetre-bright galaxies from gas infall over a billion years". In: *Nature* 525.7570, pp. 496–499. DOI: 10.1038/nature15383. arXiv: 1509.06377 [astro-ph.GA].

Narayanan, Desika et al. (Dec. 2018). "A Theory for the Variation of Dust Attenuation Laws in Galaxies". In: *The Astrophysical Journal* 869.1, 70, p. 70. DOI: 10.3847/1538-4357/aaed25. arXiv: 1805.06905 [astro-ph.GA].

Navarro, Julio F., Carlos S. Frenk, and Simon D. M. White (Dec. 1997). "A Universal Density Profile from Hierarchical Clustering". In: *The Astrophysical Journal* 490.2, pp. 493–508. DOI: 10.1086/304888. arXiv: astro-ph/9611107 [astro-ph].

Negrello, M. et al. (May 2014). "Herschel *-ATLAS: deep HST/WFC3 imaging of strongly lensed submillimetre galaxies". In: *Monthly Notices of the Royal Astronomical Society* 440.3, pp. 1999–2012. DOI: 10.1093/mnras/stu413. arXiv: 1311.5898 [astro-ph.CO].

Nelson, Dylan et al. (Mar. 2015). "The impact of feedback on cosmological gas accretion". In: *Monthly Notices of the Royal Astronomical Society* 448.1, pp. 59–74. DOI: 10.1093/mnras/stv017. arXiv: 1410.5425 [astro-ph.CO].

Nelson, Erica J. et al. (Jan. 2019). "Millimeter Mapping at z ~ 1: Dust-obscured Bulge Building and Disk Growth". In: *The Astrophysical Journal* 870.2, 130, p. 130. DOI: 10.3847/1538-4357/aaf38a. arXiv: 1801.02647 [astro-ph.GA].

Nenkova, Maia et al. (Sept. 2008). "AGN Dusty Tori. I. Handling of Clumpy Media". In: *The Astrophysical Journal* 685.1, pp. 147–159. DOI: 10.1086/590482. arXiv: 0806.0511 [astro-ph].

Neri, R. et al. (Mar. 2020). "NOEMA redshift measurements of bright Herschel galaxies". In: *Astronomy and Astrophysics* 635, A7, A7. DOI: 10.1051/0004-6361/201936988. arXiv: 1912.10416 [astro-ph.GA].

Newman, Andrew B., Sirio Belli, and Richard S. Ellis (Nov. 2015). "Discovery of a Strongly Lensed Massive Quiescent Galaxy at z = 2.636: Spatially Resolved Spectroscopy and Indications of Rotation". In: *Astrophysical Journal, Letters* 813.1, L7, p. L7. DOI: 10.1088/2041-8205/813/1/L7. arXiv: 1509.04345 [astro-ph.GA].

Nguyen, H. T. et al. (July 2010). "HerMES: The SPIRE confusion limit". In: *Astronomy and Astrophysics* 518, L5, p. L5. DOI: 10.1051/0004-6361/201014680. arXiv: 1005.2207 [astro-ph.CO].

Noeske, K. G. et al. (May 2007). "Star Formation in AEGIS Field Galaxies since z=1.1: The Dominance of Gradually Declining Star Formation, and the Main Sequence of Star-forming Galaxies". In: *The Astrophysical Journall* 660.1, pp. L43–L46. DOI: 10.1086/517926. arXiv: astro-ph/0701924 [astro-ph].

Noll, S. et al. (Dec. 2009). "Analysis of galaxy spectral energy distributions from far-UV to far-IR with CIGALE: studying a SINGS test sample". In: *Astronomy and Astrophysics* 507.3, pp. 1793–1813. DOI: 10.1051/0004-6361/200912497. arXiv: 0909.5439 [astro-ph.CO].

Nomoto, Ken'ichi, Chiaki Kobayashi, and Nozomu Tominaga (Aug. 2013). "Nucleosynthesis in Stars and the Chemical Enrichment of Galaxies". In: *Annual Review of Astron and Astrophys* 51.1, pp. 457–509. DOI: 10.1146/annurev-astro-082812-140956.

Oklopčić, Antonija et al. (Feb. 2017). "Giant clumps in the FIRE simulations: a case study of a massive high-redshift galaxy". In: *Monthly Notices of the Royal Astronomical Society* 465.1, pp. 952–969. DOI: 10.1093/mnras/stw2754. arXiv: 1603.03778 [astro-ph.GA].

Oliver, S. J. et al. (Aug. 2012). "The Herschel Multi-tiered Extragalactic Survey: HerMES". In: *Monthly Notices of the Royal Astronomical Society* 424.3, pp. 1614–1635. DOI: 10.1111/j.1365-2966.2012.20912.x. arXiv: 1203.2562 [astro-ph.CO].

Omont, A. et al. (Apr. 2013). "The Canada-France High-z Quasar Survey: 1.2 mm observations". In: *Astronomy and Astrophysics* 552, A43, A43. DOI: 10.1051/0004-6361/201221006. arXiv: 1301.6632 [astro-ph.CO].

Onodera, M. et al. (May 2016). "ISM Excitation and Metallicity of Star-forming Galaxies at z 3.3 from Near-IR Spectroscopy". In: *The Astrophysical Journal* 822.1, 42, p. 42. DOI: 10.3847/0004-637X/822/1/42. arXiv: 1602.02779 [astro-ph.GA].

Oppenheimer, Benjamin D. and Romeel Davé (Dec. 2006). "Cosmological simulations of intergalactic medium enrichment from galactic outflows". In: *Monthly Notices of the Royal Astronomical Society* 373.4, pp. 1265–1292. DOI: 10.1111/j.1365-2966.2006.10989.x. arXiv: astro-ph/0605651 [astro-ph].

Oppenheimer, Benjamin D. et al. (Aug. 2010). "Feedback and recycled wind accretion: assembling the z = 0 galaxy mass function". In: *Monthly Notices of the Royal Astronomical Society* 406.4, pp. 2325–2338. DOI: 10.1111/j.1365-2966.2010.16872.x. arXiv: 0912.0519 [astro-ph.CO].

Oteo, I. et al. (May 2016). "ALMACAL I: First Dual-band Number Counts from a Deep and Wide ALMA Submillimeter Survey, Free from Cosmic Variance". In:

The Astrophysical Journal 822.1, 36, p. 36. DOI: 10.3847/0004-637X/822/1/36. arXiv: 1508.05099 [astro-ph.GA].

Oteo, I. et al. (Sept. 2017). "Witnessing the birth of the red sequence: the physical scale and morphology of dust emission in hyper-luminous starbursts in the early Universe". In: *arXiv e-prints*, arXiv:1709.04191, arXiv:1709.04191. arXiv: 1709.04191 [astro-ph.GA].

Padovani, P. et al. (Sept. 2015). "Radio-faint AGN: a tale of two populations". In: *Monthly Notices of the Royal Astronomical Society* 452.2, pp. 1263–1279. DOI: 10.1093/mnras/stv1375. arXiv: 1506.06554 [astro-ph.GA].

Page, M. J. et al. (May 2012). "The suppression of star formation by powerful active galactic nuclei". In: *Nature Astronomy* 485.7397, pp. 213–216. DOI: 10.1038/nature11096. arXiv: 1310.4147 [astro-ph.CO].

Pagel, B. E. J. and B. E. Patchett (July 1975). "Metal abundances in nearby stars and the chemical history of the solar neighbourhood." In: *Monthly Notices of the Royal Astronomical Society* 172, pp. 13–40. DOI: 10.1093/mnras/172.1.13.

Pallottini, A. et al. (Mar. 2017). "Zooming on the internal structure of z6 galaxies". In: *Monthly Notices of the Royal Astronomical Society* 465.3, pp. 2540–2558. DOI: 10.1093/mnras/stw2847. arXiv: 1609.01719 [astro-ph.GA].

Pantoni, L. et al. (Aug. 2019). "New Analytic Solutions for Galaxy Evolution: Gas, Stars, Metals, and Dust in Local ETGs and Their High-z Star-forming Progenitors". In: *The Astrophysical Journal* 880.2, 129, p. 129. DOI: 10.3847/1538-4357/ab2adc. arXiv: 1906.07458 [astro-ph.GA].

Pantoni, L. et al. (Nov. 2021a). "An ALMA view of 11 dusty star-forming galaxies at the peak of cosmic star formation history". In: *Monthly Notice of the Royal Astronomical Society* 507.3, pp. 3998–4015. DOI: 10.1093/mnras/stab2346. arXiv: 2108.05596 [astro-ph.GA].

Pantoni, L. et al. (June 2021b). "Unveiling the nature of 11 dusty star-forming galaxies at the peak of cosmic star formation history". In: *Monthly Notices of the Royal Astronomical Society* 504.1, pp. 928–950. DOI: 10.1093/mnras/stab674. arXiv: 2103.05011 [astro-ph.GA].

Papovich, Casey et al. (Apr. 2011). "The rising star formation histories of distant galaxies and implications for gas accretion with time". In: *Monthly Notices of the Royal Astronomical Society* 412.2, pp. 1123–1136. DOI: 10.1111/j.1365-2966.2010.17965.x. arXiv: 1007.4554 [astro-ph.CO].

Pawlik, Andreas H., Joop Schaye, and Eveline van Scherpenzeel (Apr. 2009). "Keeping the Universe ionized: photoheating and the clumping factor of the high-redshift intergalactic medium". In: *Monthly Notices of the Royal Astronomical Society* 394.4, pp. 1812–1824. DOI: 10.1111/j.1365-2966.2009.14486.x. arXiv: 0807.3963 [astro-ph].

Pearson, W. J. et al. (July 2018). "Main sequence of star forming galaxies beyond the Herschel confusion limit". In: *Astronomy and Astrophysics* 615, A146, A146. DOI: 10.1051/0004-6361/201832821. arXiv: 1804.03482 [astro-ph.GA].

Pezzulli, G. and F. Fraternali (Sept. 2016). "Angular momentum, accretion, and radial flows in chemodynamical models of spiral galaxies". In: *Astronomische Nachrichten* 337.8-9, p. 913. DOI: 10.1002/asna.201612397. arXiv: 1608.04668 [astro-ph.GA].

Pillepich, Annalisa et al. (Dec. 2019). "First results from the TNG50 simulation: the evolution of stellar and gaseous discs across cosmic time". In: *Monthly Notices of the Royal Astronomical Society* 490.3, pp. 3196–3233. DOI: 10.1093/mnras/stz2338. arXiv: 1902.05553 [astro-ph.GA].

Pilyugin, L. S. (Sept. 1993). "On the evolution of helium, nitrogen and oxygen abundances in dwarf irregular galaxies." In: *Astronomy and Astrophysics* 277, pp. 42–52.

Pipino, A., S. J. Lilly, and C. M. Carollo (June 2014). "On the relation between specific star formation rate and metallicity". In: *Monthly Notices of the Royal Astronomical Society* 441.2, pp. 1444–1456. DOI: 10.1093/mnras/stu579. arXiv: 1403.6146 [astro-ph.GA].

Pitts, E. and R. J. Tayler (Sept. 1989). "The chemical evolution of a galactic disc with infall and radial motions". In: *Monthly Notices of the Royal Astronomical Society* 240, pp. 373–395. DOI: 10.1093/mnras/240.2.373.

Planck Collaboration et al. (Sept. 2020). "Planck 2018 results. VI. Cosmological parameters". In: *Astronomy and Astrophysics* 641, A6, A6. DOI: 10.1051/0004-6361/201833910. arXiv: 1807.06209 [astro-ph.CO].

Popesso, P. et al. (Feb. 2009). "The great observatories origins deep survey. VLT/VIMOS spectroscopy in the GOODS-south field". In: *Astronomy and Astrophysics* 494.2, pp. 443–460. DOI: 10.1051/0004-6361:200809617. arXiv: 0802.2930 [astro-ph].

Popesso, P. et al. (Mar. 2019). "The main sequence of star-forming galaxies - I. The local relation and its bending". In: *Monthly Notices of the Royal Astronomical Society* 483.3, pp. 3213–3226. DOI: 10.1093/mnras/sty3210. arXiv: 1812.07057 [astro-ph.GA].

Popping, Gergö, Rachel S. Somerville, and Maud Galametz (Nov. 2017). "The dust content of galaxies from z = 0 to z = 9". In: *Monthly Notices of the Royal Astronomical Society* 471.3, pp. 3152–3185. DOI: 10.1093/mnras/stx1545. arXiv: 1609.08622 [astro-ph.GA].

Porter, L. A. et al. (Dec. 2014). "Modelling the ages and metallicities of early-type galaxies in Fundamental Plane space". In: *Monthly Notices of the Royal Astronomical Society* 445.3, pp. 3092–3104. DOI: 10.1093/mnras/stu1701. arXiv: 1407.2186 [astro-ph.GA].

Pozzi, F. et al. (June 2012). "The AGN content in luminous infrared galaxies at z∼ 2 from a global SED analysis including Herschel data". In: *Monthly Notices of the Royal Astronomical Society* 423.2, pp. 1909–1920. DOI: 10.1111/j.1365-2966.2012.21015.x. arXiv: 1204.1152 [astro-ph.CO].

Pozzi, F. et al. (Sept. 2017). "CO excitation in the Seyfert galaxy NGC 7130". In: *Monthly Notices of the Royal Astronomical Society* 470.1, pp. L64–L68. DOI: 10.1093/mnrasl/slx077. arXiv: 1705.08221 [astro-ph.GA].

Pozzi, F. et al. (Feb. 2020). "The dust mass function from z ∼0 to z ∼2.5". In: *Monthly Notices of the Royal Astronomical Society* 491.4, pp. 5073–5082. DOI: 10.1093/mnras/stz2724. arXiv: 1909.11333 [astro-ph.GA].

Ranalli, P., A. Comastri, and G. Setti (Feb. 2003). "The 2-10 keV luminosity as a Star Formation Rate indicator". In: *Astronomy and Astrophysics* 399, pp. 39–50. DOI: 10.1051/0004-6361:20021600. arXiv: astro-ph/0211304 [astro-ph].

Ranalli, P. et al. (July 2013). "The XMM deep survey in the CDF-S. III. Point source catalogue and number counts in the hard X-rays". In: *Astronomy and Astrophysics* 555, A42, A42. DOI: 10.1051/0004-6361/201321211. arXiv: 1304.5717 [astro-ph.HE].

Recchi, S. and P. Kroupa (Feb. 2015). "The chemical evolution of galaxies with a variable integrated galactic initial mass function". In: *Monthly Notices of the Royal Astronomical Society* 446.4, pp. 4168–4175. DOI: 10.1093/mnras/stu2338. arXiv: 1411.0318 [astro-ph.GA].

Recchi, S. et al. (Oct. 2008). "The effect of differential galactic winds on the chemical evolution of galaxies". In: *Astronomy and Astrophysics* 489.2, pp. 555–565. DOI: 10.1051/0004-6361:200809879. arXiv: 0808.0118 [astro-ph].

Rémy-Ruyer, A. et al. (Mar. 2014). "Gas-to-dust mass ratios in local galaxies over a 2 dex metallicity range". In: *Astronomy and Astrophysics* 563, A31, A31. DOI: 10.1051/0004-6361/201322803. arXiv: 1312.3442 [astro-ph.GA].

Renzini, Alvio (Sept. 2006). "Stellar Population Diagnostics of Elliptical Galaxy Formation". In: *Annual Review of Astronomy and Astrophysics* 44.1, pp. 141–192. DOI: 10.1146/annurev.astro.44.051905.092450. arXiv: astro-ph/0603479 [astro-ph].

Renzini, Alvio and Ying-jie Peng (Mar. 2015). "An Objective Definition for the Main Sequence of Star-forming Galaxies". In: *The Astrophysical Journal, Letters* 801.2, L29, p. L29. DOI: 10.1088/2041-8205/801/2/L29. arXiv: 1502.01027 [astro-ph.GA].

Retzlaff, J. et al. (Feb. 2010). "The Great Observatories Origins Deep Survey. VLT/ISAAC near-infrared imaging of the GOODS-South field". In: *Astronomy and Astrophysics* 511, A50, A50. DOI: 10.1051/0004-6361/200912940. arXiv: 0912.1306 [astro-ph.CO].

Ricarte, Angelo et al. (Oct. 2019). "Tracing black hole and galaxy co-evolution in the ROMULUS simulations". In: *Monthly Notices of the Royal Astronomical Society* 489.1, pp. 802–819. DOI: 10.1093/mnras/stz2161. arXiv: 1904.10116 [astro-ph.GA].

Riechers, Dominik A. et al. (Sept. 2011). "Extended Cold Molecular Gas Reservoirs in z ~= 3.4 Submillimeter Galaxies". In: *The Astrophysical Journall* 739.1, L31, p. L31. DOI: 10.1088/2041-8205/739/1/L31. arXiv: 1105.4177 [astro-ph.CO].

Rieke, G. H. et al. (Feb. 2009). "Determining Star Formation Rates for Infrared Galaxies". In: *The Astrophysical Journal* 692.1, pp. 556–573. DOI: 10.1088/0004-637X/692/1/556. arXiv: 0810.4150 [astro-ph].

Rigopoulou, D. et al. (Dec. 2009). "Spectral energy distributions of type 2 quasi-stellar objects: obscured star formation at high redshifts". In: *Monthly Notices of the Royal Astronomical Society* 400.3, pp. 1199–1207. DOI: 10.1111/j.1365-2966.2009.15543.x. arXiv: 0908.2307 [astro-ph.CO].

Rizzo, F. et al. (Aug. 2020). "A dynamically cold disk galaxy in the early Universe". In: *Nature Astronomy* 584.7820, pp. 201–204. DOI: 10.1038/s41586-020-2572-6. arXiv: 2009.01251 [astro-ph.GA].

Rizzo, Francesca et al. (Feb. 2021). "Dynamical properties of z ~ 4.5 dusty star-forming galaxies and their connection with local early type galaxies". In: *arXiv e-prints*, arXiv:2102.05671, arXiv:2102.05671. arXiv: 2102.05671 [astro-ph.GA].

Rodighiero, G. et al. (Oct. 2011). "The Lesser Role of Starbursts in Star Formation at z = 2". In: *The Astrophysical Journall* 739.2, L40, p. L40. DOI: 10.1088/2041-8205/739/2/L40. arXiv: 1108.0933 [astro-ph.CO].

Rodighiero, G. et al. (Sept. 2014). "A multiwavelength consensus on the main sequence of star-forming galaxies at z ~ 2". In: *Monthly Notices of the Royal Astronomical Society* 443.1, pp. 19–30. DOI: 10.1093/mnras/stu1110. arXiv: 1406.1189 [astro-ph.GA].

Rodighiero, G. et al. (Feb. 2015). "Relationship between Star Formation Rate and Black Hole Accretion At Z = 2: the Different Contributions in Quiescent, Normal, and Starburst Galaxies". In: *The Astrophysical Journal, Letters* 800.1, L10, p. L10. DOI: 10.1088/2041-8205/800/1/L10. arXiv: 1501.04634 [astro-ph.GA].

Rodriguez-Gomez, Vicente et al. (May 2016). "The stellar mass assembly of galaxies in the Illustris simulation: growth by mergers and the spatial distribution of accreted stars". In: *Monthly Notices of the Royal Astronomical Society* 458.3, pp. 2371–2390. DOI: 10.1093/mnras/stw456. arXiv: 1511.08804 [astro-ph.GA].

Rodríguez-Puebla, Aldo et al. (Feb. 2015). "The Stellar-to-Halo Mass Relation of Local Galaxies Segregates by Color". In: *The Astrophysical Journal* 799.2, 130, p. 130. DOI: 10.1088/0004-637X/799/2/130. arXiv: 1408.5407 [astro-ph.GA].

Rodríguez-Puebla, Aldo et al. (Jan. 2016). "Is main-sequence galaxy star formation controlled by halo mass accretion?" In: *Monthly Notices of the Royal Astronomical Society* 455.3, pp. 2592–2606. DOI: 10.1093/mnras/stv2513. arXiv: 1508.04842 [astro-ph.GA].

Romano, D. et al. (Nov. 2010). "Quantifying the uncertainties of chemical evolution studies. II. Stellar yields". In: *Astronomy and Astrophysics* 522, A32, A32. DOI: 10.1051/0004-6361/201014483. arXiv: 1006.5863 [astro-ph.GA].

Romanowsky, Aaron J. and S. Michael Fall (Dec. 2012). "Angular Momentum and Galaxy Formation Revisited". In: *The Astrophysical Journal Supplement Series* 203.2, 17, p. 17. DOI: 10.1088/0067-0049/203/2/17. arXiv: 1207.4189 [astro-ph.CO].

Rosario, D. J. et al. (Sept. 2012). "The mean star formation rate of X-ray selected active galaxies and its evolution from z ∼2.5: results from PEP-Herschel". In: *Astronomy and Astrophysics* 545, A45, A45. DOI: 10.1051/0004-6361/201219258. arXiv: 1203.6069 [astro-ph.CO].

Rujopakarn, W. et al. (Dec. 2016). "VLA and ALMA Imaging of Intense Galaxy-wide Star Formation in z ∼ 2 Galaxies". In: *The Astrophysical Journal* 833.1, 12, p. 12. DOI: 10.3847/0004-637X/833/1/12. arXiv: 1607.07710 [astro-ph.GA].

Rujopakarn, W. et al. (Feb. 2018). "Cospatial Star Formation and Supermassive Black Hole Growth in z ∼ 3 Galaxies: Evidence for In Situ Co-evolution". In: *Astrophysical Journal, Letters* 854.1, L4, p. L4. DOI: 10.3847/2041-8213/aaa9b3. arXiv: 1801.07072 [astro-ph.GA].

Rujopakarn, W. et al. (Sept. 2019). "ALMA 200 pc Resolution Imaging of Smooth Cold Dusty Disks in Typical z ∼ 3 Star-forming Galaxies". In: *The Astrophysical Journal* 882.2, 107, p. 107. DOI: 10.3847/1538-4357/ab3791. arXiv: 1904.04507 [astro-ph.GA].

Saintonge, Amélie et al. (Dec. 2017). "xCOLD GASS: The Complete IRAM 30 m Legacy Survey of Molecular Gas for Galaxy Evolution Studies". In: *The Astrophysical Journal, Supplement* 233.2, 22, p. 22. DOI: 10.3847/1538-4365/aa97e0. arXiv: 1710.02157 [astro-ph.GA].

Salim, Samir, Médéric Boquien, and Janice C. Lee (May 2018). "Dust Attenuation Curves in the Local Universe: Demographics and New Laws for Star-forming Galaxies and High-redshift Analogs". In: *The Astrophysical Journal* 859.1, 11, p. 11. DOI: 10.3847/1538-4357/aabf3c. arXiv: 1804.05850 [astro-ph.GA].

Salmon, Brett et al. (Aug. 2016). "Breaking the Curve with CANDELS: A Bayesian Approach to Reveal the Non-Universality of the Dust-Attenuation Law at High Redshift". In: *The Astrophysical Journal* 827.1, 20, p. 20. DOI: 10.3847/0004-637X/827/1/20. arXiv: 1512.05396 [astro-ph.GA].

Sanders, Ryan L. et al. (Feb. 2015). "The MOSDEF Survey: Mass, Metallicity, and Star-formation Rate at z ∼2.3". In: *The Astrophysical Journal* 799.2, 138, p. 138. DOI: 10.1088/0004-637X/799/2/138. arXiv: 1408.2521 [astro-ph.GA].

Santini, P. et al. (Sept. 2009). "Star formation and mass assembly in high redshift galaxies". In: *Astronomy and Astrophysics* 504.3, pp. 751–767. DOI: 10.1051/0004-6361/200811434. arXiv: 0905.0683 [astro-ph.CO].

Santini, P. et al. (Feb. 2014). "The evolution of the dust and gas content in galaxies". In: *Astronomy and Astrophysics* 562, A30, A30. DOI: 10.1051/0004-6361/201322835. arXiv: 1311.3670 [astro-ph.CO].

Saracco, Paolo et al. (Dec. 2020). "The Rapid Buildup of Massive Early-type Galaxies: Supersolar Metallicity, High Velocity Dispersion, and Young Age for an Early-type Galaxy at z = 3.35". In: *The Astrophysical Journal* 905.1, 40, p. 40. DOI: 10.3847/1538-4357/abc7c4. arXiv: 2011.04657 [astro-ph.GA].

Schaye, Joop et al. (Jan. 2015). "The EAGLE project: simulating the evolution and assembly of galaxies and their environments". In: *Monthly Notices of the Royal Astronomical Society* 446.1, pp. 521–554. DOI: 10.1093/mnras/stu2058. arXiv: 1407.7040 [astro-ph.GA].

Schmidt, Maarten (Mar. 1959). "The Rate of Star Formation." In: *The Astrophysical Journal* 129, p. 243. DOI: 10.1086/146614.

— (Apr. 1963). "The Rate of Star Formation. II. The Rate of Formation of Stars of Different Mass." In: *The Astrophysical Journal* 137, p. 758. DOI: 10.1086/147553.

Schönrich, Ralph and James Binney (June 2009). "Chemical evolution with radial mixing". In: *Monthly Notices of the Royal Astronomical Society* 396.1, pp. 203–222. DOI: 10.1111/j.1365-2966.2009.14750.x. arXiv: 0809.3006 [astro-ph].

Schreiber, C. et al. (Mar. 2017). "The ALMA Redshift 4 Survey (AR4S). I. The massive end of the z = 4 main sequence of galaxies". In: *Astronomy and Astrophysics* 599, A134, A134. DOI: 10.1051/0004-6361/201629155. arXiv: 1606.06252 [astro-ph.GA].

Schreiber, C. et al. (Jan. 2018). "Dust temperature and mid-to-total infrared color distributions for star-forming galaxies at 0 < z < 4". In: *Astronomy and Astrophysics* 609, A30, A30. DOI: 10.1051/0004-6361/201731506. arXiv: 1710.10276 [astro-ph.GA].

Schurer, A. et al. (Apr. 2009). "Modelling the effects of dust evolution on the SEDs of galaxies of different morphological type". In: *Monthly Notices of the Royal Astronomical Society* 394.4, pp. 2001–2021. DOI: 10.1111/j.1365-2966.2009.14441.x. arXiv: 0901.1207 [astro-ph.GA].

Scoville, N. et al. (Mar. 2014). "The Evolution of Interstellar Medium Mass Probed by Dust Emission: ALMA Observations at z = 0.3-2". In: *The Astrophysical Journal* 783.2, 84, p. 84. DOI: 10.1088/0004-637X/783/2/84. arXiv: 1401.2987 [astro-ph.GA].

Scoville, N. et al. (Apr. 2016). "ISM Masses and the Star formation Law at Z = 1 to 6: ALMA Observations of Dust Continuum in 145 Galaxies in the COSMOS Survey Field". In: *The Astrophysical Journal* 820.2, 83, p. 83. DOI: 10.3847/0004-637X/820/2/83. arXiv: 1511.05149 [astro-ph.GA].

Scoville, N. et al. (Mar. 2017). "Evolution of Interstellar Medium, Star Formation, and Accretion at High Redshift". In: *The Astrophysical Journal* 837.2, 150, p. 150. DOI: 10.3847/1538-4357/aa61a0. arXiv: 1702.04729 [astro-ph.GA].

Shankar, F. et al. (May 2006). "New Relationships between Galaxy Properties and Host Halo Mass, and the Role of Feedbacks in Galaxy Formation". In: *The Astrophysical Journal* 643.1, pp. 14–25. DOI: 10.1086/502794. arXiv: astro-ph/0601577 [astro-ph].

Shankar, Francesco, David H. Weinberg, and Jordi Miralda-Escudé (Jan. 2009). "Self-Consistent Models of the AGN and Black Hole Populations: Duty Cycles, Accretion Rates, and the Mean Radiative Efficiency". In: *The Astrophysical Journal* 690.1, pp. 20–41. DOI: 10.1088/0004-637X/690/1/20. arXiv: 0710.4488 [astro-ph].

Sharon, Chelsea E. et al. (Aug. 2016). "A Total Molecular Gas Mass Census in Z ~ 2-3 Star-forming Galaxies: Low-J CO Excitation Probes of Galaxies' Evolutionary States". In: *The Astrophysical Journal* 827.1, 18, p. 18. DOI: 10.3847/0004-637X/827/1/18. arXiv: 1606.02309 [astro-ph.GA].

Shi, J. et al. (July 2017). "Angular Momentum of Early- and Late-type Galaxies: Nature or Nurture?" In: *The Astrophysical Journal* 843.2, 105, p. 105. DOI: 10.3847/1538-4357/aa7893. arXiv: 1706.02165 [astro-ph.GA].

Shin, Jaejin et al. (Aug. 2019). "Positive and Negative Feedback of AGN Outflows in NGC 5728". In: *The Astrophysical Journal* 881.2, 147, p. 147. DOI: 10.3847/1538-4357/ab2e72. arXiv: 1907.00982 [astro-ph.GA].

Shull, J. Michael et al. (Mar. 2012). "Critical Star Formation Rates for Reionization: Full Reionization Occurs at Redshift z ≈ 7". In: *The Astrophysical Journal* 747.2, 100, p. 100. DOI: 10.1088/0004-637X/747/2/100.

Siebenmorgen, R. and E. Krügel (Jan. 2007). "Dust in starburst nuclei and ULIRGs. SED models for observers". In: *Astronomy and Astrophysics* 461.2, pp. 445–453. DOI: 10.1051/0004-6361:20065700. arXiv: astro-ph/0606444 [astro-ph].

Silk, Joseph and Martin J. Rees (Mar. 1998). "Quasars and galaxy formation". In: *Astronomy and Astrophysics* 331, pp. L1–L4. arXiv: astro-ph/9801013 [astro-ph].

Silva, Laura et al. (Dec. 1998). "Modeling the Effects of Dust on Galactic Spectral Energy Distributions from the Ultraviolet to the Millimeter Band". In: *The Astrophysical Journal* 509.1, pp. 103–117. DOI: 10.1086/306476.

Simpson, J. M. et al. (June 2014). "An ALMA Survey of Submillimeter Galaxies in the Extended Chandra Deep Field South: The Redshift Distribution and Evolution of Submillimeter Galaxies". In: *The Astrophysical Journal* 788.2, 125, p. 125. DOI: 10.1088/0004-637X/788/2/125. arXiv: 1310.6363 [astro-ph.CO].

Simpson, J. M. et al. (July 2015). "The SCUBA-2 Cosmology Legacy Survey: ALMA Resolves the Bright-end of the Sub-millimeter Number Counts". In: *The Astrophysical Journal* 807.2, 128, p. 128. DOI: 10.1088/0004-637X/807/2/128. arXiv: 1505.05152 [astro-ph.GA].

Simpson, J. M. et al. (Jan. 2015). "THE SCUBA-2 COSMOLOGY LEGACY SURVEY: ALMA RESOLVES THE REST-FRAME FAR-INFRARED EMISSION OF SUB-MILLIMETER GALAXIES". In: *The Astrophysical Journal* 799.1, p. 81. DOI: 10.1088/0004-637x/799/1/81. URL: https://doi.org/10.1088/0004-637x/799/1/81.

Smail, I. and F. Walter (Sept. 2014). "ALESS: An ALMA Survey of Submillimetre Galaxies in the Extended Chandra Deep Field South". In: *The Messenger* 157, pp. 41–45.

Smail, Ian et al. (Nov. 1999). "HUBBLE SPACE TELESCOPE Near-infrared and Optical Imaging of Faint Radio Sources in the Distant Cluster CL 0939+4713". In: *The Astrophysical Journal* 525.2, pp. 609–620. DOI: 10.1086/307934. arXiv: astro-ph/9905354 [astro-ph].

Smit, Renske et al. (Sept. 2012). "The Star Formation Rate Function for Redshift z ~4-7 Galaxies: Evidence for a Uniform Buildup of Star-forming Galaxies during the First 3 Gyr of Cosmic Time". In: *The Astrophysical Journal* 756.1, 14, p. 14. DOI: 10.1088/0004-637X/756/1/14. arXiv: 1204.3626 [astro-ph.CO].

Solomon, P. M. et al. (Mar. 1997). "The Molecular Interstellar Medium in Ultraluminous Infrared Galaxies". In: *The Astrophysical Journal* 478.1, pp. 144–161. DOI: 10.1086/303765. arXiv: astro-ph/9610166 [astro-ph].

Somerville, Rachel S. and Romeel Davé (Aug. 2015). "Physical Models of Galaxy Formation in a Cosmological Framework". In: *Annual Review of Astronomy and Astrophysics* 53, pp. 51–113. DOI: 10.1146/annurev-astro-082812-140951. arXiv: 1412.2712 [astro-ph.GA].

Sommariva, V. et al. (Mar. 2012). "Stellar metallicity of star-forming galaxies at z ~3". In: *Astronomy and Astrophysics* 539, A136, A136. DOI: 10.1051/0004-6361/201118134. arXiv: 1112.2403 [astro-ph.CO].

Speagle, J. S. et al. (Oct. 2014). "A Highly Consistent Framework for the Evolution of the Star-Forming "Main Sequence" from z ~0-6". In: *The Astrophysical Journal Supplement Series* 214.2, 15, p. 15. DOI: 10.1088/0067-0049/214/2/15. arXiv: 1405.2041 [astro-ph.GA].

Spilker, J. S. et al. (Oct. 2015). "Sub-kiloparsec Imaging of Cool Molecular Gas in Two Strongly Lensed Dusty, Star-forming Galaxies". In: *The Astrophysical Journal* 811.2, 124, p. 124. DOI: 10.1088/0004-637X/811/2/124. arXiv: 1508.07369 [astro-ph.GA].

Spitoni, E., F. Matteucci, and M. M. Marcon-Uchida (Mar. 2013). "Effects of the radial inflow of gas and galactic fountains on the chemical evolution of M 31". In: *Astronomy and Astrophysics* 551, A123, A123. DOI: 10.1051/0004-6361/201220401. arXiv: 1301.5153 [astro-ph.CO].

Spitoni, E., S. Recchi, and F. Matteucci (June 2008). "Galactic fountains and their connection with high and intermediate velocity clouds". In: *Astronomy and Astrophysics* 484.3, pp. 743–753. DOI: 10.1051/0004-6361:200809403. arXiv: 0803.3032 [astro-ph].

Spitoni, E., F. Vincenzo, and F. Matteucci (Mar. 2017). "New analytical solutions for chemical evolution models: characterizing the population of star-forming and passive galaxies". In: *Astronomy and Astrophysics* 599, A6, A6. DOI: 10.1051/0004-6361/201629745. arXiv: 1605.05603 [astro-ph.GA].

Spitoni, E. et al. (Sept. 2009). "Effects of galactic fountains and delayed mixing in the chemical evolution of the Milky Way". In: *Astronomy and Astrophysics* 504.1, pp. 87–96. DOI: 10.1051/0004-6361/200911768. arXiv: 0906.3400 [astro-ph.GA].

Spitoni, Emanuele et al. (Apr. 2015). "The Effect of Stellar Migration on Galactic Chemical Evolution: A Heuristic Approach". In: *The Astrophysical Journal* 802.2, 129, p. 129. DOI: 10.1088/0004-637X/802/2/129. arXiv: 1407.5797 [astro-ph.GA].

Springel, V. et al. (Dec. 2008). "The Aquarius Project: the subhaloes of galactic haloes". In: *Monthly Notices of the Royal Astronomical Society* 391.4, pp. 1685–1711. DOI: 10.1111/j.1365-2966.2008.14066.x. arXiv: 0809.0898 [astro-ph].

Springel, Volker et al. (Mar. 2018). "First results from the IllustrisTNG simulations: matter and galaxy clustering". In: *Monthly Notices of the Royal Astronomical Society* 475.1, pp. 676–698. DOI: 10.1093/mnras/stx3304. arXiv: 1707.03397 [astro-ph.GA].

Stacey, H. R. et al. (Nov. 2020). "The rocky road to quiescence: compaction and quenching of quasar host galaxies at z ∼ 2". In: *Monthly Notices of the Royal Astronomical Society*. DOI: 10.1093/mnras/staa3433. arXiv: 2009.01277 [astro-ph.GA].

Stadel, J. et al. (Sept. 2009). "Quantifying the heart of darkness with GHALO - a multibillion particle simulation of a galactic halo". In: *Monthly Notices of the Royal Astronomical Society* 398.1, pp. L21–L25. DOI: 10.1111/j.1745-3933.2009.00699.x. arXiv: 0808.2981 [astro-ph].

Steidel, Charles C. et al. (Nov. 2014). "Strong Nebular Line Ratios in the Spectra of z ∼2-3 Star Forming Galaxies: First Results from KBSS-MOSFIRE". In: *The Astrophysical Journal* 795.2, 165, p. 165. DOI: 10.1088/0004-637X/795/2/165. arXiv: 1405.5473 [astro-ph.GA].

Steinhardt, Charles L. et al. (Aug. 2014). "Star Formation at 4 < z < 6 from the Spitzer Large Area Survey with Hyper-Suprime-Cam (SPLASH)". In: *The Astrophysical Journall* 791.2, L25, p. L25. DOI: 10.1088/2041-8205/791/2/L25. arXiv: 1407.7030 [astro-ph.GA].

Stevens, Adam R. H. and Toby Brown (Oct. 2017). "Physical drivers of galaxies' cold-gas content: exploring environmental and evolutionary effects with Dark Sage". In: *Monthly Notices of the Royal Astronomical Society* 471.1, pp. 447–462. DOI: 10.1093/mnras/stx1596. arXiv: 1706.07434 [astro-ph.GA].

Stevens, Adam R. H., Darren J. Croton, and Simon J. Mutch (Sept. 2016). "Building disc structure and galaxy properties through angular momentum: the DARK SAGE

semi-analytic model". In: *Monthly Notices of the Royal Astronomical Society* 461.1, pp. 859–876. DOI: 10.1093/mnras/stw1332. arXiv: 1605.00647 [astro-ph.GA].

Stevens, Adam R. H. et al. (Dec. 2018). "Connecting and dissecting galaxies' angular momenta and neutral gas in a hierarchical universe: cue DARK SAGE". In: *Monthly Notices of the Royal Astronomical Society* 481.4, pp. 5543–5559. DOI: 10.1093/mnras/sty2650. arXiv: 1806.07402 [astro-ph.GA].

Stewart, Kyle R. et al. (Sept. 2009). "Galaxy Mergers and Dark Matter Halo Mergers in ΛCDM: Mass, Redshift, and Mass-Ratio Dependence". In: *The Astrophysical Journal* 702.2, pp. 1005–1015. DOI: 10.1088/0004-637X/702/2/1005. arXiv: 0811.1218 [astro-ph].

Straatman, Caroline M. S. et al. (July 2015). "The Sizes of Massive Quiescent and Star-forming Galaxies at z ∼ 4 with ZFOURGE and CANDELS". In: *The Astrophysical Journal, Letters* 808.1, L29, p. L29. DOI: 10.1088/2041-8205/808/1/L29. arXiv: 1506.01380 [astro-ph.GA].

Straughn, Amber N. et al. (Oct. 2009). "Emission-Line Galaxies from the Hubble Space Telescope Probing Evolution and Reionization Spectroscopically (PEARS) Grism Survey. I. The South Fields". In: *Astronomical Journal* 138.4, pp. 1022–1031. DOI: 10.1088/0004-6256/138/4/1022. arXiv: 0907.2254 [astro-ph.CO].

Sutherland, Ralph S. and M. A. Dopita (Sept. 1993). "Cooling Functions for Low-Density Astrophysical Plasmas". In: *The Astrophysical Journal, Supplement* 88, p. 253. DOI: 10.1086/191823.

Suzuki, Tomoko L. et al. (Nov. 2017). "The Interstellar Medium in [O III]-selected Star-forming Galaxies at z ∼ 3.2". In: *The Astrophysical Journal* 849.1, 39, p. 39. DOI: 10.3847/1538-4357/aa8df3. arXiv: 1709.06731 [astro-ph.GA].

Swinbank, A. M. et al. (Sept. 2006). "The link between submillimetre galaxies and luminous ellipticals: near-infrared IFU spectroscopy of submillimetre galaxies". In: *Monthly Notices of the Royal Astronomical Society* 371.1, pp. 465–476. DOI: 10.1111/j.1365-2966.2006.10673.x.

Szokoly, G. P. et al. (Dec. 2004). "The Chandra Deep Field-South: Optical Spectroscopy. I." In: *The Astrophysical Journal Supplement Series* 155.2, pp. 271–349. DOI: 10.1086/424707. arXiv: astro-ph/0312324 [astro-ph].

Tacchella, Sandro et al. (Dec. 2018). "A Redshift-independent Efficiency Model: Star Formation and Stellar Masses in Dark Matter Halos at z ≳ 4". In: *The Astrophysical Journal* 868.2, 92, p. 92. DOI: 10.3847/1538-4357/aae8e0. arXiv: 1806.03299 [astro-ph.GA].

Tacconi, L. J. et al. (Feb. 2018). "PHIBSS: Unified Scaling Relations of Gas Depletion Time and Molecular Gas Fractions". In: *The Astrophysical Journal* 853.2, 179, p. 179. DOI: 10.3847/1538-4357/aaa4b4. arXiv: 1702.01140 [astro-ph.GA].

Tadaki, Ken-ichi et al. (Sept. 2015). "SXDF-ALMA 1.5 arcmin^2 Deep Survey: A Compact Dusty Star-forming Galaxy at z = 2.5". In: *The Astrophysical Journall* 811.1, L3, p. L3. DOI: 10.1088/2041-8205/811/1/L3. arXiv: 1508.05950 [astro-ph.GA].

Tadaki, Ken-ichi et al. (Jan. 2017a). "Bulge-forming Galaxies with an Extended Rotating Disk at z ∼2". In: *The Astrophysical Journal* 834.2, 135, p. 135. DOI: 10.3847/1538-4357/834/2/135. arXiv: 1608.05412 [astro-ph.GA].

Tadaki, Ken-ichi et al. (June 2017b). "Rotating Starburst Cores in Massive Galaxies at z = 2.5". In: *The Astrophysical Journall* 841.2, L25, p. L25. DOI: 10.3847/2041-8213/aa7338. arXiv: 1703.10197 [astro-ph.GA].

Tadaki, Ken-ichi et al. (May 2019). "CNO Emission of an Unlensed Submillimeter Galaxy at z = 4.3". In: *The Astrophysical Journal* 876.1, 1, p. 1. DOI: 10.3847/1538-4357/ab1415. arXiv: 1903.11234 [astro-ph.GA].

Tadaki, Ken-ichi et al. (Sept. 2020). "Structural Evolution in Massive Galaxies at z ∼ 2". In: *The Astrophysical Journal* 901.1, 74, p. 74. DOI: 10.3847/1538-4357/abaf4a. arXiv: 2009.01976 [astro-ph.GA].

Talbot Raymond J., Jr. and W. David Arnett (Dec. 1971). "The Evolution of Galaxies. I. Formulation and Mathematical Behavior of the One-Zone Model". In: *The Astrophysical Journal* 170, p. 409. DOI: 10.1086/151228.

Talia, M. et al. (May 2018). "ALMA view of a massive spheroid progenitor: a compact rotating core of molecular gas in an AGN host at z = 2.226". In: *Monthly Notices of the Royal Astronomical Society* 476.3, pp. 3956–3963. DOI: 10.1093/mnras/sty481. arXiv: 1802.06083 [astro-ph.GA].

Talia, Margherita et al. (Nov. 2020). "Illuminating the dark side of cosmic star formation two billion years after the Big Bang". In: *arXiv e-prints*, arXiv:2011.03051, arXiv:2011.03051. arXiv: 2011.03051 [astro-ph.CO].

Targett, T. A. et al. (July 2013). "The properties of (sub-)millimetre-selected galaxies as revealed by CANDELS HST WFC3/IR imaging in GOODS-South". In: *Monthly Notices of the Royal Astronomical Society* 432.3, pp. 2012–2042. DOI: 10.1093/mnras/stt482. arXiv: 1208.3464 [astro-ph.CO].

Thomas, Daniel et al. (Mar. 2005). "The Epochs of Early-Type Galaxy Formation as a Function of Environment". In: *The Astrophysical Journal* 621.2, pp. 673–694. DOI: 10.1086/426932. arXiv: astro-ph/0410209 [astro-ph].

Thomas, Daniel et al. (June 2010). "Environment and self-regulation in galaxy formation". In: *Monthly Notices of the Royal Astronomical Society* 404.4, pp. 1775–1789. DOI: 10.1111/j.1365-2966.2010.16427.x. arXiv: 0912.0259 [astro-ph.CO].

Thomson, A. P. et al. (July 2014). "An ALMA survey of submillimetre galaxies in the Extended Chandra Deep Field South: radio properties and the far-infrared/radio correlation". In: *Monthly Notices of the Royal Astronomical Society* 442.1, pp. 577–588. DOI: 10.1093/mnras/stu839. arXiv: 1404.7128 [astro-ph.GA].

Tingay, S. J. and M. de Kool (Aug. 2003). "An Investigation of Synchrotron Self-absorption and Free-Free Absorption Models in Explanation of the Gigahertz-peaked Spectrum of PKS 1718-649". In: *Astronomical Journal* 126.2, pp. 723–733. DOI: 10.1086/376600.

Tinker, Jeremy et al. (Dec. 2008). "Toward a Halo Mass Function for Precision Cosmology: The Limits of Universality". In: *The Astrophysical Journal* 688.2, pp. 709–728. DOI: 10.1086/591439. arXiv: 0803.2706 [astro-ph].

Tinsley, B. M. (Sept. 1974). "Constraints on models for chemical evolution in the solar neighborhood." In: *The Astrophysical Journal* 192, pp. 629–641. DOI: 10.1086/153099.

Toft, S. et al. (Feb. 2014). "Submillimeter Galaxies as Progenitors of Compact Quiescent Galaxies". In: *The Astrophysical Journal* 782.2, 68, p. 68. DOI: 10.1088/0004-637X/782/2/68. arXiv: 1401.1510 [astro-ph.GA].

Toft, Sune et al. (June 2017). "A massive, dead disk galaxy in the early Universe". In: *Nature* 546.7659, pp. 510–513. DOI: 10.1038/nature22388. arXiv: 1706.07030 [astro-ph.GA].

Tollet, Édouard et al. (May 2019). "NIHAO XIX: how supernova feedback shapes the galaxy baryon cycle". In: *Monthly Notices of the Royal Astronomical Society* 485.2, pp. 2511–2531. DOI: 10.1093/mnras/stz545. arXiv: 1902.03888 [astro-ph.GA].

Toomre, A. (May 1964). "On the gravitational stability of a disk of stars." In: *The Astrophysical Journal* 139, pp. 1217–1238. DOI: 10.1086/147861.

Torrey, Paul et al. (Apr. 2019). "The evolution of the mass-metallicity relation and its scatter in IllustrisTNG". In: *Monthly Notices of the Royal Astronomical Society* 484.4, pp. 5587–5607. DOI: 10.1093/mnras/stz243. arXiv: 1711.05261 [astro-ph.GA].

Totani, Tomonori et al. (Dec. 2008). "Delay Time Distribution Measurement of Type Ia Supernovae by the Subaru/XMM-Newton Deep Survey and Implications for the Progenitor". In: *Publications of the ASJ* 60, p. 1327. DOI: 10.1093/pasj/60.6.1327. arXiv: 0804.0909 [astro-ph].

Trayford, James W. and Joop Schaye (June 2019). "Resolved galaxy scaling relations in the EAGLE simulation: star formation, metallicity, and stellar mass on kpc scales". In: *Monthly Notices of the Royal Astronomical Society* 485.4, pp. 5715–5732. DOI: 10.1093/mnras/stz757. arXiv: 1812.06984 [astro-ph.GA].

Tremonti, Christy A. et al. (Oct. 2004). "The Origin of the Mass-Metallicity Relation: Insights from 53,000 Star-forming Galaxies in the Sloan Digital Sky Survey". In: *The Astrophysical Journal* 613.2, pp. 898–913. DOI: 10.1086/423264. arXiv: astro-ph/0405537 [astro-ph].

Turner, O. J. et al. (Oct. 2017). "The KMOS Deep Survey (KDS) - I. Dynamical measurements of typical star-forming galaxies at z 3.5". In: *Monthly Notices of the Royal Astronomical Society* 471.2, pp. 1280–1320. DOI: 10.1093/mnras/stx1366. arXiv: 1704.06263 [astro-ph.GA].

Übler, Hannah et al. (Sept. 2014). "Why stellar feedback promotes disc formation in simulated galaxies". In: *Monthly Notices of the Royal Astronomical Society* 443.3, pp. 2092–2111. DOI: 10.1093/mnras/stu1275. arXiv: 1403.6124 [astro-ph.GA].

Valiante, Rosa et al. (Aug. 2009). "Stellar sources of dust in the high-redshift Universe". In: *Monthly Notices of the Royal Astronomical Society* 397.3, pp. 1661–1671. DOI: 10.1111/j.1365-2966.2009.15076.x. arXiv: 0905.1691 [astro-ph.CO].

Vallini, L. et al. (Dec. 2019). "Impact of X-rays on CO emission from high-z galaxies". In: *Monthly Notices of the Royal Astronomical Society* 490.4, pp. 4502–4514. DOI: 10.1093/mnras/stz2837. arXiv: 1910.07550 [astro-ph.GA].

van de Sande, Jesse et al. (July 2013). "Stellar Kinematics of z ~2 Galaxies and the Inside-out Growth of Quiescent Galaxies". In: *The Astrophysical Journal* 771.2, 85, p. 85. DOI: 10.1088/0004-637X/771/2/85. arXiv: 1211.3424 [astro-ph.CO].

van der Burg, R. F. J., H. Hildebrandt, and T. Erben (Nov. 2010). "The UV galaxy luminosity function at z = 3-5 from the CFHT Legacy Survey Deep fields". In: *Astronomy and Astrophysics* 523, A74, A74. DOI: 10.1051/0004-6361/200913812. arXiv: 1009.0758 [astro-ph.CO].

van der Wel, A. et al. (Dec. 2012). "Structural Parameters of Galaxies in CANDELS". In: *The Astrophysical Journal Supplement Series* 203.2, 24, p. 24. DOI: 10.1088/0067-0049/203/2/24. arXiv: 1211.6954 [astro-ph.CO].

van der Wel, A. et al. (June 2014). "3D-HST+CANDELS: The Evolution of the Galaxy Size-Mass Distribution since z = 3". In: *The Astrophysical Journal* 788.1, 28, p. 28. DOI: 10.1088/0004-637X/788/1/28. arXiv: 1404.2844 [astro-ph.GA].

van der Wel, Arjen et al. (Nov. 2008). "Recent Structural Evolution of Early-Type Galaxies: Size Growth from z = 1 to z = 0". In: *The Astrophysical Journal* 688.1, pp. 48–58. DOI: 10.1086/592267. arXiv: 0808.0077 [astro-ph].

van Dokkum, Pieter G. et al. (Apr. 2008). "Confirmation of the Remarkable Compactness of Massive Quiescent Galaxies at z ~2.3: Early-Type Galaxies Did not Form in a Simple Monolithic Collapse". In: *The Astrophysical Journall* 677.1, p. L5. DOI: 10.1086/587874. arXiv: 0802.4094 [astro-ph].

van Dokkum, Pieter G. et al. (Aug. 2014). "Dense Cores in Galaxies Out to z = 2.5 in SDSS, UltraVISTA, and the Five 3D-HST/CANDELS Fields". In: *The Astrophysical Journal* 791.1, 45, p. 45. DOI: 10.1088/0004-637X/791/1/45. arXiv: 1404.4874 [astro-ph.GA].

van Dokkum, Pieter G. et al. (Nov. 2015). "Forming Compact Massive Galaxies". In: *The Astrophysical Journal* 813.1, 23, p. 23. DOI: 10.1088/0004-637X/813/1/23. arXiv: 1506.03085 [astro-ph.GA].

Vanzella, E. et al. (Jan. 2008). "The great observatories origins deep survey. VLT/FORS2 spectroscopy in the GOODS-South field: Part III". In: *Astronomy and Astrophysics* 478.1, pp. 83–92. DOI: 10.1051/0004-6361:20078332. arXiv: 0711.0850 [astro-ph].

Vattakunnel, S. et al. (Mar. 2012). "The radio-X-ray relation as a star formation indicator: results from the Very Large Array-Extended Chandra Deep Field-South". In: *Monthly Notices of the Royal Astronomical Society* 420.3, pp. 2190–2208. DOI: 10.1111/j.1365-2966.2011.20185.x. arXiv: 1111.3285 [astro-ph.CO].

Velander, Malin et al. (Jan. 2014). "CFHTLenS: the relation between galaxy dark matter haloes and baryons from weak gravitational lensing". In: *Monthly Notices of the Royal Astronomical Society* 437.3, pp. 2111–2136. DOI: 10.1093/mnras/stt2013. arXiv: 1304.4265 [astro-ph.CO].

Venemans, Bram P. et al. (Oct. 2018). "Dust Emission in an Accretion-rate-limited Sample of $z \gtrsim 6$ Quasars". In: *The Astrophysical Journal* 866.2, 159, p. 159. DOI: 10.3847/1538-4357/aadf35. arXiv: 1809.01662 [astro-ph.GA].

Vincenzo, F., F. Matteucci, and E. Spitoni (Apr. 2017). "A simple and general method for solving detailed chemical evolution with delayed production of iron and other chemical elements". In: *Monthly Notices of the Royal Astronomical Society* 466.3, pp. 2939–2947. DOI: 10.1093/mnras/stw3369. arXiv: 1606.08469 [astro-ph.GA].

Vincenzo, F. et al. (Feb. 2016). "Modern yields per stellar generation: the effect of the IMF". In: *Monthly Notices of the Royal Astronomical Society* 455.4, pp. 4183–4190. DOI: 10.1093/mnras/stv2598. arXiv: 1503.08300 [astro-ph.GA].

Vogelsberger, Mark et al. (Oct. 2014). "Introducing the Illustris Project: simulating the coevolution of dark and visible matter in the Universe". In: *Monthly Notices of the Royal Astronomical Society* 444.2, pp. 1518–1547. DOI: 10.1093/mnras/stu1536. arXiv: 1405.2921 [astro-ph.CO].

Walcher, C. J. et al. (Oct. 2016). "Self-similarity in the chemical evolution of galaxies and the delay-time distribution of SNe Ia". In: *Astronomy and Astrophysics* 594, A61, A61. DOI: 10.1051/0004-6361/201528019. arXiv: 1607.00015 [astro-ph.GA].

Walter, Fabian et al. (June 2012). "The intense starburst HDF 850.1 in a galaxy overdensity at $z \approx 5.2$ in the Hubble Deep Field". In: *Nature Astronomy* 486.7402, pp. 233–236. DOI: 10.1038/nature11073. arXiv: 1206.2641 [astro-ph.CO].

Wang, Ran et al. (Nov. 2008). "Thermal Emission from Warm Dust in the Most Distant Quasars". In: *The Astrophysical Journal* 687.2, pp. 848–858. DOI: 10.1086/591076. arXiv: 0806.3022 [astro-ph].

Wang, Ran et al. (Aug. 2013). "Star Formation and Gas Kinematics of Quasar Host Galaxies at $z \sim 6$: New Insights from ALMA". In: *The Astrophysical Journal* 773.1, 44, p. 44. DOI: 10.1088/0004-637X/773/1/44. arXiv: 1302.4154 [astro-ph.CO].

Watson, William A. et al. (Aug. 2013). "The halo mass function through the cosmic ages". In: *Monthly Notices of the Royal Astronomical Society* 433.2, pp. 1230–1245. DOI: 10.1093/mnras/stt791. arXiv: 1212.0095 [astro-ph.CO].

Weigel, Anna K. et al. (Apr. 2015). "The systematic search for $z \gtrsim 5$ active galactic nuclei in the Chandra Deep Field South". In: *Monthly Notices of the Royal Astronomical Society* 448.4, pp. 3167–3195. DOI: 10.1093/mnras/stv184. arXiv: 1501.06580 [astro-ph.GA].

Weinberg, David H., Brett H. Andrews, and Jenna Freudenburg (Mar. 2017). "Equilibrium and Sudden Events in Chemical Evolution". In: *The Astrophysical Journal* 837.2, 183, p. 183. DOI: 10.3847/1538-4357/837/2/183. arXiv: 1604.07435 [astro-ph.GA].

Weiß, A. et al. (Dec. 2009). "The Large Apex Bolometer Camera Survey of the Extended Chandra Deep Field South". In: *The Astrophysical Journal* 707.2, pp. 1201–1216. DOI: 10.1088/0004-637X/707/2/1201. arXiv: 0910.2821 [astro-ph.CO].

Whitaker, Katherine E. et al. (Nov. 2014). "Constraining the Low-mass Slope of the Star Formation Sequence at 0.5 < z < 2.5". In: *The Astrophysical Journal* 795.2, 104, p. 104. DOI: 10.1088/0004-637X/795/2/104. arXiv: 1407.1843 [astro-ph.GA].

White, Simon D. M. and Carlos S. Frenk (Sept. 1991). "Galaxy Formation through Hierarchical Clustering". In: *The Astrophysical Journal* 379, p. 52. DOI: 10.1086/170483.

Williams, Christina C. et al. (Oct. 2019). "Discovery of a Dark, Massive, ALMA-only Galaxy at z ∼ 5-6 in a Tiny 3 mm Survey". In: *The Astrophysical Journal* 884.2, 154, p. 154. DOI: 10.3847/1538-4357/ab44aa. arXiv: 1905.11996 [astro-ph.GA].

Willott, Chris J., Jacqueline Bergeron, and Alain Omont (Mar. 2015). "Star Formation Rate and Dynamical Mass of 10^8 Solar Mass Black Hole Host Galaxies At Redshift 6". In: *The Astrophysical Journal* 801.2, 123, p. 123. DOI: 10.1088/0004-637X/801/2/123. arXiv: 1501.07538 [astro-ph.GA].

Windhorst, Rogier A. and Seth H. Cohen (Nov. 2010). "How HST/WFC3 and JWST Can Measure Galaxy Assembly and AGN Growth". In: *First Stars and Galaxies: Challenges for the Next Decade*. Ed. by Daniel J. Whalen, Volker Bromm, and Naoki Yoshida. Vol. 1294. American Institute of Physics Conference Series, pp. 225–233. DOI: 10.1063/1.3518858.

Wisnioski, E. et al. (Feb. 2015). "The KMOS^{3D} Survey: Design, First Results, and the Evolution of Galaxy Kinematics from 0.7 <= z <= 2.7". In: *The Astrophysical Journal* 799.2, 209, p. 209. DOI: 10.1088/0004-637X/799/2/209. arXiv: 1409.6791 [astro-ph.GA].

Wojtak, Radosław and Gary A. Mamon (Jan. 2013). "Physical properties underlying observed kinematics of satellite galaxies". In: *Monthly Notices of the Royal Astronomical Society* 428.3, pp. 2407–2417. DOI: 10.1093/mnras/sts203. arXiv: 1207.1647 [astro-ph.CO].

Wolf, C. et al. (July 2004). "A catalogue of the Chandra Deep Field South with multi-colour classification and photometric redshifts from COMBO-17". In: *Astronomy and Astrophysics* 421, pp. 913–936. DOI: 10.1051/0004-6361:20040525. arXiv: astro-ph/0403666 [astro-ph].

Worthey, G. (Jan. 1999). "The Age-Metallicity Degeneracy". In: *Spectrophotometric Dating of Stars and Galaxies*. Ed. by Ivan Hubeny, Sally Heap, and Robert Cornett. Vol. 192. Astronomical Society of the Pacific Conference Series, p. 283.

Wuyts, Stijn et al. (Nov. 2009). "Optical Spectroscopy of Distant Red Galaxies". In: *The Astrophysical Journal* 706.1, pp. 885–895. DOI: 10.1088/0004-637X/706/1/885. arXiv: 0910.1836 [astro-ph.CO].

Xue, Y. Q. et al. (Sept. 2010). "Color-Magnitude Relations of Active and Non-active Galaxies in the Chandra Deep Fields: High-redshift Constraints and Stellar-mass Selection Effects". In: *The Astrophysical Journal* 720.1, pp. 368–391. DOI: 10.1088/0004-637X/720/1/368. arXiv: 1007.1453 [astro-ph.CO].

Xue, Y. Q. et al. (July 2011). "The Chandra Deep Field-South Survey: 4 Ms Source Catalogs". In: *The Astrophysical Journal Supplement Series* 195.1, 10, p. 10. DOI: 10.1088/0067-0049/195/1/10. arXiv: 1105.5643 [astro-ph.CO].

Yang, C. et al. (Dec. 2017). "Molecular gas in the Herschel-selected strongly lensed submillimeter galaxies at z 2-4 as probed by multi-J CO lines". In: *Astronomy and Astrophysics* 608, A144, A144. DOI: 10.1051/0004-6361/201731391. arXiv: 1709.04740 [astro-ph.GA].

Yıldırım, Akın et al. (July 2017). "The structural and dynamical properties of compact elliptical galaxies". In: *Monthly Notices of the Royal Astronomical Society* 468.4, pp. 4216–4245. DOI: 10.1093/mnras/stx732. arXiv: 1701.05898 [astro-ph.GA].

Yun, Min S. et al. (Feb. 2012). "Deep 1.1 mm-wavelength imaging of the GOODS-S field by AzTEC/ASTE - II. Redshift distribution and nature of the submillimetre galaxy population". In: *Monthly Notices of the Royal Astronomical Society* 420.2, pp. 957–985. DOI: 10.1111/j.1365-2966.2011.19898.x. arXiv: 1109.6286 [astro-ph.CO].

Zahid, H. J. et al. (Sept. 2014). "The FMOS-COSMOS Survey of Star-forming Galaxies at z ∼1.6. II. The Mass-Metallicity Relation and the Dependence on Star Formation Rate and Dust Extinction". In: *The Astrophysical Journal* 792.1, 75, p. 75. DOI: 10.1088/0004-637X/792/1/75. arXiv: 1310.4950 [astro-ph.CO].

Zhao, D. H. et al. (Feb. 2003). "The growth and structure of dark matter haloes". In: *Monthly Notices of the Royal Astronomical Society* 339.1, pp. 12–24. ISSN: 0035-8711. DOI: 10.1046/j.1365-8711.2003.06135.x. eprint: https://academic.oup.com/mnras/article-pdf/339/1/12/3551163/339-1-12.pdf. URL: https://doi.org/10.1046/j.1365-8711.2003.06135.x.

Zhukovska, S., H. P. Gail, and M. Trieloff (Feb. 2008). "Evolution of interstellar dust and stardust in the solar neighbourhood". In: *Astronomy and Astrophysics* 479.2, pp. 453–480. DOI: 10.1051/0004-6361:20077789. arXiv: 0706.1155 [astro-ph].

Zhukovska, Svitlana et al. (Nov. 2016). "Modeling Dust Evolution in Galaxies with a Multiphase, Inhomogeneous ISM". In: *The Astrophysical Journal* 831.2, 147, p. 147. DOI: 10.3847/0004-637X/831/2/147. arXiv: 1608.04781 [astro-ph.GA].

Zjupa, Jolanta and Volker Springel (Apr. 2017). "Angular momentum properties of haloes and their baryon content in the Illustris simulation". In: *Monthly Notices of the Royal Astronomical Society* 466.2, pp. 1625–1647. DOI: 10.1093/mnras/stw2945. arXiv: 1608.01323 [astro-ph.CO].

Zolotov, Adi et al. (July 2015). "Compaction and quenching of high-z galaxies in cosmological simulations: blue and red nuggets". In: *Monthly Notices of the Royal Astronomical Society* 450.3, pp. 2327–2353. DOI: 10.1093/mnras/stv740. arXiv: 1412.4783 [astro-ph.GA].